Study of graphene-based Josephson junctions in the quantum Hall effect regime

Hadrien Vignaud

THÈSE

Pour obtenir le grade de

DOCTEUR DE L'UNIVERSITÉ GRENOBLE ALPES

École doctorale : PHYS - Physique
Spécialité : Physique de la Matière Condensée et du Rayonnement
Unité de recherche : Institut Néel

Etude de jonctions Josephson à base de graphène dans le régime d'effet Hall quantique

Study of graphene-based Josephson junctions in the quantum Hall effect regime

Présentée par :

Hadrien VIGNAUD

Direction de thèse :

Hervé COURTOIS PROFESSEUR DES UNIVERSITES, UNIVERSITE GRENOBLE ALPES	Directeur de thèse
Benjamin SACEPE CHARGE DE RECHERCHE HDR, CNRS DELEGATION ALPES	Co-directeur de thèse

Rapporteurs :

HELENE BOUCHIAT
DIRECTRICE DE RECHERCHE, CNRS DELEGATION ILE-DE-FRANCE SUD
FRANÇOIS PARMENTIER
CHARGE DE RECHERCHE HDR, CNRS DELEGATION ILE-DE-FRANCE SUD

Thèse soutenue publiquement le **20 décembre 2023**, devant le jury composé de :

SILVANO DE FRANCESCHI, DIRECTEUR DE RECHERCHE, CEA CENTRE DE GRENOBLE	Président
HELENE BOUCHIAT, DIRECTRICE DE RECHERCHE, CNRS DELEGATION ILE-DE-FRANCE SUD	Rapporteure
FRANÇOIS PARMENTIER, CHARGE DE RECHERCHE HDR, CNRS DELEGATION ILE-DE-FRANCE SUD	Rapporteur
JULIA MEYER, PROFESSEURE DES UNIVERSITES, UNIVERSITE GRENOBLE ALPES	Examinatrice
SRIJIT GOSWAMI, DOCTEUR EN SCIENCES, DELFT UNIVERSITY OF TECHNOLOGY	Examinateur

RÉSUMÉ/ABSTRACT

FRANÇAIS La combinaison de l'effet Josephson, soit le transfert de paires de Cooper entre deux blocs supraconducteurs séparés par une barrière suffisamment fine, avec le régime d'effet Hall quantique, dans lequel un courant circule via des canaux unidimensionnels le long des bords d'un gaz d'électron bi-dimensionnel, pourrait, sous certaines conditions, générer un nouveau type de quasi-particules présentant une statistique d'échange non-abélienne.

Bien que ces deux effets aient été indépendamment observés il y a maintenant plus de 40 ans, la mise en évidence d'un supercourant médié par les états de bord de l'effet Hall quantique, dit *supercourant chiral*, reste encore à démontrer.

Dans cette thèse, nous étudions des jonctions Josephson dont la partie normale est constituée de graphène en régime d'effet Hall quantique. L'emploi de nanorubans de graphène pour nos échantillons, combiné à l'utilisation d'électrodes à base de MoGe, un supraconducteur désordonné ayant un champ critique supérieur à 12 T, nous a permis d'observer un supercourant dans le plateau de résistance d'effet Hall quantique $\nu = 2$ jusqu'à une valeur de champ magnétique de 8 T, un record pour ce type de dispositif. Sous rayonnement micro-onde, le supercourant forme des pas de Shapiro indiquant une relation courant-phase 2π-périodique.

L'emploi d'une carte d'acquisition permettant d'effectuer des mesures de courbes I/V ultra-rapides a rendu possible l'étude systématique de ce supercourant en fonction de la tension de grille, du champ magnétique et du courant de polarisation appliqué.

En particulier, dans le plan tension de grille – champ magnétique, la valeur maximale du supercourant (extraite des courbes I/V successives) présente des oscillations dans la région correspondant au plateau d'effet Hall quantique $\nu = 2$. Nous observons également des oscillations dans la résistance différentielle calculée à partir de ces courbes I/V.

A tension de grille fixée, dans nos jonctions les plus petites, la période en champ magnétique de ces oscillations ne peut être reliée à la valeur usuelle du quantum de flux supraconducteur $h/2e$, et ce même en tenant compte de l'incertitude sur l'estimation de l'aire de nos dispositifs.

Toutefois, à facteur de remplissage ν constant, la période correspond à un quantum de flux h/e, une valeur anticipée par les théories traitant d'un supercourant médié par les états de bord de l'effet Hall quantique.

En outre, l'application d'une analyse de Fourier sur ces oscillations permet de mettre en évidence une réduction de leur période à mesure que le facteur de remplissage augmente, une observation nous permettant d'accéder à la dispersion des niveaux de Landau aux bords de l'échantillon.

L'analyse de Fourier révèle également une réduction de la période de ces oscillations avec le champ magnétique, ce que nous expliquons par l'influence de ce dernier sur l'extension spatiale des fonctions d'onde des canaux de bords de l'effet Hall quantique. Enfin, l'étude de la dépendance des oscillations de résistance à la tension mesurée aux bornes des jonctions révèle un motif en damier, une observation rappelant les signatures d'effets d'interférence habituellement reportés dans des analogues d'interféromètres Fabry-Perot en régime d'effet Hall quantique. En poussant cette analogie, il est possible d'estimer l'énergie de Thouless associée aux porteurs de charge impliqués dans ces effets d'interférence et par suite, de mettre en évidence une renormalisation de la vitesse des canaux de bords de l'effet Hall quantique le long des interfaces graphène-supraconducteur.

ENGLISH Combining the Josephson effect, i.e. the transfer of Cooper pairs between two superconducting blocks separated by a sufficiently thin barrier, with the quantum Hall effect regime, in which a current flows via one-dimensional channels along the edges of a two-dimensional electron gas, could, under certain conditions, generate a new type of quasiparticle with non-Abelian exchange statistics.

Although these two effects were independently observed more than 40 years ago, the identification of a supercurrent mediated by the edge states of the quantum Hall effect, termed *chiral supercurrent*, has yet to be demonstrated.

In this PhD work, we study Josephson junctions whose normal part is made of graphene in the quantum Hall effect regime. The use of graphene nanoribbons for our samples, combined with electrodes made of MoGe, a disordered superconductor with a critical field above 12 T, has enabled us to observe a supercurrent in the $\nu = 2$ quantum Hall plateau up to a magnetic field value of 8 T, a record for this type of device. Under microwave radiation, the supercurrent forms Shapiro steps indicating a 2π-periodic current-phase relation.

The use of an acquisition card enabling ultra-fast I/V curve measurements has made it possible to systematically investigate this supercurrent as a function of gate voltage, magnetic field and applied current bias.

In particular, in the gate voltage-magnetic field plane, the switching current value (extracted from successive I/V curves) exhibits oscillations in the region corresponding to the $\nu = 2$ quantum Hall plateau. We also observe oscillations in the differential resistance calculated from these I/V curves.

At fixed gate voltage, in our smallest junctions, the magnetic field period of these oscillations cannot be related to the usual value of the superconducting flux quantum $h/2e$, even considering the uncertainty in the estimated area of our devices.

However, at constant filling factor ν, the period corresponds to a flux quantum h/e, a value anticipated by theories dealing with a supercurrent mediated by the quantum Hall edge states.

In addition, the application of a Fourier analysis to these oscillations unveils a reduction in their period as the filling factor increases, an observation that gives us an access to the dispersion of Landau levels at the graphene's edges.

Fourier analysis also reveals a reduction in the oscillations' period as the magnetic field increases, which we explain by the latter's influence on the spatial extension of the wave functions of the quantum Hall edge channels.

Finally, a study of the dependence of the resistance oscillations on the voltage reveals a checkerboard-like pattern, an observation reminiscent of the interference effects signatures usually reported in analogues of Fabry-Perot interferometers in the quantum Hall effect regime. Extending this analogy, it is possible to estimate the Thouless energy associated with the charge carriers involved in these interference effects, and consequently to demonstrate a renormalization of the velocity of the quantum Hall edge states along the graphene-superconductor interfaces.

Remerciements/Acknowledgments

Grenoble, Février 2024.

Clap de fin. Le doctorat (enfin) en poche, un chapitre se clore pour laisser place à de nouvelles aventures qui, je l'espère, seront au moins aussi riches que celles vécues au cours de ces dernières années. Dans une tentative maladroite de manifester ma reconnaissance envers tous les personnages clés impliqués dans cette période, je souhaiterai ici leur dédier ces toutes dernières lignes, tâche au combien délicate à mesure que de nombreux souvenirs affleurent à l'esprit…

Le fil directeur de ces dernières années a sans conteste été Benjamin Sacépé qui, au-delà de la « simple » supervision de thèse, fut un vrai mentor. L'un des facteurs clés dans la réussite de cette thèse a, je pense, grandement tenu à cette remarquable capacité qu'il a d'« imprégner » ses collaborateurs de son enthousiasme pour une idée, une vision ou un cap, un atout clé pour un thésard impliqué par nature dans des travaux de long terme. Outre ce sens de l'inspiration, une disponibilité hors-norme (week-ends et soirées inclus) a sans conteste contribué à assurer le succès de ce projet. Je tiens donc ici à exprimer toute ma gratitude envers Benjamin.

Ces quelques années à l'Institut Néel m'ont également permis de côtoyer d'autres chercheurs de grand talent à qui je souhaiterai également rendre tous les honneurs. Tout d'abord, Hervé Courtois qui, en dépit d'un emploi du temps extrêmement chargé, a toujours suivi attentivement le déroulement de ces travaux de thèse tout en sachant se rendre disponible pour répondre à nos questions/apporter le regard d'un expert de la physique des jonctions Josephson. Autre acteur majeur de cette aventure, Hermann Sellier, dont une maîtrise impressionnante de la physique dans tous ses aspects a souvent grandement enrichi nos discussions de groupe. Je tiens aussi à remercier Julien Renard et Manuel Houzet qui, ayant accepté d'être membres de mon jury de CSI, ont suivi attentivement et dans un esprit bienveillant l'avancement de mes travaux de thèse. Toute ma gratitude également envers Zheng (Vitto) Han et l'ensemble des membres de son groupe pour m'avoir chaleureusement accueilli à la veille du tout début de ma thèse afin de m'enseigner leurs méthodes de fabrication. Je conclurai cette partie en remerciant tout particulièrement les membres de mon jury de thèse pour avoir accepté d'évaluer mes travaux, à savoir, Hélène Bouchiat, François Parmentier, Silvano De Franceschi, Julia Meyer et Srijit Goswami.

Ces premiers paragraphes ne doivent en aucun cas éclipser les rôles clés joués par le personnel technique de l'Institut Néel sans qui, je tiens tout particulièrement à le souligner ici, rien n'aurait été possible. En premier lieu, Frédéric Gay et Florent Blondelle nous ont sans conteste épargné de nombreuses difficultés grâce à leur remarquable savoir-faire en cryogénie, électronique et Labview, une richesse que je jalouse encore au moment d'écrire ces lignes. Autre artisan de nos succès, Edouard Wagner, dont le talent pour Labview nous permis d'exploiter pleinement le potentiel de la carte d'acquisition, outil capital dans l'obtention des résultats les plus importants de cette thèse. Plus proche des problématiques en lien avec la fabrication d'échantillons, nerf de la guerre dans notre domaine, j'ai toujours pu compter sur l'aide précieuse de Simon Le Denmat et son incroyable expertise concernant l'utilisation des microscopes à force atomique. Son comparse de bureau, Thierry Crozes, n'est pas en reste : sachant toujours se rendre disponible, ce dernier nous a grandement aidé

pour arriver à nos fins avec la lithographie électronique. Je tiens au passage à remercier l'équipe Nanofab pour tout le support apporté au cours de ces années, et plus particulièrement Bruno Fernandez et Gwénaëlle Julie qui ont toujours su répondre promptement à nos demandes concernant la salle blanche.
J'en profite également pour remercier ici le personnel administratif de l'institut, et plus particulièrement Angélique Simoes et Anne-Laure Jaussent qui ont toujours fait le maximum pour nous accompagner au fil de ces années de thèse.
Viens maintenant l'hommage à mes chers camarades de mine, plutôt d'exfoliation diront certains… J'ai eu la chance de connaître deux « générations » de membres du groupe de Benjamin.
Lors de mon arrivée, Louis Veyrat et Corentin Déprez m'ont pris sous leur aile pour m'apprendre les arcanes de la fabrication d'échantillons en salle blanche tout en me mettant le pieds à l'étrier pour les mesures de transport. Au-delà de l'aspect purement professionnel, j'ai rencontré ici deux véritables amis. Mention spéciale aux discussions dédiées aux pre-print ArXiv du jour autour du petit café matinal. A quelques bureaux de là se trouvait les deux autres « personnages » de l'équipe, à savoir Alexis Coissard et Marco Guerra, qui, au fil de nombreuses soirées vin – charcuterie – fromages du groupe (la sainte trinité des bons vivants), devinrent également de très bons amis. Outre un bonapartiste fantasmant le retour de l'empire et un italien défendant bec-et-ongles que le berceau de la civilisation se trouvait à Turin, j'eus également la chance de rencontrer Thibault Charpentier qui, du fait de son amour du vin, de la ripaille et des belles lettres françaises, s'est parfaitement marié à l'esprit de la troupe.
Petite parenthèse ici pour mentionner aussi les bons moments passés avec Guilliam Butseraen (et Susanne De Conti), Nicolas Apariccio, Aloïs Arrighi, Juliette Letellier et Goutham Nayak. Autre rencontre remarquable au cours de ces années, Danial Majidi et sa femme Tabassom Arnand, dont le sens de l'amitié n'a d'égale que leur incroyable savoir-vivre. Amitiés à tous.
Vient maintenant l'expression de ma gratitude envers la « deuxième » génération de membres ayant constitué le groupe de Benjamin. Tout d'abord, Bilal Kousar et son sens du professionalisme « à l'américaine » qui, combiné à son expérience acquise lors de son passage à QDev (Copenhague), ont contribué à élever les standards de qualité pour la fabrication d'échantillons dans le groupe. Petite dédicace également à Diego Foisson, force tranquille de l'équipe, tenant toujours une calebasse à maté à la main. Ensuite Wenmin Yang, notre experte en quantum Hall interferometers, post-doc aussi discrète qu'attachante de l'équipe, toujours ouverte à la discussion. Pour finir, David Perconte, l'homme à chats de l'équipe, un post-doc plus que patient avec le thésard que j'étais.
Je tiens aussi à mentionner les quelques stagiaires ayant pris part aux travaux de l'équipe au fil de ces années : Andres, Asma, Oliver et Karl. Petite dédicace également à Gao Xiang et sa charmante épouse, qui, je l´espère, ont apprécié leur séjour en France.
Jusqu'à présent, mes remerciements se sont adressés aux membres du monde académique. Toutefois, et ce déjà bien avant le début de la thèse proprement dite, j'ai bénéficié d'un soutien sans faille des membres de ma famille. Au-delà de l'encouragement à poursuivre mes rêves, mes parents, ma sœur et Bandit (et maintenant Filou) ont toujours été présents, aussi bien dans les nombreux moments de joie que de difficultés. Bien qu'ayant conscience que ces quelques mots de remerciement demeurent bien maigres en comparaison de leur investissement, je tiens ici à leur dédier tous les honneurs de ces travaux de thèse qui, j'en suis convaincu, n'auraient pas été aussi fructueux sans eux.
Pour finir, je souhaiterai consacrer ces derniers mots à ma chère libanaise, Ramla Msheik, qui, il faut bien le dire, m'a patiemment supporté au quotidien durant ces années et sans qui, et je pèse mes mots, cette thèse n'aurait pas été possible. Ton affection, ton soutien, ta patience et ton sourire en toute circonstance, pour ne citer que quelques unes de tes nombreuses qualités, m'ont permis de relever tous les défis.

MORE MAJORUM.
Devise des légionnaires parachutistes.

Table of Contents

Introduction

Since its initial prediction in 1962, the Josephson effect - the transfer of Cooper pairs between 2 superconducting blocks connected by a link made of another material - has been, and continues to be, one of the most studied topics in condensed matter physics, a fact presumably reflecting the wealth of materials that can be interleaved between the 2 superconducting electrodes.
In recent years, Josephson effect and more generally proximity-induced superconductivity, experienced a surge of interest driven by the promise of realizing novel quasiparticles with exotic properties that might be of interest for quantum computation.
Among the various approaches put forward, one of the most promising is to induce superconductivity in a 2-dimensional electron gas (2DEG) placed in the quantum Hall effect (QHE) regime.
The latter, discovered in 1980 by K. von Klitzing in Grenoble, typically emerges in weakly disordered 2DEG, at low temperature and under high magnetic field. In this regime, transport takes place via 1-dimensional edge channels, propagating ballistically around the bulk, which remains insulating. Its main experimental manifestation is the observation of resistance plateaus whose values are quantized as a multiple of h/e^2, h and e denoting the Planck constant and the elementary charge.
Yet, quantum Hall effect and superconductivity are fundamentally antagonistic, as high magnetic field is required to induce the former one. In addition, for decades, QHE was mainly studied using semiconductor-based heterostructures in which proximity-induced superconductivity was hindered by the formation of Schottky barriers.
Therefore, the ability to successfully isolate a single sheet of graphene from 2004, together with the ease with which superconducting contacts can be interfaced to it, have clearly opened up a new avenue for the study of quantum Hall - superconducting electrodes hybrids.
In this PhD work, we investigated such a coupling using high-quality graphene-based Josephson junctions contacted with MoGe, a disordered superconductor withstanding superconductivity up to an upper critical magnetic field of about 12.5 T, thus enabling us to study Josephson effect in the quantum Hall regime.

This thesis manuscript is organized as follows:

- **Chapter 1:** We introduce the band structure of graphene, as well as the properties derived from it for the quantum Hall effect regime and for Andreev reflection. The Blonder-Tinkham-Klapwijk formalism is also briefly described. Following this, we discuss the theory of proximity-induced superconductivity in a 2DEG placed in the quantum Hall effect regime.
  In a second part, we focus on the physics of quantum Hall Josephson junctions. We introduce the key signature associated with a supercurrent mediated by the quantum Hall edge states, termed *chiral supercurrent*, that is an anomalous h/e-flux periodicity. Then, we discuss the quantum Hall edge channels velocity renormalization along NS interfaces - a consequence of the successive Andreev reflections - and how it affects the Thouless energy associated with the supercurrent-carrying particles. In conclusion, we address specificities

of proximity-induced superconductivity in graphene placed in the QHE regime.

- **Chapter 2:** A state of the art review of Josephson junctions in the quantum Hall regime. It includes the earliest historical attempts using semiconductor-based two-dimensional electron gases, the first graphene-based Josephson junctions, the work of G. Finkelstein's group, a pioneer in the study of graphene-based Josephson junctions in the quantum Hall regime, as well as a brief presentation of the approach used by the P. Kim's group and based on the crossed Andreev conversion mechanism.

- **Chapter 3:** In this chapter, we present a set of measurements to characterize our Josephson junctions. This includes the field effect in graphene, the supercurrent dependence on the back-gate voltage, I/V characteristics using high current bias to estimate the transparency of our contacts, Fraunhofer pattern measurements as well as a characterization of the quantum Hall effect.

- **Chapter 4:** This chapter is dedicated to preliminary investigations of the Josephson effect occurrence within the quantum Hall regime. First, we demonstrate the presence of a robust supercurrent within the $\nu = 2$ quantum Hall plateau for junctions whose NS interfaces length is short ($W < 300$ nm). Results on control devices with $\sim$2 μm-long NS interfaces are also discussed in the light of theories dealing with the chiral supercurrent.
  In order to characterize the supercurrent observed in the $\nu = 2$ quantum Hall plateau, we perform Shapiro steps measurements to deduce the current-phase relation.
  Finally, we discuss the effect that the use of superconducting electrodes can have on the quantum Hall resistance quantization, i.e. the chiral Andreev edge states physics.

- **Chapter 5:** This chapter is devoted to the main result of this PhD work, namely the demonstration of the chiral supercurrent occurence within our quantum Hall Josephson junctions. First, we report on the observation of switching current oscillations accross the $\nu = 2$ quantum Hall plateau in the B-V_{g} plane. Then, we explain the need to consider these oscillations with the magnetic field B at constant filling factor ν, rather than at constant back-gate voltage value V_{g}, a consequence of the smallness of our devices.
  Fourier analysis of the switching current oscillations in the B-ν plane then demonstrate a h/e-flux periodicity, the key signature of a quantum Hall edge states-mediated supercurrent.
  We also report on the observation of low bias resistance oscillations accross the $\nu = 2$ quantum Hall plateau in the B-V_{g} plane. Similarly to the switching current case, these oscillations have to be considered at constant filling factor, rather than constant back-gate voltage, to unveil a h/e-flux periodicity in magnetic field. The latter, which is supported by several Fourier analysis, is typical of oscillations associated with Aharonov-Bohm interferences, indicating the presence of a coherent loop within our junctions.
  Studying the voltage dependence of the above-mentioned resistance oscillations leads to the observation of checkerboard patterns, strongly reminiscent of what is observed in the context of quantum Hall Fabry-Perot interferometers. Going further with this analogy, we extract a Thouless energy which, in turn, enables us to estimate the velocity of the quantum Hall edge channels propagating along the NS interfaces.
  Finally, we discuss the presence of Coulomb diamonds at the edge of the $\nu = 2$ quantum Hall plateau.

Part I

Chiral supercurrent: theory and present experimental status

Chapter 1

Chiral supercurrent: a theoretical introduction

This chapter starts with an introduction to the theoretical background of the graphene transport properties. In detail, this includes the graphene's linear dispersion relation, together with the resulting properties. Among them is the half-integer quantum Hall effect, to which we dedicate a specific section.
This work being dedicated to proximity-induced superconductivity in the quantum Hall regime, we then introduce the Andreev reflection mechanism, which allows for a current flowing in a normal metal to be converted into a supercurrent upon crossing a superconducting interface. The latter having a finite-transparency value in actual devices, we also shortly describe the Blonder-Tinkham-Klapwijk (BTK) formalism [1] that enables to account for the effect of a barrier of arbitrary height at the NS interface.
Crucially, this discussion allows us to introduce the Bogoliubov-De Gennes approach, which forms the heart of most models treating proximity-induced superconductivity in the quantum Hall regime.
Next, we dedicate a specific part to *quantum Hall Josephson junctions*. The main signature of quantum Hall edge states-mediated supercurrent, or *chiral supercurrent*, is an anomalous h/e-flux periodicity.
We also highlight how crucial is the edge states velocity renormalization along the NS interfaces in a dedicated discussion.
Finally, we discuss how the interplay between disorder and graphene specificities may affect this physics.

1.1 Basic building blocks

1.1.1 Graphene's band structure and massless Dirac fermions

Graphene is a two-dimensional crystal made of carbon atoms arranged in a regular honeycomb lattice[1]. Each atom hosts four valence electrons and is linked to three neighbors by σ-bonds as shown in Figure 1.1.a. These bonds result from the hybridization of the in-plane valence electrons orbitals 2s, $2p_x$ and $2p_y$, an effect that follows from the graphene two-dimensional nature. The remaining out-of-plane $2p_z$ orbital, which holds the fourth valence electron, can bend to form a delocalized covalent π-bond with neighboring carbon atoms. Electrons involved in the σ-bonds are tightly bound to carbon atoms and consequently lie at very low energy scales

[1] If one consider two neighboring atoms in a hexagonal lattice, the bonds they form with the surrounding atoms do not have the same orientation: while the first one has one neighbor on the left and two neighbors on the right (see a blue site in Figure 1.1.a), the second one has two neighbors on the left and one neighbor on the right (see a red site in Figure 1.1.a). This necessarily implies that there is no way to reconstruct the whole lattice using basis vectors defined by the bounds between adjacent atoms i.e. the hexagonal structure does not constitute a Bravais lattice. The graphene can rather be considered as made of two triangular sub-lattices (denoted A and B in 1.1.a). Introducing basis vectors linking atoms of the sub-lattice A say, it is possible to define a Bravais unit cell enabling to tile the whole graphene lattice, each cell containing one site A and one site B.

irrelevant for graphene transport properties. In contrast, delocalized π-electrons band crosses the graphene's intrinsic Fermi level, the energy scale that determines electron transport characteristics.

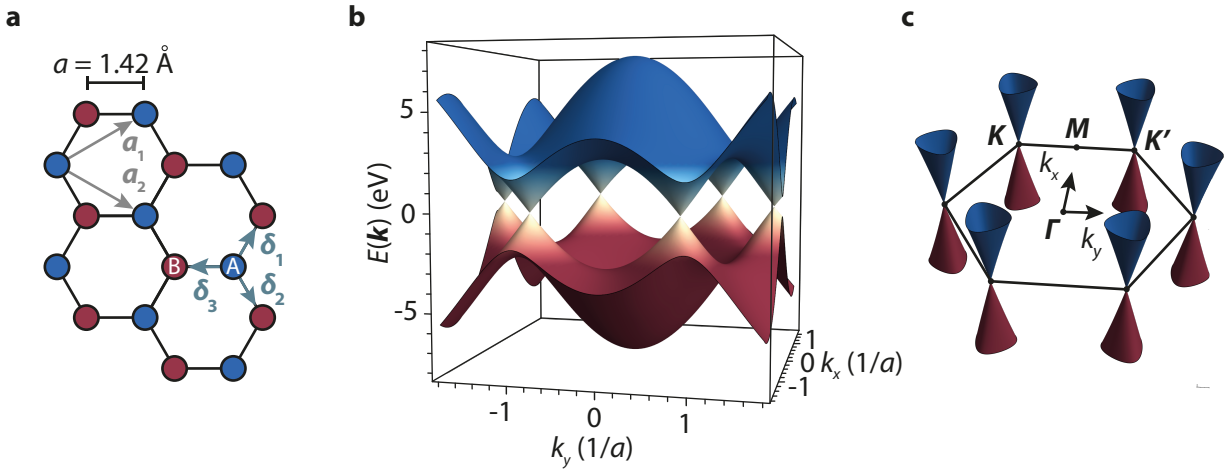

Figure 1.1: **Graphene's band structure. a)** Honeycomb lattice structure of the graphene. The blue (resp. red) color denotes the sites belonging to the sub-lattice A (resp. B). Vectors $\boldsymbol{a}_1$ and $\boldsymbol{a}_2$ are the primitive translation vectors of the sub-lattice A. Vectors $\boldsymbol{\delta}_1$, $\boldsymbol{\delta}_2$ and $\boldsymbol{\delta}_3$ translate the different paths an electron located on a site A can take to reach an atom belonging to the sub-lattice B. **b)** Dispersion relation of the graphene obtained from the tight-binding model described in the text. The positive (resp. negative) part of the band structure corresponds to the conduction (resp. valence) band. **c)** Zoom on the first Brillouin zone of graphene. The Dirac cones locate at the corners of the first Brillouin zone. Note that successive corners are not equivalent in the sens that the set of reciprocal space vectors attached to the sub-lattice A do not allow to locate the six Dirac cones at once. This unequivalence, termed *valley*, translates as two distinct sets of Dirac cones, denoted $\boldsymbol{K}$ and $\boldsymbol{K'}$ that alternate at the corners of the first Brillouin zone.

Graphene's transport properties can be further understood by introducing a tight-binding model that essentially captures how π-electrons hop from one atomic site to a neighboring one. Here, for the sake of simplicity, we only consider hopping to nearest neighbors which translates as the following Hamiltonian:

$$\hat{H} = -t \sum_{\boldsymbol{r}_\mathrm{A}} \sum_{\alpha=1,2,3} [\hat{c}_\mathrm{B}^\dagger(\boldsymbol{r}_\mathrm{A} + \boldsymbol{\delta}_\alpha) \cdot \hat{c}_\mathrm{A}(\boldsymbol{r}_\mathrm{A}) + \mathrm{h.c.}] \tag{1.1}$$

where $t \approx 2.7$ eV is the hopping energy and h.c. refers to the hermitian conjugate of the first term. The summation runs over the set of vectors $\boldsymbol{r}_\mathrm{A}$ defining the sub-lattice A site positions. The connection from sites A to sites B is then specified using a second summation term running over the $\boldsymbol{\delta}_\alpha$ vectors index, these vectors being defined as:

$$\boldsymbol{\delta}_1 = \frac{a}{2} \cdot \begin{pmatrix} 1 \\ \sqrt{3} \end{pmatrix} \quad , \quad \boldsymbol{\delta}_2 = \frac{a}{2} \cdot \begin{pmatrix} 1 \\ -\sqrt{3} \end{pmatrix} \quad , \quad \boldsymbol{\delta}_3 = -a \cdot \begin{pmatrix} 1 \\ 0 \end{pmatrix} \tag{1.2}$$

with $a = 1.42$ Å the inter-atomic distance between adjacent carbon atoms. In order to obtain the graphene dispersion relation $E(\boldsymbol{k})$, we can re-express the Hamiltonian (1.1) in the momentum space. Using the Fourier transform of the creation and annihilation operators, we then obtain the following expression:

$$\hat{H} = \sum_{\boldsymbol{k}} (\hat{c}_\mathrm{A}^\dagger \quad \hat{c}_\mathrm{B}^\dagger) \begin{pmatrix} 0 & \gamma^*(\boldsymbol{k}) \\ \gamma(\boldsymbol{k}) & 0 \end{pmatrix} \begin{pmatrix} \hat{c}_\mathrm{A} \\ \hat{c}_\mathrm{B} \end{pmatrix} \tag{1.3}$$

with $\gamma(\boldsymbol{k}) = -2t[\mathrm{e}^{-iak_x/2} \cdot \cos(a\sqrt{3}k_y/2) + \mathrm{e}^{iak_x}]$.
Ultimately, the Hamiltonian diagonalization leads to the following eigenvalues:

$$E(\boldsymbol{k}) = \pm t\sqrt{4\cos^2\left(\frac{a\sqrt{3}}{2}k_y\right) + 4\cos\left(\frac{a\sqrt{3}}{2}k_y\right)\cos\left(\frac{3a}{2}k_x\right) + 1} \tag{1.4}$$

The corresponding energy spectrum is portrayed in Figure 1.1.b. As the π-orbitals are half-filled (each carbon atom providing one electron per spin-degenerate π-orbital), the resulting band structure is half-filled. Thus, following the energy spectrum symmetry with respect to the $E(\boldsymbol{k}) = 0$ eV plane, graphene's intrinsic Fermi level lies at zero energy.

Remarkably, the gap between the conduction ($E(\boldsymbol{k}) > 0$) and valence ($E(\boldsymbol{k}) < 0$) bands gets closed into a discrete set of points corresponding to the corners of the first Brillouin zone (see Figure 1.1.c). Using the set of reciprocal space lattice vectors attached to one of the graphene's sub-lattices, it is impossible to connect two successive corners, only every second Dirac cones can be successively linked to the others.
This inequivalence between successive Dirac cones, termed *valley*, constitutes an extra degree of freedom for the charge carriers in graphene, in addition to the usual spin degree of freedom. As we shall see in the next, this quantum number plays a fundamental role in the graphene physics.

To further capture the consequences of the graphene's conical band structure, it is possible to expand (1.4) around the points $\boldsymbol{K}$ and $\boldsymbol{K}'$ introducing $\boldsymbol{q} = \boldsymbol{k} - \boldsymbol{K}^{(\prime)}$, such that $|\boldsymbol{q}| \ll |\boldsymbol{K}^{(\prime)}|$:

$$E(\boldsymbol{q}) \approx \pm\hbar v_\mathrm{F}|\boldsymbol{q}| + \mathcal{O}[(|\boldsymbol{q}|/|\boldsymbol{K}^{(\prime)}|)^2] \tag{1.5}$$

with $v_\mathrm{F} = 3ta/2 \approx 10^6$ m/s the Fermi velocity.
Here comes one of the most striking properties of graphene's charge carriers: a dispersion relation exhibiting a linear dependence on $\boldsymbol{q}$, a feature usually associated with massless relativistic particles such as photons[2].
A direct consequence of such a linear dispersion relation is a mass-independant Fermi velocity, at odds with conventional two-dimensional electron gases (2DEGs) for which $v_\mathrm{F} = \hbar|\boldsymbol{k}_\mathrm{F}|/m$, with $\boldsymbol{k}_\mathrm{F}$ the Fermi momentum and m denoting the electrons effective mass.

Going further with the relativistic physics analogy, the low-energy Hamiltonian (1.5) can be shown to express as a Dirac Hamiltonian [2]:

$$\hat{H}_\mathrm{D}(\boldsymbol{q}) = \pm\hbar v_\mathrm{F}\boldsymbol{q}\cdot\boldsymbol{\sigma} = \pm\hbar v_\mathrm{F}(q_x\sigma_x + q_y\sigma_y) = \pm\hbar v_\mathrm{F}\begin{pmatrix} 0 & q_x - iq_y \\ q_x + iq_y & 0 \end{pmatrix} \tag{1.6}$$

where $\boldsymbol{\sigma} = (\sigma_x, \sigma_y)$ denotes the Pauli matrices[3].
This low-energy Hamiltonian will prove central for deriving the charge carriers spectrum in graphene when the latter is exposed to a perpendicular magnetic field, a subject to which is devoted the next section.

[2] As a reminder, the dispersion relation for relativistic particles reads as $E(\boldsymbol{k})^2 = |\boldsymbol{k}|^2c^2 + m^2c^4$ with c the speed of light and m the particle's mass. Thus, for massless particles such as photons, the dispersion relation expression becomes linear in $|\boldsymbol{k}|$.

[3] $\sigma_x = \begin{pmatrix} 0 & 1 \\ 1 & 0 \end{pmatrix}, \sigma_y = \begin{pmatrix} 0 & -i \\ i & 0 \end{pmatrix}$.

1.1.2 Quantum Hall effect in graphene

A direct consequence of this relativistic physics is the observation of a *half-integer* quantum Hall effect under perpendicular magnetic fields.
This transport regime, specific to two-dimensional electron gases and whose first evidence dates back to 1980 [3], is usually studied using a set of contacts forming a so-called quantum Hall bar geometry, a typical device schematic being shown in Figure 1.2.a.
Provided the temperature and the disorder are low enough, this effect translates into a vanishing longitudinal resistance R_{xx} while, simultaneously, the transverse resistance R_{xy} exhibits a plateau whose value is an integer multiple of h/e^2 (see Figure 1.2.b).

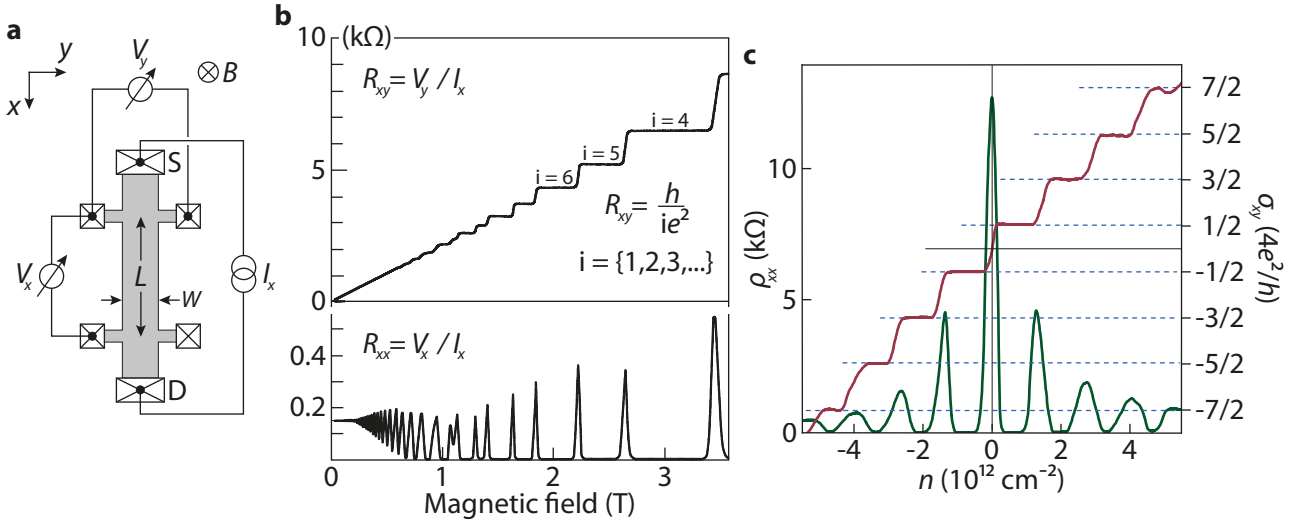

Figure 1.2: **Quantum Hall effect. a)** Schematic of a typical quantum Hall bar. The longitudinal (resp. transverse) voltage V_x (resp. V_y) is measured while a current bias I_x is set between the source (S) and the drain (D) contacts. **b)** Top part: transverse resistance $R_{xy} = V_y/I_x$ versus magnetic field. Bottom part: longitudinal resistance $R_{xx} = V_x/I_x$ versus magnetic field. Both curves were obtained using a 2DEG embedded within a GaAs/AlGaAs heterostructure. Each time R_{xy} exhibits a plateau, R_{xx} drops to zero. The temperature and the density were not specified. Figures taken from [4]. **c)** Longitudinal resistivity ρ_{xx} (resp. transverse conductivity σ_{xy}) versus the charge carriers density n, measured in graphene at $B = 14$ T and $T = 4$ K. While ρ_{xx} and σ_{xy} behave the same way as in GaAs/AlGaAs-based 2DEGs i.e. a vanishingly small ρ_{xx} each time σ_{xy} exhibits a plateau, the latter's quantized values lie at $\sigma_{xy} = \pm 4(\mathrm{N} + 1/2)e^2/h$, a feature specific to the quantum Hall effect in graphene. Figure taken from [5].

In the graphene specific case, the term *half-integer* refers to the unconventional sequence of quantum Hall plateaus that appear each time the ratio between R_{xy} and the constant h/e^2 equates $\pm 4(\mathrm{N}+1/2)$ with $\mathrm{N} \in \{0, \pm 1, \pm 2, ...\}$, rather than simply N as with conventional 2DEGs[4].

The origin of these features can be understood by including the effect of a perpendicular magnetic field in the graphene's Dirac Hamiltonian (1.6)[5]. The resulting discrete set of eigenenergies, termed *Landau levels* (LLs), reads as:

[4] While the factor 4 translates the four-fold degeneracy of the charge carriers in graphene (2 for the spin degree of freedom and 2 for the valley degree of freedom), the term $+1/2$ relates to the non-zero Berry phase in graphene [5].

[5] Details of this procedure can be found in [6].

$$E_{\mathsf{N}}(B_\perp) = \mathrm{sgn}(\mathsf{N}) v_{\mathsf{F}} \sqrt{2\hbar e |\mathsf{N}| B_\perp} \tag{1.7}$$

where e is the absolute value of the electron´s charge, N an integer labelling each Landau level (see Figure1.3.a) and $B_\perp$ the magnitude of the applied perpendicular magnetic field.
While Landau levels in conventional 2DEGs disperse linearly with $B_\perp$, the graphene's LLs follow a square-root dependence on $B_\perp$. Moreover, the cyclotron gap between successive Landau levels, which is constant for a given $B_\perp$-field in conventional 2DEGs, here varies with the Landau levels under consideration[6].

Crucially, the above result was derived assuming a boundless graphene. However, in practice, samples have a finite-size, an element key to the quantum Hall effect physics.
Samples limits are usually captured adding an effective electrostatic confining potential within the Hamiltonian describing the 2D electrons under magnetic field [7; 8][7].
As shown in Figure 1.3.b, this confining potential bends the Landau levels spectrum in the vicinity of the 2DEG edges. Assuming the Fermi level locates within a given cyclotron gap[8], some bent Landau levels intersect with it, thus giving rise to ballistic 1D edge channels[9].
Importantly, the group velocity attached to the edge states reads as:

$$v_{\text{group}} = \frac{1}{\hbar}\frac{\partial E_{\mathsf{N}}(y_*)}{\partial k}\bigg|_{y_*=l_B^2 k_x} = \frac{1}{eB}\frac{\partial V(y_*)}{\partial y_*}\bigg|_{y_*=l_B^2 k_x} \tag{1.8}$$

with V the confining potential and $y_* = l_B^2 k_x$ the guiding center coordinate, which relates the position of the electrons wavefunctions along the y-axis to their momentum in the x direction, i.e. the axis along which the edge states propagate.
The derivate of the LLs spectrum with respect to the position being reversed on either side of the 2DEG, this implies that edge states run in opposite direction along either edges, a feature termed *quantum Hall edge states chirality*.
Provided opposite edges are far apart enough with respect to each others, the transport solely takes place through a discrete set of 1D ballistic edge channels, hence explaining the quantized resistance value in units of h/e^2 [10].
As the edge states tranport regime relates to the position of the Fermi level, that is to the filling of the Landau levels, it is convenient for the next to introduce the so-called *filling factor* parameter ν.
In detail, $\nu = n/n_B$ with n the electron density (whose variation corresponds to the Fermi level increase/decrease)

[6] For instance, the cyclotron gap between the N $= 0$ and the N $= \pm 1$ Landau levels is about 36.2·$\sqrt{B_\perp[\mathsf{T}]}$ meV, that is 420.1·$\sqrt{B_\perp[\mathsf{T}]}$ K.

[7] Note that in alternative approaches, samples boundaries are encoded by stating that the wavefunctions describing the electrons vanish at the edges of the 2DEG [9; 10].

[8] Strictly speaking, if we stick to the drawing shown in Figure 1.3.b, the Fermi level would directly jump from one Landau level to the next one, as no states are available within the bulk to pin the Fermi level within the cyclotron gap. Ultimately, this would prevent edge states physics to develop and therefore prevent R_{xy}-plateaus to be resolved in transport measurements. In actual samples, however, disorder broadens Landau levels. This gives rise to some localized states randomly distributed accross the 2DEG's bulk and to which the Fermi level can be pinned. Provided the density of localized states remains low enough i.e. no conducting paths connecting opposite edge channels via these localized states develop, quantized transport signatures are expected each time the Fermi level get pinned within a cyclotron gap. It is in this sense that disorder is essential to the observation of the quantum Hall effect.

[9] For the sake of clarity, we leave aside edge states reconstruction physics here.

[10] The link between the presence of 1D ballistic channels and the measure of a resistance whose value is quantized in units of h/e^2 in the quantum Hall regime was thoroughly investigated by M. Büttiker in [11].

and $n_B = B/\Phi_0$, the density of flux quanta $\Phi_0 = h/e$ threading the 2DEG. Actually, the latter is directly proportional to the Landau level degeneracy per unit area $D = 4B/\Phi_0$, the factor 4 again accounting for the four-fold degeneracy attached to charge carriers within graphene.

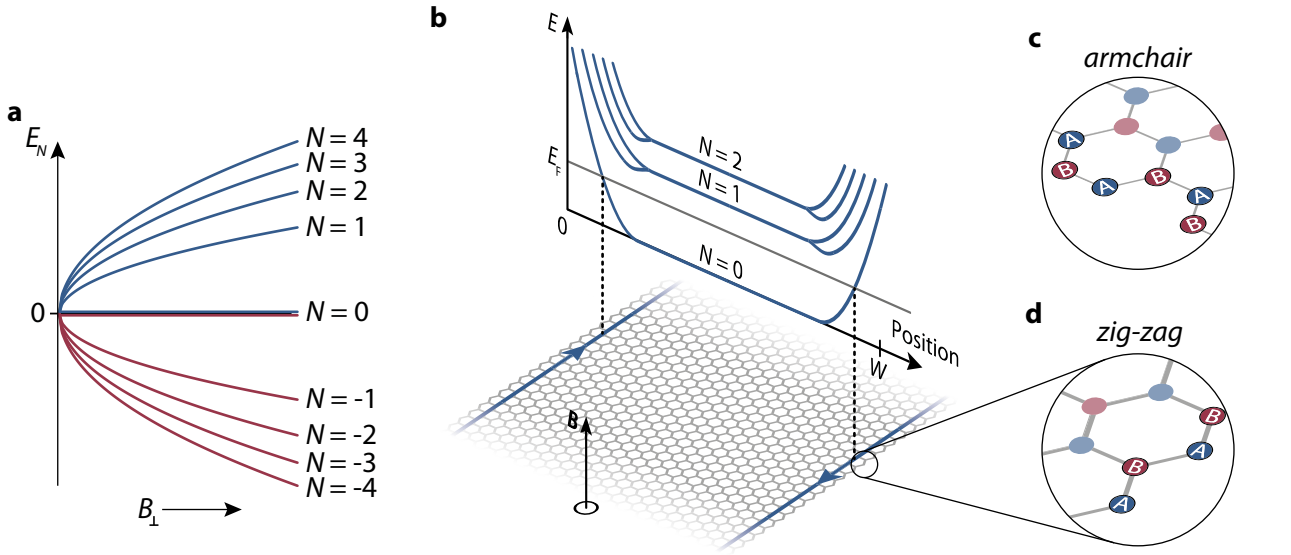

Figure 1.3: **Landau levels in graphene. a)** Landau levels spectrum E_N, N being an integer index, versus the perpendicular magnetic field $B_\perp$. The Zeeman gap $E_Z = g\mu_B|\boldsymbol{B}| \approx 0.116{\cdot}|\boldsymbol{B}|[\mathrm{T}]$ meV and the valley gap $E_V = 0.31{\cdot}|\boldsymbol{B}|[\mathrm{T}]/\epsilon_r$ meV, with a dielectric constant value $\epsilon_r \sim 4$ for SiO_2 and h-BN, attached to the zeroth Landau level being much smaller than the cyclotron gap between the N $= 0$ and N $= \pm 1$ levels (about $36.2{\cdot}\sqrt{B_\perp[\mathrm{T}]}$ meV [6]), we do not represent them here. **b)** Landau levels spectrum as a function of the position accross a graphene ribbon. Provided the Fermi level lies within a cyclotron gap, its intersect with the Landau level(s) on either side of the graphene results into the formation of 1D conducting channels having opposite direction of propagation on each side of the graphene. **c,d)** In graphene, the details of the LL edge states dispersion relate to the cristallographic structure along the last atomic row. In **(b)**, the ribbon was depicted with zig-zag terminations (see the zoomed view provided in **(d)**). In that case, Landau levels get split into two valley-polarized, spin-degenerate, sub-levels while approaching the graphene's edges. Note that an other kind of disorder-free crystal terminations, termed armchair, is possible (see in **(c)**). In that case, LLs split into 2 sub-levels, that are both spin- and valley-degenerate.

Contrary to conventional 2DEGs, whose limits are electrostatically defined using gates, graphene's edges naturally arise from the finite size of the crystal. In details, assuming an ideal situation with no structural disorder, graphene's cristallographic terminations can take different forms: *armchair*, *zig-zag* or a combination of both (see schematics in Figures 1.3.c,d).
These structural considerations directly influence the wavefunctions of the electrons in the vicinity of the last atoms of the crystal, hence the Landau levels dispersion along the edges [10; 12]:

- For the armchair case, the N > 0 (resp. N < 0) LLs bend upwards (resp. downwards) while approaching the edges. Each of these Landau levels get split into two sub-levels, both spin- and valley-degenerate, in the edges vicinity. For the zeroth Landau level, the Landau level will split into one upwards and one downwards branch, each of them being both spin and valley-degenerate.

- For the zig-zag case, the N > 0 (resp. N < 0) LLs bend upwards (resp. downwards) while approaching the edge. As the last atomic row lies within one of the valleys, the corresponding degeneracy is lifted.

Thus, each Landau levels is splitted into two valley-polarized, spin-degenerate, sub-Landau levels along the graphene's edges. For the N $= 0$ Landau level more specific case, this valley degeneracy lifting yields one valley polarized, spin-degenerate, branch to bend upwards while a second branch attached to the same valley and spin-degenerate as well, bends downwards. The states belonging to the other valley form a dispersionless level at zero energy.

As we shall see later on, the valley polarization for the N $= 0$ Landau level edge states will turn out be central when considering Andreev reflection in graphene placed in the quantum Hall effect regime.

1.1.3 Proximity-induced superconductivity in the quantum Hall regime

In recent years, graphene has proven to be a fertile playground for another paradigmatic condensed matter physics phenomenon, namely superconductivity.
This culminated in 2018 with the observation of an intrinsic superconducting phase within the so-called "magic angle" twisted bilayer graphene [13], the report of which triggering intense efforts, both on the experimental and theoretical sides, still underway for a better understanding of this physics [14].
In addition to its intrinsic superconducting properties, the ease with which graphene couples with superconducting electrodes, when compared to standard semiconductor-based devices[11], strongly favoured the study of the so-called proximity-induced superconductivity in graphene, a subject to which is dedicated the following section.

1.1.3.1 Andreev reflection mechanism

Proximity-induced superconductivity, in a very broad sense, refers to the physics occuring when a superconducting electrode (S) is interfaced with a normal metal (N) or a semiconductor. Central to this effect is the Andreev-Saint James reflection process [15; 16], a quantum mechanical scattering mechanism that allows for converting a dissipative current, flowing within the normal part, into a dissipationless Cooper pairs-based current into the superconducting electrode.

In order to support the following discussion, we refer the reader to the NS interface schematic shown in Figure 1.4.a.
Let's consider a given electron state $k = k_F + \delta k$[12,13] in the normal metal part whose energy E_k is such that $E_k - E_F < \Delta_0$, Δ_0 being the electrode superconducting gap, that impiges the NS interface.
At first sight, the absence of single particle states within the superconducting gap prevents charge transfer to the electrode[14]. In particular, this is in line with the early observation that the thermal resistance of a superconductor placed in the intermediate state is higher [18]: successive NS interfaces are expected to limit the transfer of charge, and hence heat. However, in the intermediate state, a superconductor always conducts electricity perfectly. This contradiction, i.e. a material that is both a good thermal insulator and an excellent

[11] See Chapter 2 Section 2.1 for a detailed discussion.

[12] For the sake of simplicity, one assume here a disorder-free metal such that k remains a good quantum number to label single particle states within the normal part.

[13] The density of states of the normal metal being subjected to Fermi-Dirac statistics, non-zero temperature naturally leads to thermally-excited states above the Fermi level.

[14] Interestingly, I. Giaever took advantage of this fact to achieve the first measurement of the density of state of a superconducting material through tunnel current measurements accross a normal metal - insulator - superconductor (NIS) junction [17], a work which earned him the Nobel Prize in Physics in 1973.

electrical conductor, led A. F. Andreev [16; 19][15] to consider a second-order process in which the incoming electron state $(k_F + \delta k, \uparrow)$ pairs up with a sub-Fermi level state $(k_F - \delta k, \downarrow)$ to form a Cooper pair entering the superconducting electrode. Following momentum, charge and spin conservation, this process leaves aside a hole state $(-k_F + \delta k, \downarrow)$ that moves away from the interface[16].
In addition, Andreev reflection is a coherent mechanism i.e. there is a precise relation between the phase of the incoming electron and the one attached to the Andreev-reflected hole which is defined as $\delta\phi = \varphi + \arccos(\epsilon/\Delta_0)$, with φ the phase attached to the superconducting order parameter of the electrode and ϵ the initial electron's energy with respect to the Fermi level.

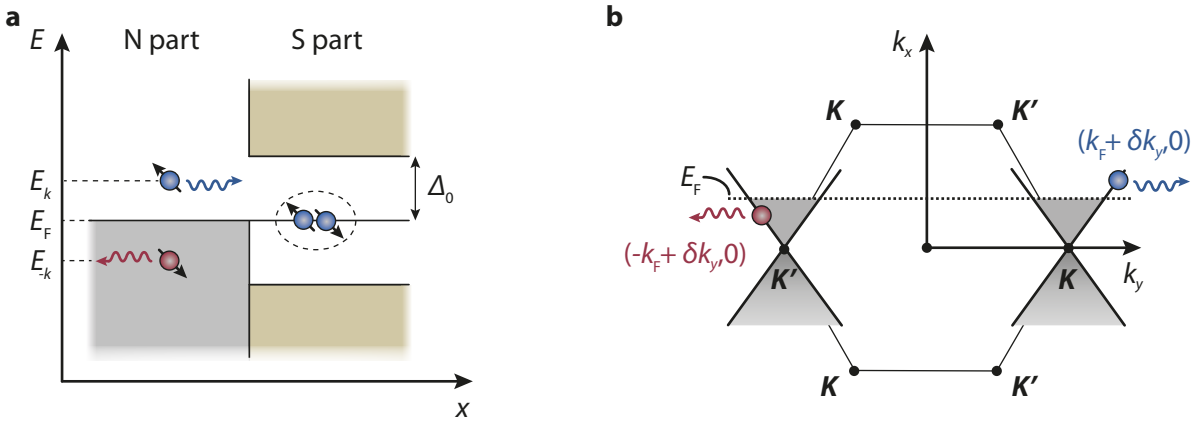

Figure 1.4: **Schematic of the Andreev scattering process. a)** An incoming electron (blue particle) whose energy E_k lies in-between the Fermi level E_F and $E_F+\Delta_0$, Δ_0 being the superconducting gap of the electrode, pairs up with a second electron to enter the superconducting condensate as a Cooper pair (right-sided blue particles pair). This process leaves aside a hole (red particle) propagating away from the NS interface. **b)** Following the graphene's band structure, together with the momentum conservation attached to the Andreev reflection mechanism, an electron state (blue particle) lying within a given valley, say $\boldsymbol{K}$, which undergoes an Andreev reflection event, will necessarily lead to the reflection of a hole (red particle) within the opposite-valley state $\boldsymbol{K'}$.

Note that in the more specific case of graphene, the Andreev reflection momentum preservation translates as a switch in the valley quantum numbers between the incident electron and the corresponding reflected hole (see Figure 1.4.b), a fact that will appear to be crucial when considering proximity-induced superconducitivity in graphene placed in the quantum Hall effect regime (see Section 1.2.3).

1.1.3.2 Non-ideal NS interface: BTK formalism

Previous discussion on the Andreev scattering process assumed an ideal NS interface. However, most of the experimental situations have to deal with semi-transparent interfaces, a scenario that was carefully investigated by G. Blonder, M. Tinkham and T. Klapwijk in the celebrated "BTK" paper [1] that we now shortly introduce.

[15] In details, A. F. Andreev first considered charge transfer for quasiparticles whose energy are above the superconducting gap [16]. The scattering mechanism for quasiparticles having an energy smaller than the superconducting gap was subsequently treated in a second paper in 1965 [20].

[16] Note that the energy difference 2ϵ between the incident electron and the corresponding Andreev reflected hole reads as:

$$2\epsilon = \frac{\hbar^2}{2m}\left[(k_F + \delta k)^2 - (k_F - \delta k)^2\right] = \frac{2\hbar^2 k_F \delta k}{m} \tag{1.9}$$

Ultimately, this yields $\delta k = \epsilon/\hbar v_F$. Thus, perfect retro-reflection occurs only for incident electrons that lies at the Fermi energy.

This model considers a 1-dimensional NS interface, the N and S part respectively extending indefinitively from the NS interface that locates at $x = 0$. All sources of scattering are treated through the introduction of a potential barrier of the form $V(x) = \hbar v_F Z \delta(x)$, v_F being the Fermi velocity in the normal part and $\delta(x)$ the usual δ-function. The Z-parameter translates the barrier height and directly relates to the barrier transmission such that $t = 1/(1 + Z^2)$.

Using the Bogoliubov-De Gennes formalism[17] (BdG) together with the proper boundary conditions, the BTK framework enables to assess the energy-dependent probabilities for the different scattering process that can occur at the NS interface.

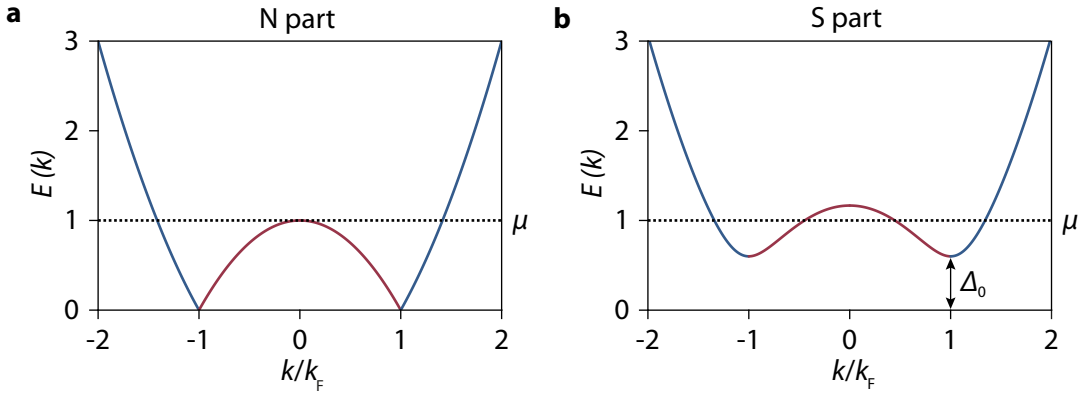

Figure 1.5: **Bogoliubov-De Gennes excitations spectrums. a)** Bogoliubov-De Gennes excitations spectrum $E(k)$ versus the quasi-momentum k for the normal metal part. Blue (resp. red) branches correspond to the electron-like (resp. hole-like) excitations. The parameter μ denotes the chemical potential. **b)** Similar spectrum for Bogoliubov-De Gennes quasiparticles within the superconducting part. The key difference with respect to the normal part spectrum is the opening of a gap Δ_0 around $k = \pm k_F$. Spectrum in **(a)** (resp. **(b)**) was obtained with $\mu = 1$, $\Delta_0 = 0$ (resp. 0.6) and $\hbar^2/m = 2$.

Formally, the BdG equations read as:

$$\begin{pmatrix} H(x) & \Delta_0(x) \\ \Delta_0(x) & -H(x) \end{pmatrix} \begin{pmatrix} f_k(x) \\ g_k(x) \end{pmatrix} = E \begin{pmatrix} f_k(x) \\ g_k(x) \end{pmatrix} \tag{1.10}$$

with $\Delta_0(x) = \Delta_0 \Theta(x)$ the pairing gap coupling the electron/hole wavefunctions $f_k(x)$ and $g_k(x)$, $\Theta(x)$ the usual Heavyside step function and:

$$H(x) = -\frac{\hbar^2}{2m}\frac{\partial}{\partial x} - \mu + V(x) \tag{1.11}$$

Assuming plane wave-like eigensolutions, that is $f_k(x,t) = \tilde{u} e^{ikx - iEt/\hbar}$ and $g_k(x,t) = \tilde{v} e^{ikx - iEt/\hbar}$[18], solving the BdG equation for the normal (resp. superconducting) part yields the quasiparticle spectrum $E(k)$ shown in Figure 1.5.a (resp. Figure 1.5.b).

[17] This mean-field approach allows to treat quasiparticle excitations in a superconductor, even in the presence of a spatially varying superconducting order parameter or a magnetic field.

[18]
$$\tilde{u}^2 = 1 - \tilde{v}^2 = \frac{1}{2}\left[1 \pm \frac{(E^2 - \Delta_0^2)^{1/2}}{E}\right] \tag{1.12}$$

To handle NS interface physics, the BTK approach first considers an electron travelling from the N part to the S part whose BdG-like wavefunction reads as:

$$\psi_{\text{inc.}} = \begin{pmatrix} 1 \\ 0 \end{pmatrix} e^{+iq^+x} \tag{1.13}$$

with $q^{\pm} = (\sqrt{2m}\sqrt{\mu \pm E})/\hbar$.
Following scattering at the NS interface, all the possible outcomes are encompassed within two wavefunctions describing, respectively, the reflected and transmitted quasiparticles as a superposition of BdG-like eigentstates:

$$\psi_{\text{ref.}} = a \begin{pmatrix} 0 \\ 1 \end{pmatrix} e^{+iq^-x} + b \begin{pmatrix} 1 \\ 0 \end{pmatrix} e^{-iq^+x} \tag{1.14}$$

$$\psi_{\text{trans.}} = c \begin{pmatrix} u_0 \\ v_0 \end{pmatrix} e^{+ik^+x} + d \begin{pmatrix} v_0 \\ u_0 \end{pmatrix} e^{-ik^-x} \tag{1.15}$$

with the coefficients a, b, c and d directly related to the energy-dependent probabilities $A(E) = aa^*$, $B(E) = bb^*$, $C(E) = cc^*(u_0^2 - v_0^2)$[19] and $D(E) = dd^*(u_0^2 - v_0^2)$ corresponding, respectively, to an Andreev-reflected hole, an electron undergoing normal reflection, a transmitted electron-like excitation and a hole-like excitation entering the superconducting electrode.
The key result of the BTK paper then consisted in computing these energy-dependent coefficients applying boundary conditions at $x = 0$, the NS interface position, together with the probability conservation constraint $A(E) + B(E) + C(E) + D(E) = 1$.
Table 1.1 summarizes the corresponding expressions for excitations such that $E < \Delta_0$:

$A(E)$	$B(E)$	$C(E)$	$D(E)$
$\dfrac{\Delta_0^2}{E^2 + (\Delta_0^2 - E^2)(1 + 2Z^2)^2}$	1 - $A(E)$	0	0

Table 1.1: **BTK-formalism transmission and reflection coefficients for $E < \Delta_0$.**

1.1.3.3 Andreev reflection under magnetic field

In addition to a spatially varying superconducting order parameter, the Bogoliubov-De Gennes equations also allow for the effect of a magnetic field to be included in describing the NS interface physics. This approach, that we now carefully describe, was initially employed in [21; 22; 23] to treat proximity-induced superconductivity in a quantum Hall system. The derivation of the energy spectrum of the resulting quasiparticles, whose obtention provides an access to the velocity of the proximitized edge states, will shed light on the various details

[19]
$$u_0^2 = 1 - v_0^2 = \frac{1}{2}\left[1 + \frac{(E^2 - \Delta_0^2)^{1/2}}{E}\right] \tag{1.16}$$

of the physics specific to this system[20].
Note that graphene peculiarities, such as the presence of a valley degree of freedom, will be carefully considered in a subsequent part.

A scheme of the system under consideration is provided in Figure 1.6. The NS interface here locates at $x = 0$ and extends over a finite length L_y along the y-axis. The shaded region within the superconducting electrode (see left part) denotes the London penetration depth λ_L. As we shall see in the next, the latter results in a shift of the guiding center coordinate X attached to the cyclotron orbits of the Andreev-reflected quasiparticles.

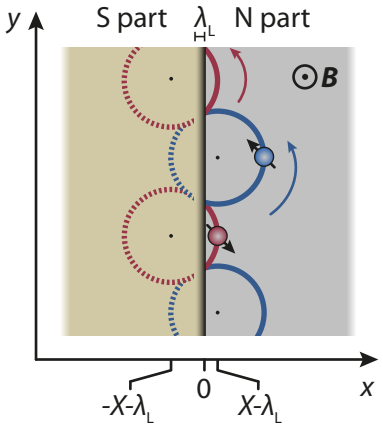

Figure 1.6: **NS interface in the quantum Hall regime.** The boundary between the superconducting lead and the 2DEG in the quantum Hall regime locates at $x = 0$. In the semiclassical picture, a proximitized quantum Hall edge state can be viewed as successive Andreev reflections along the interface. Note that as an Andreev-reflected hole (color-coded in red) undergoes both effective mass and charge sign reversals, its cyclotron motion is directed towards the same direction as the electrons (color-coded in blue). The London penetration depth λ_L shifts the guiding center coordinate X of these cyclotron orbits towards the superconducting electrode.

Variations of the charge carriers effective mass, Fermi level as well as of the module of the superconducting pair potential[21] accross this hybrid system translate as:

$$m(x) = m_s\Theta(-x) + m_n\Theta(x) \tag{1.17}$$

$$E_F(x) = E_F^s\Theta(-x) + E_F^n\Theta(x) \tag{1.18}$$

$$\Delta(x) = \Delta\Theta(-x) \tag{1.19}$$

the index s and n denoting respectively the superconducting electrode and the normal metal and $\Theta(x)$ being the Heavyside step function.
Note that under the application of a perpendicular magnetic field, which is required to induce quantum Hall effect in the normal part, the phase φ attached to the superconducting order parameter will acquire a non-trivial spatial-dependence.
Assuming the magnetic field is screened in the superconducting electrode, we have:

$$\boldsymbol{B}(x) = \left\{Be^{x/\lambda_L}\Theta(-x) + B\Theta(x)\right\}\boldsymbol{z} \tag{1.20}$$

[20]Note that prior to this specific work, NS interface in the quantum Hall regime had already been studied using numerics [24; 25].

[21]Note that we use the notation Δ_0 for the superconducting gap at zero magnetic field and Δ for non-zero magnetic field situations.

where λ_L stands as the London penetration depth and $B = |\boldsymbol{B}|$.
As a result of the translational invariance along the y-axis, the corresponding vector potential $\boldsymbol{A}(x)$, whose expression will be required to express single-particle Hamiltonians later on, can be choosen as:

$$\boldsymbol{A}(x) = \left\{ \lambda_L B(e^{x/\lambda_L} - 1)\Theta(-x) + xB\Theta(x) \right\} \boldsymbol{y} \tag{1.21}$$

These expressions, together with Maxwell and London equations[22], finally yield:

$$\varphi(x,y) = -\frac{\lambda_L}{l_B^2} e^{x/\lambda_L} \mathrm{sgn}(eB) y + e\lambda B(e^{x/\lambda_L} - 1)y + \varphi_0 \tag{1.25}$$

with φ_0 a constant and $l_B = \sqrt{\hbar/eB} \approx 26$ nm at $B = 1$ T, the magnetic length.

In a vein similar to the BTK paper, the approach will now consist in finding solutions of the Bogoliubov-De Gennes equations for the superconducting and the 2DEG parts, respectively, while imposing the matching of the corresponding solutions at the NS interface.

In our case, very general considerations allow to assume the following form for the eigenstates of the Bogoliubov-De Gennes equations:

$$u_X(x,y) = \frac{1}{\sqrt{L_y}} f_X(x) e^{i[\varphi(0,y) + y(X/l_B^2)\mathrm{sgn}(eB)]} \tag{1.26}$$

$$v_X(x,y) = \frac{1}{\sqrt{L_y}} g_X(x) e^{i[-\varphi(0,y) + y(X/l_B^2)\mathrm{sgn}(eB)]} \tag{1.27}$$

Note that the BdG equations eigenstates are labelled by $X = l_B^2 p_y/\hbar + \lambda_L$, the QH edge states guiding center coordinate, rather than k_y.

The next step consists in looking for single-particle Hamiltonian expressions in the N and S parts, respectively. As a reminder, the Hamiltonian describing a single particle of mass m, subjected to both a magnetic field and the Zeeman effect[23], reads as:

$$H(\boldsymbol{r}) = \frac{1}{2m}(\hat{p} - e\boldsymbol{A})^2 + \frac{g}{2}\mu_B \boldsymbol{\sigma} \cdot \boldsymbol{B} - E_F \tag{1.28}$$

[22] In details, we use the Maxwell equation relating the magnetic field $\boldsymbol{B}$ to the screening supercurrent $\boldsymbol{j}_s$ flowing within the superconducting electrode over the London penetration depth λ_L from the NS interface:

$$\boldsymbol{\nabla} \times \boldsymbol{B} = \mu_0 \boldsymbol{j}_s \tag{1.22}$$

with $\mu_0 = 4\pi$ x 10^{-7} H/m the vacuum magnetic permeability.
Then, according to London equation, $\boldsymbol{j}_s$ directly relates to the spatial gradient of the superconducting order parameter phase term $\varphi(x,y)$ as:

$$\boldsymbol{j}_s = \frac{\hbar}{e\mu_0\lambda_L^2}[\boldsymbol{\nabla}\varphi - e\boldsymbol{A}] \tag{1.23}$$

Combining (1.22) and (1.23), we obtain:

$$\boldsymbol{\nabla}\varphi = \frac{\lambda_L^2 e}{\hbar}[\boldsymbol{\nabla} \times \boldsymbol{B}] + e\boldsymbol{A} \tag{1.24}$$

Upon injecting the expressions (1.20) and (1.21) for the superconducting part in this last equation, we finally derive a general expression for $\varphi(x,y)$.
Note that the corresponding equation in [23] is given for $x = 0$, that is the superconducting order parameter phase term at the NS interface.

[23] Anticipating discussions regarding proximity-induced superconducitivity in the $\nu = 1$ spin-polarized quantum Hall edge state, we include Zeeman splitting effect in the model.

with $\hat{p}$ the momentum operator, g the Landé factor, μ_B the Bohr magneton, $\boldsymbol{\sigma}$ the Pauli matrices and E_F the Fermi level.

Using the expressions for $\boldsymbol{B}(x)$ and $\boldsymbol{A}(x)$ we introduced earlier on, the normal part Hamiltonian (i.e. for $x > 0$) can be re-written as:

$$H_0^n = \frac{\hbar\omega_c}{2}\left\{\frac{l_B^2}{\hbar^2}p_x^2 + \left[\frac{x+\lambda\mp X}{l_B}\right]^2 + \sigma\eta_Z - \nu\right\} \tag{1.29}$$

Here $\omega_c = \hbar/m_n l_B^2 = eB/m_n$ corresponds to the usual cyclotron frequency in the 2DEG, $\eta_Z = g\mu_B B/(\hbar\omega_c)$ quantifies the Zeeman splitting, and $\nu = 2E_F^n/(\hbar\omega_c)$ denotes the filling factor[24].
Similarly, the superconducting electrode Hamiltonian (i.e. $x < 0$) is expressed as follows:

$$H_0^s = \frac{p_x^2}{2m_s} + \frac{\hbar^2[X \pm l_B^2 k_s \mathrm{sgn}(eB)]^2}{2m_s l_B^4} - E_F^s \tag{1.30}$$

where k_s corresponds to the magnitude of the vector defined as:

$$\boldsymbol{k}_s = -\frac{\lambda_L}{l_B^2}e^{x/\lambda_L}\mathrm{sgn}(eB)\Theta(-x)\boldsymbol{y} \tag{1.31}$$

Note that expression (1.30) was obtained in neglecting the Zeeman splitting within the superconducting region. Consequently, the Bogoliubov-De Gennes equations read as:

$$\begin{pmatrix} H_{0,+}^{n,s}(x) + U(x) & \Delta(x)e^{i2\varphi(x,y)} \\ \Delta(x)e^{-i2\varphi(x,y)} & H_{0,-}^{*,n,s}(x) - U(x) \end{pmatrix}\begin{pmatrix} u(x,y) \\ v(x,y) \end{pmatrix} = E\begin{pmatrix} u(x,y) \\ v(x,y) \end{pmatrix} \tag{1.32}$$

with $U(x) = U_0\delta(x)$ an external potential modelling scattering at the NS interface.
The attentive reader will notice that the phase attached to the superconducting order parameter is defined as 2φ. Following the definitions of $u_X(x,y)$ and $v_X(x,y)$, this will allow to remove the superconducting phase term from the Bogoliubov-De Gennes equations (see the transition from (1.32) to (1.33)), thus simplifiyng the calculations.

Injecting $u_X(x,y)$ and $v_X(x,y)$ in (1.32), this ultimately results in the following expression:

$$\begin{pmatrix} H_{0,+}^{n,s}(x) + U(x) & \Delta(x) \\ \Delta(x) & H_{0,-}^{*,n,s}(x) - U(x) \end{pmatrix}\begin{pmatrix} f_X(x) \\ g_X(x) \end{pmatrix} = E\begin{pmatrix} f_X(x) \\ g_X(x) \end{pmatrix} \tag{1.33}$$

We then end up with a set of equations strongly resembling the 1-dimensional problem addressed in the BTK paper.

By matching the quasiparticles wavefunctions at the NS interface[25], together with the conservation of the probability current, then yields to the following secular equation:

[24] As a reminder, for conventional 2DEG, $E_F^n = \hbar^2 k_F^2/2m_n$ and $k_F = \sqrt{2\pi n}$, with n the electron density.

[25] In details, the wavefunctions attached to the N and S parts are derived as follow:

In the normal part, the analogy with the BTK treatment suggests eigensolutions for expression (1.33) consisting in a superposition of purely electron-like and hole-like BdG spinors:

$$\begin{pmatrix} f_{X,\sigma} \\ g_{X,\sigma} \end{pmatrix}_{x>0} = \begin{pmatrix} a \\ 0 \end{pmatrix}\chi_{+,\sigma}(\zeta_+) + \begin{pmatrix} 0 \\ b \end{pmatrix}\chi_{-,-\sigma}(\zeta_-) \tag{1.34}$$

$$\cos(\varphi_{+,\sigma}) + \Omega(\varphi_{-,\sigma}) = \frac{2s}{s^2+w^2+1}\frac{(E+\delta_\lambda)\sin(\varphi_{+,\sigma})}{\sqrt{\Delta^2-(E+\delta_\lambda)^2}} \tag{1.41}$$

with:

$$\varphi_{+,\sigma} = \pi\left[\frac{E}{\hbar\omega_c} - \frac{\sigma\eta_Z}{2}\right] + 2\sqrt{\nu}\frac{X}{l_B} - \frac{2}{\sqrt{\nu}}\left[\frac{E}{\hbar\omega_c} - \frac{\sigma\eta_Z}{2}\right]\frac{\lambda_L}{l_B} \tag{1.42}$$

$$\varphi_{-,\sigma} = \pi\frac{\nu}{2} + \frac{2}{\sqrt{\nu}}\left[\frac{E}{\hbar\omega_c} - \frac{\sigma\eta_Z}{2}\right]\frac{X}{l_B} - 2\sqrt{\nu}\frac{\lambda_L}{l_B} \tag{1.43}$$

$$\Omega(\alpha) = \frac{[s^2+w^2-1]\sin(\alpha) + 2w\cos(\alpha)}{s^2+w^2+1} \tag{1.44}$$

$$\delta_\lambda = \hbar\omega_c\frac{m_n}{m_s}\frac{X\lambda_L}{l_B^2}. \tag{1.45}$$

where $s = [E_F^s m_n/(E_F^n m_s)]^{1/2}$ translates the Fermi-velocity mismatch between the S and N parts, and $w = [2m_n U_0^2/(\hbar^2 E_F^n)]^{1/2}$ measures the scattering occuring at the NS inteface.

At last, solving the secular equation (1.41) gives the energy spectrum of the Andreev levels attached to the NS interface. For non-ideal interface ($w \neq 0$ and $s \neq 1$) and low energies i.e. $|E - \sigma g\mu_B B| \ll \hbar\sqrt{E_F^n/(2m_n X^2)}$, we have:

$$E_\sigma = \Delta\frac{(2n+1)\pi \pm \arccos(\Omega_0) - 2X\sqrt{2m_n E_F^n}/\hbar - \pi/2\sigma\eta_Z}{q + \pi\Delta/(\hbar\omega_c)} \tag{1.46}$$

---

with $\zeta_\pm = x + \lambda \mp X$ and $\chi_{\pm,\sigma}(\zeta)$ the eigensolutions of the BdG equations in the normal part.
Fortunately, BdG equations in the normal part can be shown to take a harmonic oscillator form as:

$$\frac{l_B^2}{2}\frac{d^2\chi_{\pm,\sigma}}{d\zeta^2} - \left[\frac{\zeta^2}{2l_B^2} - \frac{\nu-\sigma\eta_Z}{2} \mp \frac{E}{\hbar\omega_c}\right]\chi_{\pm,\sigma} = 0 \tag{1.35}$$

Solution to this equation is known to express in terms of parabolic cylinder functions [26] such that:

$$\chi_{\pm,\sigma}(\zeta_\pm) = F_{\pm,\sigma}U(-\frac{\nu-\sigma\eta_Z}{2} \mp \frac{E}{\hbar\omega_c}, \sqrt{2}\frac{\zeta_\pm}{l_B}) \tag{1.36}$$

with $F_{\pm,\sigma}$ a normalization constant.

In the superconducting part, considering the region in which the screening supercurrent $\boldsymbol{j}_s$ flows, the wavefunctions corresponding to the solutions of (1.33) can be expressed as:

$$\begin{pmatrix} f_{X,\sigma} \\ g_{X,-\sigma} \end{pmatrix}_{x<0} = d_-\begin{pmatrix}\gamma_- \\ 1\end{pmatrix}e^{-ixq_-} + d_+\begin{pmatrix}\gamma_+ \\ 1\end{pmatrix}e^{ixq_+}, \tag{1.37}$$

introducing the following parameters:

$$q_\pm = \left[\frac{2m_s}{\hbar^2}(E_F^s \pm \sqrt{(E+\delta_\lambda)^2-\Delta^2} - \frac{X^2+\lambda_L^2}{l_B^4}\right]^{1/2}, \tag{1.38}$$

$$\gamma_\pm = \frac{\Delta}{E+\delta_\lambda \mp \sqrt{(E+\delta_\lambda)^2-\Delta^2}}, \tag{1.39}$$

$$\delta_\lambda = \hbar\omega_c\frac{m_n}{m_s}\frac{X\lambda_L}{l_B^2}. \tag{1.40}$$

The finite value for screening current here translates as a schift δ_λ for the quasiparticles spectrum in the superconductor. Note that for $|E+\delta_\lambda| < \Delta$, we obtain an evanescent wavefunction as expected for quasiparticles entering the superconducting electrode upon Andreev reflection.

with $\Omega_0 = \Omega(\pi\nu/2)$ and $q = 2s/(s^2 + w^2 + 1)$. Note that this expression leaves aside the effect of the screening current flowing within the superconducting electrode. Qualitatively, as discussed in [23], the latter has two main consequences:

- A shift of the quasiparticles spectrum in the superconductor by δ_λ (see footnote 25). Consequently, Andreev edge states now occur only if their energy E is such that $|E + \delta_\lambda| < \Delta$.
- The guiding center coordinates attached to the electron/hole wavefunctions within the normal part are shifted to $x = -\lambda_L$.

Importantly, equation (1.46) will enable us to derive an expression for the velocity of the Andreev edge states propagating along the NS interface, a parameter that will appear to be key for the physics of the quantum Hall Josephson junctions (see Section 1.2.2).

1.2 Quantum Hall Josephson junction

We now extend our discussion to quantum Hall Josephson junction, that is a device consisting into two superconducting electrodes separated by a normal part placed in the quantum Hall effect regime.

1.2.1 Chiral supercurrent and h/e-flux periodicity

Under weak perpendicular magnetic field, the maximum supercurrent I_c a Josephson junction can withstand is modulated by the magnetic flux ϕ threading the device.
In particular, provided the supercurrent is uniformly distributed within the device at zero magnetic field, I_c forms a typical $h/2e$-flux periodic Fraunhofer-like diffraction pattern such that:

$$I_c(\phi) = \max\left[\int_0^W J_s(\Delta\varphi(x))dx\right] = I_{c,0}\left|\frac{\sin(\pi\phi/\phi_0)}{\pi\phi/\phi_0}\right| \tag{1.47}$$

with $\phi_0 = h/2e$ the superconducting flux quantum, W the NS interfaces length, $I_{c,0}$ the critical current value at zero magnetic field and $J_s(\Delta\varphi(x))$ the supercurrent density whose value directly relates to the gauge-invariant superconducting phase difference $\Delta\varphi(x)$[26] between two points facing each other at coordinate x (see Figure 1.7.a)[27].

[26] As a reminder, the gauge-invariant superconducting phase difference $\Delta\varphi(x_1, x_2)$ between points x_1 and x_2 is defined as:

$$\Delta\varphi(x_1, x_2) = [\varphi(x_2) - \varphi(x_1)] - \frac{2\pi}{\phi_0}\int_{x_1}^{x_2} \boldsymbol{A}\cdot\boldsymbol{dl} = \frac{\pi\phi}{W\phi_0}(x_1 + x_2) + \Delta\varphi_0 \tag{1.48}$$

with $\varphi(x_1)$ (resp. $\varphi(x_2)$) the phase term of the superconducting order parameter at x_1 (resp. x_2), $\boldsymbol{A}$ the vector potential and $\Delta\varphi_0$ a constant.

[27] Key to this result is the "local" nature of the supercurrent density i.e. its value at a given NS interface point, say x_1, solely depends on the phase difference between this point and the point in regards with it on the opposite electrode. Interestingly, the consequences of a "non-local" superconducting phase difference were investigated in [27]. Provided the sinusoïdal current-phase Josephson relationship holds, the supercurrent density at a given NS interface point x_1 would now read as:

$$J_s(x_1) = \int_0^W J_{s,0}\sin(\Delta\varphi(x_1, x_2))dx_2 \tag{1.49}$$

Ultimately, this would result into the following expression for the critical current dependence on the magnetic flux ϕ threading the junction:

$$I_c(\phi) = \max\left[\int_0^W J_s(x_1)dx_1\right] = I_{c,0}\left(\frac{\sin(\pi\phi/2\phi_0)}{\pi\phi/2\phi_0}\right)^2 \tag{1.50}$$

In other words, the corresponding Fraunhofer pattern would be h/e-flux periodic.

Although expression (1.47) does not explicitly show any limit of applicability in magnetic field, in practice, the Fraunhofer patterns described by $I_c(\phi)$ usually do not survive beyond few mT, an empirical limit whose microscopic origin is clarified in Chapter 2 Section 2.2 for short/ballistic Josephson junctions.

Going beyond Fraunhofer patterns physics, M. Ma and A. Y. Zyuzin have considered a Josephson junction subjected to a much higher magnetic field and consisting into 2 point-like superconducting electrodes[28] contacting a 2DEG in the quantum Hall regime [28] (see for instance Figure 1.7.b).

Importantly, the critical current within that configuration was also predicted to oscillate, yet with a $2\phi_0 = h/e$-flux periodicity. This hallmark, that was systematically derived in subsequent theoretical works dedicated to similar systems [29; 30; 31], is very specific to QH edge states-mediated supercurrent or *chiral supercurrent* and, as such, will constitute the main experimental signature for unveiling it.

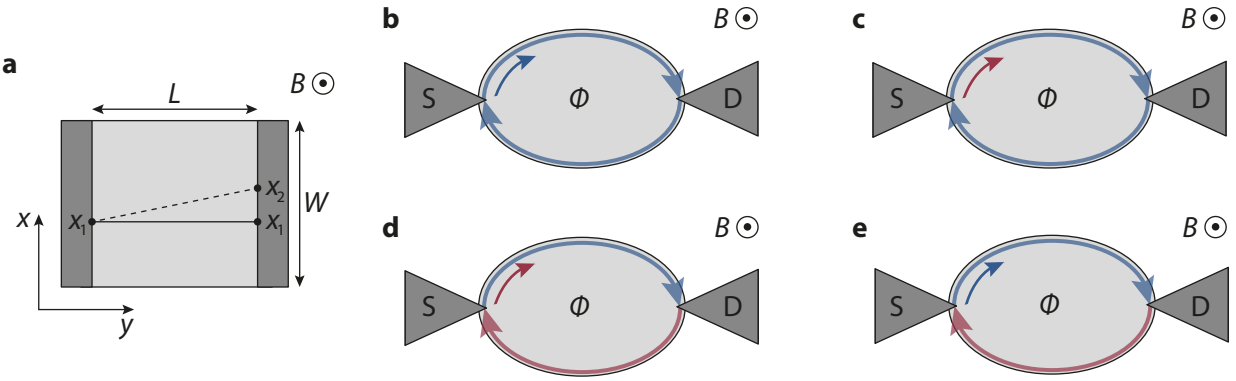

Figure 1.7: **Josephson junction's supercurrent flux-periodicity under magnetic field. a)** Top view of a Josephson junction under weak magnetic field. The critical current will display a Fraunhofer pattern dependence on B with a $h/2e$-flux periodicity as long as the supercurrent amplitude at a given NS interface point solely depends on the superconducting phase difference between that point and the point in regards with it on the opposite side electrode (say for instance between NS interfaces points located at x_1). Once the superconducting phase difference is sensitive to the phase variation accross the whole opposite-side electrode, as it can be the case in small, square-shaped ballistic Josephson junctions, the Fraunhofer pattern becomes h/e-flux periodic [27]. **b), c), d)** and **e)** At much higher magnetic field, such that the normal part is in the quantum Hall regime, the QH edge states chirality combined with the possibility for an incoming electron to undergo an Andreev reflection give rise to several distinct scenarios whose detailed descriptions are provided in the main text. Blue (resp. red) corresponds to electron (resp. Andreev reflected hole). S and D denote respectively the source and drain contacts.

This anomalous flux-periodicity originates from the non-locality of the Cooper pairs transfer process within this system. In order to illustrate this point, we refer the reader to the schematics portrayed in Figures 1.7.b,c,d and e.

As a result of the quantum Hall effect regime, charge carriers involved within the supercurrent necessarily have to flow along the 2DEG edges[29].

If one consider an electron originating from the source electrode, flowing via the top QH edge channel, four

[28] These idealized contacts allow for leaving aside NS interface physics considerations.

[29] We assume here the 2DEG is large enough to avoid any Cooper pair tunneling via the insulating bulk between the two superconducting banks.

basic scenarios are possible:

- The electron does not enter the drain electrode. Following the QH edge states chirality (see Section 1.1.2), it is then back-reflected towards the source electrode via the bottom edge.
  Provided phase coherence is preserved along the whole path, the electron carries an additional Aharonov-Bohm phase factor $\varphi_{AB} = 2\pi\phi/\phi_0$ once arriving at the source electrode, with ϕ the magnetic flux enclosed by the QH edge states and $\phi_0 = h/e$ the flux quantum. If the electron does not enter the source contact, it can self-interfere with itself which results into Aharonov-Bohm interference[30] (see Figure 1.7.b). Yet, as a result of the use of superconducting electrodes, two consecutive normal reflections implies the absence of a Cooper pair/normal electron transfer between the source and the drain electrodes. Therefore, this scenario is not expected to produce any measurable Aharonov-Bohm oscillations in both the critical current I_c and the conductance.

- In fact, as long as the initial electron does not undergo Andreev conversion at the drain electrode, no Cooper pair is transfered. Therefore, in the scenario (2) (see Figure 1.7.c), in which the back-reflected electron is Andreev-reflected at the source electrode, no supercurrent can develop.

- In Figures 1.7.d and 1.7.e, the initial electron undergoes an Andreev reflection at the drain electrode i.e. a Cooper pair is transfered.
  Then, once the corresponding Andreev-reflected hole is back to the source electrode, it can undergo either a normal reflection or an Andreev conversion.
  In the former case (see Figure 1.7.d), Aharonov-Bohm interference cannot take place as the latter require for a given particle to interfer with itself i.e. Aharonov-Bohm interference cannot result from the hole interfering with the initial electron.
  Therefore, in this third scenario, although a Cooper pair is transfered to the drain electrode, the supercurrent attached to this process does not exhibit Aharonov-Bohm oscillations.

- If, conversely, the hole is subjected to an Andreev reflection at the source electrode (see Figure 1.7.e), one recover the initial electron with an additional Aharonov-Bohm phase factor: a Cooper pair has been transfered from the source to the drain throughout the entire process and Aharonov-Bohm self-interference is possible for the electron involved within this transfer.
  Consequently, in this fourth scenario, the supercurrent, and therefore I_c, should exhibit h/e-flux periodic Aharonov-Bohm oscillations.

Note that finite-length NS interfaces are not expected to call into question this feature. Each time the scenario (4) repeats, the sequences of successive Andreev and normal reflections along the NS interfaces can differ. Consequently, once back to its starting point and provided the electron's phase is still well-defined, the phase term that follows from the successive normal/Andreev reflections can take any value. Therefore, this NS interfaces-related phase term is expected to average out to zero over repetitions, leaving only the Aharonov-Bohm phase term as the source of interferences.

1.2.2 Edge states velocity renormalization

In the very first work dedicated to chiral supercurrent, the superconducting electrodes were assumed to form point-like contacts to the 2DEG, a deliberate way to leave aside NS interfaces physics.

[30] Note that this scenario is only valid if the normal reflection on the point-like superconducting contacts does not destroy the electron's phase coherence.

Although it does not call into question the chiral supercurrent hallmark i.e. the anomalous h/e-flux periodicity, this simplication puts out of sight an effect central to the very existence of the chiral supercurrent: the QH edge states velocity renormalization along the NS interfaces.

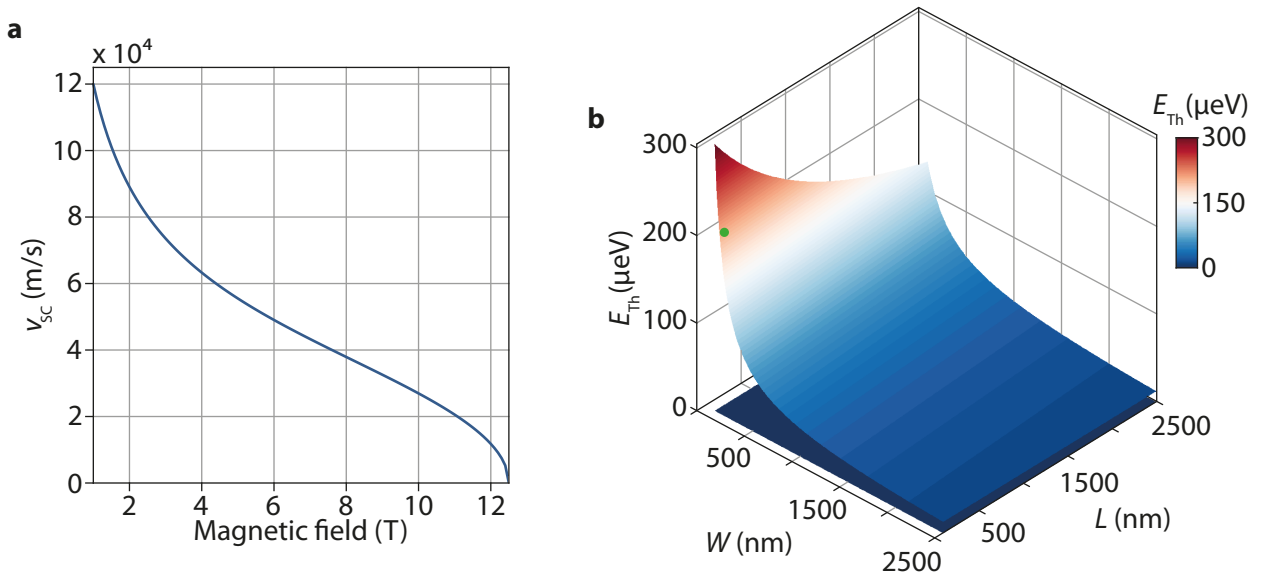

Figure 1.8: **QH edge states velocity renormalization along the NS interfaces. a)** Chiral Andreev edge states velocity v_{SC} versus the magnetic field obtained using expression (1.52) with $v_n = 10^6$ m/s, the graphene's Fermi velocity, a transparency $t = 0.5$, $\Delta = \Delta_0\sqrt{1-(B/B_{c,2})^2}$ with $\Delta_0 = 895$ μeV, the superconducting gap of the MoGe at zero magnetic field and $B_{c,2} = 12.5$ T, the MoGe upper critical field. **b)** Thouless energy $E_{Th} = h/(L/v_{QH} + W/v_{SC})$ as a function of both L and W with $v_{QH} = 1.4$ x 10^5 m/s [32], $B = 5$ T and $t = 0.5$. The green dot indicates E_{Th} for $L = W = 150$ nm, the typical dimensions for our Josephson junctions. Importantly, this energy is about 236 times larger than k_BT (here denoted by the horizontal dark plan), with $T = 10$ mK, the temperature of our measurements.

As highlighted in the work of Y. Alavirad *et al.* [30], each electron-hole Andreev conversion event takes a finite amount of time $T_{AR} \sim \hbar/\Delta$[31], that adds up to the time $T_{QH} = \pi/\omega_c$ a classical cyclotron bounce would take (ω_c denoting the usual cyclotron frequency).

It should be noted, however, that this reasoning does not include finite-transparency effect, which further complicates the picture.

In [30], the transparency t was assumed to directly equate the Andreev reflection probability[32], hence leading the authors to express the time taken by an Andreev-reflected cyclotron bounce as $T_{SC} \sim \pi(1/\omega_c + \hbar/\Delta)$. Ultimately, this implies $T_{QH} = T_{SC}(1+t\hbar\omega_c/\Delta)^{-1}$ and, provided each cyclotron bounce along the NS interface undergoes Andreev reflection[33], $v_{SC} = v_{QH}(1+t\hbar\omega_c/\Delta)^{-1}$ with v_{SC} (resp. v_{QH}) the quantum Hall edge states

[31] Once entering the superconducting electrode, the electrons involved in the formation of a Cooper pair typically have to travel over the electrode's superconducting coherence length ξ_s to pair-up. For a clean superconductor, we have $\xi_s = \hbar v_s/\pi\Delta$, with v_s the Fermi velocity within the superconductor and Δ the electrode's superconducting gap. Consequently, the time attached to the formation of a Cooper pair, and therefore to the Andreev reflection process, equates to $\xi/v_s = \hbar/\pi\Delta$. Yet, as this expression is derived in the clean-limit case, it should be considered as a mere order of magnitude.

[32] An assumption far from being that trivial. See for instance the Table 1.1 in Section 1.1.3.2, in which the general expression for the Andreev reflection probability $A(E)$ within the BTK paper framework is provided.

[33] An assumption in contradiction with the finite-transparency value, the latter making unlikely to have only Andreev-reflected cyclotron bounces along the NS interface.

velocity along the NS interfaces (resp. along the graphene pristine edges). Despite the intuitive mechanism this semi-classical approach relies on, the way finite transparency effect is handled clearly does not stand up to scrutinity (see footnotes 32 and 33).

In an attempt to develop more rigorous reasoning, it is possible to start with the energy spectrum that was derived for proximitized QH edge states along a NS interface in Section 1.1.3.3.
As a reminder, for a non-ideal interface, we have:

$$E_\sigma = \Delta \frac{(2n+1)\pi \pm \arccos(\Omega_0) - 2X\sqrt{2m_\mathsf{n}E_\mathsf{F}^\mathsf{n}}/\hbar - \pi/2\sigma\eta_Z}{q + \pi\Delta/(\hbar\omega_\mathsf{c})} \tag{1.51}$$

where X stands for the guiding center coordinate of the QH edge states and $\Omega_0 = \Omega(\pi\nu/2)$ is an oscillatory function of the filling factor (see equation (1.44)).
The parameter $q = 2s/(1+s^2+w^2)$ relates to both the Fermi velocity mismatch $s = v_\mathsf{n}/v_\mathsf{s}$ between graphene and the superconductor as well as to the scattering parameter $w = k_\mathsf{F}^\mathsf{n}U_0/E_\mathsf{F}^\mathsf{n}$[34].
As the edge states velocity relates to E as $v_\mathsf{SC} = -(l_B^2/\hbar)(\partial E/\partial X)$, we obtain:

$$v_\mathsf{SC} = \frac{2v_\mathsf{n}}{\pi + q\hbar\omega_\mathsf{c}/\Delta} \tag{1.52}$$

While Fermi velocities for both the graphene and the MoGe are known, hence allowing to estimate the parameter s, the lack of knowledge about the barrier U_0 prevents an estimation for w and subsequently, for q and v_SC.
Luckily though, an explicit link between the transparency t and U_0 was established in [33] with $t = v_\mathsf{n}v_\mathsf{s}/[(v_\mathsf{n}+v_\mathsf{s})^2/4 + U_0^2]$. Noticing that $t = 4s/((1+s)^2+w^2)$, this allows to write $q = t/(2-t)$ and thus, to compute v_SC (see Figure 1.8.a).
Crucially, v_SC is about half of the quantum Hall edge states velocity $v_\mathsf{QH} = 1.4$ x 10^5 m/s that was estimated at $B = 14$ T in graphene-based quantum Hall Fabry-Pérot interferometry experiments [32] [35].

Following the Y. Alavirad *et al.* line of reasoning, we now investigate how does this edge states velocity renormalization influences the Josephson supercurrent.
Using Green's functions formalism, the chiral supercurrent was shown to read as [30]:

$$I_\mathsf{SC}(\phi,\phi_\mathsf{e}) = -\sum_{\omega_m} \frac{4e}{\beta\hbar}\sin(\phi)\sin^2\left(\frac{\Delta W}{\hbar v_\mathsf{SC}}\right) \cdot \left[(\cos(\phi_\mathsf{e})+\cos(\phi))\cos\left(\frac{2\Delta W}{\hbar v_\mathsf{SC}}\right) + \cos(\phi_\mathsf{e}) - \cos(\phi) - 2\cosh\left(\frac{2\omega_m}{\hbar}\left(\frac{L}{v_\mathsf{QH}}+\frac{W}{v_\mathsf{SC}}\right)\right)\right]^{-1} \tag{1.53}$$

with ϕ the superconducting phase difference between opposite-sided electrodes, $\phi_\mathsf{e} = LWB\pi/\Phi_0$ the dimensionless external magnetic flux[36], $\omega_m = (2m+1)\pi/\beta$ the fermionic Matsubara frequency ($m \in \{0, \pm1, \pm2, ...\}$) and $\beta = 1/k_\mathsf{B}T$ the inverse temperature[37].

Several comments can be made about the above expression:

[34] Note that w equates $2Z$ in the BTK framework.

[35] Note that several experiments in GaAs/AlGaAs quantum wells evidenced a $1/B$-dependence for the quantum Hall edge states velocity [34; 35], hence suggesting the actual value for v_QH at $B = 5$ T is probably larger.

[36] Here, $\Phi_0 = h/2e$, the usual superconducting flux-quantum.

[37] Note that in the so-called high temperature limit, that is $\hbar/(L/v_\mathsf{QH} + W/v_\mathsf{SC}) \ll k_\mathsf{B}T$, the chiral supercurrent expression can be

- From (1.53), it is possible to derive the following expression for the critical current $I_c = I_{SC}(\phi = \pi/2)$, that is the highest supercurrent value the Josephson junction can sustain:

$$I_c = -\sum_{\omega_m} \frac{4e}{\beta\hbar} \sin^2\left(\frac{\Delta W}{\hbar v_{SC}}\right) \left[\cos(\phi_e)\cos\left(\frac{2\Delta W}{\hbar v_{SC}}\right) + \cos(\phi_e) - 2\cosh\left(\frac{2\omega_m}{\hbar}\left(\frac{L}{v_{QH}} + \frac{W}{v_{SC}}\right)\right)\right]^{-1} \tag{1.55}$$

  For conventional Josephson junctions, the Ginzburg-Landau theory explicitely relates I_c to the junction's dimensions as $I_c = (2e\hbar\psi_\infty^2/m^*)(A/L)$[38], an expression from which stems the well-known $I_c R_N$-product invariance [36].
  Going back to equation (1.55), such a trivial link between the critical current value and the junction's dimensions clearly does not hold here, thus preventing us to decipher whether or not the $I_c R_N$-product is constant for a quantum Hall Josephson junction. It should be noted, however, that according to the few other theoretical works dealing with the chiral supercurrent, its maximum value would be inversely proportional to the perimeter of the Josephson junction [28; 31; 29].

- In the regime relevant for the experiments[39], the term $\cosh(2\omega_m/\hbar(L/v_{QH} + W/v_{SC}))$ largely dominates over the other factors within the denominator of (1.55). Interestingly, the argument within this term relates to the ratio of two energy scales, namely the temperature $k_B T$ and $h/(L/v_{QH} + W/v_{SC})$ (see Figure 1.8.b for a comparison), whose expression mimics the Thouless energy usually found in the quantum Hall Fabry-Perot interferometers context [32].

To further clarify the dependence of I_c on the junction's parameters, we plot in Figure 1.9.a its value as a function of both the magnetic field and the lead-to-lead distance L while keeping $T = 10$ mK, $W = 150$ nm, $t = 0.5$, $v_{QH} = 1.4$ x 10^5 m/s and using equation (1.52) to compute the magnetic field-dependent value of v_{SC}.
As the chiral supercurrent amplitude oscillates with the magnetic flux $\phi = BLW$, we consistently observe I_c oscillations both with L and B.

Remarkably, taking a linecut along the magnetic field at $L = 150$ nm (see blue curve in Figure 1.9.c), we observe critical current maxima spaced with a magnetic field period matching the h/e-flux periodicity, in agreement with the chiral supercurrent hallmark we mentioned in Section 1.2.1.
Intriguingly, while the I_c oscillations amplitude first exhibits a decrease as the magnetic field rises up, with maxima passing from 4.1 nA at $B = 3.86$ T to 0.25 nA $B = 4.23$ T, it then experiences a revival with the applied magnetic field, at odds with the intuitive idea that higher magnetic field would be necessarily detrimental to the supercurrent. In addition, we note that I_c does not necessarily drop to zero in-between the maxima,

---

approximated as:

$$I_{SC} \approx \frac{8e}{\beta\hbar} \sin(\phi)\sin^2\left(\frac{\Delta W}{\hbar v_{SC}}\right) \exp\left[-\frac{2\pi}{\beta\hbar}\left(\frac{L}{v_{QH}} + \frac{W}{v_{SC}}\right)\right] \tag{1.54}$$

For a square-shaped device, the order of magnitude difference between v_{QH} and v_{SC} makes the W-dependent term dominates in the exponential factor, an indication that NS interface length is the critical parameter to reliably observe the chiral supercurrent.

[38] Here ψ_∞ relates to the ratio of the Ginzburg-Landau parameters α and β as $|\psi_\infty|^2 = -\alpha/\beta$, m^* is the charge carriers effective mass, A is the cross-section area of the Josephson junction and L is the lead-to-lead distance. The normal state resistance of the junction being proportional to L/A, this necessarily implies that the $I_c R_N$ product equates a constant value.

[39] Typically, at $T = 10$ mK and $B = 5$ T, with $L = W = 150$ nm, the term $\cosh\left(\frac{2\omega_0}{\hbar}\left(\frac{L}{v_{QH}} + \frac{W}{v_{SC}}\right)\right)$ equates 1.005 while $\cos(2\Delta W/\hbar v_{SC}) =$ -0.5174.

which further invalidate analogies with conventional Josephson junctions[40].

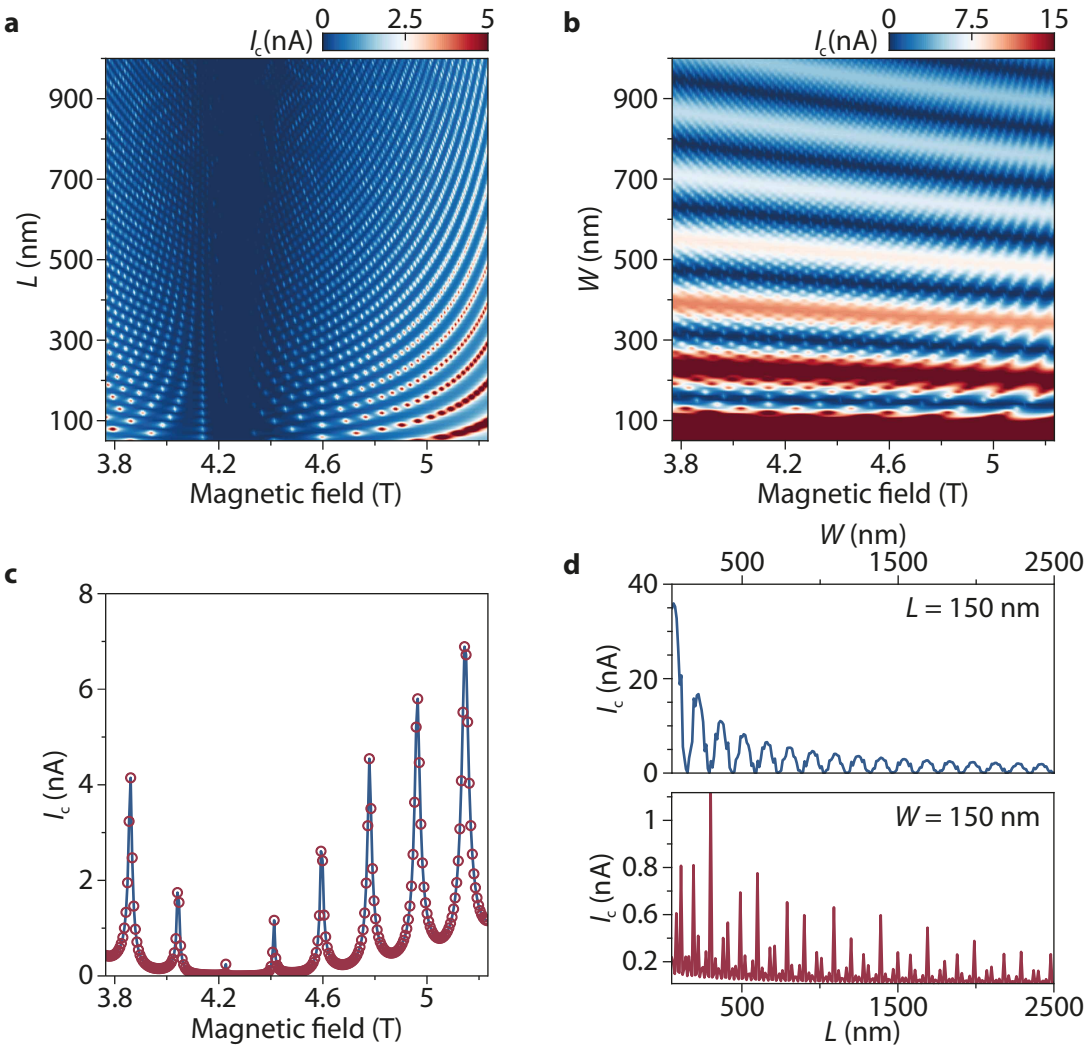

Figure 1.9: **Critical current dependence on L and W in QH-Josephson junctions. a)** I_c versus the magnetic field and the lead-to-lead distance L with $W = 150$ nm, $t = 0.5$ and $T = 10$ mK computed using (1.55). **b)** Colormap of I_c versus the magnetic field and W, the NS interfaces length computed with the same parameters values as in **(a)** and with $L = 150$ nm. **c)** I_c linecuts versus the magnetic field. The blue curve was taken at $L = 150$ nm in **(a)** while the red dots were obtained taking a linecut at $W = 150$ nm in **(b)**. The two curves overlap as expected. **d)** I_c versus W (blue curve) and L (red curve) at $B = 4.5$ T, with $t = 0.5$ and $T = 10$ mK. The critical current decay with W is much faster than with L, a direct consequence of QH edge states velocity renormalization along the NS interfaces. The Thouless energy attached to the chiral supercurrent is mainly sensitive to W.

In the same spirit, Figure 1.9.b shows the I_c dependence on both B and W, computed setting $L = 150$ nm and using the same values than in Figure 1.9.a for the other parameters.
We consistently recover h/e-flux periodic oscillations accross the entire W-B plan (see linecut in Figure 1.9.c

[40]This non-vanishing I_c amplitude in-between maxima was also obtained with the chiral supercurrent theory of J.A.M. van Ostaay *et al.* (see [29]).

for instance): the higher the magnetic field (resp. the width) is, the sharper are the needle-like features formed by the critical current maxima (see for instance the top-right region in Figure 1.9.b).

Finally, by comparing the dependence of I_c on L and W for a given magnetic field value (as in Figure 1.9.d), it turns out that the chiral supercurrent amplitude decays much faster with W than with L, a direct consequence of the QH edge states velocity renormalization along the NS interfaces.
Looking at the Thouless energy $E_{\text{Th}} = h/(L/v_{\text{QH}} + W/v_{\text{SC}})$, the fact that $v_{\text{SC}} \ll v_{\text{QH}}$ makes this energy scale, hence the critical current value, much more sensitive to W than L. This suggests that the key parameter for chiral supercurrent occurence is the NS interfaces length.

1.2.3 Additional considerations on graphene-based quantum Hall Josephson junction

As mentionned in Section 1.1.3.1, in graphene, Andreev reflection couples electron and holes having opposite valley polarization, a feature whose consequences for proximity-induced superconductivity in the QH regime are now addressed.

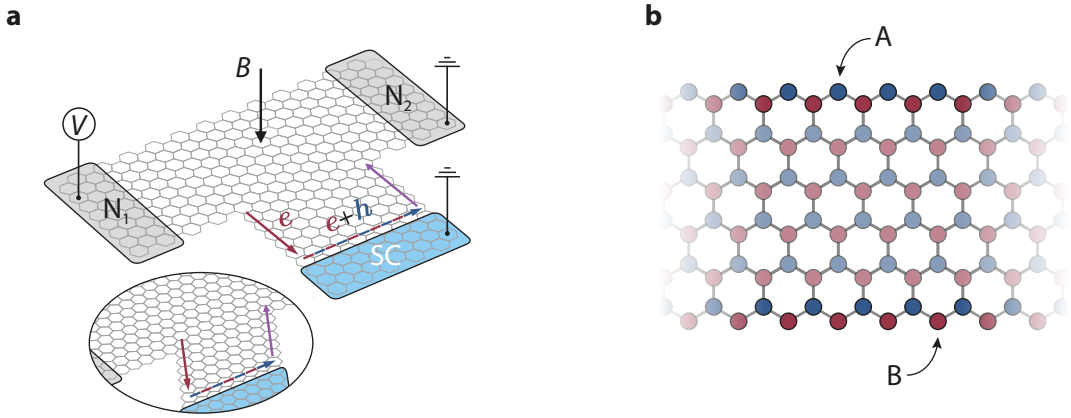

Figure 1.10: **Probing chiral Andreev edge states physics. a)** 3-terminals graphene-based device consisting into 2 normal metal contacts, denoted N1 and N2, in-between which a superconducting electrode (color-coded in blue) have been implemented along one of the graphene's pristine edges. For disorder-free edges, the value expected for G_{xx}, that is the two-terminal conductance measured in-between N1 and N2, depends on the graphene lattice terminations along the edges going from N1 to the superconductor and from the latter to N2. In their simulations, the authors assumed zig-zag edges (see inset), a way to ensure that the N = 0 QH edge states are valley-polarized at the NS interface entrance (resp. exit) which, the authors believe, is the most general case. Figure taken from [37]. **b)** Graphene nanoribbon schematic showing that the last atomic row for zig-zag edges necessarily holds within a different sub-lattice (here denoted in blue and red) on either edge of the graphene. As a result of the valley sub-lattice locking for the N = 0 Landau level, the QH channels have an opposite-valley polarization along opposite edges.

As these considerations have been thoroughly investigated by A. L. R. Manesco *et al.* in [37], this part mainly follows their line of reasoning.
The authors considered the three-terminal system depicted in Figure 1.10.a, a configuration mimicking the actual device that was employed by the G. Finkelstein's group to look for Andreev edge states signatures (see Chapter 2 Section 2.4 for a detailed discussion).
The whole point of this paper then consisted in computing the QH two-terminal conductance G_{xx} measured in-between contacts N1 and N2, taking into account the fact that quantum Hall edge channels along one of the

graphene's edges are locally proximitized by a superconducting lead. Importantly, a particular care was taken to investigate graphene lattice terminations structure as well as disorder influences. The ensuing conclusions being applicable to Josephson junctions, we devote this part to the key insights provided by this work.

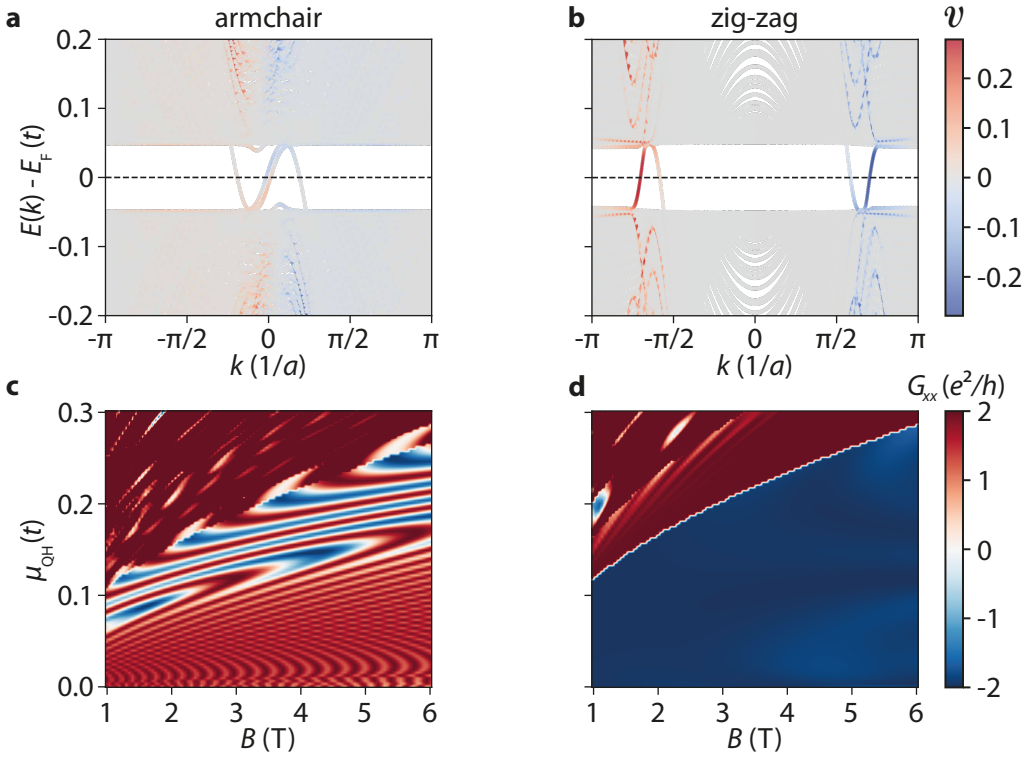

Figure 1.11: **Chiral Andreev edge states spectrum. a)** Band structure attached to the NS interface. It was computed assuming zig-zag graphene termination along the pristine edges adjacent to the superconducting electrode and armchair termination along the boundary with the superconducting lead. The magnetic field was set to $B = 1$ T and there is no Fermi level mismatch between the graphene and the superconductor. The color (whose scale is provided in **(b)**) indicates the valley polarization flavor. The 2 positive-slope branches correspond to the 2 chiral Andreev edge states co-propagating along the NS interface. The bands with a negative slope arise from the QH edge channels entering/leaving the NS interface. **b)** Band structure attached to the NS interface computed for a piece of graphene having edges termination as shown in Figure 1.10.a inset, i.e. zig-zag structure along both the pristine edges and the NS interface. **c)** Conductance G_{xx} versus the magnetic field B and μ_{QH}, the on-site energy within the normal part, assuming armchair termination along the NS interface. A regular oscillatory pattern accross the whole B-μ_{QH} emerges, indicative of interferences between the chiral Andreev edge states. **d)** Conversely, for zig-zag termination along the NS interface, G_{xx} is expected to be constant. Figures taken from [37].

Before going any further, we emphasize here that these results are based on the assumption that graphene with generic lattice terminations (i.e. neither fully armchair or zig-zag, a configuration more likely to describe actual samples) supports valley-polarized edge states in the N = 0 QH regime, a working hypothesis originating from [38] and to which we will return once their reasoning has been exposed.
Following the A.L.R. Manesco *et al.* work, graphene cristallographic edges on sides adjacent to the NS interface are assumed to form a zig-zag structure in the next[41].

[41] Again in order to emulate the valley-polarization behavior of generic cristallographic boundaries, the relevant situation for actual devices according to the authors.

Note that in such a configuration, the last atomic rows necessarily lie within different graphene sub-lattices (see Figure 1.10.b). The valley degree of freedom being tight to graphene sub-lattices for the N = 0 quantum Hall state, this implies that the QH edge channels on each side of the NS interface have opposite valley polarization.

Now looking along the NS interface, the proximitized quantum Hall edge state can be described as made of 2 co-propagating *chiral Andreev edge states* (CAESs), each of them consisting in a weighted mixture of electron-like states lying within a given valley $|e, K\rangle$ and hole-like states within the other valley $|h, K'\rangle$ i.e. $|\psi_1\rangle = \alpha|e, K\rangle + \beta|h, K'\rangle$ and $|\psi_2\rangle = \alpha^*|e, K'\rangle - \beta^*|h, K\rangle$. As the Andreev reflection couples electrons and holes having opposite valley-polarization, this implies that an electron originating from one of the CAESs cannot be Andreev-reflected within the second CAES. Thus, as long as a valley-flip mechanism is absent, no cross-talk between CAESs takes place while they propagate along the NS interface.

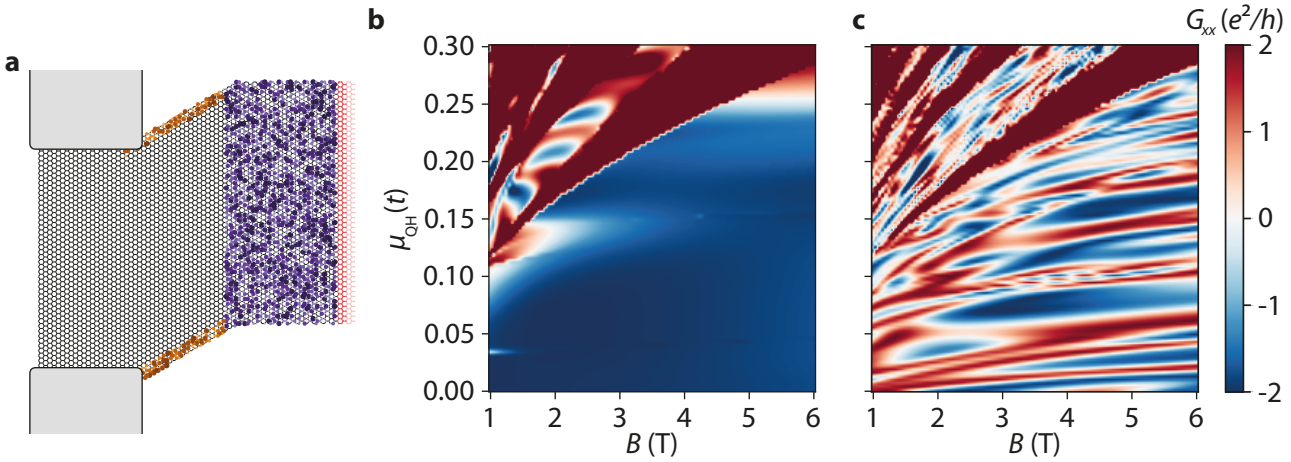

Figure 1.12: **Effects of disorder. a)** Map of the disorder landscape used to compute the conductance shown in **(b)** and **(c)**. **b)** Conductance versus B and μ_{QH} computed for ziz-zag terminations along both the NS interface and the graphene pristine edges, the latters including disorder over the few last atomic rows (see yellow dots in **(a)**). No conductance fluctuations emerge. **c)** Similar conductance map obtained after the addition of disorder along both the graphene pristine edges and the NS interface. Noise-like conductance oscillations now span the entire B-μ_{QH} plan. Figures taken from [37].

Using numerics, A. Manesco *et al.* computed the spectrum $E(k)$ attached to the CAESs for both the armchair and zig-zag termination cases i.e. assuming the last atomic row in contact with the superconducting electrode forms one of these idealized boundaries[42].

In the former case, the bands attached to each CAESs almost merge around $k = 0$ (see Figure 1.11.a). Such proximity in the momentum-space enables a cross-talk between the CAESs via lattice mismatch-induced inter-valley scattering[43]. In other words, CAESs in the armchair case interfer with each others, which ultimately translates as regular G_{xx} oscillations with both the magnetic field B and the electron density (see Figure 1.11.c).

[42] In details, the last atomic row of the graphene hexagonal lattice is connected to a square lattice with a non-zero superconducting pairing potential to modelize the superconductor.

[43] The slight shift between CAESs bands originates from the mismatch between the graphene hexagonal lattice and the square grid used to model the superconductor.

Conversely, for the zig-zag specific case, the branches attached to each CAES are far apart from each other in the momentum space (see Figure 1.11.b). Thus, the weak inter-valley scattering provided by the lattice mismatch along the NS interface is by no means enough to allow for a cross-talk between CAESs, hence resulting into no interferences between them and therefore, a constant value for G_{xx} as shown in Figure 1.11.d.

Emphasizing once again that the zig-zag case is supposed to be the closest from actual devices, the authors noticed their prediction was at odds with experimental observations, in which conductance exhibits stricking noise-like oscillations (see Chapter 2 Section 2.4 for a detailled discussion).
In order to stick a little closer to experimental reality, they then considered the effect of disorder. When solely located along the graphene's edges on either side of the NS interface, which breaks the valley-polarization constraint at both the entrance and exit of the NS interface, disorder did not yield any noticeable changement in the constant G_{xx} value (see Figure 1.12.b).
However, once adding disorder-induced scattering along the NS interface, G_{xx} exhibits irregular oscillations within the μ_{QH}-B plan (see Figure 1.12.c), in closer agreement with the experimental observations.

Most of the above discussion assumed valley-polarization is preserved along both the NS interface and the graphene pristine edges, an assumption which, we believe, is far from being that obvious for actual samples. Typically, most of the graphene-based Josephson junctions in the literature are defined using reactive ion etching (RIE), a process that usually involves a CHF_3/O_2 plasma. In addition to the structural disorder this etching step produces along the graphene edges, it adds chemical contamination (see the discussion at the end of Chapter 2 Section 2.3). Therefore, preservation of the N = 0 QH edge states valley polarization is quite unlikely in actual samples, which puts the importance of the points raised in this section into perspective.

1.3 Conclusion

In this chapter, we first dealt with basic elements of graphene physics together with the quantum Hall effect and proximity-induced superconductivity in this material.
Then, we discussed a model, first introduced by H. Hoppe *et al.* [21], to capture the NS interface physics when the N part is in the quantum Hall regime. This allowed us to extract an expression for the velocity of the proximitized QH edge states running along the superconductor, the so-called "chiral Andreev edge states" (CAESs).
In a second part, we further extended the discussion by considering a SNS Josephson junction in the quantum Hall regime, or *quantum Hall Josephson junction*. In particular, origin of the QH edge states-mediated supercurrent or *chiral supercurrent* hallmark, that is an anomalous h/e-flux periodicity, was clarified.
Next, we addressed the effect of the CAESs velocity renormalization along the NS interfaces on the chiral supercurrent occurence. Importantly, this enabled us to understand how critical was the NS interfaces length for Josephson effect in the quantum Hall regime.
Finally, we introduced the work of A.L.R. Manesco *et al.* [37] to clarify the peculiarities of proximity-induced superconductivity in graphene placed in the quantum Hall regime.

Chapter 2

Andreev reflection under magnetic field: review of the experimental state of the art

In 1993, 13 years after the first experimental report on the quantum Hall effect [3], M. Ma and A. Y. Zyuzin theoretically envisioned a Josephson junction whose normal part consisted in a two-dimensional electron gas (2DEG) placed in the quantum Hall effect regime and proximitized by two point-like superconducting electrodes[1] [28].

Crucially, upon varying the applied magnetic field, the critical current was anticipated to exhibit an anomalous h/e-flux periodicity, a prediction also derived in subsequent theoretical works [29; 30]. Yet, despite numerous experimental efforts over the last 30 years, evidence for this so-called *chiral supercurrent* is still lacking.

In this chapter, we start by briefly reviewing the results and difficulties the very first semiconductor-based quantum Hall Josephson junctions had to cope with. Although showing signatures of Andreev reflection (AR), these semiconductor-based 2DEGs did not allow for observing a supercurrent co-existing with the quantum Hall effect.

More recently, reports on graphene-based Josephson junctions have shown supercurrent surviving at increasingly high magnetic fields. This culminated in 2016 with the very first observation of a supercurrent in the quantum Hall regime by the G. Finkelstein's group [39], a result we carefully discuss in a third section. We also examine a subsequent experiment that elucidates the decisive effect of charge accumulation along the graphene edges [40] together with an other study dedicated to the investigation of chiral Andreev edge states [41].

Finally, in a last section, we discuss recent results obtained by the Harvard group using the crossed Andreev conversion approach [42; 43], an alternative that could induce a superconducting pairing between quasiparticles carrying fractional charges, a key ingredient in obtaining the long-sought parafermions [44].

[1] A way to keep aside NS interface-related physics and the calculations hurdles that could ensue.

2.1 Quantum Hall Josephson junctions: first attempts

While the very first work devoted to the Andreev reflection mechanism under magnetic field dates back to 1983[2] [46], several difficulties have until recently eluded the direct study of the Josephson effect in the quantum Hall regime:

- Before graphene, GaAs-based 2DEG were the workhorse platform for studying the quantum Hall effect. Although a continuous improvement of the samples quality (i.e. increasing mobility) lowered down the magnetic field value required to observe it[3], the inherent formation of a Schottky barrier[4] at the 2DEG - superconducting electrode interfaces precluded a supercurrent to be observed in the quantum Hall regime[5,6].

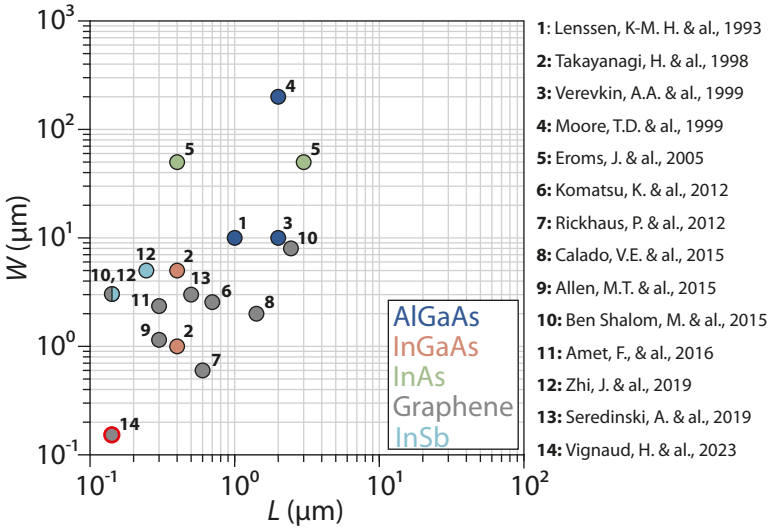

Figure 2.1: **Significance of the quantum Hall Josephson junctions size.** Diagram classifying quantum Hall Josephson junctions-related works as a function of the lead-to-lead distance L and NS interfaces width W of the involved devices. Note that our work, denoted by the red outline, clearly stands out in terms of dimensions. References from which are extracted the points are, from label 1 to label 14, [58], [59], [60], [55], [61], [62], [63], [64], [65], [66], [39], [67], [40] and [68].

- As a result of the finite amount of time it takes for each Andreev reflection to occur, the velocity v_{SC} of a quantum Hall (QH) edge state running along a NS interface can typically drop by an order of magnitude when

[2] Note that Josephson effect under small magnetic field was reported for the first time from 1963 by J. M. Rowell [45].

[3] The interested reader can find a review on GaAs-based 2DEG mobility improvements along the years in [47].

[4] When a semiconductor is interfaced with a metal/superconductor, the respective Fermi levels tend to align to ensure the thermodynamic equilibrium of the system. Together with the necessary continuity between the respective vacuum levels, these effects result in a bending of the energy bands diagrams near the interface. The latter translates as a potential barrier, termed *Schottky barrier*, whose height $\phi_{B,n}$ is defined as the difference between the metal/superconductor work function ϕ_m and the semiconductor electron affinity χ.

[5] Several strategies have been introduced in an attempt to overcome this issue, including penetrating contacts [48; 49], heavily doped surface layers [50; 51] as well as the inclusion of a MBE-growth Si-based bilayer within low doped and low-In-content $In_xGa_{1-x}As$/Si/Al heterostructures [52; 53; 54]. Surprinsingly, though, we found only two references [55; 56] reporting on an attempt to develop GaAs-based quantum Hall Josephson junctions (see further in this chapter).

[6] Note that high transparency NbN-based superconducting contacts to gallium arsenide heterostructures were recently achieved in [57].

compared to its velocity v_{QH} along pristine edges (see Chapter 1 Section 1.2.2 for a detailed discussion). For devices with $L \ll W$, that is, the vast majority of the quantum Hall Josephson junctions-related works (see Figure 2.1 for a non-exhaustive overview), this QH edge states velocity renormalization makes the ballistic Thouless energy[7], defined as $E_{Th} = h/\tau$ with $\tau = L/v_{QH} + W/v_{sc}$, to approximate as $E_{Th} \approx hv_{sc}/W$. Therefore, it turns out that increasingly wider NS interfaces decrease the Thouless energy attached to the chiral supercurrent-carrying particles, presumably explaining the systematic absence of Josephson effect in the quantum Hall regime for the widest devices.

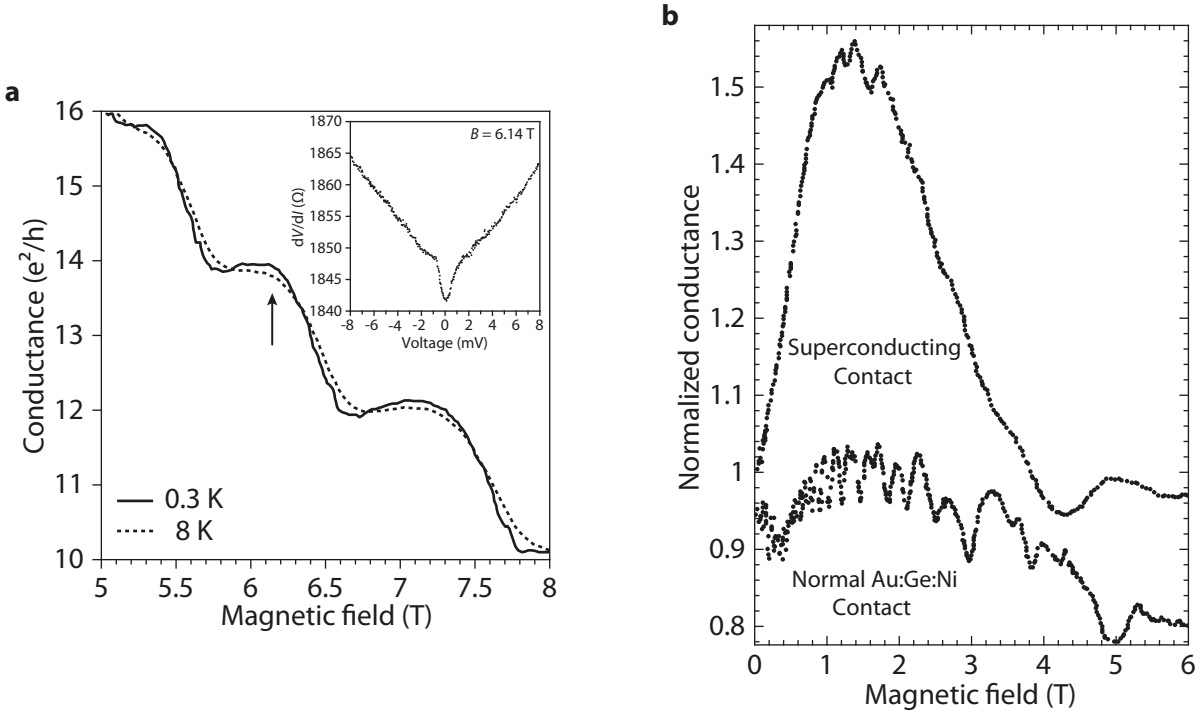

Figure 2.2: **Quantum Hall conductance in semiconductor-based Josephson junctions. a)** Zero-bias conductance versus magnetic field obtained in a $In_{0.52}Al_{0.48}As/In_{0.53}Ga_{0.47}As$-based Josephson junction with superconducting electrodes made of NbN. Inset: a dV/dI-V characteristic at $T = 0.3$ K and $B = 6.14$ T (whose location in the main figure is indicated by the black arrow). Figure adapted from [59]. **b)** Comparison between the magnetic field dependencies of the normalized conductance (see footnote 13) obtained for a Josephson junction (upper curve) and a junction equipped with normal metal electrodes (bottom curve), having similar dimensions and implemented in a $GaAs/Al_xGa_{1-x}As$-based 2DEG. The temperature at which these measurements were done is not provided. Figure adapted from [55].

First experimental attempts with S-2DEG-S Josephson junctions, the 2DEG being in the quantum Hall regime, were reported independently by two groups in the late 90s [55; 59].

In the H. Takayanagi and T. Akazaki work [59], the Josephson junction consisted in a $In_{0.52}Al_{0.48}As/In_{0.53}Ga_{0.47}As$-based 2DEG[8] equipped with surfacic contacts made of NbN, a superconductor having an upper critical field $H_{c,2}$

[7] This quantity was initially introduced in the context of quantum Hall Fabry-Perot interferometers and relates to several effects such as thermal broadening and decoherence of the quantum Hall edge states [69; 32]. As both these devices and QH Josephson junctions host a coherent loop made of partially reflected quantum Hall edge states, we believe this energy scale is also applicable to the chiral supercurrent context.

[8] Electron mobility was estimated to be about 31000 $cm^2/V.s$ thus corresponding to a mean free path of 800 nm at $T = 4.2$ K. The

reaching 7 T at 9 K.
A look at the zero-bias conductance dependence on magnetic field at 300 mK did not show any clear enhancement when considering the quantum Hall plateaus (see Figure 2.2.a), a fact that was ascribed to poor-quality contacts to the 2DEG, which is consistent with the absence of multiple Andreev reflection signatures when looking at the $\mathrm{d}V/\mathrm{d}I$ versus V curves at zero magnetic field.
Although limited to only three $\mathrm{d}V/\mathrm{d}I$ versus V plots, of which one was obtained while in a quantum Hall plateau and the two others in the nearby percolation regime, the observation of low-bias differential resistance anomalies (in the form of zero-voltage centered $\mathrm{d}V/\mathrm{d}I$ dip or peak, see Figure 2.2.a inset) was ascribed to Andreev reflection processes by the authors without any further investigations[9].

T.D. Moore and D.A. Williams soon after reported on results obtained using a sintered alloy superconductor[10] to contact a GaAs/$Al_xGa_{1-x}As$[11] heterostructure whose mobility was estimated to be about 3.34 x 10^6 cm^2/V.s at low temperature[12] [55].
Remarkably, the normalized conductance G_s/G_n, G_s (resp. G_n) being the conductance measured in the superconducting (resp. normal[13]) state, exceeded 1.5 around $B \approx 1.5$ T in the quantum Hall regime[14] (see Figure 2.2.b). The drop in conductance enhancement as the magnetic field value approaches the superconducting electrodes critical field ($H_{c,2} = 4$ T) further supported a superconductivity-related origin.

Although showing anomalies in transport measurements when compared to standard quantum Hall devices equipped with normal metal electrodes, none of these experiments was able to resolve a supercurrent coexisting with the quantum Hall effect regime.
As we shall see in the next, the latter effect had to wait for the use of graphene to be observed.

2.2 Graphene-based Josephson junctions under magnetic field

Shortly after the first report on the insulation of a single graphene monolayer in 2004 [70], both the quantum Hall effect [5; 71] and proximity-induced superconductivity [72] were observed separately in this material.
Pioneering attempts to couple these effects in graphene were subsequently reported from 2012 by the mesoscopic physics group at *Laboratoire de physique des solides* in Orsay [62][15] as well as by the C. Schönenberger's

lead-to-lead distance being of 400 nm, the junction therefore ranges in the ballistic regime.

[9] For the sake of completness, we mention that the same authors reported on AlGaAs/GaAs-based Josephson junctions ($W = 50$ and 100 μm, $L = 3$ and 5 μm.) contacted with NbN/AuGeNi superconducting electrodes in 2002 [56]. Yet, while a slight conductance enhancement was observed at the transitions between the quantum Hall plateaus when compared with a similar junction equipped with Au/AuGeNi normal metal electrodes, the plateaus did not show any clear difference.

[10] For the interested reader, details about the microscopic structure of such an alloy can be found in [49].

[11] The x value was not specified.

[12] The authors did not provide a precise number.

[13] The way their Josephson junction was driven into the normal state is not specified (it could be temperature or the applied bias for example). Therefore, it is difficult to understand what means normalized conductance for their control sample, whose electrodes are made of a normal metal and to which are compared the Josephson junction results in Figure 2.2.b.

[14] Using a Hall bar implemented within the same wafer, the longitudinal resistance R_{xx} was observed to reach 0 Ω around $B \approx 0.6$ T.

[15] In this work, the observed quantum Hall plateaus strongly departed from the expected quantized values. In particular, the $\nu =$ -6 and $\nu =$ -10 quantum Hall plateaus zero bias differential conductance almost displayed twice the expected value, in apparent agreement with theories anticipating a doubling of the conductance value for perfectly transparent NS interfaces [73]. Yet, the authors

group in Basel [63].

In the latter case, the devices under study consisted in graphene directly lying atop a 300 nm-thick SiO_2 oxide layer and contacted by surfacic Ti/Nb (4 nm / 40 nm) superconducting electrodes[16]. At $T = 2.0$ K, the upper critical field $H_{c,2}$ of the Ti/Nb bilayer was measured to reach 4 T, thus allowing to study the interplay between Andreev reflections and the quantum Hall regime.

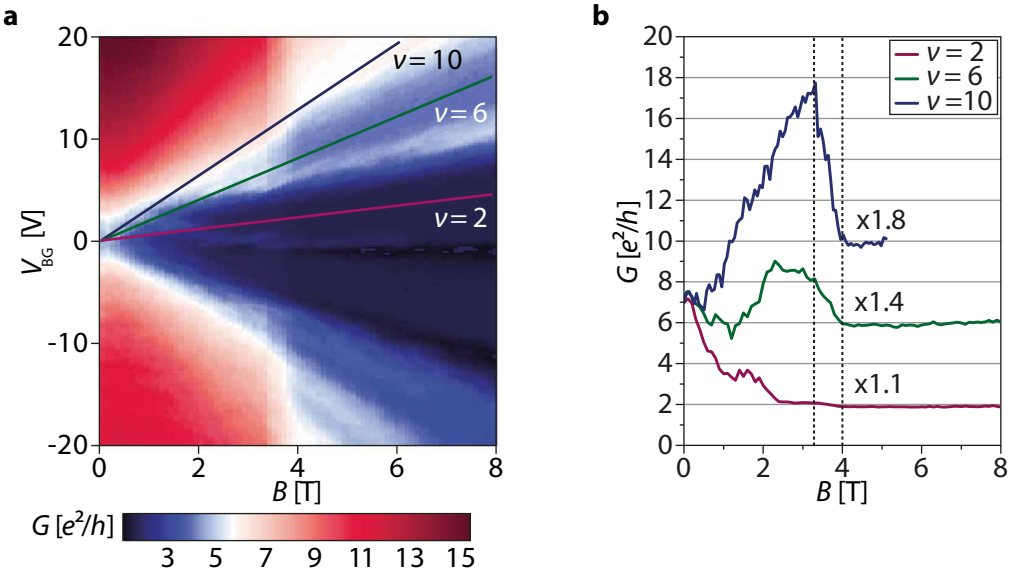

Figure 2.3: **Conductance enhancement in graphene-based quantum Hall Josephson junction. a)** Differential conductance map as a function of both the magnetic field B and the gate-voltage V_{BG} obtained at $T = 20$ mK for a square-shaped Josephson junction ($L \approx W \approx 600$ nm). **b)** Differential conductance linecuts versus the magnetic field taken along the successive integer filling factor lines indicated in **(a)**. Figures taken from [63].

This notably translated as an increase of the quantum Hall plateau conductance G once the applied magnetic field dropped below $H_{c,2}$ (see Figure 2.3.a)[17]. The reported conductance enhancement was about 10%, 40% and 80% of the normal state conductance for the quantum Hall plateaus $\nu = 2$, 6 and 10 respectively[18] (see Figure 2.3.b).

In the specific case of the $\nu = 2$ quantum Hall plateau, which belong to the N = 0 Landau level, the authors postulated that the weakness of the conductance enhancement resulted from strong inter-valley scattering.

suggested that Landau levels broadening together with sample inhomogeneities were likely to be the source of such discrepancies. However, these assumptions seem to be contradictory with the 4-fold conductance enhancement observed for the $\nu = -2$ and $\nu = 2$ plateaus. The latter having the largest cyclotron gap, they are expected to be less sensitive to disorder-related effects and consequently should be closer from the expected quantized value. The last part of the paper reports on stricking zero-bias resistance oscillations strongly reminiscient of the aforementionned H. Takayanagi and T. Akazaki work [59].

[16] Note that surfacic Ti/Al (10 nm / 70 nm) bilayer superconducting contacts were also used in [72]. This reflect the fact that, prior to the first demonstration of high quality Cr/Au-based one-dimensional contact to graphene in 2013 [74], Titanium was known to ensure good quality contact to graphene.

[17] The value of the applied bias being not specified in this work, we assume Figure 2.3.a displays the zero-bias differential conductance.

[18] In details, the conductance boost was computed as $G(B = 3.2\ \text{T})/G(B = 4\ \text{T})$.

According to theory [73], the conductance for a perfect NS interface, the N part consisting in graphene in the zeroth Landau level, solely depends on the valley polarization of the incoming/outgoing edge state, the latter being directly related to the cristallographic termination of the graphene edges.
Assuming identical edges at both ends of the junction's NS interfaces, the conductance value is expected to reach $4e^2/h$ for the $\nu = 2$ quantum Hall plateau[19]. The theory also addressed the effect of inter-valley scattering, the latter being shown to result in a reduced conductance enhancement.

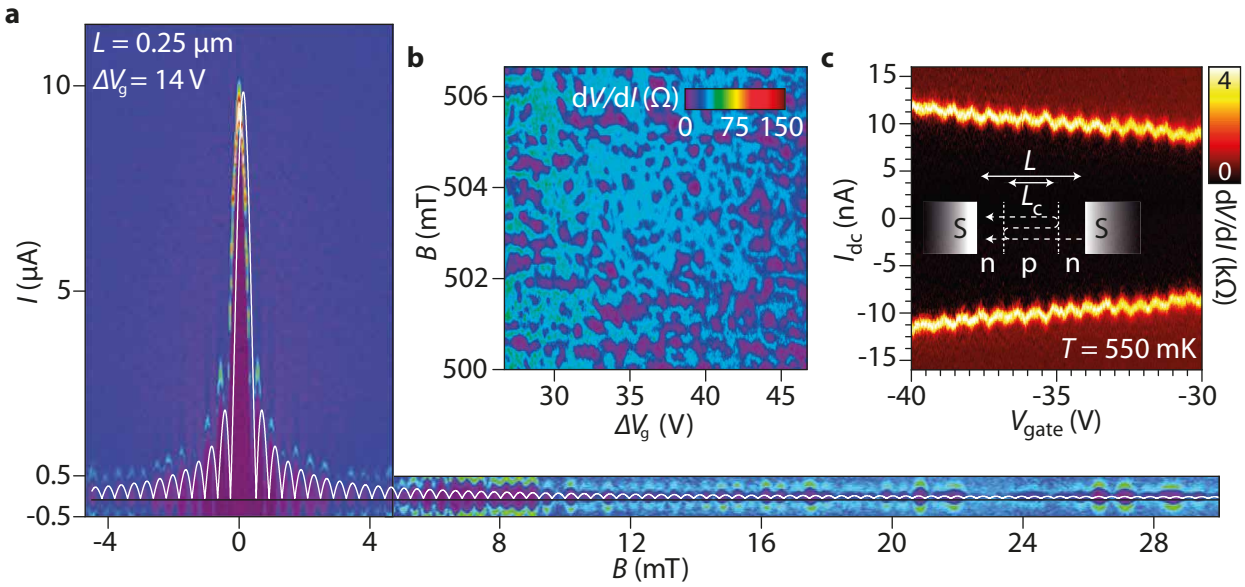

Figure 2.4: **Supercurrent interferences in ballistic graphene-based Josephson junctions. a)** Differential resistance colormap versus the applied perpendicular magnetic field B and the current bias I obtained for a [Ta/NbN/Ta]-graphene-[Ta/NbN/Ta] Josephson junction ($L = 0.25$ µm, $W = 5$ µm) at $\Delta V_g = 14$ V, the gate-voltage measured from the Dirac point, in [66]. The zero-voltage state is color-coded in purple (see the colorscale in Figure 2.4.b). The switching current, defined as the transition from the zero-voltage state to the resistive state, exhibits the usual Fraunhofer-like oscillatory pattern (see the white outline) up to $B^* \approx 5$ mT from which deviations emerge. Note that the Fraunhofer pattern periodicity is about 0.4 mT, which corresponds to an effective area larger than the device dimensions and was ascribed to flux focusing. **b)** Differential resistance colormap as a function of both ΔV_g and the magnetic field B obtained at $T \approx 10$ mK. Superconducting pockets are still present and occur randomly accross the ΔV_g-B plan. **c)** Differential resistance colormap versus the gate voltage V_{gate} and the applied current bias I_{dc} at $T = 550$ mK for a MoRe-graphene-MoRe Josephson junction ($L = 1.5$ µm, $W = 2$ µm) in [64]. The central schematic depicts the Fabry-Perot cavity formed by the contact-induced local n-type doping while the graphene is in the hole-doped regime.

The edge states of the N = 1 and N = 2 Landau levels being valley-degenerate, this scenario also agrees with the observation of a higher conductance enhancement for the $\nu = 6$ and $\nu = 10$ quantum Hall plateaus. This is further strenghened noticing that the $\nu = 10$ quantum Hall plateau, whose corresponding edge states are further away from the graphene edges and consequently less sensitive to edge disorder, displays the highest conductance increase.

[19] Such a conductance increase applies for zig-zag edges. For the armchair case, the conductance will also reach $4e^2/h$ provided the opposite edges are separated by a multiple of three hexagonal crystallographic cells. If this last condition is not fulfill, the NS interface conductance should equate e^2/h.

These promising results were then followed in 2013 by two major achievements regarding devices quality, namely the use of hexagonal boron nitride (h-BN) flakes to encapsulate the graphene together with the implementation of 1D contacts within this new kind of samples [74]. Remarkably, this approach has yielded ballistic transport signatures with mean free path l_{mfp} values reaching 15 μm at $T = 1.7$ K and high electron doping ($\sim 3 \times 10^{12}$ cm^{-2}).

Applying these methods, together with the use of disordered MoRe, an alloy known to form good quality contacts with carbon-based materials [75], enabled the group of L.M.K. Vandersypen to report on Josephson effect in a ballistic graphene-based Josephson junction in 2015 [64]. Although no evidence for superconductivity in the quantum Hall regime was mentioned[20], both the switching current and the re-trapping current exhibited regular oscillations while varying the gate-voltage for the hole-doped case (i.e. $V < V_{\text{D}}$, V_{D} denoting the gate voltage position of the Dirac point) at $T = 550$ mK and zero magnetic field (see Figure 2.4.a).
This observation, the first of its kind, was ascribed to interferences between supercurrent-carrying electrons and holes propagating ballistically within an electronic analog of a Fabry-Perot cavity. In details, the work-function mismatch between MoRe and graphene yields to the formation of a n-doped region in close vicinity of the superconducting electrodes. Consequently, when placed in the hole-doped regime, pn barriers that form nearby each NS interface define the walls of a Fabry-Perot-like cavity for charge carriers.

Note that the presence of Fabry-Perot oscillations does not constitute, in itself, a demonstration of the ballistic nature of transport within this kind of devices. In this work, the junctions ballisticity could be inferred from several additional observations such as an estimation of the Fabry-Perot cavity size slightly smaller than the lead-to-lead distance, a dispersion in magnetic field of the normal state Fabry-Perot oscillations as well as the obtention of Fraunhofer patterns whose magnetic field periodicity gave an effective surface smaller than the junction geometric area, at odds with what is usually reported [66; 39; 76].

Shortly after, ballistic transport features were also reported by M. Ben Shalom *et al.* [66] using encapsulated-graphene devices equipped with superconducting contacts consisting in nanostrips made of a Ta/NbN/Ta trilayer[21] directly lying atop the exposed graphene edges over 5 nm[22]. This peculiar configuration yielded a contact resistivity of about 35 $\Omega.\mu$m which, at the time of writing, remains one of the lowest ever-reported value for graphene-based Josephson junctions[23].

Additionally, these devices exhibited supercurrent traces persisting up to a perpendicular magnetic field of about 1 T, that is a 100-fold improvement with respect to the aforementioned graphene-based works [62;

[20] According to [64], disordered MoRe has an upper critical field $H_{c,2} \approx 8$ T at 4.2 K, which is perfectly compatible with the typical magnetic field values at which quantum Hall effect was observed in the sample under study (the $\nu = 1$ broken-symmetry state emerges from 5 T at $T = 40$ mK). Yet, we notice that the presented results were obtained using a micrometer-wide device ($L = 1.5$ μm and $W = 2.5$ μm), such long NS interfaces now being known to be detrimental to the observation of the chiral supercurrent (see Section 2.1).

[21] Note that the work functions of Ta and graphene are close, respectively about 4.3 eV (see Figure 4 p.251 in [77]) and 4.5 eV [78], which probably helps to have good quality contacts [79]. The Ta top layer was used to cap the NbN electrodes and protect them from oxidation.

[22] The latter was made possible through the development of a highly selective recipe for h-BN etching. As a result of the different material-dependent etching rates, the graphene effectively behaves as a mask while the surrounding h-BN get etched which, ultimately, exposes the edge of graphene over few nanometers.

[23] In 2018, the group of H.-J. Lee reported on a contact resistivity of 30 $\Omega.\mu$m in Al-graphene-Al Josephson junctions [76].

64]. This fact, together with the devices ballisticity, has made possible the investigation of magnetic field-related supercurrent interference effects beyond the standard Fraunhofer pattern physics.
In particular, the switching current dependence on B exhibited marked deviations from $B^* = \Delta/eLv_F \approx$ 5 mT[24] (see Figure 2.4.a), the magnetic field value upon which cyclotron deflection is expected to prevent Andreev bound states (ABSs) to form accross the bulk of the junction.

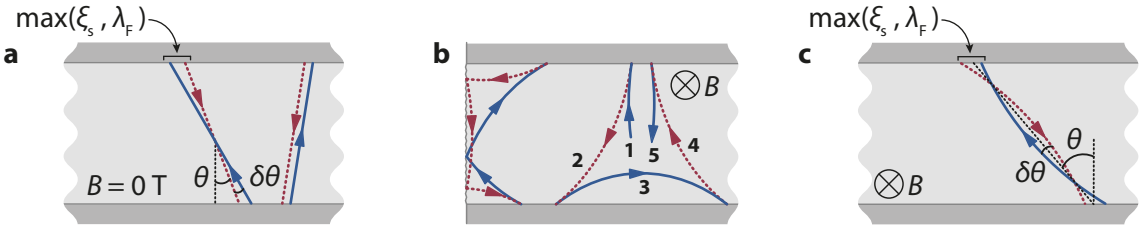

Figure 2.5: **Andreev reflection processes from zero to moderate magnetic fields. a)** Andreev reflections at $B = 0$ T. Provided the deflection angle $\delta\theta$ between the electron and the Andreev-reflected hole is low enough (i.e the trajectories ends at both NS interfaces are not separated apart by more than max(ξ_s, λ_F), ξ_s being the electrodes superconducting coherence length and λ_F the Fermi wavelength in the normal part), misaligned e-h paths can also give rise to Andreev bound states (ABSs). **b)** Under moderate magnetic field (i.e. $2r_c > L$), any sequence of successive Andreev reflections in the junction's bulk will, at some point, directly bring back a given charge carrier to the electrode from which it originates (see trajectory labeled 3), thus breaking down the Cooper pair transfer, hence preventing an ABS to develop. **c)** Yet, once considering the max(ξ_s, λ_F) tolerance window, some misaligned cyclotron-deflected e-h trajectories can form ABS-compatible loops, thus enabling for a supercurrent to survive under small magnetic field. Figures taken from [66].

In order to provide a qualitative explanation of the origin of this limit[25], we refer the reader to the schematics shown in panel 2.5.

At zero magnetic field, the ABSs stem from the electron and Andreev-reflected holes paths retracing each others (see the rightmost e-h trajectories in Figure 2.5.a). Provided both the electron and Andreev-reflected hole trajectories are close enough at each NS interfaces, that is not further apart than max(ξ_s, λ_F)[26], misaligned e-h trajectories can also contribute to ABSs[27] (an example being shown in Figure 2.5.a central part).

This last point actually turns out to be crucial when considering electron-hole trajectories under a moderate magnetic field, that is when $2r_c > L$, with r_c the cyclotron radius and L the lead-to-lead distance.
As shown in Figure 2.5.b, the magnetic field-induced deflection angle of the electron-hole trajectories changes upon each Andreev conversion event. Crucially, at some point, an Andreev reflected particle will directly

[24] Applying this formula with a superconducting gap $\Delta = 1$ meV, $L = 250$ nm the lead-to-lead distance of the sample under consideration and $v_F = 10^6$ m/s the graphene Fermi velocity, yields $B^* = 4$ mT.

[25] A detailed derivation of this value is provided in the Section 7 of the Supplementary Material in reference [66].

[26] The typical length scale attached to a Cooper pair being the superconducting coherence length ξ_s, it implies that the two electrons involved in the Cooper pair formation to be not further apart than ξ_s once entering the superconducting electrode. Moreover, in the normal metal part, the positions of two electrons cannot be discriminated if they are distant by less than the Fermi wavelength λ_F. Therefore, if $\lambda_F > \xi_s$, there is still a possibility for two electrons whose separation length ranges in-between ξ_s and λ_F to form a Cooper pair upon entering the superconducting electrode.

[27] As a reminder, electron-hole trajectories that perfectly retrace each other solely occur for charge carriers whose state lies at the Fermi energy (see Chapter 1 Section 1.1.3.1).

bounce back on the electrode from which it originates, thus effectively cancelling out the Cooper pair transfer and therefore preventing an Andreev bound state to take place (for instance, see the trajectory 3 in Figure 2.5.b). However, similarly to the zero magnetic field case, the electron-hole trajectories, here subjected to cyclotron deflection, do not necessarily have to form closed ends at the NS interfaces to enable Andreev bound states to occur (see the example shown in Figure 2.5.c). Although providing a way for a supercurrent to survive under small but finite magnetic field, this mechanism remains conditional on a low magnetic field-induced cyclotron deflection of the e-h trajectories with respect to the junction dimensions, thus explaining the value of only few mT deduced for B^* in this work.

Strikingly, some superconducting pockets were still observed to randomly occur at magnetic field values well beyond B^*. Although electrons and Andreev-reflected holes are no longer expected to form ABS-supporting loops accross the junction's bulk, the situation is quite different near the graphene edges (see the schematic in Figure 2.5.b). Here, a combination of cyclotron motion together with scattering along the graphene edges still allow for some ABS-compatible path configurations to take place. Yet, as the phase accumulated by such non-retracing trajectories can acquire large and random values, the ensuing supercurrent interference pattern displays some randomness upon varying the magnetic field and/or the gate-voltage, i.e. the charge carrier density, thus explaining the random pattern formed by the superconducting pockets in Figure 2.4.b.

Finally, despite one of the best-ever reported quality contact for graphene-based Josephson junctions, a further rise of the magnetic field did not allow for observing supercurrent signatures co-existing with the quantum Hall regime, a fact presumably resulting from the use of wide Josephson junctions with NS interfaces lengths ranging from 500 nm to 8 μm.

2.3 First observation of a supercurrent in the quantum Hall regime

The breakthrough came in 2016 with the first report of a supercurrent in the quantum Hall regime by the G. Finkelstein's group [39], a work we now further discuss.

A total of 4 low aspect ratio Josephson junctions[28] consisting in encapsulated graphene equipped with MoRe-based superconducting electrodes were studied. Using the Octavio-Blonder-Tinkham-Klapwijk (OBTK) formalism [80; 81; 82], the authors deduced a contact transparency of about 0.75[29].
The presence of regular Fabry-Perot oscillations for the hole-doped case at $B = 0$ T in one of the largest junctions ($L = 650$ nm and $W = 4.5$ μm), as a function of both the gate-voltage and the applied bias, together with an estimation of the Fabry-Perot cavity size agreeing with the device dimensions[30], suggests the junctions studied here are in the ballistic transport regime.

Applying a low perpendicular magnetic field ($B < \pm 5$ mT typically), measurements of the switching current

[28] Termed J1, J2, J3 and J4 and having dimensions ($L = 300$ nm, $W = 2.4$ μm), ($L = 800$ nm, $W = 2.4$ μm), ($L = 650$ nm, $W = 4.5$ μm) and ($L = 500$ nm, $W = 2.7$ μm) respectively.

[29] Note that the transparency estimate was done at 40 mK using an excess current estimate made at V_g = -4.8 V, that is in the hole-doped regime.

[30] In details, the Fabry-Perot cavity size estimation gave 490 nm, to be compared with a lead-to-lead distance of 650 nm. This suggests that the n-type local doping induced by the MoRe electrodes extends over 80 nm from each NS interfaces, an estimate that agrees with the 100 nm-long value that was deduced in the aforementioned L.M.K. Vandersypen's group work [64], which was also making use of MoRe-based electrodes.

dependence on B led to conventional Fraunhofer patterns, indicative of a uniformly distributed supercurrent within the devices[31]. Similarly to the M. Ben Shalom *et al.* work [66], the measured magnetic field periodicity was smaller than expected from the devices dimensions, a feature also reported in other works using such low aspect ratio micrometer-wide Josephson junctions [84; 76] and ascribed to flux-focusing effect [85].

Focusing on the smallest junction (L = 300 nm, W = 2.4 µm), a further increase of the applied magnetic field enabled quantum Hall quantization to be observed from 1 T, thus asserting the device quality.
Note aside, a plot of the differential resistance dV/dI as a function of the gate-voltage V_G at B = 1.4 T and T = 45 mK did not exhibit a global quantum Hall plateaus conductance enhancement (see Figure 2.6.b), at odds with the results obtained by the C. Schönenberger's group we mentioned in Section 2.2.

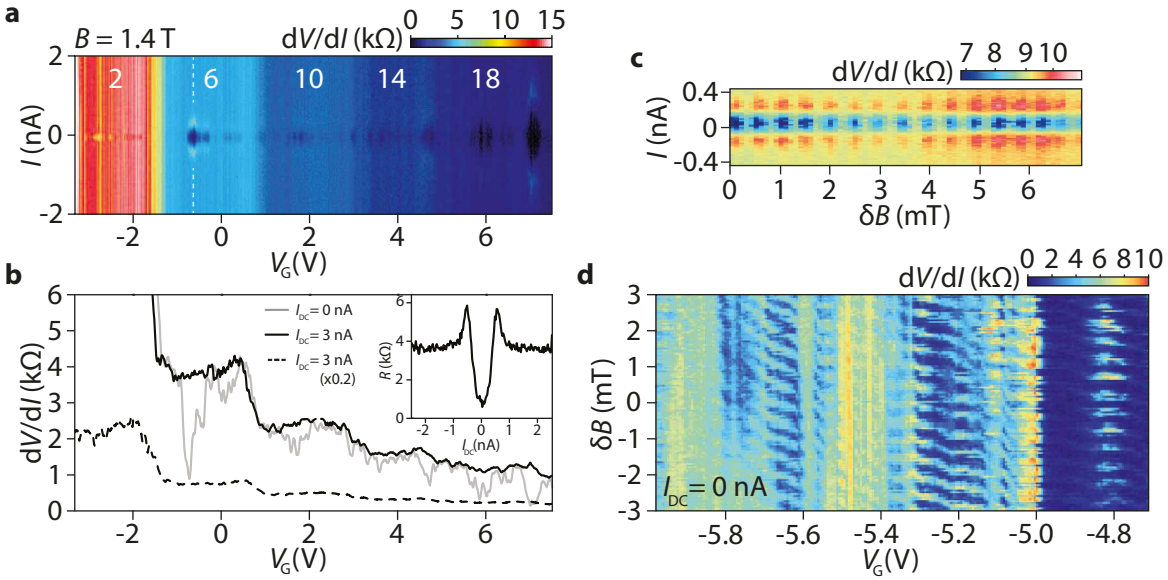

Figure 2.6: **Supercurrent in the quantum Hall regime. a)** Differential resistance dV/dI colormap as a function of both the gate voltage V_G and the current bias I obtained at B = 1.4 T and T = 45 mK in device J1. The supercurrent traces translate as black color-coded pockets centered around zero bias. **b)** Zero and finite bias (I_{DC} = 3 nA) dV/dI plots versus V_G taken in the same gate-voltage range than **(a)**. Inset: Differential resistance linecut versus current bias taken along the white dashed line in **(a)**. **c)** Differential resistance colormap versus δB, that is the magnetic field increment from B = 1 T, and the current bias. Note that the superconducting pocket under consideration lies at V_G = -2.2 V, that is at the transition between the ν = 2 and ν = 6 QH plateaus. This SQUID-like pattern has a typical periodicity of 0.5 mT, almost similar to the Fraunhofer pattern one (0.6 mT). **d)** Zero-bias differential resistance map versus V_G and δB around B = 1 T for a superconducting pocket located at the transition from the ν = -6 to ν = -2 QH plateaus, that is in the hole-doped regime. Figures adapted from [39].

A possible explanation may lie in the fact that NS interfaces structure differs in both works, the C. Schönenberger's group using superconducting electrodes forming 2D surfacic contacts with graphene whereas the present experiment makes use of 1D contacts. While graphene's honeycomb lattice under the electrodes is likely to be preserved in the former case, it is inevitably interrupted by the 1D contacts in the second situation. This type of contacts being implemented using reactive ion etching (RIE), the presence of a structual disorder

[31] These measurements were systematically done at high electron doping, presumably because the switching current dependence on B at the Dirac point has been shown to deviate from the conventional Fraunhofer pattern physics [83; 65].

at the graphene edge along the NS interfaces is very likely, a fact that numerical simulations have recently shown to boost the inter-valley scattering (see Chapter 1 Section 1.2.3), thus potentially explaining the lack of quantum Hall plateaus conductance enhancement in this experiment[32].

Low current bias investigations of the quantum Hall effect yielded the first major result of that study with the observation of superconducting pockets lying within the $\nu = 6$, 14 and 18 quantum Hall plateaus at $B = 1.4$ T and $T = 45$ mK (see Figure 2.6.a). However, the corresponding differential resistance at zero bias displayed some residual resistance (see Figure 2.6.b inset), a fact that was ascribed to phase diffusion mechanism [86; 36].

The authors then studied the evolution of some superconducting pockets at $T = 40$ mK upon varying the magnetic field, a typical example being shown in Figure 2.6.c. The resulting patterns, strongly reminiscient of the supercurrent interference signatures usually reported in SQUID devices, suggested that the supercurrent-carrying electrons/holes form a coherent loop within the junction.

To further substantiate this scenario, the dependence of these interference patterns on the gate voltage, i.e. the electron density within the graphene, was also investigated.
Figure 2.6.d shows a zero-bias differential resistance map as a function of both V_G and the magnetic field variation δB around a superconducting pocket located at $B = 1$ T.
The above-mentioned SQUID-like features, which here translate as $\mathrm{d}V/\mathrm{d}I$ oscillations along the magnetic field axis, clearly undergo a shift as V_G is changed, a fact that was interpreted as resulting from a gate voltage-dependent term in the phase picked by the electrons circulating along the junction's perimeter[33].

Although compatible with a QH edge states-mediated supercurrent at first glance, these interference patterns suffer from several drawbacks:

- First, the fringes appearing in Figure 2.6.d were obtained in the hole-doped regime, a configuration that severly complicates the previous picture due to the presence of pn-interfaces that deflect quantum Hall edge states with a finite probability [87][34].
- Second, the colormaps shown in Figures 2.6.c and 2.6.d were both obtained at the transition between QH plateaus, that is in the percolation regime in which a cross-talk between opposite QH edge states can occur[35].
- Finally, if we summarize the various periodicities reported in this work, we have:

[32] The use of RIE to define the junctions geometry makes also very unlikely the presence of crystalline edges of only the armchair or zig-zag kind at the exits of the NS interfaces, the cases with which the "NS interface conductance boost" theory initially dealt with [73]. Yet, a refinement of this theory using numerical simulations shows that the inclusion of a structural disorder only along the graphene edges at the entrance and exit of the NS interface should still result in a conductance of $4e^2/h$ [37]. It turns out that, within this theoretical framework, the key parameter avoiding the quantum Hall conductance boost is the disorder along the NS interface.

[33] According to the authors' reasoning, the flux enclosed by the ABSs attached to the chiral supercurrent expresses as $\pi BW(L - 2d)/\Phi_0$ with d the distance between the QH edge states and the superconductor. The maximal value for the supercurrent is reached when the total flux $\pi BW(L - 2d)/\Phi_0 = 2\pi$ x integer. Considering a given superconducting pocket at a fixed gate voltage value, reducing B is expected to result in a descrease of d i.e. to increase the area enclosed by the edge states. Therefore, the only way to keep a total flux equating 2π x integer, i.e. to compensate this area entension, consists in decreasing V_g. This scenario agrees with the negatively-sloped fringes observed in Figure 2.6.d.

[34] Note however that taking the length of the junction L as the distance between the pn-interfaces, the expected magnetic field periodicity for a flux quantum $\Phi_0 = h/2e$ would equate 6.2 mT, which in no way corresponds to the observed periodicity.

[35] The location of the superconducting pockets in the $V_G - B$ plan is provided in the Supplementary Material Figure S5 of [39].

- A Fraunhofer pattern periodicity of 0.6 mT, to be compared with an expected theoretical value of $\delta B = h/2eLW = 2.9$ mT. The difference here was ascribed to flux-focusing effect.
- Assuming the chiral supercurrent is present, the supercurrent interference patterns observed in the quantum Hall regime should display a periodicity $\delta B = h/eLW = 5.7$ mT, that is more than an order of magnitude larger than the reported 0.5 mT.

A possible explanation for this last discrepancy was subsequently put forward by the same group in [40]. The device under study here consisted in an encapsulated graphene-based Josephson junction equipped with side-gates to locally modulate the charge carrier density along the junction's edges (see Figure 2.7.a).

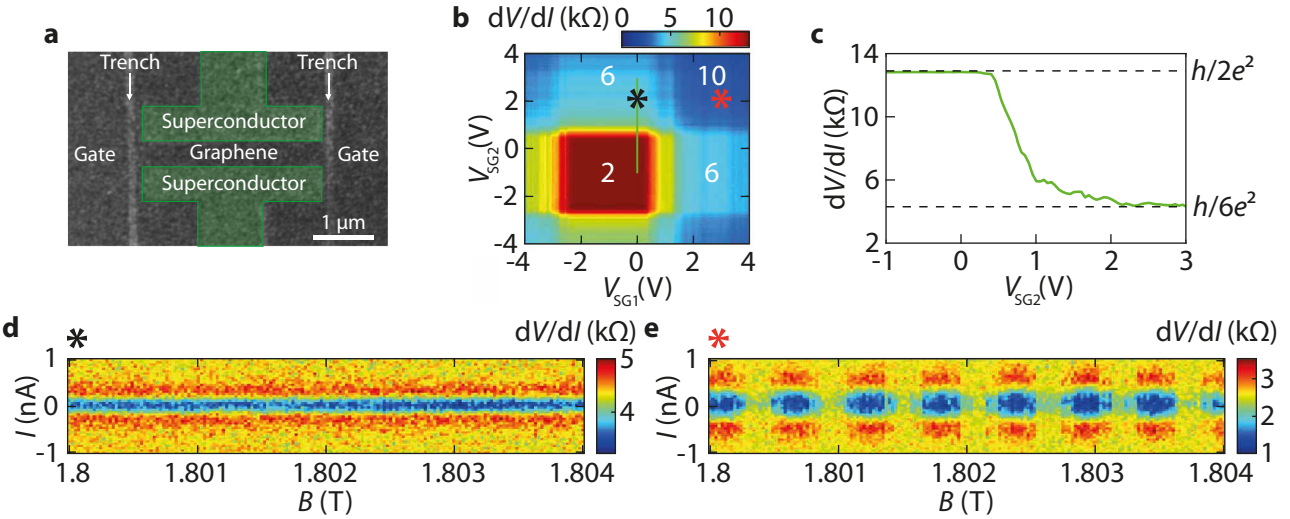

Figure 2.7: **Influence of charge accumulation along graphene edges on supercurrent interference patterns. a)** Scanning electron microscopy picture of the device under study in [40] before it undergoes RIE process. The green layers highlight the position of the subsequently implemented MoRe electrodes. The width of the trenches separating the lateral side-gates from the junction (vertical grey lines) is about 60 nm. **b)** $\mathrm{d}V/\mathrm{d}I$ colormap as a function of V_{SG1} and V_{SG2}, the voltage applied on the side-gate 1 and 2 respectively. This map was obtained at $B = 1.8$ T using a DC current bias of 10 nA while the graphene's bulk was maintained in the $\nu = 2$ quantum Hall state applying 4.7 V on the Silicon back gate. The white numbers specify the conductance attached to each plateaus in units of e^2/h. **c)** Linecut of the differential resistance versus V_{SG2} taken along the green line in **(b)**. **d)** Differential resistance colormap versus the applied magnetic field B and the current bias I obtained for a superconducting pocket whose position in the V_{SG1}-V_{SG2} plan is denoted by the black star in **(b)**, a configuration in which additional edge states are induced along a single side of the graphene. The supercurrent amplitude does not show any variation with the magnetic field. **e)** Similar measurement for a superconducting pocket whose location in the V_{SG1}-V_{SG2} plan is indicated by the orange star in **(b)**. In that configuration, additional counter-propagating edge states occurs on both side of the graphene. The supercurrent amplitude now form a SQUID-like pattern. Figures adapted from [40].

Typically, the graphene was first placed in the $\nu = 2$ QH state at $T = 100$ mK by applying a voltage on the underneath Silicon back gate while subjecting the sample to a perpendicular magnetic field of 1.8 T.
The differential resistance $\mathrm{d}V/\mathrm{d}I$ of the device was then recorded as a function of both V_{SG1} and V_{SG2}, the voltages applied on each side-gate, leading to the colormap shown in Figure 2.7.b.
Crucially, the presence of square-shaped regions within the V_{SG1}-V_{SG2} plan attested the influence of each side-

gate was highly local[36].

Taking a linecut along the V_{SG2} axis at $V_{SG1} = 0$ V, the differential resistance is seen to transit from the $\nu = 2$ QH state quantized resistance value to $h/6e^2$ (see Figure 2.7.c). As the graphene's bulk is still maintained in the $\nu = 2$ QH state, such a conductance increment of $4e^2/h$ suggests that additional fourfold degenerate edge states form nearby the side-gate 2, that is solely along one of the graphene's edges. In details, one of them would propagate along the direction imposed by the QH chirality while the other one would counter-propagate, which, from the Landauer-Büttiker formalism point of view, is similar to the $\nu = 6$ quantum Hall edge states configuration.
Note that within this scenario, adding extra edge states on either side of the graphene, i.e. nearby each side-gate, would result in a differential resistance value reaching $h/10e^2$, which agrees with the observations (see the plateau labeled 10 in 2.7.b when both side-gates are active).

A similar measurement was then repeated at zero DC current bias to locate superconducting pockets within the V_{SG1}-V_{SG2} plan.
Quite revealingly, when focusing on a superconducting pocket located in the $h/6e^2$-quantized resistance region (indicated by a dark star in Figure 2.7.b), that is when a counter-propagating channel runs along a single edge, the supercurrent amplitude is magnetic field-insensitive (see Figure 2.7.d).
In contrast, when considering a superconducting pocket in the region where side-gate-induced charge accumulation occurs along both graphene's edges (see orange star in Figure 2.7.b), a clear SQUID-like interference pattern emerges (see Figure 2.7.e).

These observations are in line with the presence of counter-propagating edge states allowing for "local" Josephson junctions to form along each graphene edges.
In the first situation, the Andreev bound states enclose an area defined by the loop formed by the side-gate induced additional channels along a single edge. Such an area being extremely small, the supercurrent flux periodicity is therefore expected to be large, thus resulting in no switching current modulation in the magnetic field window considered within this work[37].
When counter-propagating edge states are present on both side, the device behaves as 2 Josephson junctions in parallel, that is a SQUID, hence explaining the oscillatory pattern the supercurrent exhibits in this case.

Going back to reference [39], the anomalous flux-periodicity could therefore arise from charge accumulation along the edges, though its precise origin remains to be clarified.
Interestingly, we note that edges of the junctions studied in [39] were defined by reactive ion etching (RIE) using a CHF_3/O_2 plasma mixture, a process that certainly enhances the disorder along the cristallographic edges of graphene. Moreover, RIE is also likely to add chemical contamination to the terminations of the graphene

[36] For pedagogical purpose, let's imagine we have distorted squares. If we slightly move apart from a given square's edge, for instance by tuning V_{SG1}, the only way to preserve a constant resistance value i.e. returning to the edge of the square, consists in adjusting V_{SG2} to compensate the influence of V_{SG1}. This would indicate that the local charge accumulation induced by V_{SG1} can be compensated using V_{SG2}, thus necessarily implying that side-gate along a given edge acts also on the opposite edge of the graphene. In contrast, going back to the square-shaped features observed in the experiment, there is no way to compensate a V_{SG1}-induced resistance variation using V_{SG2}, which demonstrates that side-gates only influence the nearby graphene's edge.

[37] In fact, the authors estimated an upper limit of $\sim$100 nm for the distance separating the additional edge states. This implies that the switching current does not show any variation over a window of at least 40 mT, a statement which is not that clear when looking at the additional data the authors refer to (Figure S1 in the Supplementary Materials of [40]).

lattice. For instance, CHF_3 plasma was shown to induce fluorination of graphene edges [88] while O_2 plasma causes p-type doping in graphene [89].

2.4 Chiral Andreev edge states in graphene

Although not involving the Josephson effect, here we briefly digress by mentioning another very interesting work from the G. Finkelstein's group that focused on the chiral Andreev edge states (CAESs) physics [41].

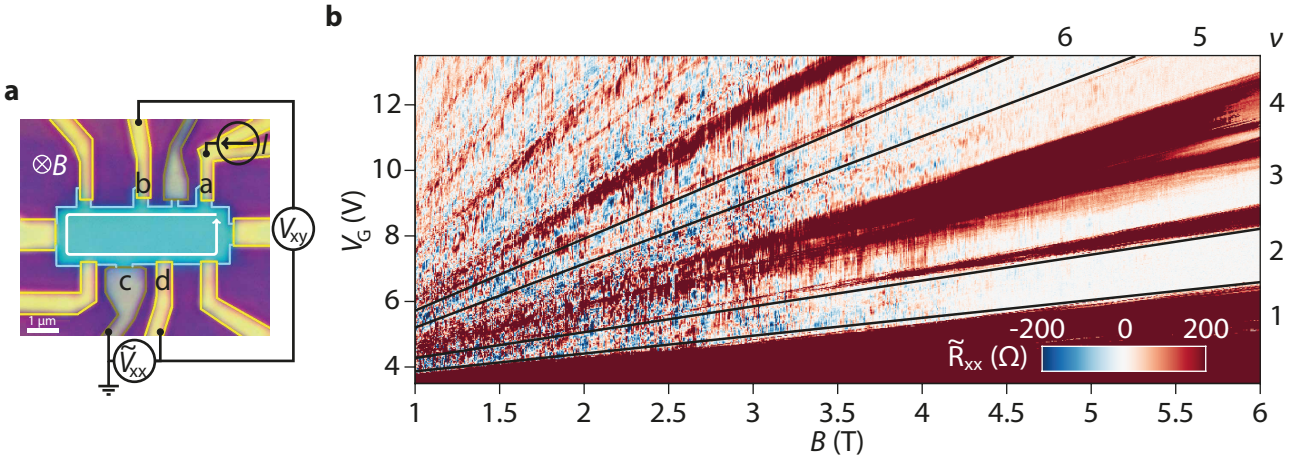

Figure 2.8: **Interference of CAESs. a)** Optical picture of the device studied in [41]. Grey (resp. yellow) electrodes correspond to the MoRe (resp. Cr/Au). Applying a perpendicular magnetic field yields quantum Hall edge states propagating along the edge of the graphene (here depicted with a white arrow). Both the Hall voltage V_{xy} and the downstream longitudinal voltage drop $\tilde{V}_{xx}$, the latter being measured in between a grounded superconducting contact (labeled c) and the nearby normal metal contact (labeled d), were recorded while applying a current bias I to the sample. The downstream longitudinal resistance $\tilde{R}_{xx}$ was deduced as $\tilde{R}_{xx} = \tilde{V}_{xx}/I$. **b)** Zero-bias $\tilde{R}_{xx}$ colormap as a function of both the magnetic field B and the gate-voltage V_G obtained at $T = 100$ mK. The black lines highlight the boundaries of the $\nu = 2$ and $\nu = 6$ quantum Hall plateaus. While in a conventional quantum Hall bar device $\tilde{R}_{xx}$ would reach zero each time the Hall resistance is quantized, here it clearly exhibits fluctuations around zero, the origin of which being ascribe to interferences between CAESs propagating along the superconducting electrode interface. Figures taken from [41].

In this experiment, a MoRe-based superconducting electrode was implemented within a standard quantum Hall bar device made of encapsulated graphene (see Figure 2.8.a). Importantly, the NS interface length $W = 600$ nm was designed on purpose such that it largely exceeded the MoRe superconducting coherence length ξ_s[38], to avoid crossed Andreev conversion events (see the next Section), while remaining smaller than the typical coherence length attached to the quantum Hall edge states $\xi_\varphi = \hbar v/2\pi k_B T \approx 12$ µm at $T = 0.1$ K [90][39].

[38] In this work, the authors defined the superconducting coherence length as $\xi_s = \hbar v/\pi\Delta_0$ where $\Delta_0 \approx 1.3$ meV is the MoRe superconducting gap and v the quantum Hall edge state velocity along the NS interface. The latter was assumed to equate the graphene Fermi velocity $v_F = 10^6$ m/s, which resulted in $\xi_s \approx 160$ nm. Yet, such an estimate is surprising knowing that the definition of ξ_s usually involves the Fermi velocity attached to the electrons within the superconducting electrode v_F^s. Additionally, the expression here employed for the superconducting coherence length estimate is valid in the clean limit case, which certainly does not apply to MoRe, a disordered superconductor. It is therefore very likely that ξ_s is even smaller than the estimate provided by the authors.

[39] Note that this estimate was done using GaAs/AlGaAs-based 2DEG. Additionally, as mentionned in Chapter 1 Section 1.2.2, the successive Andreev reflections along the NS interface renormalize the quantum Hall edge states velocity, thus lowering the value of

Figure 2.8.b displays the central result of this experiment, namely the observation of noise-like fluctuations in the zero bias QH longitudinal resistance $\tilde{R}_{xx}$ measured in-between a grounded superconducting contact and a normal metal electrode located further downstream (the precise contact configuration is indicated in Figure 2.8.a) as a function of both the magnetic field B and the gate-voltage V_G at $T = 100$ mK.

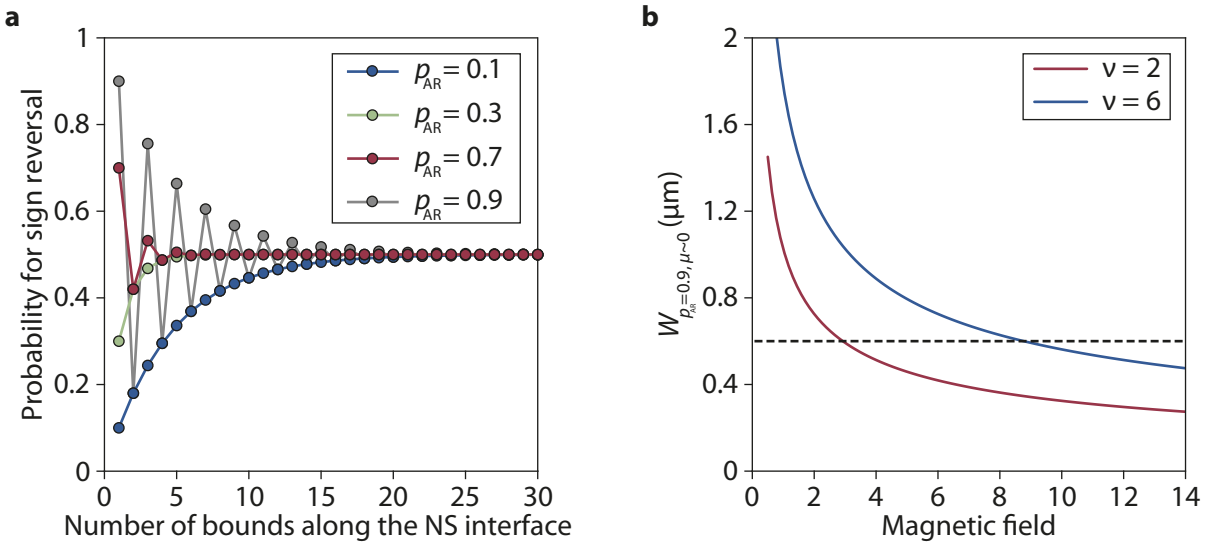

Figure 2.9: **Critical length for graphene-superconductor interface. a)** Semiclassical probability for an incoming electron to be Andreev-reflected as a hole at the NS interface exit versus the number of cyclotron bounces along the NS interface. Provided the Andreev reflection probability p_{AR} departs from 0 or 1, there is always an equal chance for the initial electron to end up as an electron or a hole at the electrode's exit beyond 20 bounces. Inspired by the discussion provided in the Supplementary Material Section 1 of [42]. **b)** Assuming a good quality graphene-superconductor interface (i.e. $p_{AR} = 0.9$), the knowledge of the applied magnetic field together with the filling factor value allows for computing a cyclotron radius value, hence the length corresponding to 20 cyclotron bounces along the NS interface and beyond which the chemical potential μ of the electron-hole mixture is expected to average out at zero. In this plot, we show the dependence of the "20 bounces-length" on the magnetic field value for the $\nu = 2$ and $\nu = 6$ quantum Hall states. The dashed line corresponds to $W = 600$ nm, that is the NS interface length in [41].

Resorting the semiclassical picture of the successive skipping orbits along the NS interface, these fluctuations may arise from variations in the NS interface outcomes, which can be either an electron or a hole. For instance, in the the latter case, the hole would lower the chemical potential of the normal metal electrode located further downstream once reaching it, thus resulting in a negative value for $\tilde{R}_{xx}$ as what is observed in some points of the B-V_G plane in the Figure 2.8.b.

At the first order, each cyclotron bounce along the NS interface has a finite probability p_{AR} to experience an Andreev conversion event. Taking this semiclassical line of reasoning a step further, it is possible to compute the probability for a given number of cyclotron bounces along the NS interface to end up with an Andreev-reflected hole (see Figure 2.9.a).
Interestingly, as long as the probability attached to Andreev reflection departs from 0 or 1, the chance for the last outcome of the successive cyclotron orbits to be a hole always reach 50/50 after 20 bounces. In other

ξ_φ. Yet, even an order of magnitude smaller value for v keeps $\xi_\varphi > W$.

words, the electron-hole mixture propagating along the NS interface is expected to become charge neutral beyond 20 bounces which, at first sight, should result into no measurable effect in $\tilde{R}_{xx}$.

If we now compute the critical NS interface length beyond which the electron-hole mixture becomes charge neutral (see Figure 2.9.b), we would expect the observed $\tilde{R}_{xx}$ fluctuations to be washed out from $B \approx 2.9$ T (resp. 8.7 T) for the $\nu = 2$ (resp. $\nu = 6$) QH state, estimates clearly at odds with the data.
While the $\nu = 6$ QH state fluctuations already disappear around 4.5 T, which could be eventually explained by a probability for Andreev reflection close from 0.5, the fact that fluctuations persist beyond the semiclassical limit for the $\nu = 2$ case indicates such a simple picture is not enough to correctly capture the physics at play here[40].

Going beyond this semiclassical approach, these fluctuations in $\tilde{R}_{xx}$ were rather interpreted as resulting from interference effects, a purely quantum mechanical phenomenon. In the framework used by the authors, an electron flowing within a quantum Hall edge channel that encounters the superconducting electrode gets decomposed into a linear superposition of two CAESs. The latters having different wavevectors, the CAESs accumulate a phase difference while co-propagating along the NS interface. Ultimately, once reaching the end of the QH-superconductor interface, interference between the 2 CAESs produces either an electron or a hole, the latter resulting into the measure of a negative chemical potential.

Key to this physics is therefore the phase acquired by the CAESs while propagating along the NS interface. This agrees with the observed sensitivity of the fluctuations to the gate-voltage whose variations shift the Fermi level, thus change the quasi-momentum of the CAESs, hence the phase difference they accumulate and therefore the outcome at the NS interface exit.
The CAESs phase terms being also sensitive to the potential vector along the superconductor, the presence of vortices affects the interference between them, thus contributing to the randomness of the fluctuations in the $B - V_G$ plane[41].
As a concluding remark, we note that the NS interface length beyond which fluctuations are washed out now relates to the distance required for the phase difference accumulated by the CAESs to average out at zero rather than the number of cyclotron bounces along the QH-superconductor interface.

2.5 The crossed-Andreev conversion approach

So far, all the above-mentioned results involved successive Andreev reflections along a NS interface. Yet, promising results were recently obtained using an alternative approach based on the crossed Andreev conversion mechanism (CAC) [42; 43], a strategy we now shortly review.

A SEM micrograph of a typical device is provided in Figure 2.10.c. It consists in a Hall bar made of encap-

[40] Regarding this specific point, the results obtained by the J. Shabani's group using InAs-based surface quantum wells contacted with a NbTiN superconducting electrode are particularly revealing [91], with CAESs-ascribe signatures observed with a 150 μm-long NS interface. Note that $k_F = \sqrt{2\pi n}$ for a conventional 2DEG rather than $k_F = \sqrt{\pi n}$ for graphene, with n the electron density. Yet, even taking into account the $\sqrt{2}$-factor difference, there is no way to reconcile the semiclassical scenario with the J. Shabani's group observations.

[41] Note that numerical simulations provided in [37] suggest that disorder along the NS interface is the source of the conductance fluctuations randomness. A detailed discussion about this specific work in provided in Chapter 1 Section 1.2.3.

sulated graphene, one of whose electrode being a narrow NbN-based superconducting finger[42] connected to the ground. In the quantum Hall regime, an electron encountering the NS interface will undergo successive Andreev reflections along the superconducting electrode thus forming a chiral Andreev edge state (see Figure 2.10.a schematic).

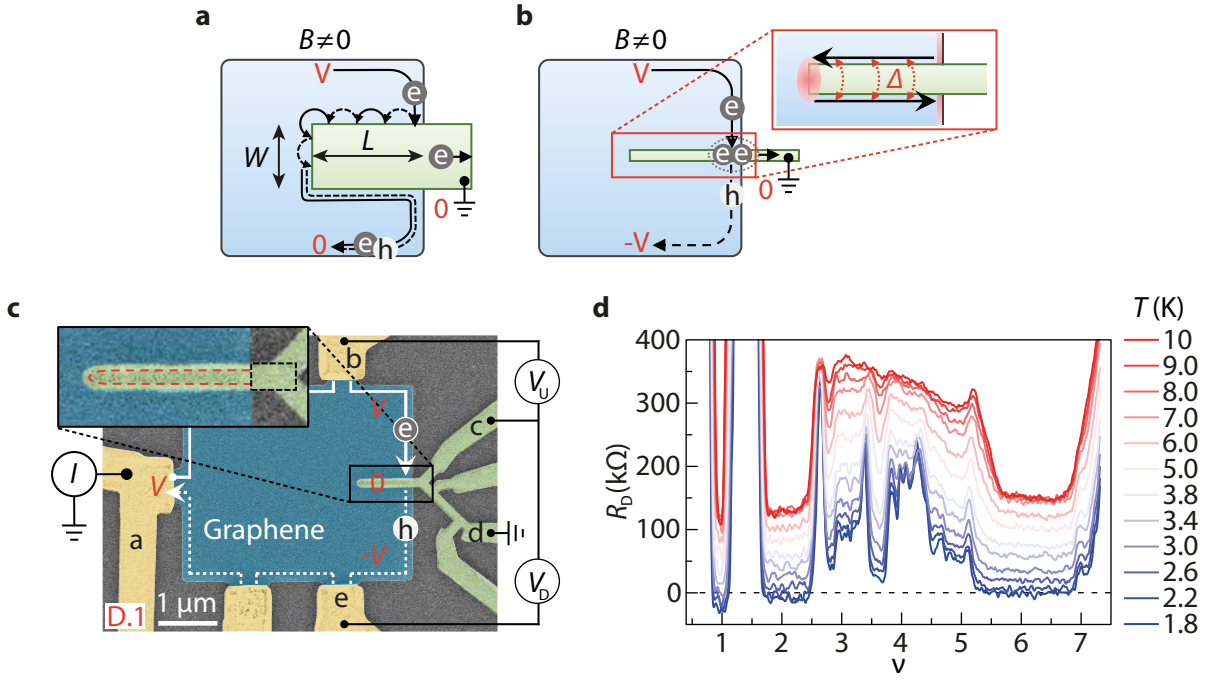

Figure 2.10: **Crossed Andreev reflection in the integer quantum Hall effect regime. a)** Schematic describing the conversion of an incident quantum Hall edge state into a chiral Andreev edge state running along the interface of a wide (i.e. $W \gg \xi_s$, ξ_s being the superconducting coherence length of the electrode) superconducting finger (here depicted in green). **b)** For a narrow enough superconducting finger (i.e. $W \ll \xi_s$), the Andreev-reflected hole attached to an incident electron has a finite probability for being directly emitted in the downstream quantum Hall edge state. Inset: provided the edge states on either side of the electrode get coupled by the superconducting pairing gap, non-abelian anyons (here symbolized by the red ellipse) are expected to emerge at the end of the superconducting finger. **c)** SEM picture of the device used in [42]. Yellow, green and blue colors denote respectively the Ti/Au electrodes, the NbN finger and the encapsulated graphene. R_D is obtained by dividing the downstream voltage V_D by the applied current I. Inset: Zoom on the superconducting finger. The red dotted line indicates the approximate position of the NS interface which, due to the etching process used to implement the contact, is not at the same position as the edges of the finger visible in the SEM image. **d)** Downstream resistance R_D versus the filling factor ν at $B = 8$ T for different temperatures. Negative resistance values are ascribed to crossed Andreev conversion mechanism. Figures taken from [42].

Note that when these results were published in 2017, the authors used the semiclassical reasoning mentioned right above to justify the fact that CAESs would not affect the QH edge channels leaving the superconducting finger, an argument we have seen invalidated by the subsequent results obtained in 2020 by the G. Finkelstein's group.

Although the NS interface length in the present experiment is 3.3 times longer than in the G. Finkelstein experiment and the temperature 18 times higher, an unambiguous demonstration that the outgoing QH edge channel is free from CAESs interference-related effects would require a test-sample of similar width but having

[42] In details, the finger consisted in a trilayer made of Ti-Nb-NbN (5nm - 5nm - 50nm).

a NS interface length far exceeding the coherence length attached to the CAESs, which remains unknown to this day[43].

Until now, the discussion implicitly assumed that the superconducting electrode width W strongly exceeded the superconducting coherence length ξ_s (see Figure 2.10.a schematic). In the opposite case, that is when $W \ll \xi_s$, the Andreev-reflected hole has a finite probability for being directly re-emitted on the other side of the superconducting electrode and propagating within the downstream quantum Hall channel, a mechanism termed crossed Andreev conversion[44] [93; 94] (see Figure 2.10.b schematic).

As the transmitted hole carries a negative chemical potential, the downstream resistance R_D (see Figure 2.10.c) is now expected to depart from the usual zero-longitudinal resistance value that would be obtained in a standard quantum Hall bar. Such a deviation was carefully studied for the $\nu = 2$ quantum Hall plateau in [42], whose large cyclotron gap (about 100 meV at $B = 8$ T) allowed to perform a study on the temperature dependence of that effect, using a $\sim$50 nm-wide superconducting finger[45].
Lowering down the temperature, R_D was indeed seen to reach negative values in the $\nu = 2$ and 6 QH plateaus at $B = 14$ T (see Figure 2.10.d).
Note that negative values for R_D were also observed in the $\nu = 1$ quantum Hall state, a surprising finding knowing its spin-polarization is expected to prohibit Andreev reflection processes, a point that will be further discussed in the next.

Although consistent with the CAC phenomenon, one critical point remained to be clarified for this experiment: the value of the superconducting coherence length attached to the superconducting finger, ξ_s.
The latter was actually derived assuming it equates the typical lengthscale required for two normal electrons entering the superconducting electrode to form a Cooper pair.
More precisely, ξ_s was deduced from a fit of the dependence of $\Delta R_D = R_D(T = 0.3\text{ K}) - R_D(T = T_c)$ on the superconducting finger width W of six devices assuming an exponential dependence i.e. $\Delta R_D = \Delta R_{D,0}\exp(-W/\xi_s)$, $\Delta R_{D,0}$ and ξ_s being the two fitting parameters[46].
Such a fit yielded $\xi_s = 52 \pm 2$ nm, a surprisingly high estimate when noticing it strongly exceeds the superconducting coherence length that would be expected in the dirty limit (in which the disordered NbN falls in) of about 10 nm according to the authors. This puzzling observation may suggest that the superconducting

[43] The beginning of an answer was recently provided in an ArXiv pre-print from the G. Finkelstein's group [92]. In details, the standard deviation of p_{eh}, that is the probability for sign reversal at the NS interface exit, was observed to follow $\sigma(p_{eh}) = A(\mathbf{r}_{vortex}) \cdot \exp(-B/B_0(L)) \cdot \exp(-T/T_0(L))$ with $A(\mathbf{r}_{vortex})$ a pre-factor depending on the vortices configuration within the superconducting electrode and $T_0(L)$ (resp. $B_0(L)$) a decay constant whose value decreases as the NS interface length increases. Importantly, p_{eh} was observed to reach 0 around $B = 2.5$ T for a 1 μm-long interface at $T = 40$ mK. Although using a different superconducting material, this suggests that the CAESs in the experiment searching for CAC signatures [42], performed at 1.8 K and with a NS interface length of 2 μm, do not affect the edge states leaving the superconducting finger.

[44] Note apart, this process was predicted to result in the formation of two non-abelian anyons provided the superconducting finger length L is such that $L \gg hv/\Delta$, v being presumably (this is not clearly stated) the velocity of the QH edge state running along the superconducting finger and Δ the induced superconducting gap [93] (see Figure 2.10.b inset).

[45] The authors mentioned that, as a result of the top h-BN etching process, the superconducting electrode has an oblique profile i.e. the width of the finger narrows down while approaching the graphene layer, thus making it difficult to precisely estimate W at the graphene level. In practice, W was obtained by substracting the thickness of the top h-BN layer to W_{NbN}, the width of the superconducting finger measured from a SEM picture.

[46] Such an exponential decay for the modes describing the two electrons entering the superconducting electrode can be found in the BTK paper [1] for instance, see equation (A12).

coherence length of the material from which the electrode is made is not the length scale to consider for the CAC process[47].

Building upon these results, the same group extended this experiment to the fractional quantum Hall regime. Since the latter requires high mobility to be obtained at a magnetic field compatible with superconductivity, double-gated devices were used[48], enabling the $\nu = 2/3$ fractional quantum Hall state to be observed from a record-low magnetic field of 3 T.

Crossed Andreev conversion-ascribed signatures were reported in both the integer filling factors 1 and 2 as well as in the fractional filling factors 1/3, 2/5, 2/3 and 5/3, this last observation being the main finding of this novel study (see Figure 2.11.a).

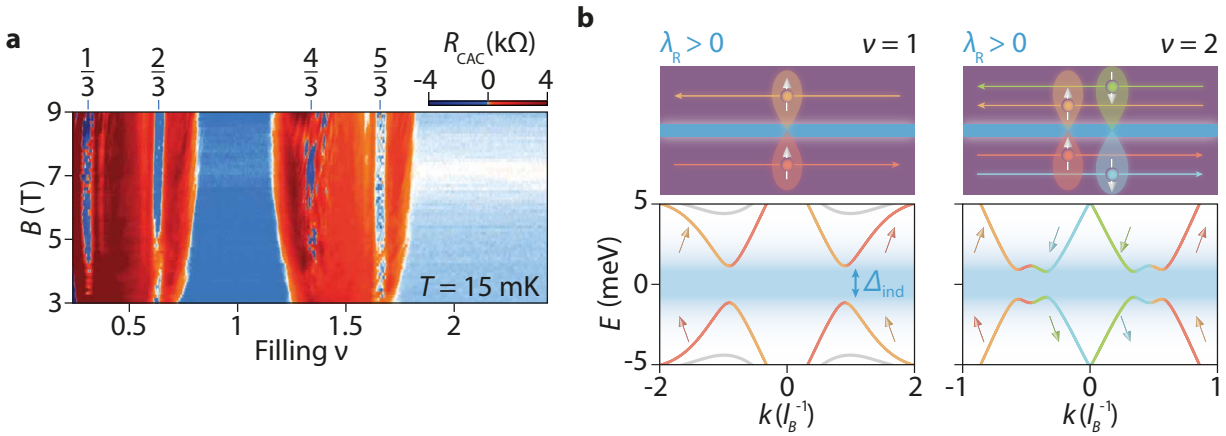

Figure 2.11: **Evidence for CAC in both the integer and fractional quantum Hall states. a)** Colormap of R_{CAC} as a function of both the filling factor ν and the perpendicular magnetic field B obtained at $T = 15$ mK. Note that CAC occurence (color-coded in blue) develops from $B = 3$ T in the $\nu = 2/3$ fractional quantum Hall state. **b)** Schematics of $\nu = 1$ (left) and $\nu = 2$ (right) quantum Hall edge states running on both side of a superconducing finger (blue rectangle). The spin-orbit coupling inherited from the superconducting electrode ($\lambda_R > 0$) tilts the spins and enables a pairing gap Δ_{ind} to develop. Right below are the corresponding Bogoliubov-De Gennes spectrums. The momentum k is expressed in units of l_B^{-1}, l_B being the magnetic length. The colors indicate the direction of propagation together with the spin polarization.

In order to interpret these findings, two ingredients were introduced by the authors:

- A propability for the crossed Andreev conversion process defined as $p_{CAC} = -V_{CAC}/V$[49] with V_{CAC} (resp. V) the chemical potential of the downstream (resp. incoming) edge state.

[47] A similar observation was reported very recently in [95], an experiment dealing with CAC signatures in a quantum anomalous Hall insulator. Applying the same analysis, the authors extracted a CAC-coherence length of ∼100 nm, to be compared with a superconducting electrode coherence length of about 30 nm. As the 160 nm-wide superconducting finger was forming a surfacic contact with the quantum anomalous Hall insulator, the authors postulated that the CAC process is mediated by the proximity-induced pairing under the superconducting finger rather than the superconductivity within the electrode, the former one having a longer length scale than the second one. Yet, this hypothesis cannot apply to the graphene-based CAC experiments in which the NS interface is 1D.

[48] For instance, double-gated devices have enabled to resolve several even-denominator fractional quantum Hall states in bilayer graphene [96]. See also the Figure S11 in the Supplementary information of [97] for a comparison between metal- and graphite-gated devices.

[49] V_{CAC} being negative, the negative sign is necessary for p_{CAC} to be positive.

- A Bogoliubov-De Gennes-like model to describe the tunneling processes between edge states running on either sides of the superconducting finger. Crucially, the observation of a CAC-ascribed signal for the $\nu = 1$ case, a spin-polarized quantum Hall state, suggested that spin polarization was broken. The Nb from which is made the superconducting finger being known to host a strong spin-orbit interaction [98], the authors included this effect in their model. Qualitatively, the latter yields the appearance of a pairing gap $\Delta_{\text{ind.}}$ coupling the edge states on either side of the superconducting finger having similar spin polarization (see Figure 2.11.b).

For the integer quantum Hall states, a *topological pairing gap*[50] should translate as $p_{\text{CAC}} = 1$.
Yet, in practice, all the integer quantum Hall states from $\nu = 1$ to $\nu = 6$ exhibited a similar magnetic field-independent p_{CAC} of about only 0.005 in the $B =$ 2-4 T range at $T =$ 15 mK. Such a discrepancy was captured by the authors' BdG-like model through the introduction of a BTK-like Z parameter, presumably translating the effect of vortices as well as cotunneling accross the superconducting finger[51].
Within the proposed BdG framework, the insensitiveness of p_{CAC} to the applied magnetic field for current bias $I_{\text{exc.}}$ and temperature T small in comparison to Δ_{ind} suggested the latter is topologically non-trivial.

Intriguingly, when considering the fractional quantum Hall states, the probability for crossed Andreev conversion is enhanced to about 0.01. Additionally, while p_{CAC} again exhibits a magnetic field-insensitive value for most of the observed fractional filling factors, the $\nu =$ 1/3 (resp. 4/3) quantum Hall state p_{CAC} further increases to 0.06 from $B =$ 9 T (resp. 0.08 from $B =$ 7 T) at $T =$ 15 mK.
Deciphering whether these variations arised from a dependence of the Z parameter on the magnetic field or from an inherent consequence of proximity-induced superconductivity in the fractional quantum Hall states remains an open question.

In an attempt to clarify the situation, a temperature-dependence study of p_{CAC} was done for the $\nu =$ 1/3, 2/5, 2/3, 1 and 2 QH states at $B =$ 14 T (see Figure 2.12.a).
As the temperature is lowered down, p_{CAC} saturates from $T \approx$ 4 K for the $\nu =$ 2/3, 1 and 2 QH states, an observation consistent with the presence of a topological gap for the integer QH states.
In contrast, the p_{CAC} value attached to the $\nu =$ 1/3 and 2/5 QH states clearly increases as the temperature goes down, a feature which, according to the authors, could stem from the superconducting pairing of fractional charges e^*. In such a scenario, depicted in Figure 2.12.a right inset, an incoming quasiparticle carrying a fractional charge $e^* =$ 1/3 would result in an outgoing quasihole excitation with a charge $-e^* =$ -1/3, leaving a fractional charge 2/3 in the superconductor.
Note that pairing of integer charges, an alternative scenario in which the superconductor couples clusters made of several fractional quasiparticles whose total effective charge reaches $e =$ 3 x 1/3e^* (see left side schematic in Figure 2.12.a) would result in a temperature-independent value for p_{CAC} while approaching $T =$ 0 K (see Figure 20 in the Appendix B of [43]).
Although the downward trend for p_{CAC} persists up to 15 mK, the lowest temperature reachable in this experiment, a definitive answer about the nature of the superconducting pairing would require alternative approach

[50] This term translates the fact that superconductivity-proximitized counter-propagating edge states are expected to effectively behave as a topological superconductor harboring Majorana (resp. parafermionic) edge modes in the integer (resp. fractional) QH regime [44].

[51] From the measure of p_{CAC}, $Z \approx$ 0.45. However, as mentioned by the authors, the model does not include quantum Hall edge states reconstruction along the NS interface, an effect they suspect could be relevant within the device under study. Interestingly, a model introduced in 2022 by N. Schiller *et al.* and dealing with the coupling between edge states and vortices seems to indicate that the latters are at the origin of the smallness of p_{CAC} [99].

such that tunneling [100; 101], shot-noise [102; 103] or supercurrent measurement [104].

To complete this discussion, we mention that a spin-orbit coupling-free explanation was put forward in 2022 by T.H. Galambos *et al.* [105]. In details, the model considered a ν =1 quantum Hall system contacted with a superconducting finger whose lateral profile is oblique (see Figure 2.12.b), a structural feature that was present in the experimental works mentioned right above. As a result of the Meissner effect, the magnetic field lines get deflected along the finger edges hence leading to a local in-plane component for the magnetic field along the NS interface. Crucially, the latter allows for crossed Andreev reflection process to develop between the spin-polarized edge states running on each side of the superconducting electrode, that is a gap opens in the proximitized quantum Hall edge states spectrum without involving any spin-orbit interaction.

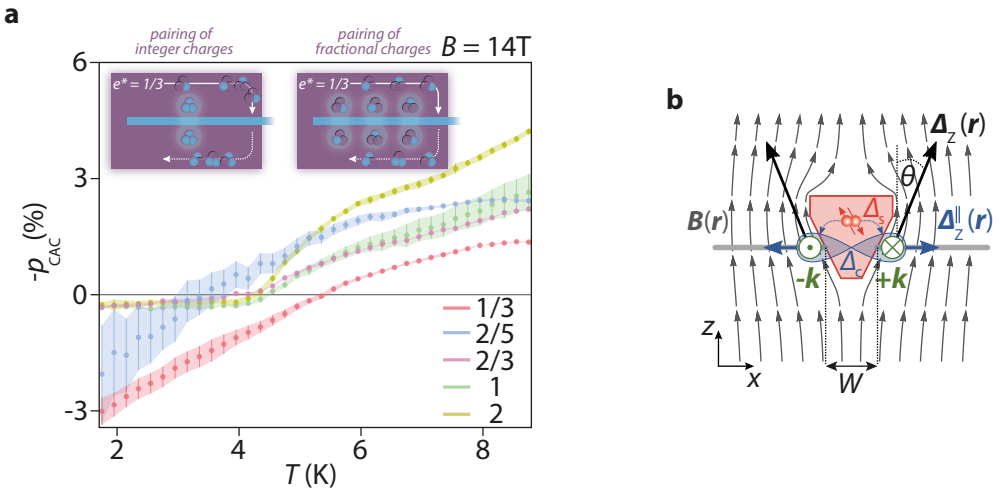

Figure 2.12: **Superconducting pairing of quasiparticles carrying fractional charges and spin-orbit coupling free CAC mechanism. a)** Temperature dependence of p_{CAC} at B = 14 T for the ν = 1/3, 2/5, 2/3, 1 and 2 quantum Hall states. While the ν = 1, 2 and 2/3 saturate as the temperature decreases, the fractional states ν = 1/3 and 2/5 clearly exhibit a downward trend, a fact potentially indicating superconducting pairing between quasiparticles carrying fractional charge. Right (resp. left) inset illustrates pairing mechanism for fractional charge quasiparticles (resp. clusters of fractional charge quasiparticles whose total effective charge reaches e). **b)** Schematic taken from [105] in which the oblique profile of the superconducting finger was shown to result in a pairing gap between opposite-side edge states running along the superconducting finger (to which are attached momentum ***-k*** and ***+k*** respectively). Here, Δ_s denotes the electrode superconducting gap (that has to be distinguished from the proximity-induced CAC gap Δ_c), ***B(r)*** the applied magnetic field, $\boldsymbol{\Delta}_Z^{\parallel}(\boldsymbol{r})$ the in-plane component of the vector $\boldsymbol{\Delta}_Z(\boldsymbol{r})$ i.e. the Zeeman term coefficient in the Hamiltonian describing the QH region.

While spin-orbit interaction is presumably inherited from the material constituting the superconducting electrode in the aforementioned works, alternative strategies using 2DEG having an intrinsic strong spin-orbit coupling interaction are also considered. Chiefly, InAs-based surface quantum wells [91] and InSbAs [106] have put back to the spotlight the semiconductor-based platforms for the study of proximity-induced in the quantum Hall regime. Although both platforms still exhibit low mobilities[52], hence preventing the observation of

[52] In the Supporting Information of [91], the mobility was measured to reach 11000 cm^2/V.s at an electron density $n \sim$ 8.51 x 10^{11} cm^{-2} (the temperature was not specified). In [106], peak mobilities ranged from 20000 cm^2/V.s to 28000 cm^2/V.s around $n \sim$ 3.5 x 10^{11} cm^{-2} at T = 300 mK.

fractional quantum Hall states thus far, the demonstration of high quality NS interfaces[53] together with the fabrication process scalability as well as the possibility to deplete the 2DEG using gates, an additional knob that is not possible with graphene, clearly make these platforms promising candidates for the study of topological superconductivity.

2.6 Conclusion

As we have seen in this chapter, graphene clearly emerged as a game-changer for the investigation of proximity-induced superconductivity in the quantum Hall regime. This mainly stems from the ease with which superconducting contacts can be interfaced with it together with the possibility to reach high mobility values.
Yet, only a handful of results have been reported for the more specific case of Josephson effect in the quantum Hall regime, a fact we mainly ascribe to the detrimental use of μm-long NS interfaces. As we shall see in the next chapters, this specific point will be our main angle of attack to look for edge states-mediated supercurrent signatures.

[53] For instance, epitaxially-grown NS interfaces in [106] led to a hard induced superconducting gap.

Part II

Andreev reflection and Josephson effect signatures in graphene-based quantum Hall junctions

Chapter 3

Device characterization

Prior to investigate the interplay between superconductivity and quantum Hall effect, we first devote a chapter to the characterization of our Josephson junctions at zero and low magnetic fields. This includes the dependence of junctions resistance and supercurrent on gate voltage, an estimate of the contacts transparency, as well as the interference patterns formed by the supercurrent when the sample is exposed to a weak perpendicular magnetic field.
For the sake of brevity, this chapter presents data from the sample HV088[1], representative of the behavior of all the junctions studied. Interested readers will find all the additional data, including that from the second sample used for this PhD work, i.e. DP024[2], in Appendix A.
Since junctions width (W) will appear as one of the key parameters for observing a supercurrent in the quantum Hall regime, we present results obtained for both wide ($W > 2$ μm) and narrow ($W < 350$ nm) junctions throughout this first section. This allows to highlight essential differences between these two kinds of junctions as well as to make comparison with state of the art devices that have, thus far, only consisted in μm-wide junctions. In a second part, we address the peculiarities of the quantum Hall effect specific to small graphene-based junctions. In particular, dependence of the two-terminal magneto-conductance on junctions aspect ratio is considered.

3.1 Josephson effect in graphene-based junctions

We discuss in this section results obtained on two representative junctions in sample HV088, namely Device C (narrow junction, L x W = 170 x 210 nm^2)[3] and Device I (wide junction, L x W = 307 x 2569 nm^2). Unless specified, we systematically performed our measurements using a pseudo-four probe terminal configuration by applying a current and measuring the voltage drop on the superconducting electrodes (see Figures 3.1.a and 3.1.b insets). Thus, provided the electrodes are in the superconducting state, the measured resistance includes both the graphene resistance as well as the contact resistance arising at each graphene - superconducting electrode interfaces.

[1] This sample consists in a graphene flake encapsulated between a 12.7 nm-thick top h-BN flake and a 23.2 nm-thick bottom h-BN flake, the resulting stack resting atop a 7.7 nm-thick graphite flake. Note that prior to encapsulation, particular care has been taken to select a graphene flake having the desired width W to avoid the need for an etching step, this process both damaging and contaminating the graphene's pristine edges (see for instance [88]). The 40 nm-thick a-MoGe electrodes were implemented using DC-sputtering. Further fabrication details can be found in Appendix A.

[2] The sample DP024 also consists in an encapsulated graphene nanoribbon resting atop a graphite flake. The thicknesses of the top h-BN, bottom h-BN and graphite flakes are respectively 25 nm, 36 nm and 20 nm.

[3] A detail of the junctions dimensions evaluation, including an uncertainty estimate, is provided in Appendix B.

3.1.1 Ballistic junctions

The blue curve in Figure 3.1.a shows the resistance versus back-gate voltage obtained for the narrow junction C at $T = 5.7$ K[4]. Resistance exhibits a clear gate voltage dependence whose main feature is a maximum at charge neutrality (i.e. the Dirac peak), here located at V_D = -0.13 V. This feature, typical of graphene-based devices, is similarly observed for the wide junction with a resistance peak centered at V_D = -0.26 V (see Figure 3.1.b).

All the junctions we measured display a Dirac peak lying at negative gate voltages indicating a graphene built-in electron doping. This may result from charges trapped within the underlying SiO_2 layer, work function mismatch between graphene and the metallic electrodes and/or fabrication process chemical residues resting atop the sample surface [107; 108].

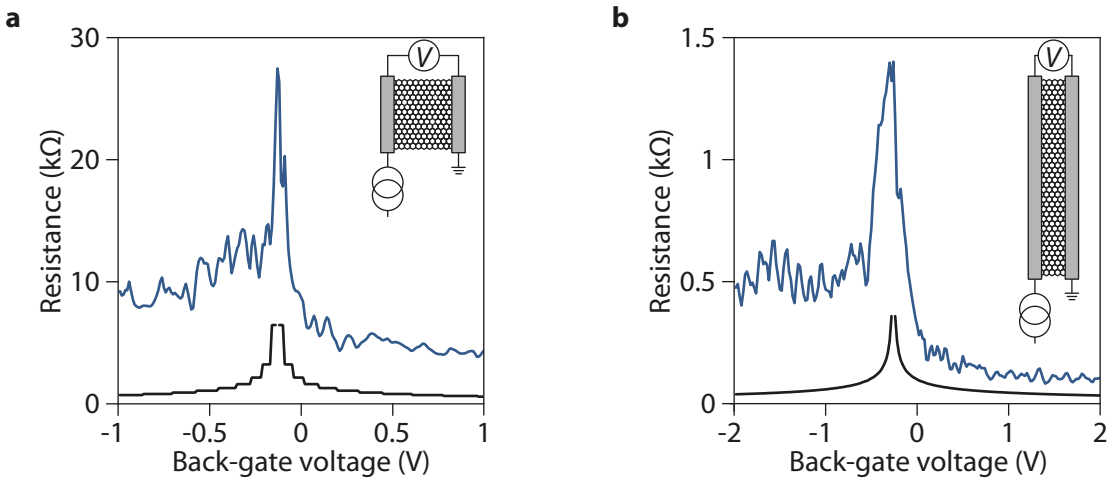

Figure 3.1: **Graphene field effect. a)** Resistance versus back-gate voltage at $T = 5.7$ K measured on Device C (L x W = 170 x 210 nm^2) using a current bias $I_{bias} = 10$ nA. Black curve describes the expected resistance in the pure quantum ballistic limit. **b)** Resistance versus back-gate voltage at $T = 1.5$ K measured on Device I (L x W = 307 x 2569 nm^2) with $I_{bias} = 10$ nA. Black curve describes the expected resistance in the pure quantum ballistic limit. Inset schematics indicate the measurement configuration and follows actual junctions aspect ratio.

Both junctions show a strong asymmetry between the hole-doped ($V_g < V_D$) and the electron-doped ($V_g > V_D$) regimes, V_g denoting the back-gate voltage, with a larger resistance in the former case. This effect is commonly ascribed to electrode-induced local doping, here of the n-type, that yields to pn-barriers along the graphene-electrode interfaces [66; 64].

These barriers also manifest through the observation of regular resistance oscillations as a function of V_g for hole-doped graphene. Provided charge carriers travel ballistically within the junction while preserving their phase coherence, pn-interfaces can be viewed as the electronic-analog of mirrors defining a Fabry-Perot cavity. In that scenario, resistance oscillations would arise from interferences between electrons trajectories within the cavity. Note that typical mean free path values for encapsulated graphene were shown to exceed 10 μm at 1.7 K [74], which is in line with our junctions being in the ballistic transport regime[5].

[4] That is just below the a-MoGe critical temperature $T_c \approx 6$ K.

[5] A validation for ballistic propagation occurence would consist in observing a junction's length-independent resistance value. Yet, the devices under study having different widths W, such an approach could not be employed here.

If one assumes that resistance only arises from the ballistic propagation of electronic modes within the junction and that pn-interfaces are not present, it is possible to compute the expected resistance in the pure quantum limit [66] (see the black curves in Figures 3.1.a and 3.1.b)[6]. The discrete steps we observe for the small junction case follow from the narrowness of the device in which only few electronic modes can propagate. Difference between ideal case and the measurements directly gives an estimation of the contact resistance[7].

Device	L [nm]	W [nm]	Contact resistivity [$\Omega.\mu$m]	Transmission probability at $V_g = 1$ V
B	140	177.5	418.1	0.23
C	170	210	400.5	0.24
D	200	247	387.9	0.24
E	240	288	349.4	0.26
F	270	334	451.5	0.22
G	107	2332	444.2	0.19
H	202	2434	508.5	0.18
I	307	2569	106.1	0.52

Table 3.1: **Dimensions and contact parameters** for junctions in sample HV088.

Device	L [nm]	W [nm]	Contact resistivity [$\Omega.\mu$m]	Transmission probability at $V_g = 1$ V
C	170	125	105.3	0.61
D	200	125	392.8	0.29

Table 3.2: **Dimensions and contact parameters** for junctions in sample DP024.

At $V_g = 1$ V, to avoid Dirac peak-related effect, junctions contact resistivity ranges from 100 $\Omega.\mu$m to 510 $\Omega.\mu$m. This yields low angle-averaged transmission probabilities[8] (see Tables 3.1 and 3.2, last column) indicating poor-quality contacts to graphene. For the sake of comparison, M. Ben Shalom *et al.* [66] reported a contact resistivity of only 35 $\Omega.\mu$m using Ta/NbN/Ta superconducting electrodes (see Chapter 2 Section 2.2 for a detailed discussion).

[6] In details, an application of the Landauer formalism yields:

$$R_Q = \frac{h}{e^2}\frac{1}{g_s g_V N} \tag{3.1}$$

where $g_s = g_V = 2$ denote respectively the spin and valley degeneracies for graphene and N is the number of tranverse modes propagating through the graphene. The latter can be estimated as the number of k_y states such that $-k_F < k_y < k_F$, with k_F the Fermi momentum.
The k_y states being equally spaced in the momentum space with $\Delta k_y = 2\pi/W$, we can define the number of propagating modes as:

$$N = \text{int}\left[\frac{2k_F}{\Delta k_y}\right] = \text{int}\left[\frac{k_F W}{\pi}\right] \tag{3.2}$$

We therefore end up with:

$$R_Q = \frac{h}{4e^2}\text{int}\left[\frac{k_F W}{\pi}\right] \tag{3.3}$$

In the specific case of graphene, $k_F = \sqrt{\pi n}$, n being the electron density defined as $n = C(V_g - V_D)/e$. Here the capacitor per unit area C was estimated to be about 1.4 mF/m^2 using a basic two-plate capacitor model with $\epsilon_{h\text{-}BN} = 3.3$ [109] and $d_{h\text{-}BN} = 23$ nm.

[7] Here contact resistance includes both the resistance related to the graphene-electrode interface as well as the one resulting from charge carriers partial transmission at pn and n'n barriers.

[8] This probability is computed as $R_Q/(R_Q + R_c)$ with R_Q the resistance deduced with the Landauer formalism and R_c half the difference between the measured resistance and R_Q.

3.1.2 Bipolar supercurrent

Although electrodes are already superconducting, proximity effect requires a further drop in temperature to develop. At few kelvins, thermal fluctuations randomize phase difference between the superconducting electrodes thus preventing a phase-dependent supercurrent to develop. Typically, the Josephson energy $E_J = \hbar I_c/2e$ dictates the maximum temperature for a Josephson junction to exhibit a supercurrent. Quantitatively, for a critical current $I_c = 100$ nA, we have $E_J \approx 200$ μeV which corresponds to a temperature of 2 K [36].

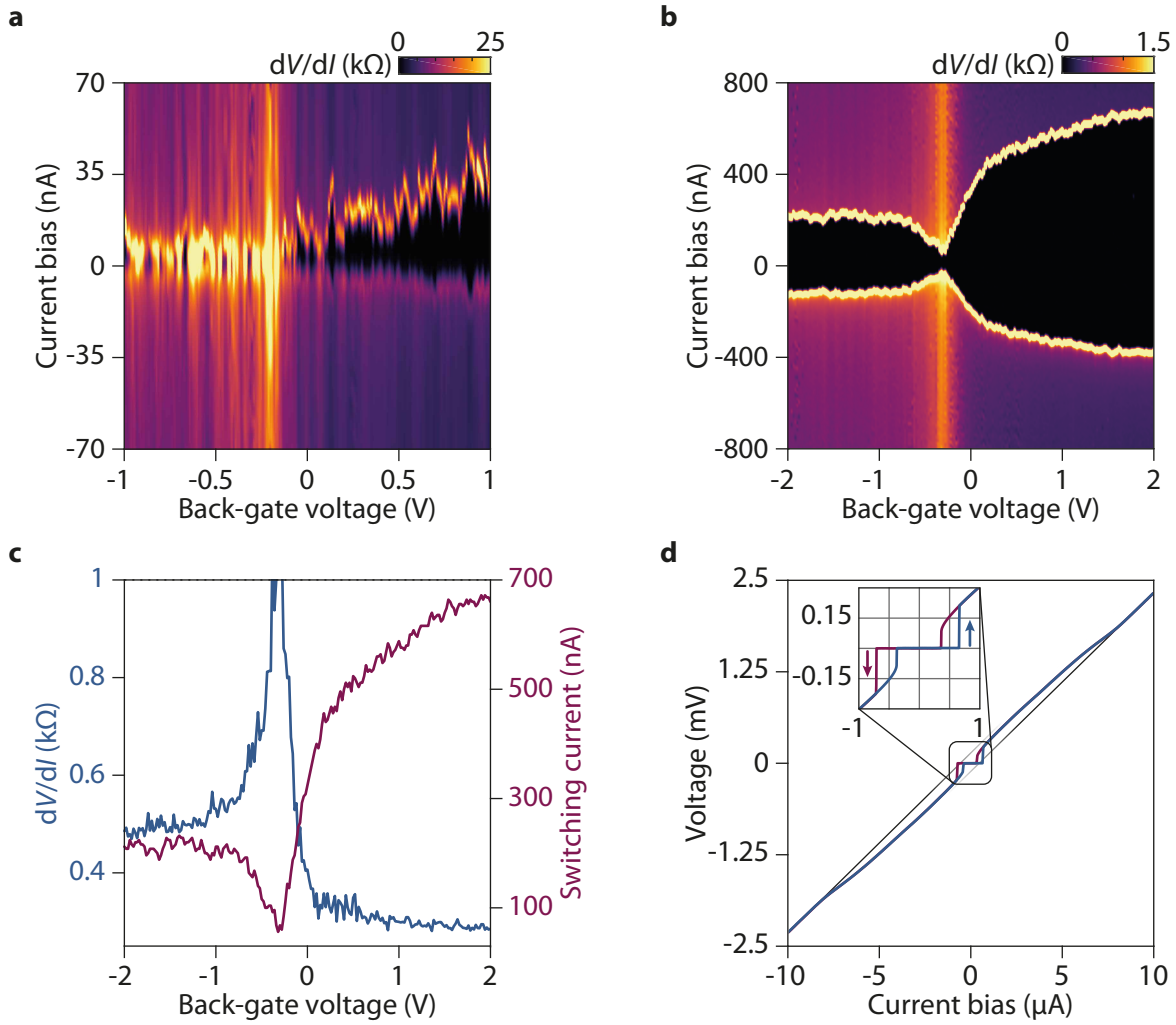

Figure 3.2: **Bipolar supercurrent. a,b)** Differential resistance $\mathrm{d}V/\mathrm{d}I$ as a function of the back-gate voltage and the current bias at $T = 10$ mK for device C in **(a)** and device I in **(b)**. These differential resistance colormaps were numerically computed from the upwards I/V characteristics done at successive gate-voltage. **c)** Differential resistance $\mathrm{d}V/\mathrm{d}I$ (blue curve, linecut taken at $I_{\mathrm{bias}} = 796$ nA) and switching current I_s (purple curve) versus the back-gate voltage for the wide junction. **d)** I/V characteristic at $V_g = 2$ V for the wide junction. Blue curve describes the trace while purple one corresponds to retrace. Black lines denote the linear part of the I/V characteristics at high current bias. The inset highlights the hysteresis between trace and retrace, a typical feature of SNS Josephson junctions [110].

Proximity effect was characterized through I/V characteristics using a DC current bias delivered by an acquisition card NI-6346 (8 inputs, 16-bits, 500 kS/s, Multifunction I/O Device). As an indication, a given I/V curve

in Figure 3.2.b (including both trace and retrace) typically lasts 4 seconds and consists in 1000 points, each of them resulting from an averaging over 500 points.

Figure 3.2.a shows a colormap of the differential resistance as a function of both the back-gate voltage and the current bias for the narrow junction C at $T = 10$ mK. Dissipationless current, the Josephson effect hallmark, translates as a zero-resistance region, color coded in black, starting from the Dirac point and extending towards positive gate voltage. The fact that no supercurrent clearly develops for the hole-doped regime presumably results from the pn-barriers opacity that adds up to the contact resistance.
Figure 3.2.b shows a similar measurement conducted on the wide junction I. Remarkably, the junction exhibits a finite supercurrent accross the whole gate-voltage range including the Dirac point, a feature only observed in large junctions (devices G,H,I, see Appendix A). While a finite supercurrent amplitude was predicted to occur at the Dirac point for short and ballistic Josephson junctions [111], this last observation could also stem from the presence of multiple charge puddles acting in parallel. Provided their typical size exceeds the lead-to-lead distance[9], they would provide channels allowing for Cooper pairs transfer between superconducting electrodes.

At positive current bias, the transition from dissipationless to resistive regime defines the switching current I_s[10]. The latter systematically increases as we move away from the Dirac point for both junctions. This behavior is consistent with the $R_N I_c$-product constancy for conventional Josephson junctions [112]: upon increasing gate voltage from the Dirac point, the normal resistance R_N decreases, which leads to a higher critical current value.
To further highlight this effect, Figure 3.2.c displays both the differential resistance dV/dI (blue curve, taken at $I_{bias} = 796$ nA) and switching current I_s (purple curve) versus the back-gate voltage for the wide junction. Considering the hole-doped situation, the two curves are clearly correlated as can be seen with antiphase oscillations. The latter directly follow from the normal resistance Fabry-Perot oscillations we mentioned previously[11].

Depending on the junction's transport regime, the $R_N I_c$-product directly relates to either the superconducting gap $\Delta_{a\text{-MoGe}}$ of the electrodes or the Thouless energy E_{Th} of the junction. For ballistic normal weak link, the length scale over which develops the proximity effect is given by $\xi_S^N = \hbar v_F^N / \Delta_{a\text{-MoGe}}$, that is about 730 nm in our case[12]. Having $L \ll \xi_S^N$[13], our junctions are therefore in the ballistic/short[14] transport regime which implies[15] $R_N I_c = 2.44 \Delta_{a\text{-MoGe}}/e$ [111].

[9] An assumption further strenghened in Section 3.1.2.

[10] In theory, the maximum supercurrent a Josephson junction can withstand is defined as the critical current I_c. However, in practice, transition to the dissipative state occurs at a smaller current bias, the so-called switching current I_s, a fact commonly attributed to electromagnetic environment influence.

[11] We point out that Fabry-Perot oscillations amplitude get significantly reduced when comparing the curves at $T = 1.5$ K (Figure 3.1.b) and $T = 10$ mK (Figure 3.2.c), an observation that remains unexplained.

[12] Fermi velocity v_F^N for graphene is conventionally estimated to be equal to 10^6 m/s while a-MoGe superconducting gap is of the order of $1.76 k_B T_c \sim 900$ μeV, with k_B the Boltzmann constant.

[13] This is equivalent to $\Delta_{a\text{-MoGe}} \ll E_{Th}$.

[14] In all rigor, a demonstration that our junctions are in the short regime would require to show that critical current amplitude is independant of the junctions length L. In particular, while $\xi_S^N = \hbar v_F^N / \Delta_{NbN} \approx 600$ nm $\gg L = 150$ nm in [66], that is a situation similar to our case, the supercurrent was observed to depend on the junction's length. In our case, the junctions width W is varying accross the different devices hence preventing this cross-check to be done.

[15] This equation was derived for a graphene-based Josephson junction having surface contact and remains valid only if $L \ll \xi_S^N, W$.

For the wide junction I, that is the one having the lowest contact resistivity, we have $R_N = 244.2\ \Omega$ and $I_s =$ 640 nA at $V_g = 2$ V thereby giving $R_N I_s = 156.3\ \mu V \approx 0.17\ \Delta_{a\text{-}MoGe}/e$.
In reference [76], such a deviation with respect to the theoretical value was ascribed to the combined effect of a finite NS interfaces transparency together with the presence of an inhomogeneous carrier density profile in the contacts vicinity, effects that were not accounted for in [111].
For comparison purpose, we mention that most of the studies on graphene-based Josephson junctions focused on devices falling either into the ballistic/long transport regime [66; 64; 40], the diffusive/short regime [113] or the diffusive/long regime [114; 84; 62]. We found only two references claiming about ballistic/short regime signatures with a ratio $eR_N I_s/\Delta$ reaching 1 [72] and 2 [76] respectively.

Figure 3.2.d shows a single I/V characteristic measured on the wide junction I at $V_g = 2$ V. A large current bias window was used to seek for non-linearities within the ohmic branches, a well-known manifestation of Andreev reflections [1]. The blue/purple trace was measured while ramping up/down the current bias. The inset clearly shows an hysteresis at low current bias between the two traces as often reported for SNS Josephson junctions. This effect was demonstrated to stem from electron overheating when junction transits to the resistive state [110].

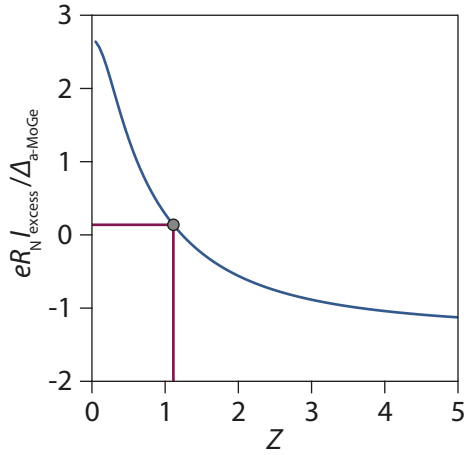

Figure 3.3: **Superconducting contacts transparency**. Normalized excess current versus the scattering parameter Z using the OBTK framework. Purple line indicates the Z parameter corresponding to the $eR_N I_{excess}/\Delta_{a\text{-}MoGe}$ value we deduced for device I at $V_g = 2$ V.

The two black asymptotes indicate that normal resistance R_N is reached once $V = 2\Delta_{a\text{-}MoGe}/e \approx \pm$ 1.62 mV, hence leading to $\Delta_{a\text{-}MoGe} = 808\ \mu eV$. Taking the intersect between the black asymptote and the zero-voltage axis, we deduce an excess current I_{excess} of 456.1 nA. Applying the Octavio-Blonder-Tinkham-Klapwijk (OBTK) formalism [80; 81; 82], the knowledge of R_N, I_{excess} and $\Delta_{a\text{-}MoGe}$ allows for estimating a Z-parameter of 1.112, hence a graphene-superconducting electrode transparency of about 0.45 (see Figure 3.3).

3.1.3 Quantum interference patterns for supercurrent under low magnetic field

One of the most fascinating properties of Josephson junction is its sensitivity to magnetic flux. This manifests as interference patterns for the critical current in magnetic field and enabled the development of the so-called SQUID, one of the most sensitive magnetometer to date [115]. Beyond the applicative aspect, direct information about the supercurrent distribution within the junction can be gained from the examination of these interference patterns. Typically, for a uniformly distributed supercurrent flowing within the junction,

critical current is expected to display a characteristic Fraunhofer-like pattern in magnetic field which follows the equation [116]:

$$I_c(B) = I_c(B = 0\,\mathrm{T}) \cdot \left[\frac{\sin(\pi\phi/\phi_0)}{(\pi\phi/\phi_0)}\right] \tag{3.4}$$

with $\phi = (L+2\lambda_L)WB$ the flux passing through the junction effective surface, λ_L being the London penetration depth in the superconducting electrodes, and $\phi_0 = h/2e \approx 2.067 \cdot 10^{-15}$ Wb the superconducting flux quantum.

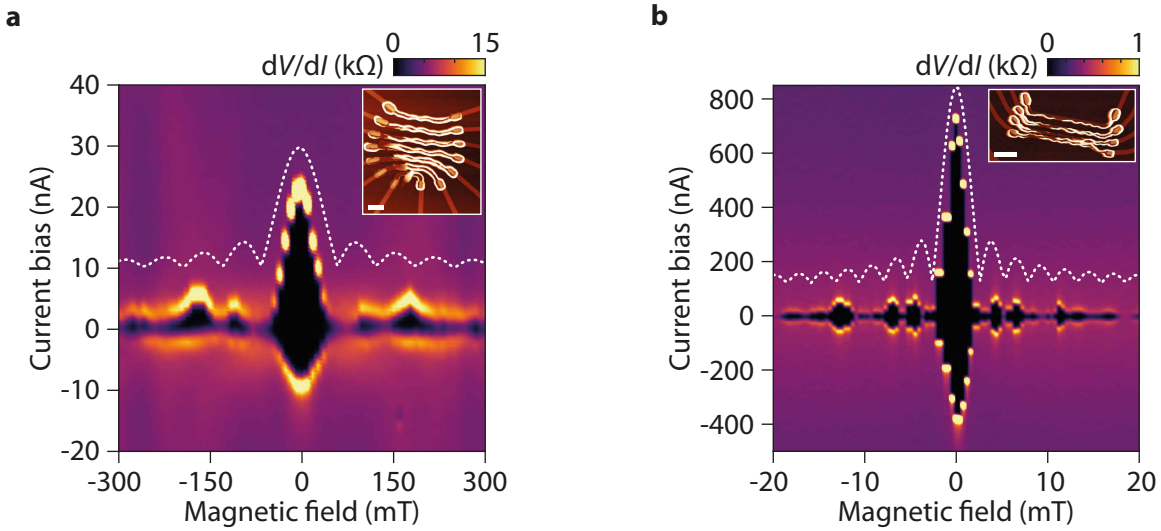

Figure 3.4: **Supercurrent interference patterns under low magnetic field.** **a**) Colormap of the differential resistance dV/dI versus magnetic field and current bias obtained for the narrow junction C (L x W = 170 x 210 nm^2) at $V_g = 1$ V and $T \approx 10$ mK. White dashed line describes the Fraunhofer pattern that would be expected from the geometric area of the junction taking into account the λ_L correction (an upward shift of 10 nA was applied to allow for clear visualization of the superconducting pockets). Inset shows an AFM picture of the narrow junctions. The bottom-left white scale bar corresponds to 300 nm. **b**) Colormap of the differential resistance dV/dI versus magnetic field and current bias obtained for the wide junction I (L x W = 307 x 2569 nm^2) at $V_g = 2$ V and $T \approx 10$ mK. White dashed line describes the Fraunhofer pattern that would be expected from the geometric area of the junction taking into account the λ_L correction (an upward shift of 120 nA was applied to allow for clear visualization of the superconducting pockets). Inset shows an AFM picture of the wide junctions. The bottom-left white scale bar corresponds to 1 μm.

In practice, however, interference patterns often depart from such a simple behavior. Figures 3.4.a and 3.4.b show typical interference patterns we obtain for respectively narrow and wide junctions. Both junctions exhibit a large zero-resistance lobe centered at zero magnetic field whose width defines a magnetic field window corresponding to $2\phi_0$. Based on this measurement, we estimate the junctions effective area, hence the London length λ_L, for the devices we characterized on samples HV088 (see Table 3.3) and DP024 (see Table 3.4). These numbers enable us to plot the expected Fraunhofer pattern as shown by the white dashed line in Figures 3.4.a and 3.4.b. Clearly, zero-resistance side lobes shape strongly departs from the ideal behavior. Additionally, London lengths we deduce from the junctions Fraunhofer patterns display strong fluctuations between devices.

Several effects may conspire to cause the observed supercurrent interferences to deviate from the ideal Fraunhofer pattern:

- As shown in Figure 3.4.a and 3.4.b insets, a-MoGe electrodes exhibit distorted sidewall as well as a local thickening inherited from the fabrication process. These local distortions likely affect magnetic flux passing through the junction and therefore critical current interferences patterns.

- The latter might also be altered through the presence of vortices within the superconducting electrodes [117; 118], an assumption consistent with the a-MoGe low $H_{c,1}$ value[16]. In particular, trapped vortices could explain the slight asymmetry we observe between positive and negative magnetic field values.

- Fraunhofer interference patterns were actually shown to strongly depend on the gate voltage in graphene-based Josephson junctions. In particular, at $V_g = V_D$, SQUID-like patterns have been reported [65][17]. Our superconducting interference patterns having been obtained relatively close from the Dirac point i.e. $V_g - V_D = 1.13$ V (resp. 2.26 V) for Figure 3.4.a (resp. Figure 3.4.b), demonstrating that such an effect is not present here would require a dedicated study.

Device	L [nm]	W [nm]	$\delta B_{expected}$ [mT]	$\delta B_{measured}$ [mT]	λ_L [nm]
B	140	177.5	83.2	62.2	23.7
C	170	210	57.9	53.3	7.4
D	200	247	41.8	48.8	-14.3
E	240	288	29.9	31.1	-4.5
G	107	2332	8.4	3.8	63.6
H	202	2434	4.2	3	40.9
I	307	2569	2.6	2.6	1.4

Table 3.3: **Magnetic field periodicities and London lengths** for sample HV088 junctions extracted from Fraunhofer patterns done at $V_g = 1$ V (resp. $V_g = 2$ V) for devices B,C,D,E (resp. G,H,I).

Device	L [nm]	W [nm]	$\delta B_{expected}$ [mT]	$\delta B_{measured}$ [mT]	λ_L [nm]
C	170	125	97.3	112	-11.2
D	200	125	82.7	52	59

Table 3.4: **Magnetic field periodicities and London lengths** for sample DP024 junctions extracted from Fraunhofer patterns done at $V_g = 1$ V for devices C and D.

- The graphene-based Josephson junctions in which Fraunhofer patterns have been reported are systematically μm-wide devices with an aspect ratio $L/W \ll 1$ (see for instance [66; 39; 76]). In these works, the Fraunhofer patterns magnetic field-periodicities are always smaller than expected from the devices dimensions, a fact ascribed to flux-focusing effect. In contrast, ballistic square-shaped devices remains very little studied in the literature. We found only two references dealing with this case [27; 64], only one of which using graphene-based Josephson junctions and reporting on a magnetic-field periodicity larger than expected from the devices dimensions [64], a feature we also uncover for some of our devices (see junctions D and E in Table 3.3 for sample HV088 and junction C in Table 3.4 for sample DP024).

[16] Although our electrodes are made of a 40 nm-thick layer of a-$Mo_{0.5}Ge_{0.5}$, we mention that vortices have been directly visualized in a 50 nm-thick a-$Mo_{0.7}Ge_{0.3}$ film at magnetic field as low as 70 mT using scanning tunneling spectroscopy [119], thus suggesting that the $H_{c,1}$ value is even smaller than that.

[17] Note that the G. Finkelstein group also reported on Fraunhofer patterns anomalies at and around the Dirac point [83]. Although the supercurrent interferences were still forming a Fraunhofer-shaped pattern, the latter displayed an anomalous h/e flux-periodicity, a feature the authors could not explain.

- We finally mention that self-induced magnetic fields, resulting from the supercurrent flowing both within the graphene as well as in the electrodes over the London length λ_L, are not expected to affect Fraunhofer physics here, as the junctions width W is systematically much smaller than the estimated Josephson length $\lambda_J = \sqrt{\phi_0/(4\mu_0 j_{c,\,2D})} \approx 61$ μm for the narrow junction C, with μ_0 the vacuum permeability and $j_{c,\,2D}$ the critical current density [96][18,19].

3.2 Quantum Hall effect in two-terminal devices

We now address junctions behavior under high magnetic field, that is, when entering the integer quantum Hall regime. Unless stated otherwise, here we discuss data obtained below the electrodes upper critical field $H_{c,2} \approx 12.5$ T to avoid electrodes normal resistance contribution to the measurements.

3.2.1 Two-terminal magneto-conductance

Conventionally, devices with a Hall bar geometry constitute the work-horse device for probing quantum Hall physics. Yet, in our case, the Josephson junctions geometry imposes 2-terminal measurements, a configuration known to result in quantum Hall plateaus distortion, thus potentially preventing clear plateau identification. In particular, a dedicated study of such an effect was carried out in [120] for graphene-based devices. Importantly, plateaus distortion was shown to depend on the junction's aspect ratio L/W. The square-shaped case (i.e. $L = W$) being free of such an effect, we therefore favoured junctions design with $L \approx W$ to limit quantum Hall plateau's distortion in our measurements. To elaborate on this effect, we now shortly discuss the model of D. A. Abanin and L. S. Levitov [121].

On very general grounds, the two-terminal conductance G can be written as:

$$G = I/V \tag{3.5}$$

where I stands for the total current flowing accross the device while V describes the source-drain bias voltage. The former can be obtained by integrating the current density along a cross-section through the sample, say at $y = 0$ along the x axis (see Figure 3.5.a):

$$I = \int_0^W j_y(x, 0)\mathrm{d}x \tag{3.6}$$

[18] The Josephson length expression we use here was derived for the specific case of co-planar Josephson junctions based on 2D materials. Contrary to the standard expression which is proportional to $1/(\sqrt{L + 2\lambda_L})$, here $\lambda_J \propto 1/\sqrt{j_{c,\,2D}} \propto 1/\sqrt{j_c t}$ with j_c the critical current density per unit cross-sectional area and t the 2D material thickness. For the wide junction I, we estimate $\lambda_J \approx 36$ μm.

[19] Note that additional effects, yet poorly-investigated, could potentially contribute to the deviations from the Fraunhofer patterns such as:

- The graphene flake from which are made these junctions has a triangular shape (see Appendix B for details). Consequently, the normal part of the Josephson junctions form a trapezoidal shape, a feature that was suspected to explain the finite-resistance of the Fraunhofer patterns side-lobes in [62].
- Structural fluctuations along our 1D graphene-superconductor interfaces are likely to be present. Yet, while theory anticipates this should result into a constant supercurrent background in the Fraunhofer patterns [116], we did not observe such an effect in our data.

Knowing that $\boldsymbol{J} = \hat{\boldsymbol{\sigma}}\boldsymbol{E}$, with $\boldsymbol{J}$, $\hat{\boldsymbol{\sigma}}$, $\boldsymbol{E}$ being respectively the current density, the conductivity tensor and the electric field, it is possible to re-express equation (3.6) in terms of conductivities and electric field components as follow:

$$I = \int_0^W \sigma_{xx}[E_y(x,0) + \tan(\delta)E_x(x,0)]\mathrm{d}x \tag{3.7}$$

with σ_{xx} the ohmic conductivity and E_x, E_y respectively the x and y components of the electric field vector $\boldsymbol{E}$. The term δ denotes the Hall angle, which is defined as $\tan(\delta) = \sigma_{xy}/\sigma_{xx}$, with σ_{xy} the Hall conductivity[20]. Similarly, the voltage accross the device between opposite electrodes ($y = \pm L/2$) can be computed through the integration of the electric field along the line connecting the points $(W/2, -L/2)$ to $(W/2, L/2)$:

$$V = -\int_{-L/2}^{L/2} E_y(W/2, y)\mathrm{d}y \tag{3.8}$$

The procedure to derive the two-terminal conductance thus requires two steps:

- The determination of the electric field components in order to get an expression for $E_y(x,0)$, $E_x(x,0)$ and $E_y(W/2, y)$.
- Finding out expressions for both the ohmic and Hall conductivities σ_{xx} and σ_{xy}.

Regarding electric field components E_x and E_y, a derivation based on conformal mapping technique was introduced in reference [122] whose main reasoning steps are developed below.

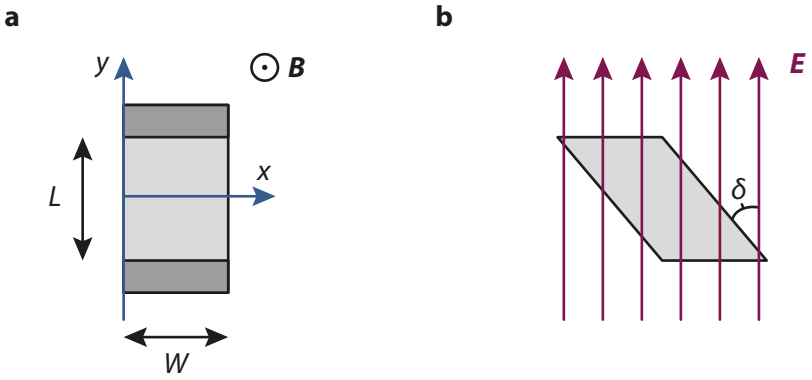

Figure 3.5: **Conformal mapping. a**) Schematics for a two-terminal device. Shaded areas denote the electrodes. **b**) Distorted 2DEG whose edges define a constant angle δ with the electric field $\boldsymbol{E}$ (purple vectors).

We first consider the 2D system depicted in Figure 3.5.a which consists in a rectangular shaped device whose extremities are connected via metallic electrodes serving as source and drain. Boundary conditions assume that current does not flow out of the system's edges and that x-axis electric field component is null at the 2D electron gas-electrode interfaces[21]. The magnetic field $\boldsymbol{B}$ is defined as pointing out of the 2DEG-plane along the $\hat{z}$ axis. In [122], the relation between the electric field $\boldsymbol{E}$ and the current density $\boldsymbol{J}$ reads as:

$$\boldsymbol{E} + \rho_H \boldsymbol{J} \mathrm{x} \hat{\boldsymbol{z}} = \sigma_{xx}^{-1}\boldsymbol{J} \tag{3.9}$$

[20] When σ_{xx} falls to zero, that is when the system displays a quantized Hall resistance, $\delta \longrightarrow \pi/2$.

[21] This assumption is equivalent to state that no Hall voltage develops within the metallic electrodes.

with $\rho_H = R_H|\boldsymbol{B}|$[22] and σ_{xx}^{-1} being respectively the Hall and ohmic resistivities. This expression implies that an angle δ, the aforementioned Hall angle, takes place between the current and the electric field[23].

The first boundary condition, that is $\boldsymbol{J} = \boldsymbol{0}$ at the system lateral edges, can be equivalently stated assuming that electric field $\boldsymbol{E}$ makes an angle δ with the sample's sides. In the case of a parallelogram-shaped system (see Figure 3.5.b), this requirement is fullfilled with a uniform electric field $\boldsymbol{E} = E_0\hat{\boldsymbol{y}}$. Thus, using equation (3.9), it is possible to trace back current distribution for this peculiar case. This is where conformal mapping approach comes in, the idea being to reduce the general problem to the parallelogram case for which a solution is derivable[24].

Once having obtained electric field vector components, we need to find out expression for conductivities σ_{xx} and σ_{xy}. These parameters were derived invoking the so-called two-phase model [123], a phenomenological theory aimed at capturing essential transport features of both the integer and fractional quantum Hall effects at once. The main result of this model stands as a universal semi-circle relationship involving both conductivities:

$$\delta_n\sigma_{xx}(\nu)^2 + (\delta_n\sigma_{xy}(\nu) - \sigma_{xy,n}^{(0)})(\delta_n\sigma_{xy}(\nu) - \sigma_{xy,n'}^{(0)}) = 0 \tag{3.15}$$

with $\sigma_{xy,n}^{(0)}$ and $\sigma_{xy,n'}^{(0)}$ the quantized Hall conductivities on neighboring plateaus, the index n and n' denoting

[22] As a reminder, using the Figure 3.5.a coordinates system, $R_H = E_x/j_y|\boldsymbol{B}|$ in the classical Hall effect.

[23] More precisely, if one assume that $\boldsymbol{J}$ is parallel with $\boldsymbol{E}$ at zero magnetic field, say along the y-axis, the magnetic field-induced Hall voltage will give rise to an additional electric field component along the x-axis such that $\boldsymbol{E} = (-\rho_H j_y, \sigma_{xx}^{-1} j_y)$. Knowing that $\boldsymbol{J}$ solely lies along the y-axis, the angle δ between $\boldsymbol{J}$ and $\boldsymbol{E}$ here necessarily follows $\tan(\delta) = \rho_H\sigma_{xx}$.

[24] The procedure is as follow:
Assuming we are in the stationary case and neglecting current-induced magnetic fields, Maxwell's equations and equation (3.9) leads to $\nabla^2\psi = 0$, ψ denoting the electrostatic potential. Together with the boundary conditions, this implies that ψ is uniquely defined accross the space.
Considering a complex plane, a conformal mapping $W(z)$ rotates local angles by a quantity $\theta(z) \equiv \arg(\frac{dW}{dz})$. Writing $\frac{dW}{dz} = e^{f(z)}$, it then follows that $\theta(z) = \mathrm{Im}(f(z))$.
Going back to the physics, one can define a complex electrostatic potential as $V = \lambda W(z)$ where λ stands for an arbitrary constant that we set to be equal to one in the next. The physical electrostatic potential corresponds to the imaginary part of the complex one, that is $\psi = \mathrm{Im}(V)$.
Thus, complex electric field follows as:

$$E = -\frac{dV}{dz} = -\frac{dW}{dz} = -e^{f(z)} \tag{3.10}$$

Note that the physical field relates to the complex field via $E = E_y + iE_x$. Therefore, finding out an expression for $f(z)$ will allow to determine the electric field.
The mapping requires that $\theta(z) = \mathrm{Im}(f(z)) = \delta$ at the sample edges and vanish at the 2D electron gas-electrode interfaces. Such an analytic function $f(z)$ satisfying both conditions was derived in [122] as:

$$f(z) = i\delta - \sum_{n>0,\mathrm{odd}} \frac{4\delta}{n\pi}\frac{\sinh(n\pi iz/W)}{\cosh(n\pi L/2W)} \tag{3.11}$$

Equating $E_y(x,y) + iE_x(x,y) = -e^{f(z)}$ with $z = x + iy$ we obtain:

$$E_y(x,0) = -\cos\left(\delta - \sum_{n>0,\mathrm{odd}} \frac{4\delta}{n\pi}\frac{\sin(n\pi x/W)}{\cosh(n\pi L/2W)}\right) \tag{3.12}$$

$$E_x(x,0) = -\sin\left(\delta - \sum_{n>0,\mathrm{odd}} \frac{4\delta}{n\pi}\frac{\sin(n\pi x/W)}{\cosh(n\pi L/2W)}\right) \tag{3.13}$$

$$E_y(\frac{W}{2},y) = -\cos\left(\delta - \sum_{n>0,\mathrm{odd}} \frac{4\delta}{n\pi}\left[\sin(\frac{n\pi}{2})\cosh(\frac{n\pi y}{W}) - \cos(\frac{n\pi}{2})\sinh(\frac{n\pi y}{W})\right]\right) \tag{3.14}$$

adjacent integers in the sequence ...-2,-1,0,1,2... for monolayer graphene. The term $\delta_n\sigma_{xx}(\nu)$ (resp. $\delta_n\sigma_{xy}(\nu)$) denotes the n^{th} plateau contribution to the total ohmic (resp. Hall) conductivity when considering the system at an arbitrary filling factor value ν.

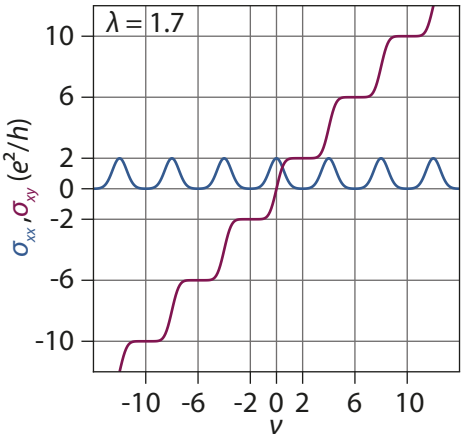

Figure 3.6: **Semi-circle model.** Ohmic (blue curve) and Hall (purple curve) conductivities obtained using the semi-circle framework. Here, the Landau level broadening parameter was arbitrarily set to $\lambda = 1.7$.

Remarkably, although $\delta_n\sigma_{xx}(\nu)$ and $\delta_n\sigma_{xy}(\nu)$ expressions are model-dependent, this relationship remains valid irrespectively the temperature or the degree of disorder.
In their approach, D.A. Abanin and L.S. Levitov modeled $\delta_n\sigma_{xx}(\nu)$ as Gaussian functions whose maxima center at transition between plateaus n' and n:

$$\delta_n\sigma_{xx}(\nu) = 2e^{-\lambda[\nu - 1/2(\nu_n+\nu_{n'})]^2} \tag{3.16}$$

where λ is a parameter describing the Landau level broadening (the higher λ is, the narrower the Landau level is). Thus, using the semi-circle relationship (i.e. equation (3.15)), it is possible to derive the $\delta_n\sigma_{xy}(\nu)$ values. Ultimatively, σ_{xx} and σ_{xy} express as:

$$\sigma_{xx}(\nu) = \sum_n \delta_n\sigma_{xx}(\nu), \quad \sigma_{xy}(\nu) = \sum_n \delta_n\sigma_{xy}(\nu) \tag{3.17}$$

We plot both these parameters as a function of ν in Figure 3.6 in which we recover the characteristic quantum Hall effect features in graphene, that is successive quantized σ_{xy} conductance plateaus $\pm 2e^2/h$, $\pm 6e^2/h$, $\pm 10e^2/h$ ... combined with vanishingly small σ_{xx} except at transitions between the plateaus.

We now apply this model to data obtained for the wide junction G (107 x 2332 nm^2).
Figure 3.7.a shows the idealized quantum Hall resistance we deduced from the two-phase model (black dashed line), the measured resistance (purple line) as well as the Abanin-Levitov fit (blue curve) at 9 T. Figures 3.7.b and 3.7.c display similar measurements, respectively done at 7 T and 5 T.

Although the measured resistance clearly shows distorted resistance plateaus, the Abanin-Levitov fit exhibits strong discrepancies with respect to the measured resistance. This mainly manisfests observing that $\nu = 2$ plateau width is systematically larger than predicted, regardless the magnetic field value. The mismatch is even more striking looking at $V_{\text{D}} =$ -0.5 V where measured resistance clearly exceeds the theoretical plot.

Overall, these differences point the limitations of the semi-circle based approach whose main assumption relies on a uniformly distributed conductivity within the device. As mentionned in reference [121], provided charge puddles having a typical size $\xi \approx W$ or L are present, the quantum Hall conductivites can strongly depart from the semi-circle model predictions, especially in the Dirac point vicinity. In particular, when $L \leq \xi \ll W$, charge puddles arranged in parallel lead to a Dirac point resistance higher than predicted by the Abanin-Levitov model. Taking the ratio $R_{\text{D, measured}}/R_{\text{D, theory}} = \xi/L \approx 6.5$ at $B = 5$ T, an application of that model yields a charge puddles size of about $\xi = 700$ nm[25] for the wide junction G[26].

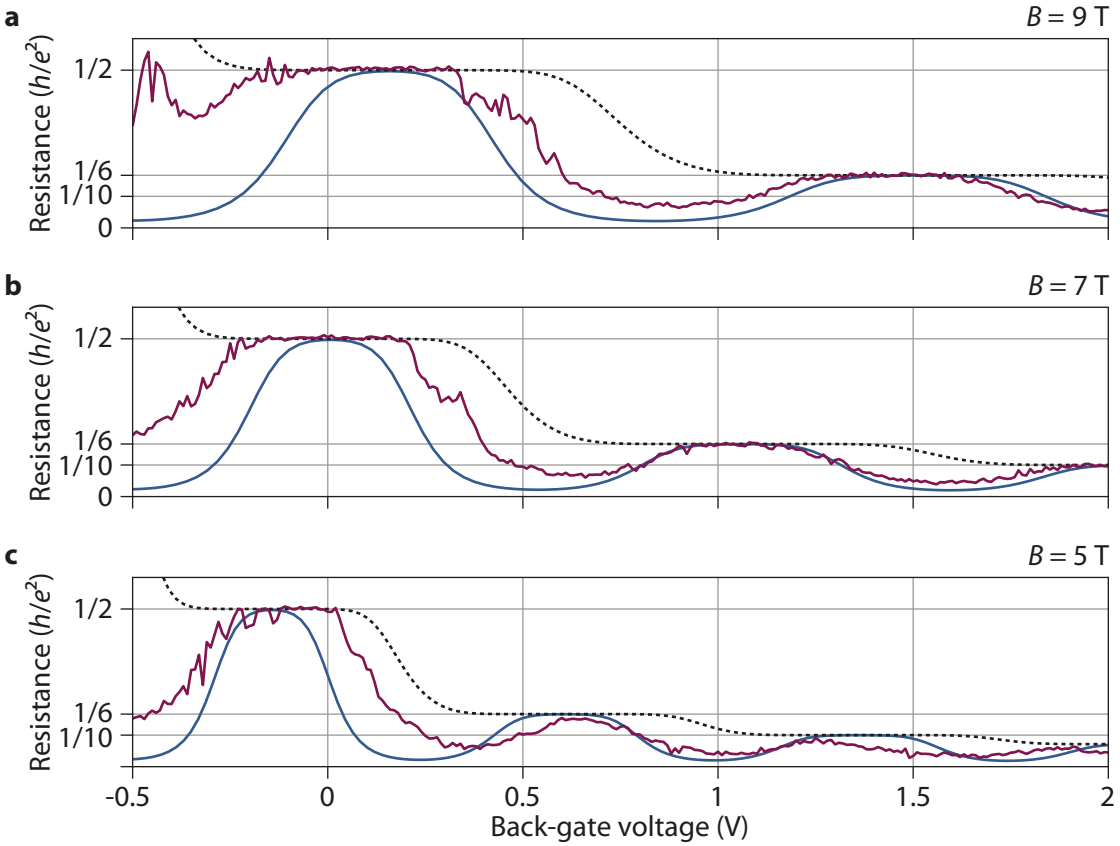

Figure 3.7: **Abanin-Levitov model.** **a**) Resistance as a function of the back-gate voltage measured for wide junction G at $B = 9$ T with a current bias $I_{\text{bias}} = 28$ nA (purple curve). Black dashed curve denotes the ideal Hall resistance computed using the σ_{xy} deduced from the semi-circle model. Blue curve corresponds to the Abanin-Levitov model with $\lambda = 2.2$. A capacitor value $C = 1.03$ x 10^{-3} F/m^2 was used to adjust the blue curve position with respect to the back-gate voltage. **b**) Similar measurement done at $B = 7$ T. **c**) Similar measurement done at $B = 5$ T.

[25] In details, the semi-circle relation yields $R_{\text{D, theory}} = hL/(2e^2W)$. Assuming a device geometry such that $L \leq \xi \ll W$, ξ being the typical charge puddles width, transport then occurs through $N \approx W/\xi$ charge puddles in parallel, each of them being characterized by a conductance $G_0 = 2e^2/h$. Such a configuration then yields $R_{\text{D,measured}} = 1/(NG_0) = \xi h/(W2e^2)$. Ultimately, this leads to $R_{\text{D, measured}}/R_{\text{D, theory}} = \xi/L$.

[26] We would like to stress here that such an estimate must be treated with caution, the ratio ξ/L being expected to keep a constant value with respect to the applied magnetic field, which is clearly at odds with our data. Our electrodes being still superconducting, it is very likely that Andreev reflections play a role in the observed deviations.

3.2.2 Quantum Hall effect in graphene nanoribbons

Theory predicts that junction's width W is the limiting factor for chiral supercurrent amplitude (see Chapter 1 Section 1.2.2). This constraint led us to implement Josephson junctions in graphene nanoribbons having a typical width $W \approx 150$ nm. Remarkably, quantum Hall effect was reported in disordered graphene nanoribbons down to 60 nm width [124]. Yet, these devices consisted in Hall bar with a typical distance between longitudinal contact of 250 nm.
Here, owing to aspect ratio considerations mentioned previously, we designed square-shaped devices with typically $L \approx W \approx 150$ nm. The question then arises to what extent quantum Hall effect could develop on such small scale.

Figure 3.8 shows the conductance as a function of the back-gate voltage we measured at $B = 8$ T for different junctions (dimensions of which are specified in the Figure 3.8 inset). We deliberately focus on the electron-doped side since quantum Hall effect never developed for the hole-doped regime in narrow junctions, a feature we ascribe to pn-barriers formation along the contacts. Although all junctions display a well-quantized $\nu = 2$ quantum Hall plateau around $V_g = 0.5$ V, the $\nu = 6$ plateau systematically exhibits a strong mismatch with the expected quantized value.

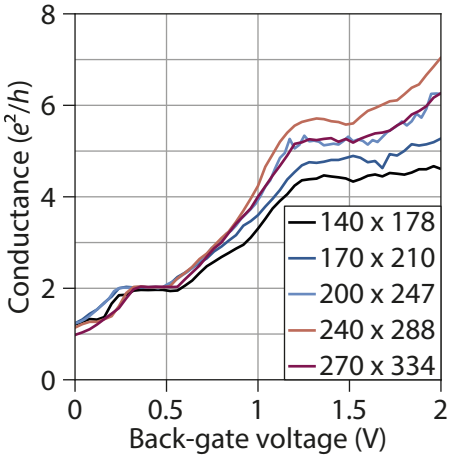

Figure 3.8: **Integer quantum Hall effect in graphene nanoribbons.** Conductance as a function of the back-gate voltage for narrow junctions in sample HV088 measured at $B = 8$ T and $T = 10$ mK. Current bias is equal to 1.86 μA. Inset indicates the devices dimensions L x W in nm^2.

In reference [124], Hall bar measurements revealed a non-vanishing σ_{xx} value while σ_{xy} was displaying quantum Hall plateaus, an indication that scattering between opposite edge channels was not fully suppressed. This interpreation was further supported observing that σ_{xx} minimum value was increasing with the filling factor ν. At fixed magnetic field, provided individual Landau level broadening $\Gamma \approx \hbar v_F / l_m$ is constant[27] (l_m denoting the mean free path), the reduction of the cyclotron gap that goes with a filling factor increase will result in less pronounced σ_{xy} plateaus for high index Landau levels.

In our case, junctions ballisticity necessarily implies $l_m \geq L$ hence setting an upper bound for Landau level broadening. Considering the smallest junction, we obtain $\Gamma \leq 4.7$ meV, to be compared with a cyclotron gap

[27] In details, Landau level broadening expresses as $\Gamma \approx h/\tau_e$, τ_e being the time between two elastic scattering events [2]. For graphene, it was actually shown that the scattering rate $1/\tau_e$ scales linearly with the charge carriers energy [125], hence suggesting that the expression for Γ mentioned in [124] should be treated with caution.

between the N = 0 and N = 1 Landau levels estimated to be about 36.2 meV$\cdot\sqrt{B[\mathrm{T}]} \approx 102$ meV at $B = 8$ T [2]. Thus, disorder considerations alone cannot explain the $\nu = 6$ plateau poor-quality quantization.

Remarkably, we point out that wide junction G, whose width W is about 10 times larger than that in narrow junctions, displays a decent $\nu = 6$ quantization (see Figure 3.7.a,b,c). A larger electrode-graphene interfaces presumably results into better current injection within the quantum Hall edge channels, a factor known to be pivotal in observing the resistance quantization attached to the quantum Hall effect [11; 126]. More precisely, if the current is not well injected, i.e. not equally distributed between the different quantum Hall edge channels, the latter will need a minimum propagation length, known as the equilibration length, over which inter-edge channels scattering will allow to equally distribute the current among the edge states and ultimately lead to resistance quantization. The narrow junctions, having a short electrode-graphene interfaces length as well as a small lead-to-lead distance, are likely to suffer from this effect. In particular, such a scenario would be consistent with the trend towards better quantization as the device size increases we observe for narrow junctions (see for instance Figure 3.8).

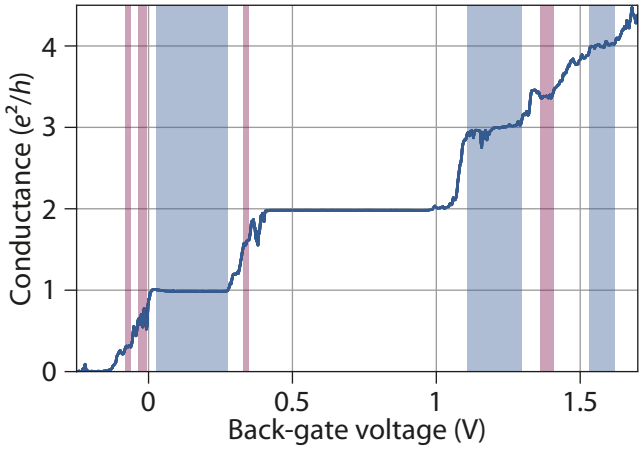

Figure 3.9: **Fractional quantum Hall effect and broken-symmetry states in narrow junctions.** Conductance as a function of the back-gate voltage at $B = 14$ T and $T = 10$ mK, for narrow junction E (240 x 288 nm^2). Purple layers highlight fractional quantum Hall plateaus while blue layers indicate broken-symmetry states.

We end up this section mentioning the remarkable observation of both broken-symmetry states as well as fractional quantum Hall effect in our junctions. Figure 3.9 shows the conductance as a function of the back-gate voltage for Device E (240 x 288 nm^2) obtained at our highest magnetic field of $B = 14$ T using standard lock-in technique ($I_{\mathrm{bias}} = 10$ nA). Purple layers highlight conductance kinks that successively match the 1/3, 2/3, 5/3 and 10/3 fractional quantum Hall plateaus. The blue layers, on the other hand, denote the broken-symmetry states at $\nu = 1$, 3 and 4. Although emerging at high magnetic field, observing this interaction-induced quantum Hall states raises the hope to combine them with superconductivity, a possibility that may be achieved provided the samples quality increases.

3.3 Conclusion

In this chapter, we first characterized the transport regime in which our Josephson junctions falls in. As the proximity-induced superconducting coherence length $\xi_S^N \sim 730$ nm strongly exceeds the junctions lead-to-lead distance, our devices lie into the short-junction regime. In addition, the observation of Fabry-Perot cavity-

ascribed resistance oscillations for hole-doped graphene suggests our junctions are ballistic.
Going a step further, we computed the resistance that would solely arise from the propagation of ballistic modes within the junctions. By substracing it to the measured resistance, one could deduce a contact resistivity ranging from 100 $\Omega.\mu$m to 510 $\Omega.\mu$m, to be compared with 30-35 $\Omega.\mu$m, the values obtained in state of the art graphene-based Josephson junctions [66; 76].
The OBTK formalism yielded typical NS interfaces transparencies of about 0.5, indicating low-quality contacts to graphene.
This PhD work being dedicated to proximity-induced superconductivity in the quantum Hall regime, we also discussed the latter's perculiarities when measured in the two-terminal geometry imposed by the junctions design. In details, quantum Hall plateaus are prone to distortion when the junction's aspect ratio L/W departs from 1, an effect we carefully discuss introducing the model of D. A. Abanin and L. S. Levitov [121].
To conclude, we reported on the observation of broken-symmetry/fractional quantum Hall states plateaus at $B = 14$ T.

Chapter 4

Josephson effect in the quantum Hall regime

In this chapter we investigate proximity-induced superconductivity in graphene-based Josephson junctions placed in the quantum Hall regime. In the next, we refer to these devices as *quantum Hall Josephson junctions* (QHJJs). The sizes and values of the various key parameters of these devices can be found in Appendix B.
We begin by reporting on the observation of finite supercurrent regions accross the $\nu = 2$ quantum Hall plateau within the $V_g - B$ plane.
Following theoretical insights highlighting the importance of junctions geometry for Josephson effect in the quantum Hall regime (see Chapter 1 Section 1.2.2), the supercurrent occurence is discussed in relation with the device size.
Then, we characterize the inverse AC Josephson effect via the measurement of Shapiro steps, which enables us to infer the periodicity of the current-phase relation.
Last, we address the sub-gap resistance fluctuations with filling factor, a feature strongly reminiscient of the chiral Andreev edge states interference signatures reported by the G. Finkelstein's group (see Chapter 2 Section 2.4).

4.1 Josephson effect in the $\nu = 2$ quantum Hall plateau

We start by presenting the first major result of this thesis, namely the observation of a robust supercurrent up to 8 T in the $\nu = 2$ quantum Hall plateau.

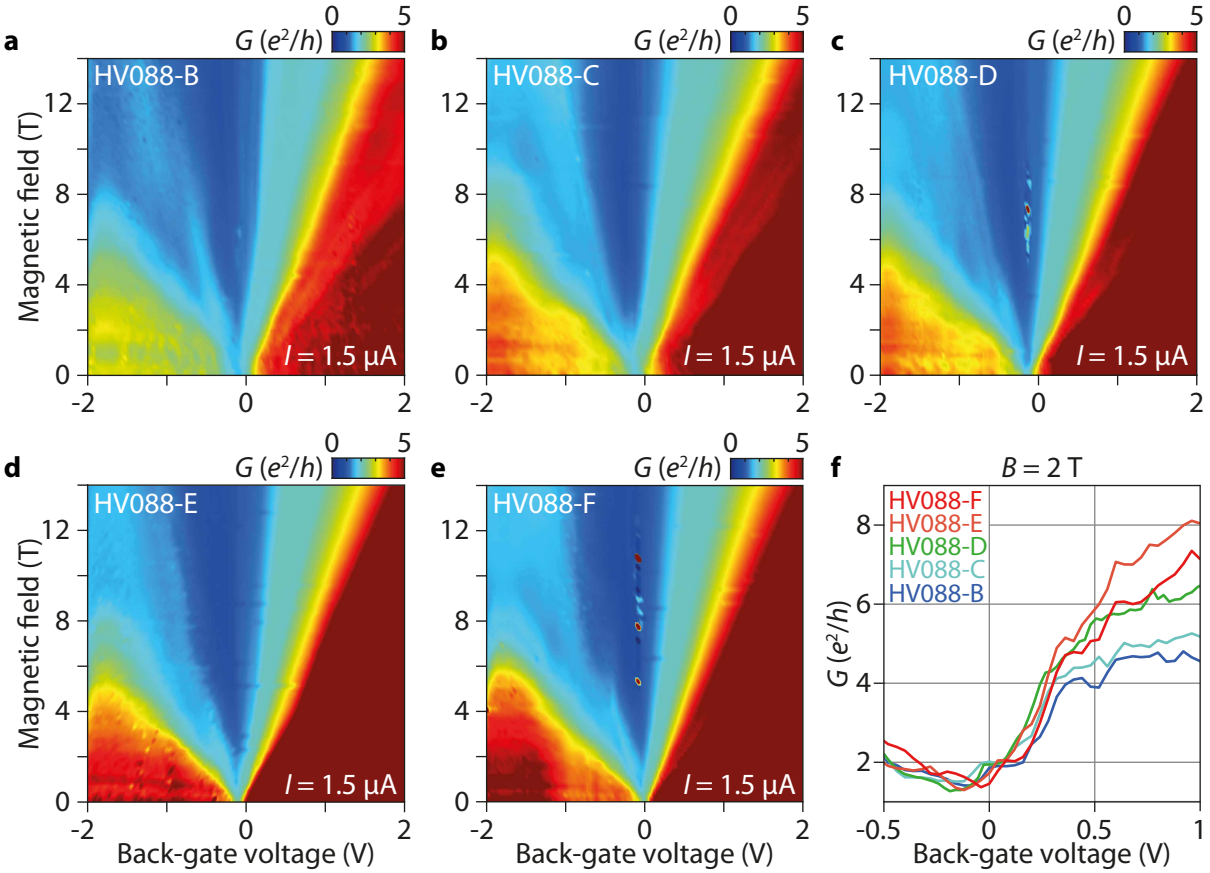

Figure 4.1: **$\nu = 2$ quantum Hall plateau position in the $V_g - B$ plane. a)** Conductance map as a function of both the back-gate voltage V_g and the magnetic field B obtained at $T = 10$ mK for narrow junction B (L x W = 140 x 177.5 nm^2) in sample HV088. The conductance was computed as the inverse of the differential resistance deduced at $I = 1.5$ µA from I/V characteristics. **b,c,d** and **e)** Similar measurements for, respectively, narrow junctions C (L x W = 170 x 210 nm^2), D (L x W = 200 x 247 nm^2), E (L x W = 240 x 288 nm^2) and F (L x W = 270 x 334 nm^2) in sample HV088. **f)** Conductance linecut versus the back-gate voltage taken in **(a),(b),(c),(d)** and **(e)** at $B = 2$ T.

As a first step, we establish the position of the $\nu = 2$ QH plateau within the $V_g - B$ plane for each of our narrow junctions in sample HV088, i.e. devices whose NS interfaces length is smaller than 350 nm.
Figures 4.1.a to 4.1.e show the corresponding conductance G maps versus both the gate voltage V_g and the magnetic field B obtained at $T = 10$ mK.
The onset of the $\nu = 2$ QH plateau, whose quantized conductance value is color-coded in light-blue, was systematically observed to take place within the 1.5 T - 2 T magnetic field range. For the sake of completness, Figure 4.1.f provides conductance linecuts taken at $B = 2$ T for each of these colormaps.

Note that G has been computed as the inverse of differential resistance, the latter being numerically derived from I/V characteristics. These I/V curves were obtained using a DC current acquisition card NI-6346 (8 inputs, 16-bits, 500 kS/s, Multifunction I/O Device). Although each point constituting a given I/V is the result of an

oversampling over typically 500 points, our DC measurements are intrinsically more sensitive to noise than AC current-based standard lock-in technique.
Furthermore, the current is not recorded in these measurements. If we take into account the 5% uncertainty on the value of the polarization resistor used (1 MΩ), all these factors can contribute to a slight shift of the QH plateaus position with respect to the expected quantized conductance value.

Incidentally, as mentioned in Chapter 3 Section 3.2.2, these conductance colormaps also show that the QHE does not develop properly in the hole-doped regime, a remark that also applies to the $\nu = 6$ QH plateau, hence explaining the focus on the $\nu = 2$ QH plateau in the next.

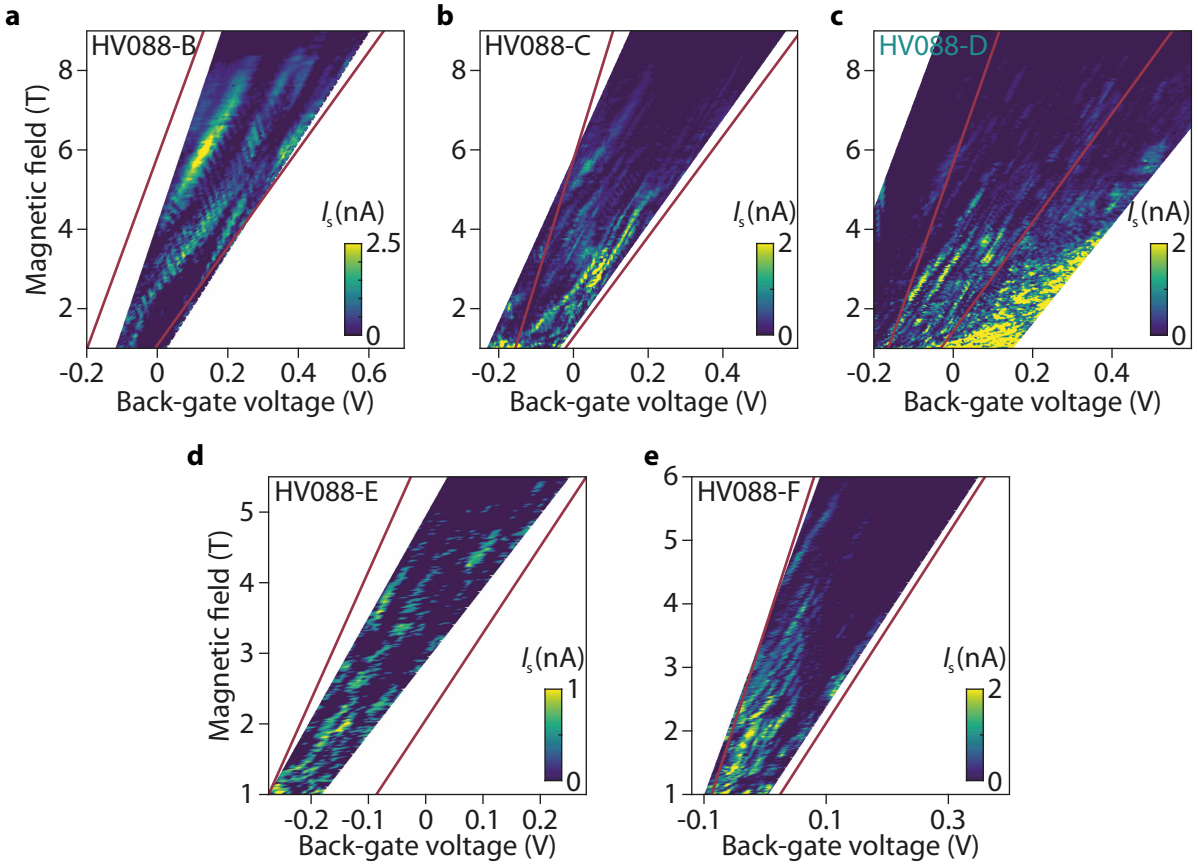

Figure 4.2: **Supercurrent in the $\nu = 2$ quantum Hall plateau.** **a**) Switching current I_s colormap versus both the back-gate voltage V_g and the magnetic field B obtained at $T = 10$ mK for narrow junction B (L x W = 140 x 177.5 nm^2) in sample HV088. Red lines indicate the $\nu = 2$ QH plateau's edges measured at $I_{bias} = 160$ nA. **b**) Similar map for narrow junction C (L x W = 170 x 210 nm^2) in sample HV088. **c**) Similar map for narrow junction D (L x W = 200 x 247 nm^2) in sample HV088. **d**) Similar map for narrow junction E (L x W = 240 x 288 nm^2) in sample HV088. **d**) Similar map for narrow junction F (L x W = 270 x 334 nm^2) in sample HV088.

Having identified the $\nu = 2$ QH plateau location within the $V_g - B$ plane, low current bias I/V characteristics were then performed within the corresponding region to sought for supercurrent signatures.

Figure 4.2.a shows a switching current I_s colormap as a function of both the gate voltage V_g and the magnetic field B obtained for sample HV088 junction B (L x W = 140 x 177.5 nm^2) at $T = 10$ mK. To assist the reader, red lines indicate the edges of the $\nu = 2$ QH plateau measured at $I_{bias} = 160$ nA, a compromise

value that limits QH resistance non-linearities arising from both the superconductivity[1] and the quantum Hall breakdown (see Section 4.3). Note apart, these boundaries were carefully estimated during the analyses that followed the experiment (see Appendix C), which explains the slight offset between the area delimited by the red lines and the region covered with the low bias measurements.

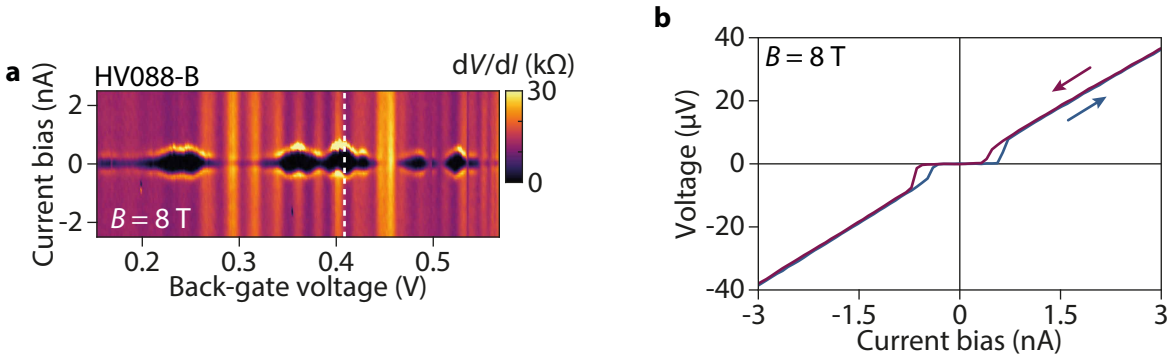

Figure 4.3: **Supercurrent at $B = 8$ T in the $\nu = 2$ quantum Hall plateau.** **a**) Colormap of the differential resistance as a function of both the back-gate voltage and current bias I_{bias} at $B = 8$ T and $T = 10$ mK for narrow junction B (L x W = 140 x 177.5 nm^2) in sample HV088. Black pockets centered at $I_{\text{bias}} = 0$ nA indicate supercurrent occurence. **b**) I/V trace (blue) and retrace (purple) taken along the vertical white dashed line in **(a)** and clearly establishing the presence of a zero voltage state.

Several comments can be made about this map:

1. First of all, the mere observation of a supercurrent within the $\nu = 2$ QH plateau is already a remarkable fact in itself, since it constitutes a first for a QHJJ (see Chapter 2 for a detailed review on the state of the art). Note that this implies a Josephson junction whose normal state resistance is about 12.9 kΩ, which clearly stands out when compared to typical normal state resistance values for SNS devices in the literature [127][2].

2. Second, this QHJJ withstand a supercurrent up to $B = 8$ T, hence establishing a new record for the magnetic field a supercurrent in the quantum Hall regime can sustain.
   To further assess this result, Figure 4.3.a shows a colormap of the differential resistance computed from the successive I/V characteristics (sweep up) done at $B = 8$ T, versus both the gate voltage and current bias. Quite remarkably, a set of superconducting pockets appears somewhat randomly as a function of the gate voltage, a point we further address in Section 4.3. Note also the presence of overlying vertical resistance stripes, the origin of which will be thoroughly discussed in the next Chapter.
   Taking a linecut along the white dashed line in Figure 4.3.a, we obtain an I/V curve demonstrating unambiguously the presence of a supercurrent in the $\nu = 2$ quantum Hall plateau at a magnetic field as high as 8 T (see Figure 4.3.b, blue/purple curves denoting respectively trace/retrace).

   For indication purpose only, we mention that $R_{h/2e^2} I_s = 7.2$ μeV. Note, however, that unlike conventional Josephson junctions, this product is not known to be directly proportional to either the electrodes superconducting gap Δ or the Thouless energy E_{Th} for QH edge states-mediated supercurrent.

[1] Typically, at zero magnetic field, Andreev reflection probability gets strongly reduced once the voltage accross the junction reaches $V = 2\Delta/e$, with $\Delta \sim 900$ μeV the MoGe electrodes superconducting gap. In the $\nu = 2$ QH plateau, this corresponds to a current bias $I_{\text{bias}} = 2\Delta/eR_{\nu=2} \approx 140$ nA.

[2] Although it differs with respect to our devices, few kΩ-normal state resistance have already been reported in Josephson junctions whose normal part was made of a single quantum dot [128].

As a reminder, based on the model of Y. Alavirad *et al.* [30] (see Chapter 1 Section 1.2.2 for a detailed discussion), the critical current for a quantum Hall Josephson junction reads as:

$$I_c = -\sum_{\omega_m} \frac{4e}{\beta\hbar} \sin^2\left(\frac{\Delta W}{\hbar v_{SC}}\right) \left[\cos(\phi_e)\cos\left(\frac{2\Delta W}{\hbar v_{SC}}\right) + \cos(\phi_e) - 2\cosh\left(\frac{4\pi\omega_m}{E_{Th}}\right)\right]^{-1} \quad (4.1)$$

with $\phi_e = LWB\pi/\Phi_0$ the dimensionless external magnetic flux[3], L and W denoting respectively the lead-to-lead distance and the NS interfaces length, $\omega_m = (2m+1)\pi/\beta$ the fermionic Matsubara frequency, $\beta = 1/k_B T$ the inverse temperature and $E_{Th} = h/(L/v_{QH} + W/v_{SC})$ a Thouless energy attached to the chiral supercurrent-carrying particles moving with a velocity v_{QH} (resp. v_{SC}) along the pristine edges of the graphene (resp. along the NS interfaces).

3. Finally, and importantly, the switching current forms negatively-sloped fringes pattern on top of a slowly varying background, the latter's origin being clarified in Section 4.3. As for the fringes pattern, we will leave it aside for the moment and return to it in greater detail in the next Chapter.

Based on the above-mentioned theory, QH edge states-mediated supercurrent is mostly sensitive to the NS interfaces length W. In details, this model states that quantum Hall edge channels undergo velocity renormalization along the NS interfaces due to the finite time $\sim \hbar/\Delta_{electrode}$ taken by each electron/hole undergoing an Andreev reflection. Such a renormalization that reads as $v_{SC} = 2v_n/[\pi + q\hbar\omega_c/\Delta]$[4] (see Chapter 1 Section 1.2.2) translates as a Thouless time τ_{Th} increase, i.e. a Thouless energy $E_{Th} = h/\tau_{Th}$ decrease.
Accordingly, for a given Andreev reflection probability, the longer NS interfaces are, the smaller E_{Th}, hence the critical current amplitude, is.

Focusing on the other narrow junctions within sample HV088, the latter systematically exhibited a supercurrent within the $\nu = 2$ quantum Hall plateau, as can be seen with the switching current colormaps provided in Figures 4.2.b,c,d and e for junctions C,D,E and F, respectively. Beyond the fact that observing a supercurrent within the $\nu = 2$ QH plateau for several devices strengthens our main result, this finding unveils a qualitative trend with junction size: the larger the device, the earlier the supercurrent disappears in magnetic field. Typically, while a zero-voltage state persists up to $B = 7.19$ T and $B = 7.77$ T for junctions C and D respectively (see Figures 4.4.a,b and 4.4.c,d), it does not survive beyond 5.09 T and 5.69 T within junctions E and F (see Figures 4.4.e,f and 4.4.g,h), i.e. the two largest narrow junctions, which is consistent with a decrease of E_{Th}. By way of comparison with theory, an application of equation (4.1) using the parameters specific to each junction (see Table A.1 in Appendix A) yields $I_c \approx 10$ nA, 0.07 nA, 1.8 nA and 9 nA for junctions C,D,E and F respectively.

Note that, at higher magnetic field values, the supercurrent was systematically found to exhibit some residual resistance[5], a feature suggesting that the critical current I_c was getting smaller than $\sim$0.4 nA, thus making it sensitive to temperature-induced phase fluctuations, i.e. phase diffusion [86; 36].
Finally, we mention that a supercurrent within the $\nu = 2$ quantum Hall plateau was also observed in sample DP024 (see Figures 4.5.a,b,c and d), hence definitively demonstrating the robustness of this result.

[3] Here, $\Phi_0 = h/2e$, the usual superconducting flux-quantum.

[4] v_n being the Fermi velocity, $q = 2s/(1+s^2+w^2)$ with $s = v_n/v_s$ translating the Fermi velocity mismatch between the graphene and the superconductor, $w = k_F^n U_0/E_F^n$ a scattering parameter, $\hbar\omega_c$ the cyclotron gap and Δ the superconducting gap of the electrode.

[5] The protocol used to detect the switching current also captured some of these superconducting pockets having a finite residual resistance, explaining the tenuous switching current traces persisting beyond the above-mentioned magnetic field values in Figures 4.2.a,b,c,d and e.

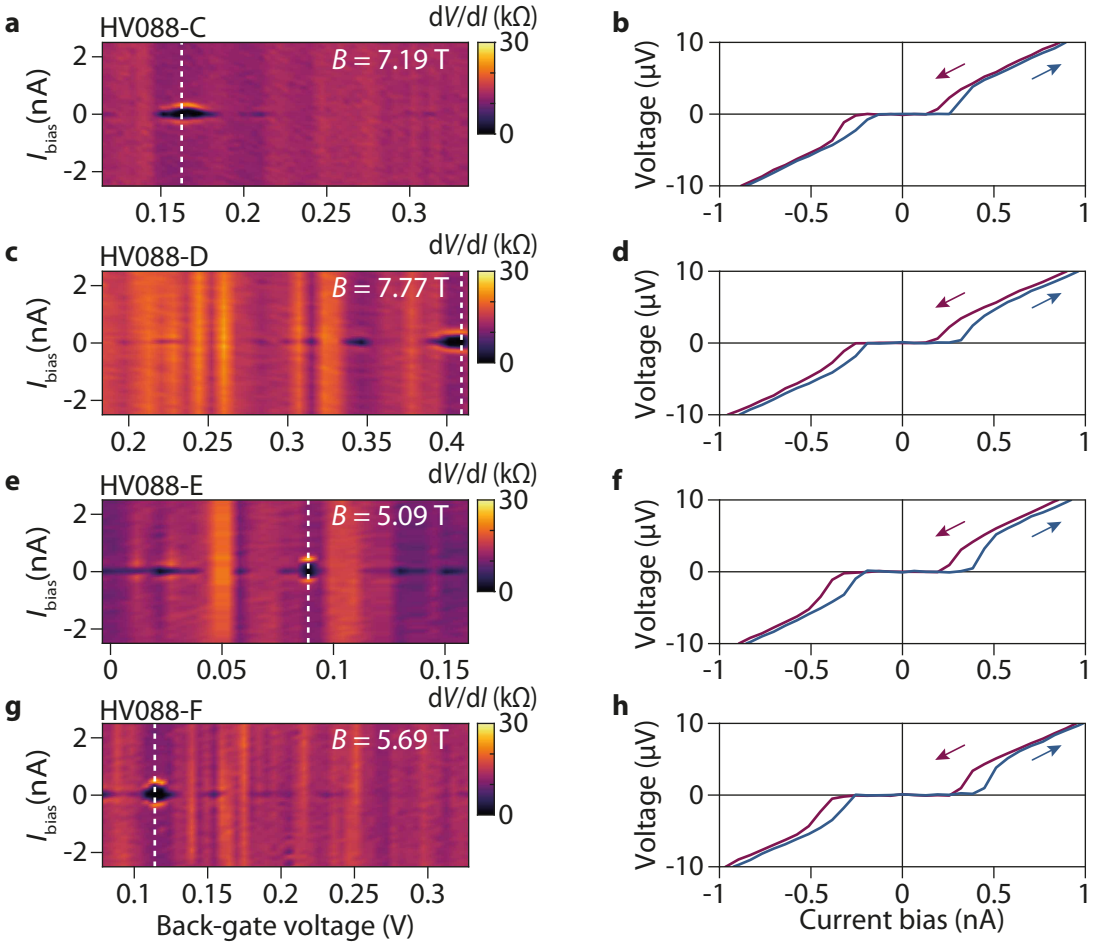

Figure 4.4: **Supercurrent in narrow quantum Hall Josephson junctions. a)** Differential resistance colormap computed from successive I/V curves (sweep up) versus both the back-gate voltage and the current bias I_{bias} at $B = 7.19$ T for junction C (L x W = 170 x 210 nm^2) in sample HV088 at $T = 10$ mK. **b)** I/V characteristic obtained along the white dashed line in **(a)**. Blue and purple traces denote respectively trace and retrace. **c)** Similar measurement as **(a)** for junction D (L x W = 200 x 247 nm^2) in sample HV088 at $B = 7.77$ T and $T = 10$ mK. **d)** I/V characteristic obtained along the white dashed line in **(c)**. **e)** Similar measurement as **(a)** for junction E (L x W = 240 x 288 nm^2) in sample HV088 at $B = 5.09$ T and $T = 10$ mK. **f)** I/V characteristic obtained along the white dashed line in **(e)**. **g)** Similar measurement as **(a)** for junction F (L x W = 270 x 334 nm^2 at $B = 5.69$ T and $T = 10$ mK. **h)** I/V characteristic obtained along the white dashed line in **(g)**. Overall, the $R_{h/2e^2} I_s$-product typically equates 3.3 μeV.

Anticipating the importance of the NS interfaces length for this physics, wide junctions ($W > 2$ μm) were also implemented in sample HV088.

Figure 4.6.a presents a dV/dI map versus current bias and back-gate voltage obtained for wide junction H (L x W = 202 x 2434 nm^2) at $B = 3.5$ T, that is the magnetic field from which plateaus $\nu = 6$ and 10 reach the expected quantum Hall quantization[6].

Strikingly, superconducting pockets solely develop at transitions between quantum Hall plateaus, that is when

[6]The $\nu = 2$ quantum Hall plateau gets already quantized from 3 T which is consistent with the fact that the N $= 0$ Landau level cyclotron gap ($\nu = 2$) is larger than the N $= 1$ ($\nu = 6$) and N $= 2$ ($\nu = 10$) ones.

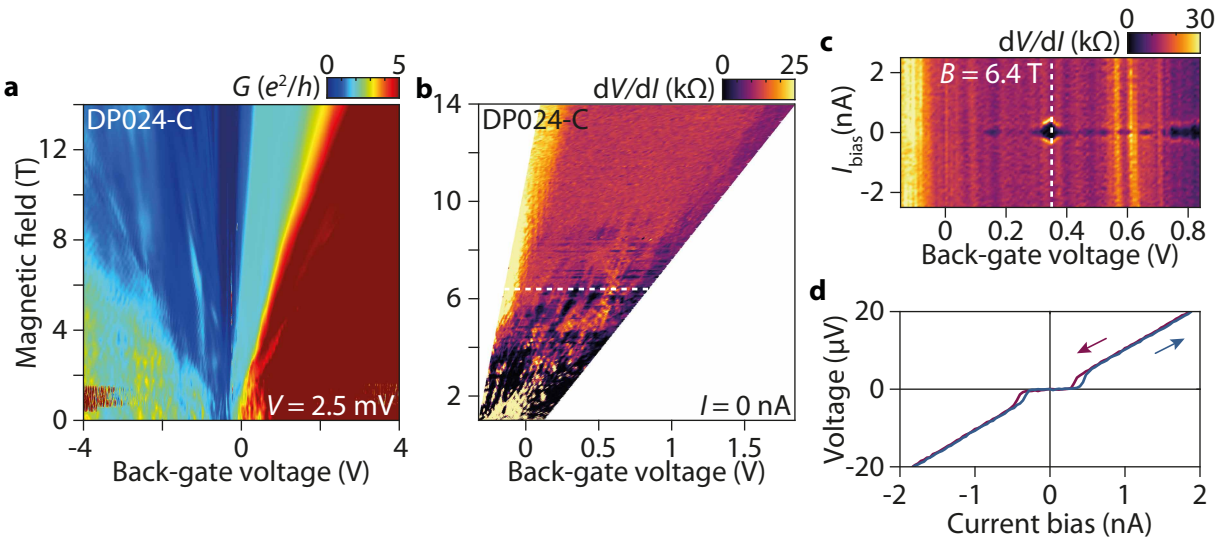

Figure 4.5: **Supercurrent in the $\nu = 2$ QH plateau for sample DP024.** **a)** Conductance G versus both the back-gate voltage V_g and the magnetic field B obtained for narrow junction C (L x W = 170 x 125 nm^2) in sample DP024 at $T = 4$ K with a voltage bias $V = 2.5$ mV. The conductance was computed as $\sqrt{I_{xx}^2 + I_{xy}^2}/\sqrt{V_{xx}^2 + V_{xy}^2}$, with I_{xx}, I_{xy}, V_{xx} and V_{xy} the current and voltage components measured using lock-in technique. **b)** Zero-bias differential resistance versus the gate voltage V_g and the magnetic field B measured in the same device at $T = 10$ mK. Successive I/V characteristics were done accross the $\nu = 2$ QH plateau from which the differential resistance was subsequently computed. **c)** Differential resistance versus the gate-voltage V_g and the current bias I_{bias} obtained by taking the I/V curves done along the white dashed line in **(b)** at $B = 6.4$ T, the last magnetic field value at which a zero-voltage state was seen. **d)** I/V characteristic taken along the vertical white dashed line in **(c)** at $V_g = 0.35$ V. The blue (resp. purple) curve denotes the trace (resp. retrace). For information purpose, the $R_{h/2e^2}I_s$-product is about 3.6 μeV.

graphene is in the percolation regime. Note that a similar result was obtained for the wide junction I (L x W = 307 x 2569 nm^2) whose Hall quantization was reached at lower magnetic fields of 2 T and 2.5 T for respectively the $\nu = 2$ and $\nu = 6$, 10 quantum Hall plateaus.
Looking at the normal resistance[7] dependence on the gate voltage (see Figure 4.6.b), transition between $\nu = 2$ and $\nu = 6$ plateaus at $V_g \approx 0.2$ V shows higher resistance ($\sim 1999.3\ \Omega$) than the $\nu = 14$ quantum Hall resistance plateau (1843.8 Ω), hence rulling out a simple $R_N I_c$-product argument explaining the absence of supercurrent within the plateaus.

We finally discuss results obtained for the wide junction G (L x W = 107 x 2332 nm^2) in Figure 4.7.a, whose lead-to-lead distance L has the crucial particularity to be smaller than that in narrow junctions[8].
This point, combined with the absence of supercurrent within the $\nu = 2$ quantum Hall plateau, leads to the following conclusions:

[7] Although normal resistance should, following Section 4.3 discussion, be estimated from high bias measurements, the corresponding set of data suffered from a very low resolution in gate voltage. We therefore opted for a normal resistance estimation based on a linear fit to the low bias data, the latter having a better resolution in gate voltage.

[8] Note apart, the wide junction G also allows for seeking supercurrent traces in other quantum Hall plateaus, though not perfectly quantized (see insets in Figure 4.7.b). Figures 4.7.c,d provide linecuts taken along white vertical dashed lines in 4.7.a for respectively the $\nu = 6$ and $\nu = 10$ plateaus. As an indication, $R_N I_s$-product equates 2.3 μeV (resp. 2.2 μeV) for the $\nu = 6$ (resp. $\nu = 10$) plateau.

1. The supercurrent observed in our $\nu = 2$ narrow quantum Hall junctions cannot rely on tunneling through the quantum Hall insulating bulk. If such a scenario was at play, one would also expect to observe a supercurrent in the $\nu = 2$ quantum Hall plateau for the wide junction G, even if the length of its NS interfaces is an order of magnitude longer than that of narrow junctions.

2. For a conventional Josephson junction, an inter-electrode distance L reduction is not expected to suppress supercurrent as what is observed here, on the contrary. This goes in line with the fact that devices width W is key to the supercurrent magnitude in quantum Hall Josephson junctions.

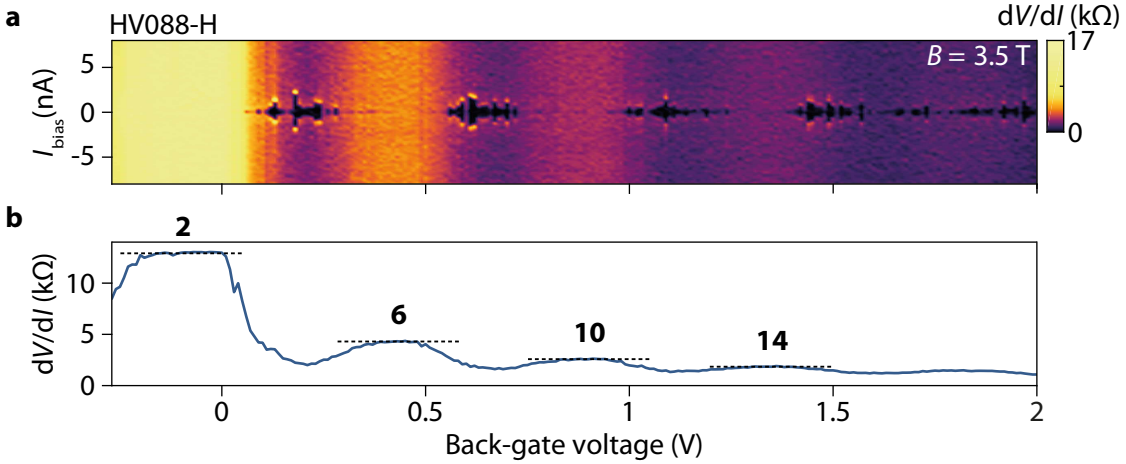

Figure 4.6: **Absence of supercurrent within quantum Hall plateaus for a wide junction. a)** Differential resistance $\mathrm{d}V/\mathrm{d}I$ colormap (sweep up) as a function of both gate voltage and current bias at $B = 3.5$ T for wide junction H (L x W = 202 x 2434 nm^2) in sample HV088. Supercurrent develops at the transitions between QH plateaus. **b)** Resistance computed from a linear fit to the aforementioned I/V curves from -19 nA to 19 nA versus the back-gate voltage for wide junction H at $B = 3.5$ T. Bold numbers indicate the integer filling factors around which the plateaus are centered.

To conclude this section, it is interesting to note that most, if not all, QHJJ-related works were using micrometer-long NS interfaces so far (see Chapter 2 for a review).
Following the above results, it is very likely that the absence of supercurrent observations in the quantum Hall effect regime until recently stems from the systematic use of devices with long NS interfaces.

4.2 Junctions under radiofrequencies: Shapiro steps

In 1963, only one year after B.D. Josephson predictions [129], S. Shapiro reported on the striking response of Josephson junctions exposed to microwave excitations [130]. This behavior, known as the inverse AC Josephson effect, translates as a staircase pattern in I/V characteristic, the Shapiro steps, with plateaus lying at quantized voltage values $V_n = nhf_{\mathrm{RF}}/2e$, n being an integer indexing the Shapiro steps and f_{RF} the microwave excitation frequency.
Importantly, this effect directly relates to the periodicity of the current-phase relation, the latter having never been characterized for a QHJJ to date.
Here we report on Shapiro steps measurements performed on a superconducting pocket located within the $\nu = 2$ quantum Hall plateau for narrow junction C (L x W = 170 x 210 nm^2) in sample HV088. Radiofrequency excitation was supplied via an antenna approximatively 1 mm above the junction using a microwave source

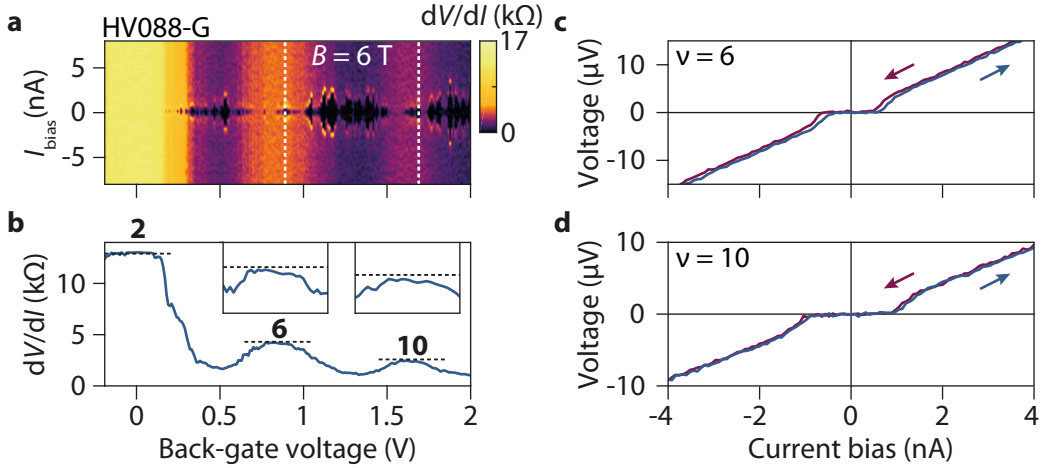

Figure 4.7: **Supercurrent in the $\nu = 6$ and $\nu = 10$ quantum Hall plateaus for wide junction G. a)** Differential resistance $\mathrm{d}V/\mathrm{d}I$ colormap numerically computed from successive I/V-curves (sweep up) as a function of both the gate-voltage and the current bias at $B = 6$ T for wide junction G (L x W = 107 x 2332 nm^2). Bold numbers indicate the integer filling factors around which the plateaus are centered. Supercurrent traces are visible in $\nu = 6$ and $\nu = 10$ quantum Hall plateaus. **b)** Resistance computed from linear fit to the aforementioned I/V curves from -28.8 nA to 28.8 nA versus the back-gate voltage for wide junction G (sample HV088) at $B = 6$ T. Insets show that $\nu = 6$ and $\nu = 10$ quantum Hall plateaus are not fully quantized. **c)** Single I/V characteristic (trace in blue, retrace in purple) in the $\nu = 6$ quantum Hall plateau at $V_g = 0.89$ V. **d)** Single I/V characteristic (trace in blue, retrace in purple) in the $\nu = 10$ quantum Hall plateau at $V_g = 1.69$ V.

Rhodes and Schwarz SMB 100 signal generator.

Figure 4.8.a shows a Shapiro map as a function of both the current bias and radiofrequency power[9] at $B = 3.451$ T and $V_g = 0.063$ V that was obtained while subjecting the junction to a microwave excitation frequency $f_{RF} = 3$ GHz. From $P \approx$ -9 dBm, a typical tree-structure formed by successive differential resistance minimums emerges while increasing the radiofrequency power. In Figure 4.8.b, a linecut taken at $P =$ -4.4 dBm (see white dashed line in Figure 4.8.a) shows that voltage plateaus lying at $V_{1,-1} = \pm$ 6.2 μV are attached to the first zero-resistance lobes (left and right), in agreement with the value of 6.2 μV expected for the Shapiro steps $n =$ -1 and $n = 1$.
Keeping the same magnetic field and gate-voltage values, repeating this measurement with $f = 1$ GHz yielded the Shapiro map shown in Figure 4.8.c with Shapiro steps $n = \pm 1, \pm 2$ lying also at the expected voltage values[10] (see linecut in Figure 4.8.d).

Overall, the presented measurements indicate a 2π-periodic current-phase relation for the supercurrent ob-

[9] Strictly speaking, the power of the RF signal reaching the sample is not known due to the impedance mismatch between the antenna and the sample. Consequently, we attribute to each given I/V curve the power delivered by the microwave source.

[10] Surprisingly, the n = -1 plateau crosses the $I_{bias} = 0$ nA axis and extends over positive bias.
Interestingly, similar patterns were already reported in graphene-based Josephson junctions [131]. This "zero crossing step" effect was demonstrated to stem from the simultaneous existence of different stable plateaus for a given current bias value. Looking at both the I/V characteristic trace and retrace at $P =$ -13.8491 dBm (see Figure 4.8.d), the hysterese between the two curves clearly results into the co-existence of two plateau values in the current bias range $I_{bias} \approx \pm$ 0.13 nA. The seemingly abnormal voltage step at $I_{bias} =$ 0.107 nA (resp. $I_{bias} =$ -0.107 nA) simply results from the direct transition from the $n =$ -1 to the $n = 1$ Shapiro steps (resp. from the $n = 1$ to $n =$ -1 plateau).

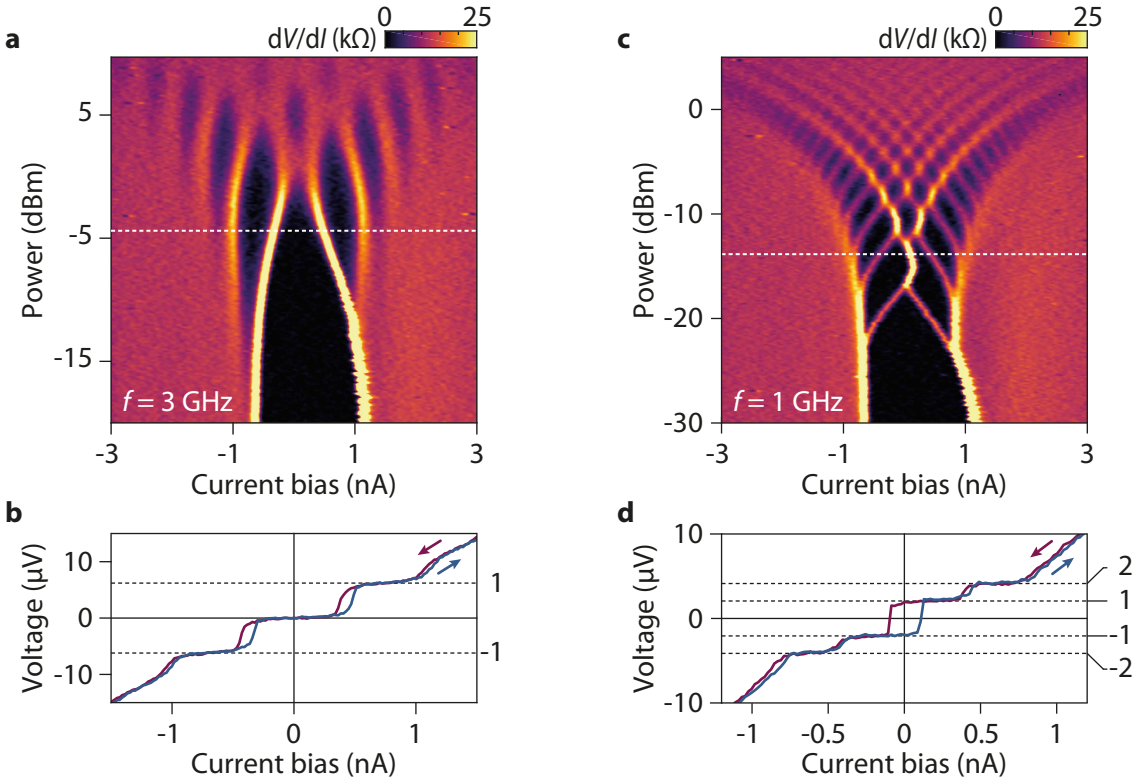

Figure 4.8: **Shapiro steps measurement in the $\nu = 2$ quantum Hall plateau. a)** Shapiro map obtained at $V_g =$ 0.063 V and $B = 3.451$ T applying a radiofrequency excitation $f_{RF} = 3$ GHz on narrow junction C (170 x 210 nm^2) in sample HV088. **b)** Linecut taken along the white dashed line in **(a)** at $P =$ -4.4 dBm. Blue/purple curves denote respectively the trace/retrace. **c)** Shapiro map obtained at $V_g = 0.063$ V and $B = 3.451$ T applying a radiofrequency excitation $f_{RF} = 1$ GHz on narrow junction C (170 x 210 nm^2) in sample HV088. **d)** Linecut taken along the white dashed line in **(c)** at $P =$ -13.8491 dBm. Blue/purple curves denote repectively the trace/retrace.

served in the $\nu = 2$ quantum Hall state.

4.3 Chiral Andreev edge states signatures

Beyond supercurrent-related features, the interplay between superconductivity and the quantum Hall regime also manisfested within the resistive state of our QHJJs, signatures to which is dedicated this discussion.
In particular, the elements discussed below suggest that QH edge channels do propagate along NS interfaces, which in turn implies that supercurrent-carrying particles travel along the junction's perimeter, a first indication of the presence of a chiral supercurrent within our junctions (see Chapter 5).

Figures 4.9.a to 4.9.g show the differential resistance dV/dI colormaps versus both the filling factor ν and the voltage V measured accross the narrow junction C (170 x 210 nm^2) in sample HV088, at $T = 10$ mK and increasingly high magnetic field values.
The gate voltage window was purposely selected to cover the $\nu = 2$ quantum Hall plateau range[11].

[11]Conversion from gate voltage V_g to filling factor ν simply follows from $\nu = n_e/n_B$ with $n_e = C(V - V_D)/e$ the electron density, $C = 1.389$ x 10^{-3} F/m^2 and $V_D = -0.1443$ V being respectively the capacitor per unit area we deduced from a fit to the $\nu = 2$ plateau's

Yet, some parts of these resistance maps exhibit clear departures from the expected quantized value $h/2e^2 \approx$ 12.9 kΩ. This is readily seen looking at the regions centered around $V = 0$ mV where resistance systematically shows strong fluctuations as a function of the filling factor.

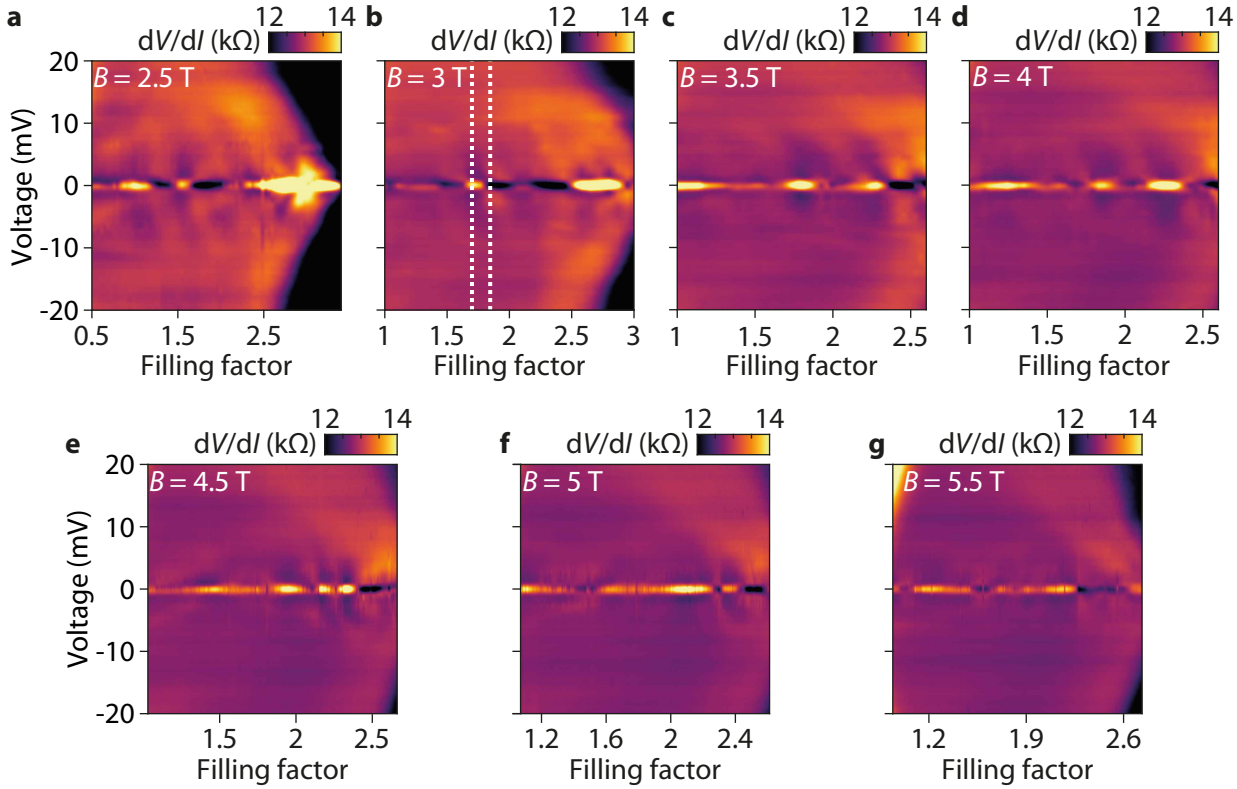

Figure 4.9: $\nu = 2$ **quantum Hall resistance fluctuations with the filling factor.** Differential resistance dV/dI colormaps versus both the filling factor ν and the voltage measured accross the narrow junction C (170 x 210 nm^2) in sample HV088 at $T = 10$ mK. **(a)**, **(b)**, **(c)**, **(d)**, **(e)**, **(f)** and **(g)** were respectively obtained at $B = 2.5$ T, 3 T, 3.5 T, 4 T, 4.5 T, 5 T and 5.5 T.

To further investigate them, dedicated measurements were subsequently performed with higher resolution in filling factor.

Focusing on the representative colormap shown in Figure 4.9.b, the corresponding high-resolution linecut at $V = 0$ μV[12] (see the black curve in Figure 4.10.a) exhibits local peaks, either above or below the expected quantized value (see for instance at $\nu \approx 2.08$ (resp. $\nu \approx 1.48$) with dV/d$I = 3.38$ kΩ (resp. dV/d$I = 18.78$ kΩ))[13].

Remarkably, linecuts at slightly higher voltage values show that the differential resistance also fluctuates with V. For instance, at $\nu = 1.83$, the differential resistance goes from 0 Ω at $V = 0$ μV to 36.3 kΩ at $V = 7$ μV, and then drop to 11.1 kΩ with $V = 49$ μV.

This feature translates as tenuous fluctuation patterns centered along the zero-voltage axis in the above-mentioned colormaps.

---

center position and V_D the Dirac point position we obtained from that fit (see Appendix C for details). The term $n_B = B/\phi_0$, with $\phi_0 = h/e$ the flux quantum, corresponds to the flux quanta density.

[12] The latter results from an average taken over points going from I_{bias} = -0.19 nA to I_{bias} = 0.13 nA.

[13] Note that the set of successive maxima around $\nu \approx 2.7$ relates to the h/e-flux periodic resistance oscillations that will be addressed in Chapter 5 Section 5.1.2.2.

To gain further insight, cross-sections taken along the white dashed lines in Figure 4.9.b are shown in Figure 4.10.b. The zero-voltage differential resistance peak (resp. dip) is framed by lobes on either side, the minima (resp. maxima) of which almost matching $V = \pm 2\Delta_0/e \approx 1.8$ mV (denoted by the gray band), $\Delta_0 = 852$ μeV being the superconducting gap at $B = 0$ T that was estimated for the junction C electrodes (see Appendix A). Averaging over the filling factor range from $\nu = 0.53$ to $\nu = 2.94$[14], the side lobes maxima (resp. minima) locate at $V \approx \pm 1.4$ mV.
This energy scale, above which Andreev reflections probability is expected to become very small in conventional Josephson junction and that was consistently found in the other colormaps, goes in line with a superconductivity-related mechanism to explain these oscillations.

Remarkably, resembling sub-$2\Delta/e$ features have already been reported in numerous works involving quantum Hall - superconductor hybrids structures.
For the specific case of QHJJ, similar signatures were seen in the very first experiment seeking for supercurrent in the quantum Hall regime [59], zero-voltage resistance maxima being reported at transition between plateaus while, conversely, a single resistance dip was observed when in a quantum Hall plateau. More recently, a work involving long and diffusive graphene-based Josephson junctions also reported on similar signatures [62] (see Chapter 2 Sections 2.1 and 2.2 for a review of these results).

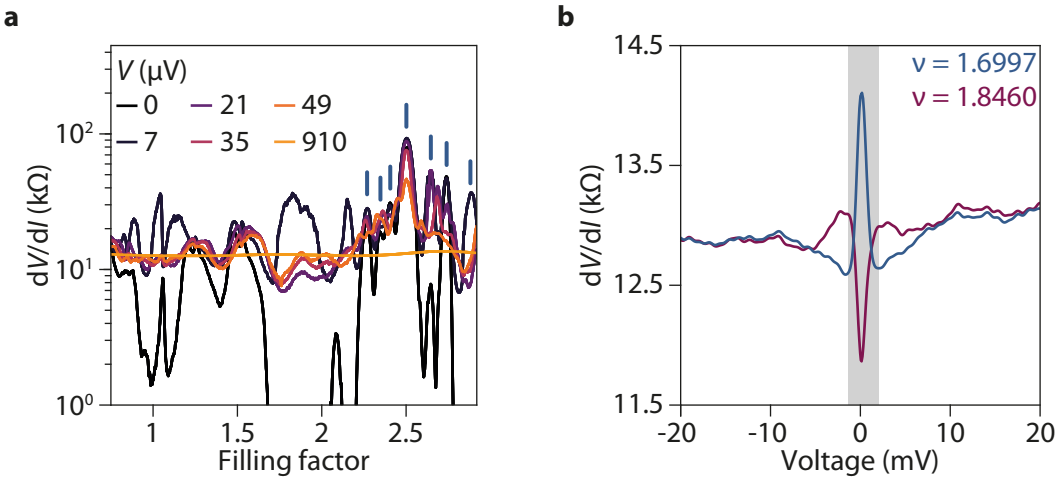

Figure 4.10: **Chiral Andreev edge states signatures. a)** $\mathrm{d}V/\mathrm{d}I$ linecuts at several voltages versus filling factor. The blue dashes indicate the peaks corresponding to the h/e-flux periodic oscillations, which will be discussed in Chapter 5. **b)** Differential resistance cross-sections taken along the white dashed lines in Figure 4.9.b at respectively $\nu = 1.6997$ (blue curve) and $\nu = 1.846$ (purple curve). Side lobes maxima (minima) match relatively well $V = \pm 2\Delta_0/e$, with $\Delta_0 = 852$ μeV the electrodes superconducting gap that was estimated at $B = 0$ T.

These findings were interpreted using results initially obtained for single NS interfaces in the quantum Hall regime:

- On the experimental side, the conductance measured in hybrid S/semiconductor-based 2DEG/N structures systematically displayed regular oscillations with the filling factor ν (constant electron density, varying magnetic field) [132; 61], a feature anticipated by numerics and ascribed to Aharonov-Bohm-like interferences between cyclotron orbits along the NS interface [25].

[14] To avoid quantum Hall breakdown contribution.

- Meanwhile, the theory anticipated conductance oscillations consisting of a superposition of harmonics of the form $\cos(2\pi n)$ with $n = \{1,2,3...\}$ [133], at odds with experiments in which only the first harmonic was observed to survive, a discrepancy that the model put forward by N.M. Chtchelkatchev and I.S. Burmistrov recovered by taking into account the disorder along the NS interface [134].

More recently, numerical simulations by A. Manesco *et al.* [37], dedicated to the specific case of an NS interface with the N part consisting in graphene placed in the $\nu = 2$ quantum Hall state, have yielded results looking very much like our observations (see Figure 1.12 in Chapter 1 Section 1.2.3).
Key to this last result was the consideration of disorder along the NS interface, the latter favoring intervalley-scattering between the chiral Andreev edge states propagating along the NS interface.
These numerics were intended to explain the results obtained by the G. Finkelstein's group using a similar device (see Chapter 2 Section 2.4 for a detailed discussion), in which the longitudinal quantum Hall resistance was observed to display stricking random fluctuations around 0 Ω, a feature that was ascribe to interferences between chiral Andreev edge states propagating along the NS interface.

Overall, although a theory dedicated to CAESs interferences physics in the specific case of a graphene-based QHJJ is still lacking, the similarity between our results and those mentioned above is in complete agreement with the presence of CAESs within our devices.
These CAESs interferences-related QH resistance fluctuations are also likely to explain the large scale modulation of the switching current amplitude that was observed accross the $\nu = 2$ quantum Hall plateau (see Section 4.1).

Note that another anomaly in the quantum Hall quantization became apparent during these measurements: the breakdown of the quantum Hall plateau[15,16] as can be readily seen in Figures 4.9.a,b and g with the black color-coded regions on the right side.
Although here the breakdown becomes significant at relatively large bias with respect to superconducting features, the situation may be detrimental for other QH plateaus with small energy gaps as those of the fractional QH states. For these correlated states, the need to reduce the superconducting interface width to obtain a robust supercurrent should therefore meet another constraint related to edge transport, since QH breakdown critical current is significantly weakened in narrow structures.

4.4 Conclusion

In this chapter, we reported on the presence of a supercurrent within the $\nu = 2$ quantum Hall plateau up to a record-high magnetic field value of 8 T for narrow junctions, a first.
Remarkably, experiments involving micrometer-wide junctions exhibited supercurrent traces only at the transitions between quantum Hall plateaus i.e. when the graphene's bulk is compressible. This observation demonstrates how key is the NS interfaces length in observing a supercurrent in quantum Hall systems, as anticipated

[15] For information purpose, we estimate that quantum Hall breakdown mechanism leads to a shrinkage of the $\nu = 2$ quantum Hall plateau's width of about 30 $\%$ within our devices for an applied current bias going from $I_{\text{bias}} = 0$ nA to $I_{\text{bias}} \approx 1$ µA. This estimation was deduced from junctions B,C,D,E and F data obtained at $B = 3,4$ and 5 T.

[16] Note that several theories have attempted to account for this effect, particularly because of its importance for metrological applications. Proposed models include quasi-elastic inter-Landau-level scattering [135] and heating effects [136] to name a few, though none of them capture all the reported experimental results in the literature. The interested reader can find a very thorough review in the Chapter 5 of [137].

by chiral supercurrent theories [30; 29].

In addition, we further characterized the supercurrent observed in the $\nu = 2$ quantum Hall plateau through the inverse AC Josephson effect, which is also a first. The resulting Shapiro maps indicate a conventional 2π current-phase relation.

Finally, $\nu = 2$ quantum Hall plateau resistance fluctuations with both the filling factor and the voltage measured accross the junction were evidenced. Remarkably, these features were systematically observed in the voltage range corresponding to $\pm 2\Delta_0/e$, in agreement with the presence of chiral Andreev edge states, the latter having produced similar signatures in the literature [59; 62; 41].

Chapter 5

Chiral supercurrent

This final chapter is devoted to the central result of this thesis, namely the observation of a chiral supercurrent in our quantum Hall Josephson junctions.
In a first part, we take a closer look at the switching current oscillations mentioned in Chapter 4 Section 4.1. In particular, a study of the magnetic field period of these oscillations, when considered at constant back-gate voltage (i.e. electron density), does not allow to draw any reliable conclusion regarding their flux-periodicity (h/e or $h/2e$) for our smallest devices. This leads us to reconsider these oscillations in the ν - B plane, ν being the filling factor. Applying Fourier analysis on these oscillations, we unambiguously demonstrate that they are h/e-flux periodic, which is the hallmark of the chiral supercurrent.
In a second section, we report on the presence of oscillations in the resistive state across the V_g-B plane, an observation closely resembling Aharonov-Bohm interference signatures usually observed in quantum Hall Fabry-Perot interferometers. Similarly to the switching current case, the expected h/e-flux periodicity is recovered once considering them at constant filling factor, demonstrating the Aharonov-Bohm interference origin of these oscillations.
Next, an investigation of the dependence of these resistance oscillations on the voltage measured accross the junctions enables us to evaluate the Thouless energy attached to the devices and, consequently, the QH edge states velocity along the NS interfaces.
Finally, we consider charging effect physics with the observation of Coulomb diamonds at the $\nu = 2$ quantum Hall plateau edges, a feature we ascribe to backscattering between opposite edge states through the compressible bulk.

5.1 h/e-flux periodic oscillations

So far, we have demonstrated that the observed supercurrent cannot tunnel via the insulating bulk in-between the electrodes or along parasitic edge channels (see Chapter 4 Section 4.1), elements that are consistent with the presence of a quantum Hall edge states mediated supercurrent.
Yet, the decisive signature of the chiral supercurrent remains the observation of h/e-flux periodic critical current oscillations (see Chapter 1 Section 1.2.1 for a detailed discussion), a feature which is the focus of the first part of this section.
In a second part, the presence of a coherent loop within our junctions is further strenghened via the observation of Aharonov-Bohm oscillations in the low bias resistance.

5.1.1 Switching current oscillations: the chiral supercurrent

5.1.1.1 Switching current oscillations in the V_g-B plane: magnetic field periodicity

We begin with a look back at the switching current oscillations mentioned in Chapter 4 Section 4.1, the data set in question being shown again in Figure 5.1.a, that is a map of the switching current I_s versus the back-gate voltage V_g and the magnetic field B for sample HV088 junction B (L x W = 140 x 177.5 nm^2). This device being one the smallest available, the magnetic field periodicity $\Delta B = h/eLW$ of I_s is accordingly expected to be one of the largest one, hence making the corresponding oscillations easier to resolve.

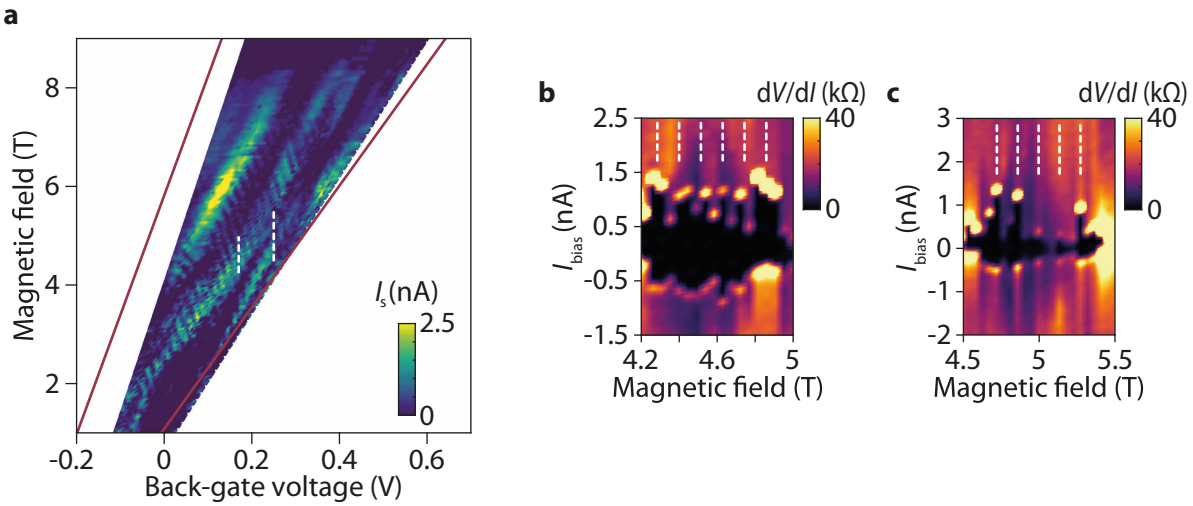

Figure 5.1: **Switching current oscillations accross the V_g-B. a)** Switching current I_s colormap versus both the back-gate voltage V_g and the magnetic field B obtained at T = 10 mK for narrow junction B (L x W = 140 x 177.5 nm^2) in sample HV088. Red lines indicate the $\nu = 2$ QH plateau's edges measured at $I_{bias} = 160$ nA. **b)** Colormap of the differential resistance dV/dI versus the magnetic field B and the current bias I_{bias} computed from the successive I/V characteristics done along the leftmost white dashed line in **(a)**, i.e. at V_g = 0.17 V. Periodicity of the overlying white comb is 114.8 mT, a value that falls within the window of magnetic field period values compatible with the $h/2e$-flux periodicity (i.e. from 63 mT to 122 mT, see Appendix B for uncertainty on the area estimation). **c)** Colormap of the differential resistance dV/dI versus the magnetic field B and the current bias I_{bias} computed from the successive I/V characteristics done along the rightmost white dashed line in **(a)**, i.e. at V_g = 0.25 V. Periodicity of the overlying white comb is 137.8 mT, a value that falls within the window of magnetic field period values compatible with the h/e-flux periodicity (125 mT to 243 mT).

To gain further insight, Figure 5.1.c shows a colormap of the differential resistance $\mathrm{d}V/\mathrm{d}I$ as a function of both B and I_{bias}, computed from the successive I/V characteristics taken along the rightmost white dashed line in Figure 5.1.a, i.e. at $V_{\text{g}} = 0.25$ V. Remarkably, successive maxima of the supercurrent, here color-coded in black, closely match the 137.8 mT-spaced vertical dashes of the overlying white comb. Taking into account the uncertainty in the assessment of the junction's area (see Appendix B), this value is compatible with a h/e-flux periodicity (the expected value being between 125 mT and 243 mT), hence agreeing with the chiral supercurrent occurence.
Yet, taking a second linecut along the leftmost white dashed line in Figure 5.1.a, that is at $V_{\text{g}} = 0.17$ V, yields switching current oscillations with a magnetic field periodicity of 114.8 mT (see Figure 5.1.b), which does not fall into the h/e-flux periodicity window. In fact, it appears that the latter value, still taking into account the uncertainty on the junction's area, is consistent with a $h/2e$-flux periodicity (the expected value being between 63 mT and 122 mT).
The preceeding discussion is a typical example of the difficulty of establishing a general conclusion regarding the flux periodicity of the switching current oscillations at fixed back-gate voltage, a point we will also come across when studying Aharonov-Bohm oscillations in the next (see Section 5.1.2.1).

5.1.1.2 Switching current oscillations in the ν-B plane: h/e-flux periodicity

Following the above-mentioned elements, we were led to reconsider the switching current oscillations within the ν-B plane, ν denoting the filling factor, instead of the V_{g}-B plane. Indeed, at constant filling factor, the area, hence the magnetic flux, encircled by the quantum Hall edge channels is constant, within a magnetic length $l_B = \sqrt{\hbar/eB}$ correction (see Section 5.1.2.2), which should make easier to analyse the oscillations flux-periodicity.

Figure 5.2.a shows the same switching current colormap as in Figure 5.1.a, but as a function of the filling factor ν[1] and the magnetic field. A similar back-gate voltage-to-filling factor conversion was applied to the switching current colormaps attached to the devices C (L x W = 140 x 177.5 nm^2) and D (L x W = 200 x 247 nm^2) in sample HV088, resulting in the colormaps shown in Figures 5.2.b and 5.2.c, respectively. Once this conversion had been carried out, we again considered switching current oscillations, this time at constant filling factor.

Figure 5.3.a shows a differential resistance colormap as a function of both the magnetic field and the current bias obtained for junction B (L x W = 140 x 177.5 nm^2) in sample HV088 at $\nu = 1.9$ (along the leftmost white dashed line in Figure 5.2.a).
Superconducting pockets, color-coded in black, co-exist with regular resistance oscillations (their origin being clarified in Section 5.1.2), a linecut of which being provided in Figure 5.3.b (purple curve, obtained at $I_{\text{bias}} =$ 3 nA). Remarkably, switching current also shows clear oscillations with $\Delta B \approx$ 236.2 mT from $B = 4.859$ T to $B = 6.88$ T (to be compared with the h/e-flux periodicity compatible window going from 125 mT to 243 mT), agreeing with the chiral supercurrent occurence.

To further highlight this behavior, the corresponding switching current plot is displayed in Figure 5.3.b (see blue curve). Strikingly, while superconducting pockets occurs at resistance minima from $B = 4.859$ T to $B =$ 5.502 T, a gradual shift of the switching current maximums with magnetic field is observed, ultimately resulting in switching current pockets matching resistance oscillations maximums around $B \approx$ 6.696 - 7.431 T, a feature

[1] The capacitor per unit area value as well as the position in gate-voltage of the Dirac point that were used to carry out the back-gate voltage-to-filling factor conversion have been carefully estimated using the procedure described in Appendix C.

that could be explained by the fact that the phase accumulated by CAESs may differ from that accumulated by electrons in the resistive state by an additional phase shift picked up because of Andreev reflections. Importantly, this finding disregard a switching current oscillatory behavior resulting from a trivial $R_N I_c$ product constancy modulation effect arising from the resistance oscillations.

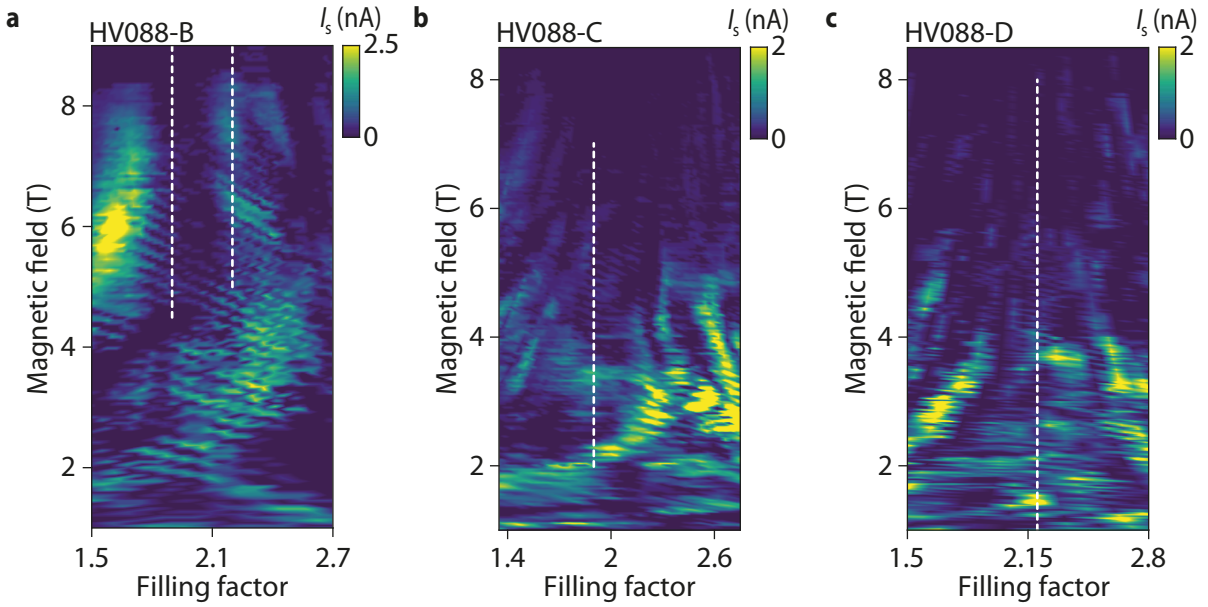

Figure 5.2: **Switching current oscillations accross the ν-B plane. a)** Switching current I_s colormap as a function of both the filling factor ν and the magnetic field B for junction B (L x W = 140 x 177.5 nm^2) in sample HV088 at T = 10 mK. The vertical white dashed lines indicate the points along which I/V characteristics were taken to generate the colormaps shown in Figures 5.3.a and 5.4.a,c. **b)** Similar map for the junction C (L x W = 170 x 210 nm^2) in sample HV088. The white dashed line indicates the region along which the Fourier transform shown in Figure 5.5.b was done. **c)** Similar map for the junction D (L x W = 200 x 247 nm^2) in sample HV088. The white dashed line indicates the region along the Fourier transform shown in Figure 5.5.c was done.

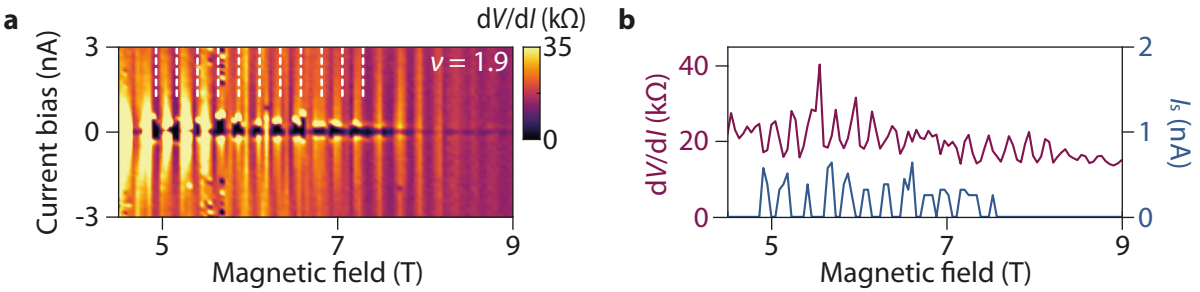

Figure 5.3: **Switching current oscillation at fixed filling factor a)** $\mathrm{d}V/\mathrm{d}I$ colormap versus magnetic field and current bias for sample HV088 narrow junction B (L x W = 140 x 177.5 nm^2) at ν = 1.9 and T = 10 mK. The white comb corresponds to a periodicity of 236.2 mT, in agreement with the expected h/e-flux periodicity (expected value between 125 mT and 243 mT). **b)** $\mathrm{d}V/\mathrm{d}I$ linecut obtained at I_{bias} = 3 nA within the same magnetic field range (purple curve). Blue curve shows the switching current attached to the superconducting pockets visible in **(a)**.

We also see that h/e-flux periodic supercurrent oscillations do not always fall to zero in-between the successive lobes.

An illustrative example is provided in Figure 5.4.c for sample HV088 junction F (L x W = 270 x 334 nm^2). The superconducting pockets (see blue curve in Figure 5.4.d), whose amplitude still exhibits h/e-flux periodic oscillations with $\Delta B \approx$ 53.3 mT (see white comb, the expected h/e-flux periodicity being between 40 mT and 54 mT), clearly shows a non-vanishing magnitude accross several oscillations.

Remarkably, this feature was anticipated in the model of Y. Alavirad *et al.* [30] dealing with chiral supercurrent (see Chapter 1 Section 1.2.2 discussion).
Though initially developed to treat spin-triplet supercurrent mediated by the ν = 1 spin polarized quantum Hall edge state in graphene [29], the model introduced by J. A. M. van Ostaay, A. R. Akhmerov and C. W. J. Beenakker also predicted a non-oscillating contribution to the supercurrent in addition to the oscillating one for the spin singlet case, that is our situation. In particular, the magnitude of the residual supercurrent was shown to depend on the ratio W/ξ_c, with $\xi_c = \hbar v_c/\Delta_0$, v_c being the drift velocity along a pristine edge in the limit of a sharp confining potential and Δ_0 the electrodes superconducting gap. Provided ξ_c is similar for each devices, this suggests that a non-vanishing switching current background becomes more likely as the junctions get wider. Note, however, that a non-zero supercurrent background was also observed in sample HV088 junction B (L x W = 140 x 177.5 nm^2), our smallest device (see Figures 5.4.a,b).

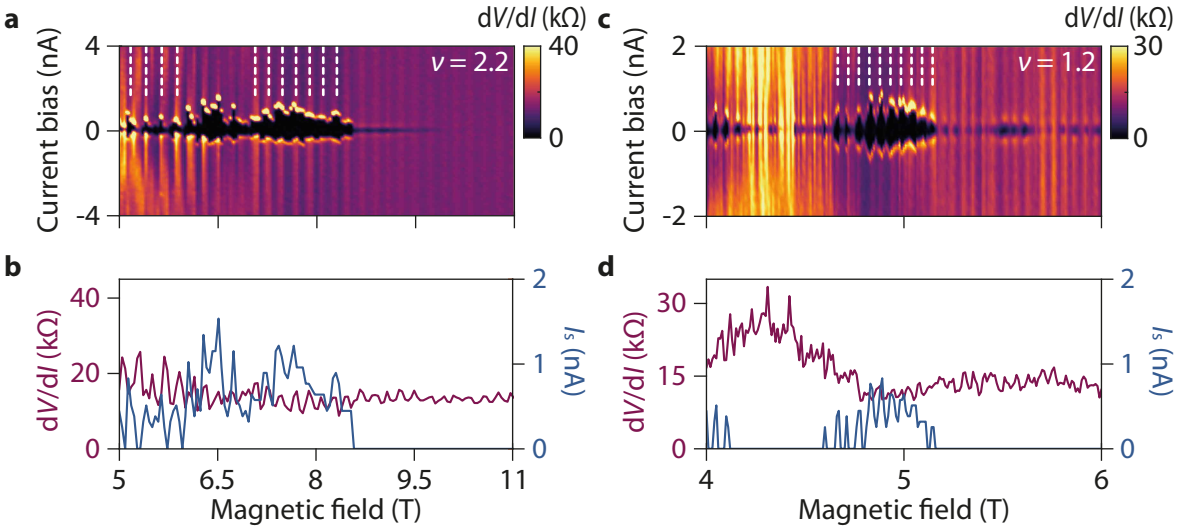

Figure 5.4: **Additional switching current oscillation patterns. a)** dV/dI colormap versus magnetic field and current bias for sample HV088 junction B (L x W = 140 x 177.5 nm^2) at ν = 2.2 and T = 10 mK. The left (resp. right) white comb indicates a magnetic field periodicity of 236.2 mT (resp. 206.7 mT) which is compatible with a h/e-flux periodicity (expected value between 125 mT and 243 mT). The period reduction stems from the area increase with magnetic field (see main text). **b)** dV/dI linecut obtained at I_{bias} = 3 nA within the same magnetic field range (purple curve). Blue curve shows the switching current attached to the superconducting pockets visible in **(a)**. **c)** dV/dI colormap versus magnetic field and current bias for sample HV088 junction F (L x W = 270 x 334 nm^2) at ν = 1.2 and T = 10 mK. The white comb corresponds to a periodicity of 53.3 mT (the expected h/e-flux periodicity is between 40 mT and 54 mT). **d)** dV/dI linecut obtained at I_{bias} = 3 nA within the same magnetic field range (purple curve). Blue curve shows the switching current attached to the superconducting pockets visible in **(c)**.

Finally, looking at Figures 5.4.a,c, we can also see that the amplitude of the superconducting pockets does not necessarily decrease as the magnetic field increases, a characteristic of the chiral supercurrent that was also anticipated by the theory of Y. Alavirad *et al.* (see the discussion in Chapter 1 Section 1.2.2).

In order to address the chiral supercurrent occurence in a more systematic way, a fast Fourier transform was performed on the switching current extracted accross the $\nu = 2$ plateau, as a function of the filling factor, for sample HV088 junction B (L x W = 140 x 177.5 nm^2) which resulted in the colormap shown in Figure 5.5.a. The latter provides a number of important insights:

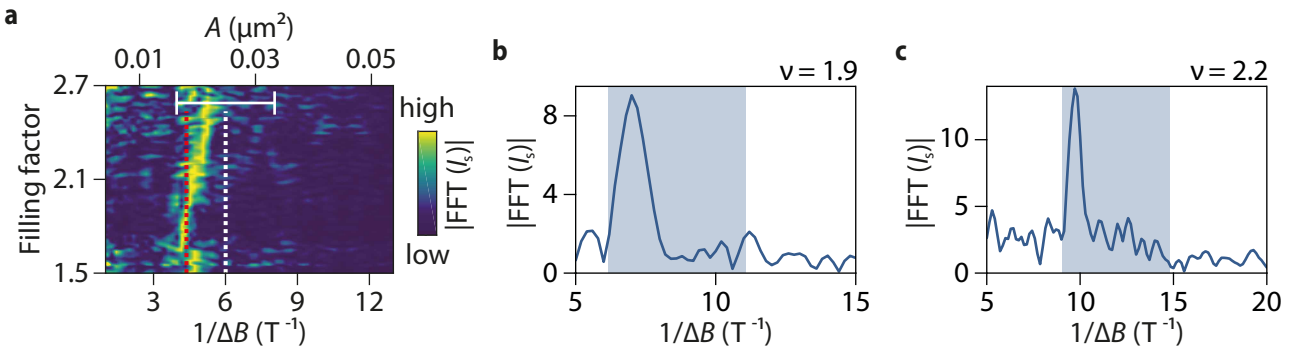

Figure 5.5: **h/e-flux periodic switching current oscillations. a)** Fourier transform of the switching current oscillations as a function of the frequency $1/\Delta B$, versus the filling factor ν for sample HV088 junction B (L x W = 140 x 177.5 nm^2). White vertical dashed line indicates the magnetic field frequency that would be expected for h/e-flux periodicity taking the junction's area. Red vertical dashed line indicates the magnetic field frequency that would be expected for h/e-flux periodicity taking the junction's area corrected by the magnetic length i.e. $A = (L - 2l_B) \times (W - 2l_B)$. In details, we took the magnetic length value corresponding to the middle of the magnetic field window over which the Fourier transform was done i.e. from 2 T to 7.5 T. The white horizontal line indicates the frequency window in which the h/e-flux periodicity FFT peak is expected, a finite frequency range that follows from the uncertainty on the estimation of the junction's area (see Appendix B). **b)** FFT transform of the switching current oscillations for sample HV088 junction C (L x W = 170 x 210 nm^2), at ν = 1.9, with a magnetic field window ranging from 2 T to 7 T (see white dashed line in 5.2.b). The blue rectangle is centered at the frequency attached to the h/e-flux periodicity deduced from the device dimensions, its width corresponds to the uncertainty of the area estimation. **c)** Similar analysis for sample HV088 junction D (L x W = 200 x 247 nm^2), at ν = 2.2, with a magnetic field window ranging from 1 T to 8 T (see white dashed line in 5.2.c). The blue rectangle is centered at the frequency attached to the h/e-flux periodicity deduced from the device dimensions, its width corresponds to the uncertainty of the area estimation.

- First, the Fourier transform signal peak falls within the frequency window corresponding to the h/e-flux periodicity (see the white error bar), the latter arising from the uncertainty on the junction's area estimate (see Appendix B). Together with the absence of any signal around $1/\Delta B \approx 12$ T^{-1}, i.e. the frequency that would be expected for a usual $h/2e$-flux periodic supercurrent, this analysis definitively establishes that the switching current observed within the $\nu = 2$ QH plateau is h/e-flux periodic, which is the chiral supercurrent hallmark.

- Having a closer look at the Fourier transform peak, we see that it does not perfectly match the frequency expected for the h/e-flux periodicity attached to the junction's geometric area, that is $1/\Delta B = 1/(h/eLW)$ (here denoted by the white dashed line). Instead, it has a better match with the vertical red line, which corresponds to the h/e-flux periodicity deduced from the geometric area of the junction corrected by the magnetic length $l_B = \sqrt{\hbar/eB}$, i.e. $\Delta B = h/eA$ with $A = (L - 2l_B) \times (W - 2l_B)$. This finding goes in line

with the typical spatial extension of the QH edge states wavefunctions, the latter being expected to relate to l_B. Note that we have also been able to resolve this area correction effect with the magnetic field using Fourier analysis on the low-bias resistance oscillations (see Section 5.1.2.2).

- Finally, a slight dispersion towards higher frequencies, i.e. lower magnetic field periodicities, is observed with the filling factor. To explain this observation, we refer the reader to the schematics shown in Figure 5.6.
  Typically, at fixed magnetic field, the area enclosed by the quantum Hall edge states is filling factor-dependent due to the Landau levels dispersion at the graphene edge. For instance, increasing the filling factor from ν to ν' is expected to generate an outward shift of the QH edge states. Consequently, the area delineated by the loop they form is expected to increase with filling factor, which necessarily implies a decrease of the magnetic field periodicity as what is observed here.

Note that a similar analysis could be applied on sample HV088 junctions C and D as shown in Figure 5.5.b and 5.5.c. In both cases, the Fourier signal peak lies within the h/e-flux periodicity frequency window (here denoted by the light blue squares), further supporting the presence of a chiral supercurrent within our devices.

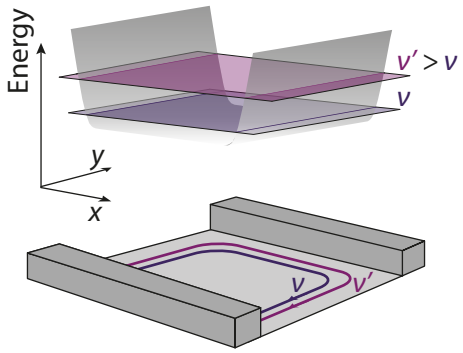

Figure 5.6: **Filling factor dependence of the area encircled by the QH edge states.** Schematic of Landau levels and edge states in the device for two different filling factors at a fixed magnetic field.

5.1.2 Resistive state oscillations at low bias

Resistance fringes patterns are also readily visible accross the $\nu = 2$ QH plateau, a finding to which is dedicated this second part.

5.1.2.1 Resistance fringes pattern in the V_g-B plane: magnetic field periodicity

Figure 5.7.a shows a differential resistance colormap as a function of both the magnetic field and gate voltage obtained at T = 10 mK using a current bias I_{bias} = 4 nA[2] for junction B (L x W = 140 x 177.5 nm^2) in sample HV088. The differential resistance value was numerically derived from I/V characteristics successively performed in a parametrized region within the $\nu = 2$ quantum Hall plateau in the V_g-B plan. The blue lines indicate plateau's edges positions obtained at I_{bias} = 160 nA.

[2]This current bias was selected on purpose to, on one side, preserve low bias features, and, on the other side, avoid supercurrent occurence in order to make easier oscillations visualization.

This $\mathrm{d}V/\mathrm{d}I$ colormap, taken above the switching current, presents a regular set of negatively-sloped resistance lines (color coded in yellow) whose typical value goes from 19.07 kΩ at $[V_g$ = 0.345 V, B = 6.145 T$]$ to 13.98 kΩ at $[V_g$ = 0.57 V, B = 11.06 T$]$, similar to that of the supercurrent (see e.g. Figures 5.1.a).

Such a regular fringes pattern is very reminiscent of the "pyjama maps" usually reported in quantum Hall interferometry experiments [138]. In that specific context, Aharonov-Bohm interferences result in a characteristic resistance striped pattern in the V_{SG}-B plane, V_{SG} being the voltage applied on a side-gate to modulate the area encircled by the edge states within the interferometer cavity, hence the Aharonov-Bohm phase[3].
Provided that quasiparticles going along the junction's perimeter preserve their phase coherence along both NS interfaces[4], a similar physics is likely to be at play within our device, as we will explain in the next sections.

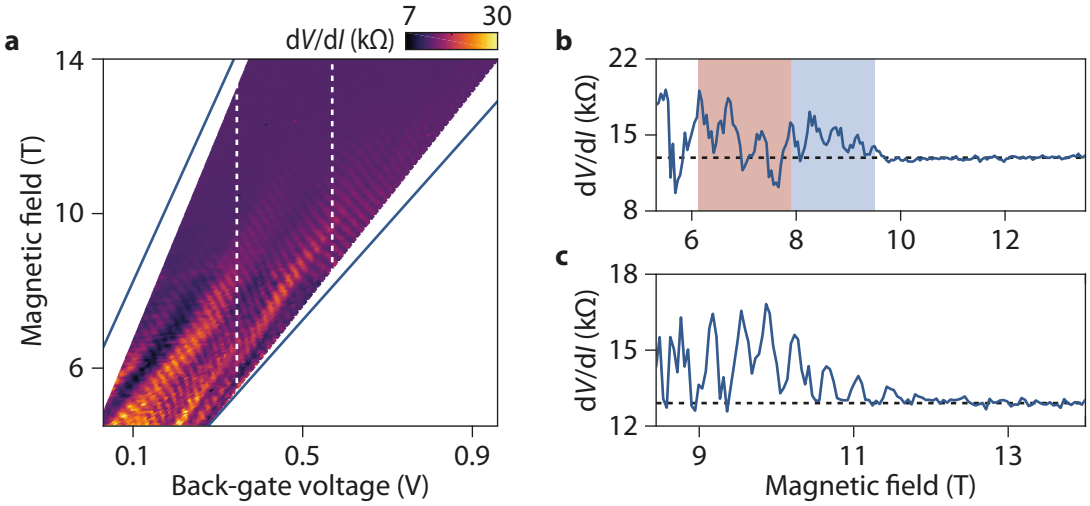

Figure 5.7: **Low bias resistance oscillations in the ν = 2 quantum Hall plateau. a)** $\mathrm{d}V/\mathrm{d}I$ colormap versus back-gate voltage and magnetic field for narrow junction B (L x W = 140 x 177.5 nm^2) in sample HV088 obtained with I_{bias} = 4 nA at T = 10 mK . Blue lines denote the ν = 2 quantum Hall plateau edges deduced from a measurement at I_{bias} = 160 nA. **b)** Cross-section of the differential resistance versus magnetic field taken at V_g = 0.345 V in the colormap shown in **(a)** (see leftmost vertical white dashed line). The light-orange and light-blue areas indicate magnetic field range with oscillations having different averaged periodicity. **c)** A similar cross-section taken at V_g = 0.57 V in colormap **(a)** (see rightmost vertical white dashed line).

To further investigate this oscillatory pattern, Figure 5.7.b provides a $\mathrm{d}V/\mathrm{d}I$ linecut versus magnetic field taken along a line at constant gate-voltage V_g = 0.345 V (see the leftmost white dashed line in Figure 5.7.a). Considering these oscillations from 6.145 T to 9.498 T yields an averaged periodicity ΔB = 475 mT.
Yet, the oscillation period reduces as the magnetic field increases, passing from $\Delta B \approx$ 572 mT in the low field range (indicated by the light orange layer in Figure 5.7.b) to $\Delta B \approx$ 402 mT in the high field region (denoted by the light blue layer in Figure 5.7.b).
Note that an even greater reduction in magnetic field periodicity is seen at both higher gate-voltage and magnetic field values as shown in Figure 5.7.c in which a similar $\mathrm{d}V/\mathrm{d}I$ cross-section, obtained at V_g = 0.57 V (see

[3] In our case, assuming we are at a given point in the $V_g - B$, a slight increase of the gate-voltage will increase the area S encircled by the QH edge states. Consequently, to maintain a constant flux $\phi = B \times S$, the magnetic field B has to decrease, hence presumably explaining the negative slope of the fringes pattern we observe.

[4] Note that quantum Hall edge states coherence length was estimated to be about 10 µm at B = 14 T and T = 20 mK [32], which suggests that dephasing effects most probably arise at the NS interfaces.

rightmost white dashed line in Figure 5.7.a), shows a periodicity of about 376 mT between B = 9.177 T and B = 11.43 T. Overall, the reported periodicities systematically exceeds 166.4 mT, that is the h/e-flux periodicity one would expect for a pattern arising from Aharonov-Bohm interferences, and is not consistent either with 83.2 mT, i.e. the $h/2e$-flux periodicity.
Similar fringes patterns within the $\nu = 2$ quantum Hall plateau were also observed in 5 other devices (see Figures 5.8.a,b and c in which data attached to the 3 other smallest devices, i.e. those for which these oscillations can be distinguished most easily, are shown), hence asserting the robustness of this effect.

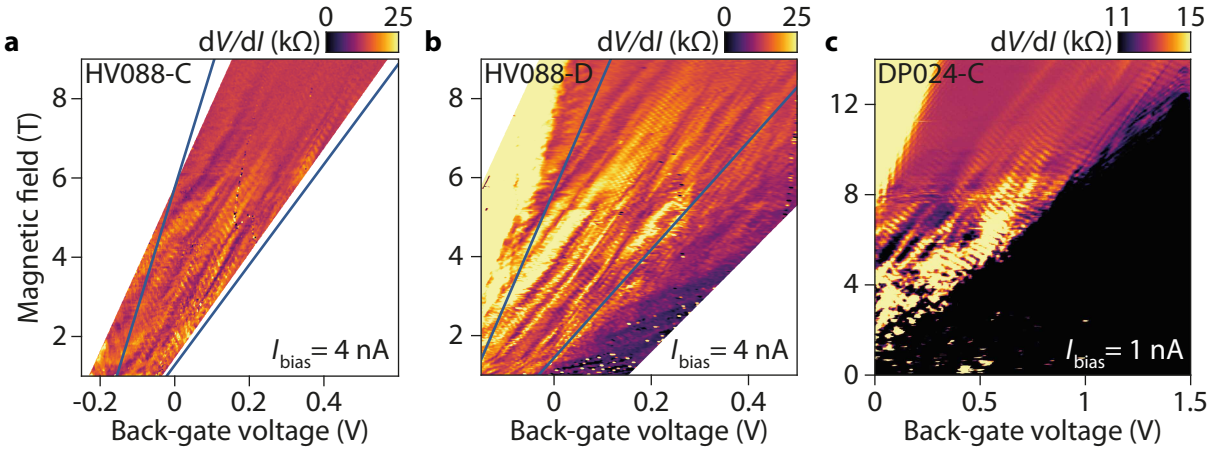

Figure 5.8: **Low bias resistance oscillations in the ν = 2 quantum Hall plateau for additional devices a)** $\mathrm{d}V/\mathrm{d}I$ colormap versus back-gate voltage and magnetic field for junction C (L x W = 170 x 210 nm^2) in sample HV088 obtained with I_{bias} = 4 nA at T = 10 mK . The blue lines denote the ν = 2 quantum Hall plateau edges deduced from a measurement at I_{bias} = 160 nA. **b)** Similar measurements for junction D (L x W = 200 x 247 nm^2) in sample HV088. **c)** $\mathrm{d}V/\mathrm{d}I$ colormap versus back-gate voltage and magnetic field for junction C (L x W = 170 x 125 nm^2) in sample DP024 measured at T = 11 mK with a lock-in using a current bias I_{bias} = 1 nA. The purplish area corresponds to the ν = 2 quantum Hall plateau.

Looking at the corresponding magnetic field periodicities, whose typical values are summarized in Tables 5.1 and 5.2, the periodicities of the patterns observed in the smallest device of each sample (device C in sample HV088, device C in sample DP024) systematically deviate from the h/e-flux periodicity, .

Device	L [nm]	W [nm]	h/e-flux periodicity [mT]	ΔB [mT]	Expected ΔB for h/e-flux periodicity [mT]
C	170	210	115.8	204 - 279	92 to 153
D	200	247	83.7	75 - 83	69 to 109
F	270	334	45.8	48 - 63	40 to 54

Table 5.1: **HV088** $\nu = 2$ fringe patterns typical periodicities in the $V_{\mathrm{g}} - B$ plan.

Device	L [nm]	W [nm]	h/e-flux periodicity [mT]	ΔB [mT]	Expected ΔB for h/e-flux periodicity [mT]
C	170	125	195	352 - 405	143 to 318
D	200	125	165	201 - 269	125 to 243

Table 5.2: **DP024** $\nu = 2$ fringe patterns typical periodicities in the $V_{\mathrm{g}} - B$ plan.

Taken together, these last elements further establish the inherent difficulty to relate the magnetic field period

of these oscillations patterns to the flux quantum when considered within the V_g-B plane for small devices.

5.1.2.2 Resistance oscillations in the ν-B plane

Similarly to the switching current case, we now reconsider the ν = 2 quantum Hall plateau resistance oscillations (see Section 5.1.2.1), this time in the ν - B plane.

Figure 5.9.a shows a differential resistance $\mathrm{d}V/\mathrm{d}I$ colormap versus both the magnetic field and the filling factor, whose value was computed using the capacitance estimation done in Appendix C, for sample HV088 junction B (L x W = 140 x 177.5 nm^2) using a current bias $I_{\text{bias}} = 4$ nA, i.e. above the switching current, at $T =$ 10 mK (the same set of data used for Figure 5.7.a in Section 5.1.2.1). For the sake of completness, we provide similar data for sample HV088 junctions C and D (see Figures 5.9.b and 5.9.c), as well as for sample DP024 junctions C and D (see Figures 5.9.d and 5.9.e), i.e. the smallest junctions for which resistance oscillations with magnetic field are most easily visible.

In order to properly extract the latter periodicities in magnetic field, Fourier transforms at fixed filling factor were systematically applied[5], leading to the plots shown in Figure 5.10.a. We add on this figure colored rectangles that correspond to the h/e-flux periodicity, and hatched rectangles that correspond to the $h/2e$-flux periodicity. The finite width of these rectangles stem from the uncertainty on the estimation of the junctions areas (see Appendix B for detail). We clearly see that the Fourier peaks, for all junctions, are compatible with the h/e-flux periodicity. Note that similar results, shown in Figure 5.10.b, were obtained for sample DP024 junctions. This finding, observed in several devices, supports Aharonov-Bohm interferences as being the origin of the observed resistance fringes patterns.

Going into more details, Fourier analysis also allows for revealing a slight magnetic field periodicity variation with the filling factor as portrayed in Figure 5.11.a. The latter was obtained running Fourier transforms at successive filling factor values for sample HV088 junction B (L x W = 140 x 177.5 nm^2) from $\nu = 1.5$ to $\nu =$ 2.7 between $B = 4$ T and $B = 10$ T. As mentioned in Section 5.1.1.2, at fixed magnetic field, area encircled by quantum Hall edge states is filling factor dependent due to the Landau levels dispersion at the edge. In Figure 5.11.a, white and blue vertical dashed lines indicate the h/e-magnetic field periodicity we expect taking

[5] Details of the Fourier transform analysis shown in Figure 5.10.a:

- For sample HV088 junctions B, the FFT signal was computed using the differential resistance at $I_{\text{bias}} = 3$ nA (after a background substraction), at $\nu = 2.1135$, from $B = 4$ T to $B = 10$ T. Blackman windowing was applied for the FFT computation.
- For sample HV088 junctions C, the FFT signal was computed using the differential resistance at $I_{\text{bias}} = 5$ nA (after a background substraction), at $\nu = 2.3068$, from $B = 2.5$ T to $B = 7$ T. Blackman windowing was applied for the FFT computation.
- For sample HV088 junctions D, the FFT signal was computed using the differential resistance at $I_{\text{bias}} = 6$ nA (after a background substraction), at $\nu = 1.9$, from $B = 3$ T to $B = 7$ T. Blackman windowing was applied for the FFT computation.
- For sample HV088 junction E, FFT signal was computed from the resistance average from -0.384 nA to 0.256 nA (no background substraction), at $\nu = 2.5$, from $B = 1$ T to $B = 5$ T. A Blackman windowing was applied for the FFT computation.
- For sample HV088 junction F, FFT signal was computed from the resistance average from -0.256 nA to 0.256 nA (no background substraction), at $\nu = 1.62$, from $B = 3$ T to $B = 6$ T. A Blackman windowing was applied for the FFT computation.
- For sample DP024 junction C, FFT signal was computed from the resistance measured at 0 nA (after a background substraction), at $\nu = 3$, from $B = 4$ T to $B = 10$ T. A Blackman windowing was applied for the FFT computation.
- For sample DP024 junction D, FFT signal was computed from the resistance measured at 0 nA (after a background substraction), at $\nu = 1.4$, from $B = 6$ T to $B = 14$ T. A Blackman windowing was applied for the FFT computation.

respectively the junction's area (rightmost line) and the area defined by an edge state located at $l_{B=7\,\mathrm{T}} \approx 9.7$ nm[6] from the junction edges (leftmost line). The frequency window compatible with the h/e-flux periodicity (see white horizontal line) results from the uncertainty on the estimation of the junction area.

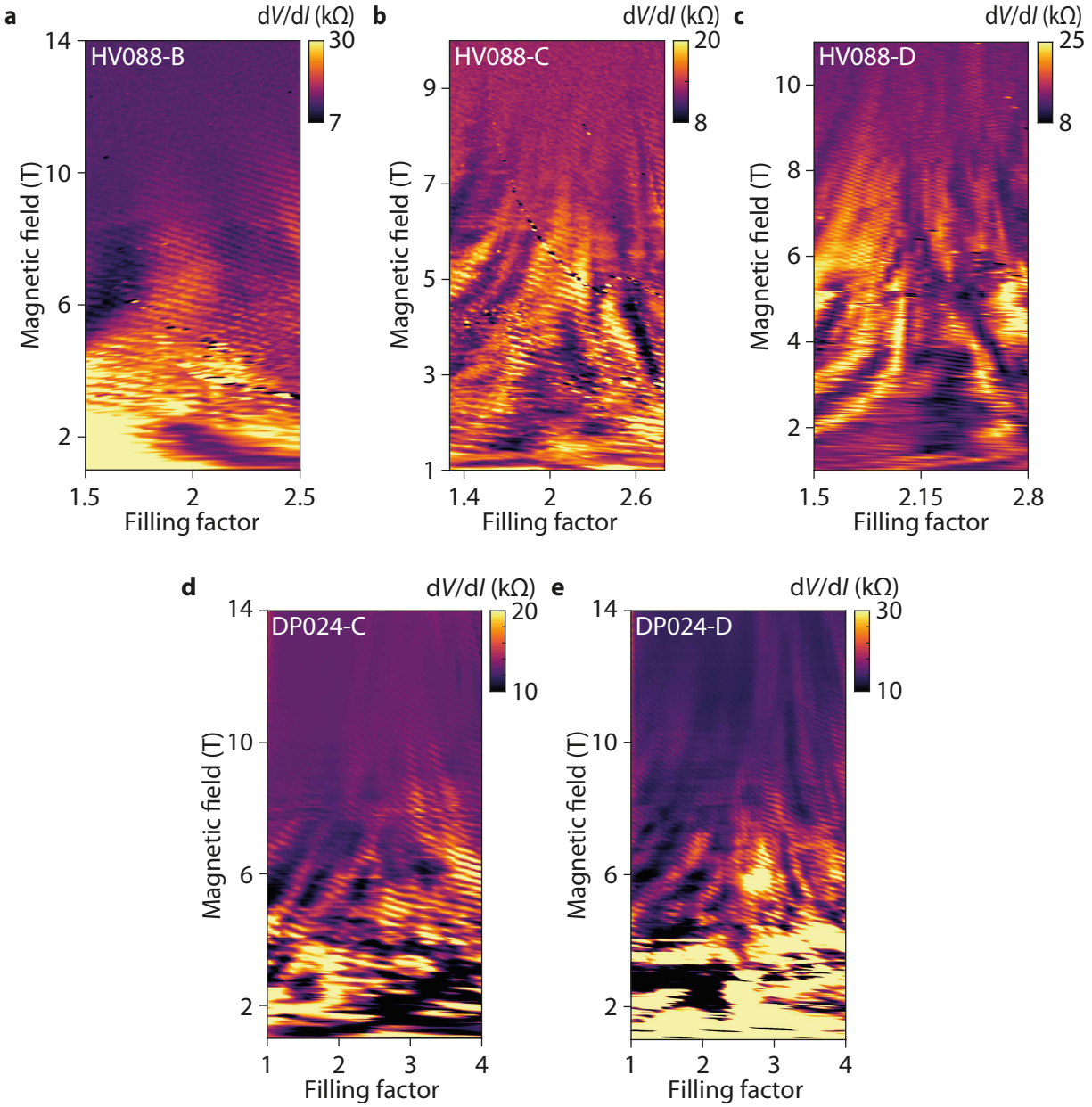

Figure 5.9: **Resistance oscillations in the ν - B plane. a)** $\mathrm{d}V/\mathrm{d}I$ colormap versus filling factor and magnetic field obtained for sample HV088 narrow junction B (L x W = 140 x 177.5 nm^2) with $I_{\mathrm{bias}} = 4$ nA at $T = 10$ mK. **b)** Similar measurement for sample HV088 narrow junction C (L x W = 170 x 210 nm^2). **c)** Similar measurement for sample HV088 narrow junction D (L x W = 200 x 247 nm^2). **d)** $\mathrm{d}V/\mathrm{d}I$ colormap as a function of the filling factor ν and the magnetic field for junction C (L x W = 170 x 125 nm^2) in sample DP024 measured at $T = 11$ mK with a lock-in using a current bias I_{bias} = 1 nA. **d)** Similar measurement for junction D (L x W = 200 x 125 nm^2) in sample DP024.

[6] As the magnetic field range over which the FFT was done goes from B = 4 T to B = 10 T, we indicate the magnetic length corresponding to the intermediate magnetic field, i.e. $B = 7$ T.

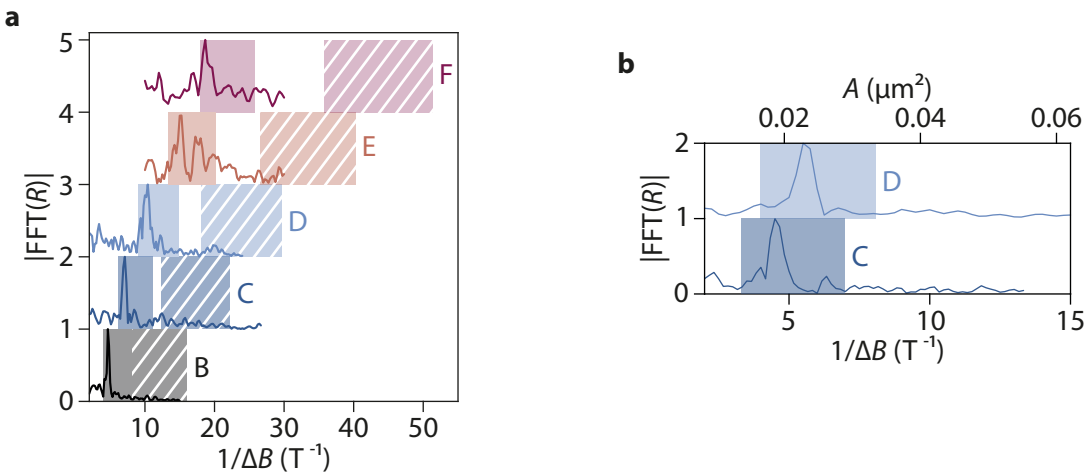

Figure 5.10: **h/e-flux periodicity for resistance oscillations at fixed filling factor. a)** Normalized FFT amplitude versus the frequency in magnetic field for narrow junctions in sample HV088. See footnote (5) for detail of the FFT procedure. Each plain rectangle is centered around the frequency expected from the corresponding junction's area. Widths of these rectangles correspond to the uncertainty on the estimation of the junctions areas (See Appendix B for details). Dashed rectangles on the right side are centered around the frequency that would be expected for the $h/2e$-flux periodicity. **b)** Similar analysis for sample DP024 junctions C and D. The upper axis indicates the area $A = (h/e) \times (1/\Delta B)$.

Remarkably, the dispersion of the magnetic field periodicity with filling factor lies within this frequency range. Moreover, the Fourier signal does not exhibit any signal around $1/\Delta B \approx 12$ T^{-1}, that is the frequency corresponding to the $h/2e$-flux periodicity, which is consistent with the Fourier transforms shown in Figure 5.10.a. Note that similar results were obtained for sample HV088 Josephson junctions C and D as shown in Figures 5.11.b. Note that for the smallest junction on which this analysis was carried out (see Figure 5.11.a), the dispersion of the resistance oscillations frequency with ν enables us to estimate an area variation of 4.5 x 10^{-3} μm^2, which corresponds to a QH edge channel displacement of 7 nm from the edge.

Interestingly, when looking back at the low bias resistance map shown in Figure 5.9.a, a slight decrease in the oscillation period with a magnetic field increase can be distinguished, an observation supported by a Fourier analysis shown in Figure 5.12.a. The latter was done at $\nu = 1.9$ in a magnetic field window of 3 T sliding from 3 T to 11 T.
Quite revealingly, the dispersion of the FFT signal peak perfectly matches the frequency dispersion that is expected for the h/e-flux periodicity provided the junction area decreases with the magnetic field as $A = (L - 2l_B) \times (W - 2l_B)$, with $l_B = \sqrt{\hbar/eB}$ the magnetic length. This area correction corresponds to the shrinkage of the gaussian wavefunction of the zeroth Landau level whose spatial extent scales as l_B [2] (see 5.12.b).
Resolving such a l_B shrinkage (see schematic in Figure 5.12.b) stems from our device smallness, which is about 40 times smaller than typical micrometer-wide quantum Hall Fabry-Perot interferometers cavities where such an effect has negligible influence on the period of the Aharonov-Bohm oscillations[7].

[7]Typically, at $B = 1$ T, the magnetic length-corrected area of a micrometer-wide square-shaped QH Fabry-Perot interferometer cavity varies by only 5% with respect to the geometric area.

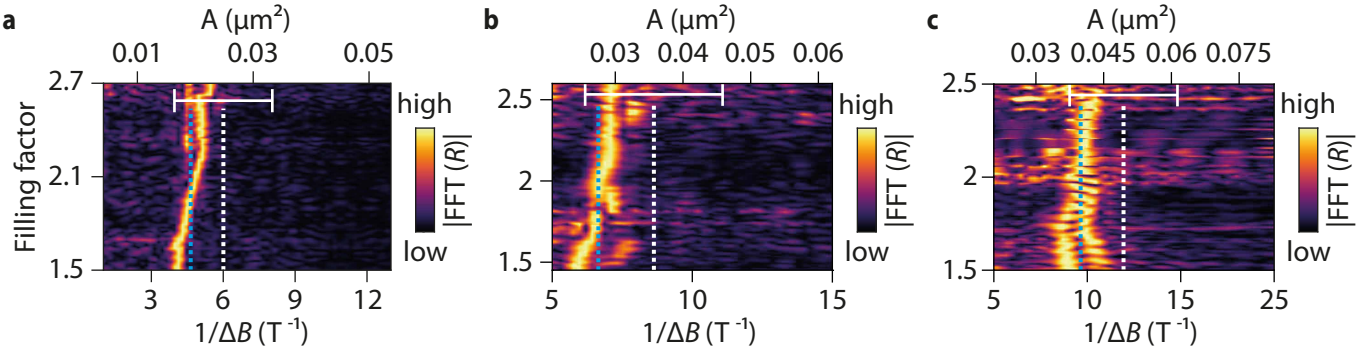

Figure 5.11: **Resistance oscillations frequency dependence on ν. a)** Normalized Fourier transform of the resistance oscillations at $I_{\text{bias}} = 3$ nA versus the filling factor ν for sample HV088 junction B (L x W = 140 x 177.5 nm^2). White vertical dashed line indicates the magnetic field frequency that would be expected for h/e-flux periodicity taking the junction's area. Blue vertical dashed line indicates the magnetic field frequency that would be expected for h/e-flux periodicity taking the junction's area corrected by the magnetic length i.e. $A = (L - 2l_B) \times (W - 2l_B)$. In details, we took the magnetic length value corresponding to the middle of the magnetic field window over which the Fourier transform was done (see footnote (5) for detail). The white horizontal line indicates the frequency window in which the h/e-flux periodicity Fourier peak is expected, a finite frequency range that follows from the uncertainty on the estimation of the junction's area (see Appendix B). The Fourier transform peak slightly disperses with the filling factor. **b),c)** Similar analysis for sample HV088 junctions C (L x W = 170 x 210 nm^2) and D (L x W = 200 x 247 nm^2).

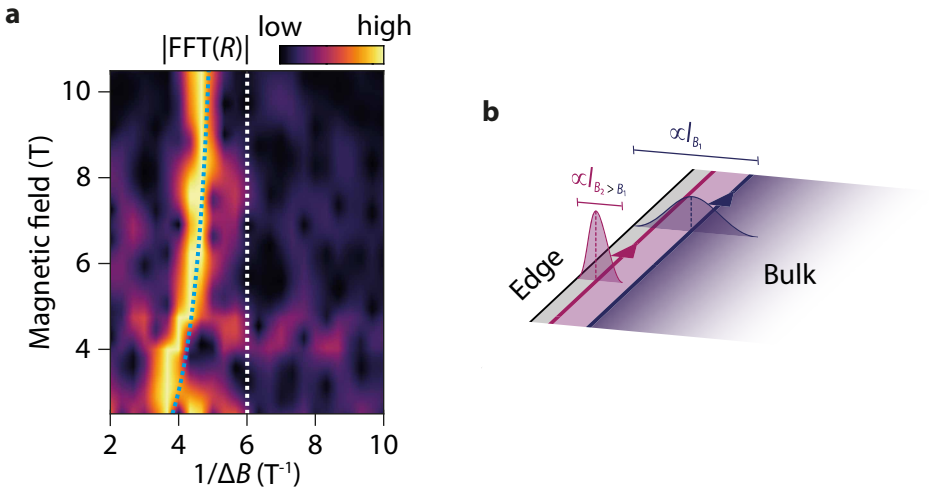

Figure 5.12: **Resistance oscillations frequency dependence on B at fixed ν. a)** Fourier transform of the resistance measured with current bias $I_{\text{bias}} = 3$ nA at $\nu = 1.9$ for sample HV088 junction B (L x W = 140 x 177.5 nm^2). The white dashed line indicates the frequency expected for h/e-flux periodic resistance oscillations taking the junction geometric area i.e. $A = L \times W$. The blue dashed line indicates the frequency expected for h/e-flux periodic resistance oscillations taking into account the effect of QH edge states wavefunctions shrinkage as the magnetic field increases i.e. $A = (L - 2l_B) \times (W - 2l_B)$, with $l_B = \sqrt{\hbar/eB}$ the magnetic length. This last curve perfectly matches the dispersion of the Fourier signal peak. **b)** Schematics of the QH edge states wavefunction shrinkage mechanism. At fixed filling factor ν, the higher the magnetic field is, the smaller the spatial extension of the quantum Hall edge states wavefunction is.

5.2 Checkerboard-like patterns

In order to further address interference physics within our devices, we now investigate the non-equilibrium properties of the h/e-flux periodic resistance oscillations at finite bias.

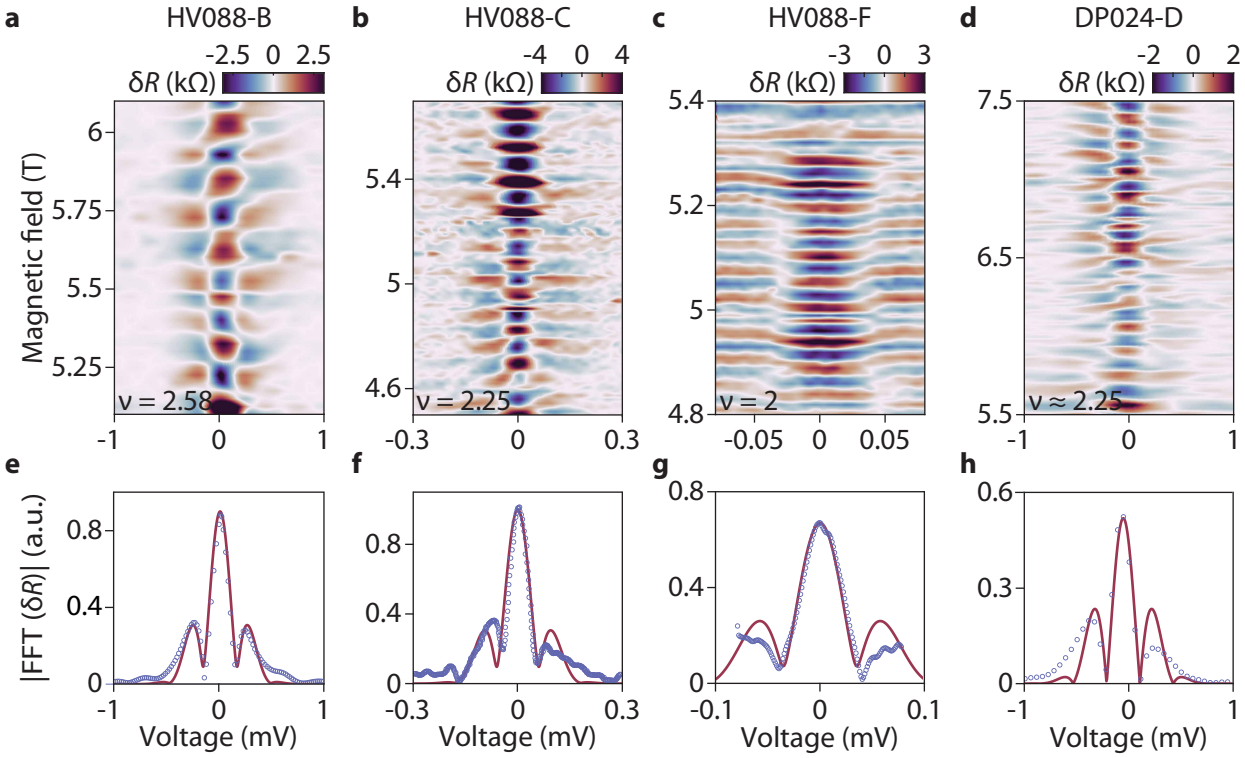

Figure 5.13: **Checkerboard-like patterns. a)** Differential resistance colormap (after background substraction) as a function of both the magnetic field and the voltage measured accross the junction B (L x W = 140 x 177.5 nm^2) in sample HV088 at T = 10 mK and $\nu = 2.58$. **b)** Similar kind of differential resistance colormap for junction C (L x W = 170 x 210 nm^2) in sample HV088 at $\nu = 2.25$. **c)** Similar kind of differential resistance colormap for junction F (L x W = 270 x 334 nm^2) in sample HV088 at $\nu = 2$. **d)** Similar kind of differential resistance colormap for junction D (L x W = 200 x 125 nm^2) in sample DP024 at $\nu \approx 2.25$ and $T \approx 20$ mK. **e,f,g,h)** Each of these figures gives the amplitude of the Fourier transform of the checkerboard pattern just above, taken at the checkerboard pattern oscillation's frequency (pale blue points). The purple curve is a fit to the data obtained by applying the same procedure as in [32]. In detail, the values of the parameters used for the fit (see equation (5.1)), i.e. the Thouless energy E_{Th}, a bias assymetry parameter x, and the width of the Gaussian envelope V_0 are: 640 μeV, 0.02 and 320 μV for **(e)**, 240 μeV, 0.02 and 97 μV for **(f)**, 140 μeV, 0.02 and 65 μV for **(g)**, 640 μeV, 0 and 330 μV for **(h)**.

Figure 5.13.a displays resistance oscillations - following a background substraction - as a function of both the magnetic field and the measured voltage accross the sample HV088 narrow junction B (L x W = 140 x 177.5 nm^2) at fixed filling factor $\nu = 2.58$.

Within the magnetic field range under consideration, the successive zero-voltage centered resistance maximums, that is the h/e-flux periodic oscillations we report on previously, display a significant shift in magnetic field as the voltage departs from zero, an effect also observed on three other devices (see Figures 5.13.b,c and d). Such voltage-dependent oscillatory patterns strongly remind the checkerboard-like features usually reported in quantum Hall interferometry experiments [32; 139].

In that specific context, source-to-drain voltage drop V confers an extra phase term, defined as $\delta\phi_{\text{dyn}} = \delta\epsilon/E_{\text{Th}} = P\delta\epsilon/\hbar v$ with $\delta\epsilon$ an energy increment with respect to the Fermi level, to the Aharonov-Bohm (AB) phase picked by quasiparticles circulating with a velocity v along the perimeter P of the interferometer's cavity [140]. Accordingly, Aharonov-Bohm resistance oscillations experience a shift in magnetic field when changing the applied bias that produces characteristic checkerboard-like patterns in the B-V plane which, in QH Fabry-Perot interferometers, approximate to resistance oscillations $\delta R \propto \cos(2\phi/\phi_0)\cos(2\pi eV/E_{\text{Th}})$ with $2\pi\phi/\phi_0$ the Aharonov-Bohm phase. Interestingly, applying a Fourier transform over such a checkerboard pattern can provide a direct estimate of the Thouless energy E_{Th} associated to charge carriers flowing along the interferometer's cavity loop [32; 139].

Assuming that partial transfer of electrons to superconducting electrodes along NS interfaces is similar to the partial transmission of electrons accross the quantum point contacts used to define a quantum Hall Fabry-Perot interferometer cavity, we applied the same approach to analyse our checkerboard patterns in an attempt to extract the corresponding Thouless energy.

Typically, successive Fourier transforms at each voltage bias are carried out to Figure 5.13.a. In the frequency space, the resulting Fourier peak leads to 3 lobes located around the frequency attached to the checkerboard pattern. Finally, a linecut of the Fourier signal at this frequency yields the dotted curve shown in Figure 5.13.e. Following [32], a fit $A(V)$ to the latter's amplitude can be done (see purple curve in 5.13.e) with the following equation:

$$A(V) \propto \sqrt{\cos\left(2\pi\frac{eV}{E_{\text{Th}}}\right) + 4x^2\sin^2\left(2\pi\frac{eV}{E_{\text{Th}}}\right)}\exp\left(-\frac{V^2}{2V_0}\right) \tag{5.1}$$

with x a parameter translating the asymmetry in the voltage drop applied to the device[8] and V_0 the width of the corresponding Gaussian envelope. In the QH interferometers context, such a decay of the oscillations amplitude with the voltage was ascribed to electronic noise-induced fluctuations of the phase attached to the interfering electrons [141].
Applying a similar approach to Figures 5.13.b-f, 5.13.c-g and 5.13.d-h allows us to estimate the corresponding Thouless energies E_{Th} (see Table 5.3 (resp. Table 5.4) for sample HV088 (resp. DP024)), the latter typically corresponding to the distance between the maxima of the two side-lobes of the Fourier signal.

As a reminder, Thouless energy for quantum Hall Josephson junctions is defined as $E_{\text{Th}} = h/(L/v_{\text{QH}} + W/v_{\text{SC}})$ which, due to the typical difference of an order of magnitude between the QH edge states velocity along the pristine edges v_{QH} and along the NS interfaces v_{SC}, approximates to $E_{\text{Th}} \approx hv_{\text{SC}}/W$, with W the NS interfaces length (see Chapter 1 Section 1.2.2). Consequently, a fit of E_{Th} versus $1/W$ enables us to infer a value for v_{SC} of about 2.1 $\pm$ 0.5 x 10^4 m/s (see Figure 5.14[9]), that is an order of magnitude smaller than typical values for

[8] The above-mentioned approximate for δR is valid only provided the voltage drop accross the device is symmetric, i.e. if the source (resp. drain) has a voltage $+V/2$ (resp. $-V/2$). Yet, in practice, the bias is applied only to the source electrode, resulting in an assymetric voltage drop accross the device, a parameter to which are sensitive the electrons involved in this interference mechanism.

[9] In details, cherckerboard patterns used to extract these points were obtained with:

- Sample HV088 device B: $\nu = 1.8$, 2.4, 2.55 and 2.575, with B ranging from 5 T to 6.2 T.
- Sample HV088 device C: $\nu = 1.8$, 2, 2.3 and 2.5, with B ranging from 4.5 T to 5.8 T.
- Sample HV088 device F: $\nu = 2$, 2.27, 2.53 and 2.6, with B ranging from 4 T to 5 T.
- Sample DP024 device D: $\nu = 2.1$ and 2.25, with B ranging from 5.5 T to 7.5 T.

the quantum Hall edge states velocity along graphene pristine edges, i.e. $v_{QH} = 1.4$ x 10^5 m/s at $B = 14$ T[10]. Quite remarkably, the value of v_{SC} extracted from the measured Thouless energies is in relatively good agreement with 6 x 10^4 m/s, that is the theoretical value one would expect[11].

To allow for comparison, Tables 5.3 and 5.4 also provide the Thouless energy values for a QH Fabry-Perot interferometer cavity of similar size, i.e. in which no Andreev reflections take place, with $E_{Th,n} = hv_{QH}/(L+W)$[12]. Beyond the estimation of v_{SC}, the discrepancy between E_{Th} and $E_{Th,n}$ clearly establishes that QH edge states velocity renormalization is at play within our devices.

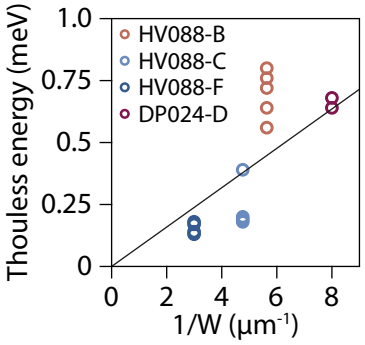

Figure 5.14: **Extraction of the QH edge states velocity along the NS interfaces.** Thouless energy values extracted from checkerboard patterns for various devices versus $1/W$, with W the NS interfaces lengths. A fit to these points enables us to estimate $v_{SC} = 2.1 \pm 0.5$ x 10^4 m/s.

Note that v_{QH} has been shown to vary with magnetic field as $1/B$ in AlGaAs/GaAs-based heterostructures [34; 35]. For graphene, apart from the above-mentioned estimate at $B = 14$ T, we found only one other value in the literature, with $v_{QH} \approx 2$ x 10^5 m/s around $B \approx 8$ T for the $\nu = 2$ QH edge states [139]. Importantly, this implies that the actual value of $E_{Th,n}$ within the magnetic field ranges under consideration - typically between 4 T and 7.5 T - is even larger than our estimation, the latter being based on the value of v_{QH} at $B = 14$ T.

Device	L [nm]	W [nm]	B-field window	E_{Th} [μeV]	$E_{Th,n}$ at $B = 14$ T [μeV]
B	140	177.5	5 - 6.2	640	1884
C	170	210	4.5 - 5.8	240	1524
F	270	334	4 - 5	140	959

Table 5.3: **Thouless energies** extracted from the checkerboard patterns obtained for sample HV088 junctions B, C and F. E_{Th} (resp. $E_{Th,n}$) corresponds to the Thouless energy extracted from the checkerboard patterns (resp. computed for a quantum Hall interferometer cavity having similar dimensions than the corresponding Josephson junction).

[10] A value deduced from the Aharonov-Bohm interferences smearing with temperature observed in the C. Déprez interferometers [32].

[11] Using the equation (1.52) in Chapter 1 Section 1.2.2, with the graphene Fermi velocity $v_n = 10^6$ m/s, $q = 0.3$ (obtained taking a transparency of 0.5), a superconducting gap of 820 μeV (i.e. an estimate of the superconducting gap at $B = 5$ T) and $\hbar\omega_c = 81$ meV, the cyclotron gap between the N = 0 and N = ± 1 Landau levels in graphene at $B = 5$ T.

[12] As a reminder, for the quantum Hall Fabry-Perot interferometers case, the Thouless energy relates to the distance separating the two quantum point contacts defining the Fabry-Perot cavity, that is half of the latter's perimeter.

Device	L [nm]	W [nm]	B-field window	E_{Th} [μeV]	$E_{\text{Th,n}}$ at $B = 14$ T [μeV]
D	200	125	5.5 - 7.5	640	1782

Table 5.4: **Thouless energies** extracted from the checkerboard patterns obtained for sample DP024 junctions D. E_{Th} (resp. $E_{\text{Th,n}}$) corresponds to the Thouless energy extracted from the checkerboard patterns (resp. computed for a quantum Hall interferometer cavity having similar dimensions than the corresponding Josephson junction). The checkerboard pattern under consideration was obtained at $\nu \approx 2.25$.

Such an influence of the QH edge states velocity renormalization along the NS interfaces on the Thouless energy is further strenghened looking back at checkerboard patterns around $B \approx 12.5$ T, that is the upper critical field of the junction's electrode[13] (see Figure 5.15.a).

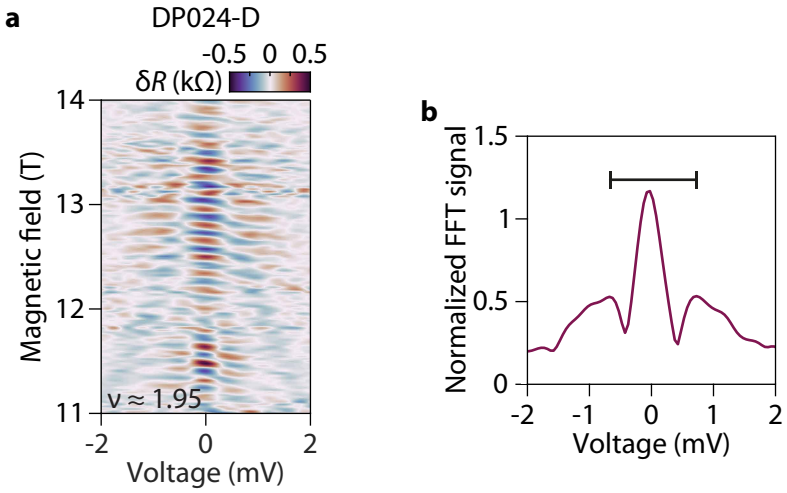

Figure 5.15: **Checkerboard pattern beyond $H_{c,2}$.** Differential resistance colormap as a function of both the magnetic field and the voltage measured accross the narrow junction D (L x W = 200 x 125 nm^2) in sample DP024 at T = 20 mK and $\nu \approx 1.95$. A background consisting in a sliding-average over 20 points in magnetic field was substracted to the initial signal. **b)** Normalized FFT signal of the map shown in **(a)** over a magnetic field window ranging from 12 T to 14 T. The voltage difference between side-lobes maxima is 1.4 meV (see the black horinzontal line).

Qualitatively, the checkerboard pattern lobes are wider, indicative of a Thouless energy increase. Applying a Fourier transform around the corresponding magnetic field range yields a Thouless energy of about 1.4 meV (see purple curve in Figure 5.15.b), in good agreement with $E_{\text{Th,n}} = hv_{\text{QH}}/(L+W)$ = 1.782 meV at $B = 14$ T, that is the Thouless energy one would expect for a device of similar size without any Andreev reflection-related QH edge states velocity renormalization.
This shows that some normal electrons still form a coherent-loop within the junction, thus allowing for interference signatures to be observed beyond the electrodes upper critical field.

5.3 Coulomb diamonds in the quantum Hall regime

So far, analogy with quantum Hall Fabry-Perot interferometry in describing our features has proven to successfully capture, at least qualitatively, the physics at play within our junctions. Taking this equivalence further,

[13] The latter was characterized in a dedicated measurement, see Appendix A.

the question then naturally arises to what extent Coulomb interactions, namely charging effects, influence our results.

This consideration appears particularly acute in our case with typical device size of 150 x 150 nm^2, that is about 40 times smaller than interferometer devices in which charging effects were demonstrated to strongly alter interference physics [142]. This regime, termed "Coulomb-dominated" in the next, translates as characteristic positively-sloped resistance stripes pattern in the $V_{sd} - B$ plan[14] of quantum Hall Fabry-Perot interferometers, a bias study of which yielding Coulomb diamonds [35].

In the course of our measurements on sample DP024 junctions, negatively sloped h/e-flux periodic resistance oscillations were observed to co-exist with another set of positively sloped resistance oscillations located at the $\nu = 2$ plateau's edges in the V_g-B plane, a typical example being shown in Figure 5.16 for junction C (L x W = 170 x 125 nm^2).

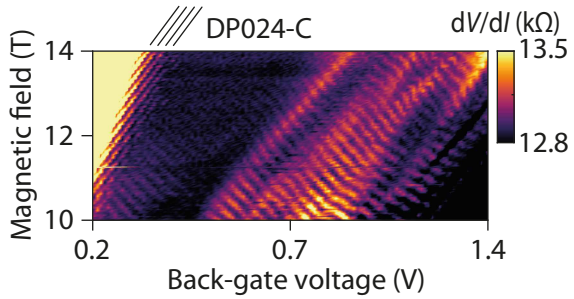

Figure 5.16: **Charging effect signatures within the V_g-B plane.** Colormap of the differential resistance dV/dI versus gate voltage and magnetic field for sample DP024 junction C (L x W = 170 x 125 nm^2) obtained with a current bias I_{bias} = 1 nA at $T = 11$ mK using a lock-in. Positively-sloped resistance oscillations are readily seen on the left-side of the plateau, a direct consequence of the presence of Coulomb diamonds.

The location of these oscillations at the plateau's left edge (highlighted with the black lines on the top of the Figure 5.16), that is when back-scattering between opposite quantum Hall edge states is on the verge to disappear, strongly suggests a bulk-related origin.

Looking at these specific features at $B = 14$ T unveils a regular Coulomb diamond shaped pattern as shown in Figure 5.17.a in which conductance is displayed as a function of the gate voltage V_g and the voltage measured accross the device[15]. Note that similar Coulomb diamonds signatures were also observed for the sample DP024 narrow junction D (L x W = 200 x 125 nm^2). Although diamonds here exhibit a contrast change around $V_g \approx 0.45$ V, they faintly persist up to $V_g \approx 0.58$ V, deep in the $\nu = 2$ quantum Hall plateau where the aforementioned h/e-periodic oscillations takes over in the form of a checkerboard-like pattern (see Figure 5.17.b). Strikingly, the edges of the observed diamonds follow conductance minima, at odds with the conductance-maxima delineated diamonds usually reported in standard quantum dots. Moreover, we note that the inner part of the diamonds usually shows a suppression of conductance [35], in contrast to the constant $2e^2/h$ value observed here.

[14] V_{sd} being a voltage applied on a side-gate to modulate the area of the QH interferometer cavity.

[15] Although much less well defined, diamonds have also been distinguished on the right edge of the plateau.

Similar diamond-shaped patterns were already reported in graphene nanoribbons[16] placed in the quantum Hall regime [143]. The latter were ascribed to tunneling events through a single bulk-localized quantum dot connecting opposite edge states. In such a configuration, illustrated in Figure 5.17.c schematic, a quasiparticle that tunnels through the compressible bulk, the latter acting as a quantum dot, necessarily returns to the electrode from which it originated, via the opposite edge states, due to the quantum Hall edge states chirality. Therefore, when occuring, tunneling event accross the compressible bulk-based quantum dot translates as a deficit in the measured current between the electrodes of the junction, hence a lowered conductance along the lines defining the diamonds in Figures 5.17.a and 5.17.b.

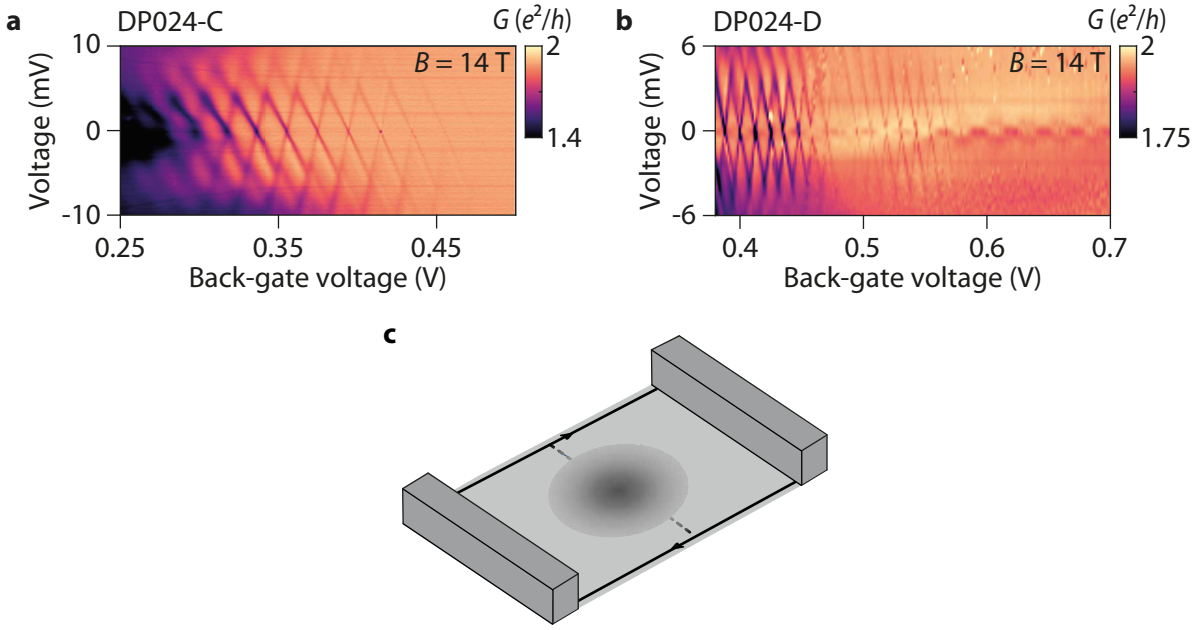

Figure 5.17: **Coulomb diamonds in the quantum Hall regime. a)** Colormap of the conductance versus gate voltage and voltage measured accross the junction C (L x W = 170 x 125 nm^2) in sample DP024 at B =14 T and T = 10 mK using the acquisition card NI-6348 in a voltage-bias configuration. **b)** Same measurement for the junction D (L x W = 200 x 125 nm^2) in sample DP024. **c)** Schematic illustrating the compressible bulk that enables back-scattering between opposite edge states.

Device	E_c [meV]	C_s [F]	C_d [F]	C_g [F]	ξ_{C_s}	ξ_{C_d}
C	2.55	1.00 x 10^{-17}	1.29 x 10^{-17}	8.36 x 10^{-18}	0.55	0.61
D	1.79	1.72 x 10^{-17}	1.41 x 10^{-17}	1.35 x 10^{-17}	0.56	0.51

Table 5.5: $\nu = 2$ **quantum Hall plateau left edge diamonds** charging energy E_c, source-to-dot capacitance value C_s, dot-to-drain capacitance value C_d and effective gate-to-dot capacitance value C_g for sample DP024 junctions C (L x W = 170 x 125 nm^2) and D (L x W = 200 x 125 nm^2). ξ_s and ξ_d correspond respectively to the ratio $C_s/[C_s + C_g]$ and $C_d/[C_d + C_g]$ (See footnote 17).

Interestingly, we can extract from the Coulomb diamonds the corresponding charging energy as well as the different capacitance values governing the quantum dot's behavior, a summary of which being provided in

[16] More precisely, a suspended 1.1 μm-long graphene ribbon with a 200 nm-wide constriction at half-way.

Table 5.5 [17,18]. We note that the value $C_g/(LW)$ is about an order of magnitude smaller than the capacitor per unit area that was deduced from the linear fit to the ν = 2 plateau's center (see Appendix C). Such a discrepancy presumably arises from electric field lines focusing at the dot boundaries, an assumption that makes sens in view of the dot smallness. Applying a basic parallel plate capacitor model to estimate the dot radius as $R = \sqrt{(C_g d)/(\epsilon_0 \epsilon_{\text{h-BN}} \pi)}$ with $d = 36$ nm the bottom h-BN thickness and $\epsilon_{\text{h-BN}} = 3.3$, yields $R \approx 57$ nm (resp. $R \approx 73$ nm) for junction C (resp. junction D).

5.4 Conclusion

In this chapter, we have established the presence of a coherent loop within our junctions through the observation of robust h/e-flux periodic Aharonov-Bohm resistance oscillations at constant filling factor.
We observed that the supercurrent, at constant filling factor, also exhibited h/e-flux periodic oscillations, which is the hallmark of the chiral supercurrent. The latter was observed to not systematically correlate with AB resistance oscillations, hence prohibiting a simple $R_N I_c$-product constancy modulation effect to explain the observed switching current oscillations.
A study of the Aharonov-Bohm resistance oscillations dependence on the voltage measured accross the junctions yielded checkerboard-like patterns, from which Thouless energy estimates could be extracted. Importantly, the latter enabled us to evaluate the QH edge states velocity along the NS interfaces, one of the key parameter for the chiral supercurrent occurence.
Finally, we investigated Coulomb interactions influence within our devices through the observation of Coulomb blockade features at the ν = 2 plateau's edges.

[17] We define the total system capacitance as $C_\Sigma = C_s + C_d + C_g$. Here C_s denotes the effective capacitance value between a first edge state and the dot, C_d the capacitance value between the dot and the opposite-side edge state, and C_g the effective capacitance translating the quantum dot - backgate coupling.
Considering a given diamond, slopes of the left and right diamond's edges are respectively given by:

$$\alpha_1 = \frac{C_g}{C_s} \tag{5.2}$$

$$\alpha_2 = -\frac{C_g}{C_g + C_d} \tag{5.3}$$

Then, defining the charging energy as $E_c = e^2/2C_\Sigma$, we derive:

$$C_g = \frac{e^2}{2E_c}\left[\frac{\alpha_2\alpha_1}{\alpha_2 - \alpha_1}\right] \tag{5.4}$$

[18] In the quantum Hall interferometers theory, the predominance of the Coulomb-dominated regime over the Aharonov-Bohm one translates in the ratio $\xi = C_{eb}/[C_{eb} + C_b]$ with C_{eb} the capacitance assigned to the edge-to-bulk coupling and C_b the capacitance between the bulk localized states and the back gate [140]. While for $\xi \ll 1$ edge-to-bulk coupling is negligible thus allowing for Aharonov-Bohm signatures to manifest, having $\xi \approx 1$ indicates a Coulomb-dominated regime. In an attempt to apply this theory to our system with $C_{eb} = C_s$ (or $C_{eb} = C_d$) and $C_b = C_g$, we estimate a typical ξ parameter ranging from 0.5 to 0.6 (see Table 5.5), thus indicating that our junctions, when considering the $\nu = 2$ quantum Hall plateau left edge, lies in a mixed regime dominated by Aharonov-Bohm interferences.

Chapter 6

Final notes

Main findings of this PhD work

In this PhD work, we have made use of graphene nanoribbon-based Josephson junctions contacted with MoGe electrodes, a disordered superconductor having an upper critical field of about 12.5 T. This feature, together with the ease with which this material couples to graphene, has enabled us to study the interplay between Josephson effect and the quantum Hall effect regime, leading to the following key results:

- **Josephson effect in the $\nu = 2$ quantum Hall plateau:** A supercurrent, co-existing with a normal state resistance corresponding to the $\nu = 2$ QH plateau, was observed up to a record-high magnetic field of 8 T. By way of comparison, previous state of the art results using similar systems could not report on supercurrent co-existing with quantum Hall regime beyond 1.4 T and only at $\nu \geq 6$. Importantly, this result raises hopes for inducing Josephson effect in the fractional quantum Hall effect regime, the latter having been observed in graphene at magnetic fields as low as 3 T, potentially paving the way for parafermions.
  To further characterize the Josephson effect in this peculiar regime, we also performed Shapiro steps measurements for supercurrents in the $\nu = 2$ QH plateau. In details, one obtained conventional Shapiro maps, indicative of a standard 2π-periodic current-phase relation.

- **h/e-flux periodic critical current:** The central result of this PhD was the observation of a h/e-flux periodic critical current, the chiral supercurrent hallmark. The presence of a coherent loop made up of an electron-hole mixture propagating along the perimeter of the junctions was further supported noticing the presence of h/e-flux periodic Aharonov-Bohm oscillations in the resistive state.
  Importantly, both sets of oscillations had to be considered at constant filling factor ν rather than at constant electron density to unveil this h/e-flux periodicity with magnetic field, a direct consequence of our devices smallness. The oscillations flux-periodicity was extracted via Fourier analysis accross the $\nu = 2$ QH plateau of several devices, strengthening our result. Crucially, it has been shown that even taking into account the uncertainty in the junctions area estimate, the signal obtained in the Fourier transform cannot match the $h/2e$-flux periodicity, i.e. the periodicity that would be expected for supercurrent in conventional Josephson junctions.

- **Importance of the junctions geometry:** Key to unveil the chiral supercurrent occurence was the use of narrow Josephson junctions (i.e. $W < 350$ nm), at odds with most, if not all, previous works on quantum Hall Josephson junctions, that were systematically making use of micrometer-wide devices. In particular, our widest devices (i.e. $W > 2$ μm) have never shown a supercurrent co-existing with a well-quantized quan-

tum Hall resistance plateau.

The importance of the NS interfaces length was further strengthened looking at the bias-dependence of the h/e-flux periodic resistance oscillations, the latter resulting into checkerboard-like patterns strongly resembling interference signatures usually reported in QH Fabry-Perot interferometers. Going further with this analogy enabled us to extract the Thouless energy attached to the charge carriers involved in the chiral supercurrent loop, yielding results agreeing with the QH edge states velocity renormalization along the NS interfaces.

As anticipated by theories dedicated to quantum Hall Josephson junctions, the NS interfaces length is the key parameter to unveil the chiral supercurrent.

Discussion

How to increase the chiral critical supercurrent?

In Chapter 4, we reported the observation of a supercurrent in the $\nu = 2$ quantum Hall plateau up to 8 T in our smallest device, with an amplitude of about ~ 0.5 nA. We demontrated in this PhD work that the key to obtain a chiral supercurrent was to maximize the Thouless energy by minimizing the length of the NS interfaces, a parameter over which we have direct control when fabricating our samples. However, there are other parameters that we could consider playing with in the expression of the Thouless energy $E_{\text{Th}} = h/(L/v_{\text{QH}} + W/v_{\text{SC}})$:

- **NS interfaces transparency:** Paradoxically, reducing the NS interfaces transparency, and hence the number of Andreev reflections along the superconducting electrodes, should help to preserve the amplitude of the chiral supercurrent by limiting the drop in Thouless energy arising from the QH edge channels velocity renormalization as they propagate along NS interfaces. To illustrate this point quantitatively, Figure 6.1 shows a map of the critical current I_c from equation (1.55), i.e. the expression derived from the Y. Alavirad *et al.* theory [30], as a function of the transparency and the length of the NS interfaces W at $B = 4$ T and $T = 10$ mK.

  We see that the supercurrent amplitude is maximal for very small NS interfaces length with high transparency. Yet, as the length of the NS interfaces increases, transparency must decrease accordingly to preserve the chiral supercurrent amplitude i.e. to keep constant the number of Andreev reflections along the NS interfaces. This suggests that through carefull control of the NS interfaces transparency, chiral supercurrent may be observable in devices of width W nearly half a micron.

- **Quantum Hall edge states velocity along pristine edges:** The Thouless energy also involves the velocity of the QH edge channels along the pristine edges, i.e. v_{QH}. Intuitively, for a given junction size, increasing the value of this velocity without affecting the other junction parameters would result into an increase of the Thouless energy. The velocity of the QH edge channels is typically proportional to E/B, E being the electric field associated with the 2DEG confining potential at the edge and B the magnetic field [35; 144]. As the boundaries of graphene are defined by the crystal lattice terminations, the confinement potential, and consequently E, is already one of the sharpest among 2DEGs used for studying the quantum Hall effect[1]. Note that the sensitivity of v_{QH} to E also implicitly suggests that the chiral supercurrent is more likely to emerge for low filling factor QH edge states, i.e. the latter being closest to the edge of the 2DEG, they have higher velocity.

  The second knob for increasing the QH edge channels velocity would be to obtain a quantum Hall effect at

[1] As a reminder, in semiconductor-based 2DEGs, edges are electrostatically defined using gates, the latter resulting in a smoother confinement potential.

the lowest possible magnetic field values. Interestingly, for the integer quantum Hall effect, $\nu = 2$ QH state has been observed at sub-100 mT magnetic field values in graphene interfaced with CrOCl [145]. For the conventional fractional quantum Hall effect, the lowest magnetic field value at which it has been observed is 3 T, with the $\nu = 2/3$ quantum Hall state in dual-gated graphene-based devices [43]. In the same vein, results concerning the fractional quantum anomalous Hall effect [146; 147; 148; 149], i.e. a somewhat zero-field quantum Hall effect, are clearly an avenue to investigate. In particular, for the M.I.T. group work [149], the fractional quantum anomalous Hall effect has been observed in rhombohedral pentalayer graphene/hBN Moiré superlattice. This last platform has the advantage of high mobility, while being easy to interface with a superconducting material, as already anticipated by the authors[2].

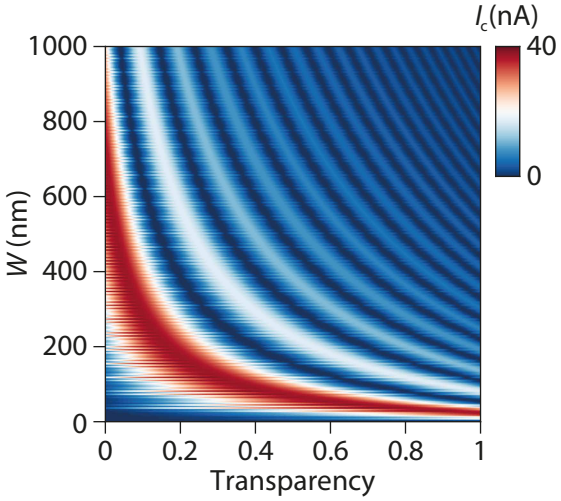

Figure 6.1: **Influence of the NS interfaces transparency on the chiral supercurrent amplitude. a**) Colormap of the critical current I_c for a quantum Hall Josephson junction versus the NS interfaces transparency and the NS interfaces length W obtained with equation (1.55) at $T = 10$ mK and $B = 4$ T for a lead-to-lead distance $L =$ 150 nm. The value of v_{SC}, in which transparency comes into play, was computed as $2v_n/(\pi + q\hbar\omega_c/\Delta)$ with $q = t/(2-t)$, t being the NS interfaces transparency, $\hbar\omega_c$ the cyclotron gap and $\Delta = \Delta_0\sqrt{1-(B/B_{c,2})^2}$, Δ_0 being the superconducting gap of the electrodes at $B = 0$ T and $B_{c,2}$ the electrode's upper critical field (see Chapter 1 Section 1.2.2).

Note that other important points, left aside by the theory of Y. Alavirad *et al.* [30], could be also considered:

- **Quantum Hall breakdown:** Following the previous remarks, we might also ask why not simply reduce the length of the NS interfaces even further? In fact, it turns out that reducing the length of NS interfaces to promote the emergence of the chiral supercurrent will also favor the so-called quantum Hall breakdown, that is the disappearance of the quantum Hall effect due to the application of a current bias exceeding a critical current value $I_{c,QHB}$. In particular, the value of $I_{c,QHB}$ was found to be linearly dependent on the 2DEG's width for samples with low and moderate mobilities (i.e. $\sim 10^5$ cm^2/V.s) and sub-linearly dependent on the sample's width for high mobilities 2DEGs (i.e. $\sim 10^6$ cm^2/V.s) (see [150]). Note that these conclusions were drawn from measurements on GaAs/AlGaAs-based 2DEGs, as studies for encapsulated graphene remain scarce. Typically, we found only one study dedicated to quantum Hall breakdown mechanism in encapsulated graphene [151] without any investigation of the dependence of $I_{c,QHB}$ on the samples width, which

[2]The attentive reader will notice that the expression of v_{SC} is directly proportional to the Fermi velocity v_n within the normal part (see Figure 6.1 caption). The M.I.T. group strategy being based on flat bands physics, hence presumably low Fermi velocity, it therefore suggests that the Thouless energy attached to a chiral supercurrent within such a system would be very low.

limits the present discussion to a qualitative aspect.

- **Influence of the vortices within the electrodes:** We recall that chiral Andreev edge states interfer between them while propagating along the NS interfaces, a mechanism sensitive on the one hand to disorder (see Chapter 1 Section 1.2.3) but also to the presence of vortices in the electrodes, a point that was left aside in the theory of Y. Alavirad *et al.* [30].
  Interestingly, the latter are believed to act as quasiparticles sink [37; 99], which ultimately lower the probability for an incoming electron to result in a outgoing Andreev reflected hole, hence the chiral supercurrent amplitude. In addition, vortices are also expected to locally affect the potential vector along the NS interfaces, hence the relative phase difference between the two co-propagating CAESs [41] which should also affect the chiral supercurrent amplitude.
  It would therefore be interesting to think about a strategy to move away the vortices from the NS interfaces. For instance, no vortices can develop within a superconducting wire whose diameter is smaller than $d = \pi\sqrt{2}\xi(0)$, with ξ_0 the zero-temperature Ginzburg-Landau coherence length [152; 153]. The upper critical field of the MoGe being of the order of 12.5 T, the corresponding Ginzburg-Landau coherence length is about 5 nm, which implies $d \sim 23$ nm. Consequently, though technically challenging to fabricate, forming a Josephson junction using such nanowires as superconducting electrode could be an interesting approach to pursue.

Josephson effect in other quantum Hall states

In this PhD work, we have focused on the study of a supercurrent in the $\nu = 2$ quantum Hall plateau, that is in the integer quantum Hall regime. Although being an elegant result in itself, the main motivation for inducing superconductivity in the quantum Hall effect regime remains the obtention of *topological superconductivity*, i.e. a phase of matter hosting quasiparticles with non-Abelian exchange statistics, the key element for topologically protected quantum computation. Here we discuss some of the proposals for quantum Hall effect-based topological superconductor[3] in the light of the results obtained in the course of this PhD work.

- **Josephson effect in the $\nu = 1$ quantum Hall state:** Following the results presented in this PhD work, a first very attractive prospect would be to study the chiral supercurrent in the $\nu = 1$ spin-polarized quantum Hall state, a configuration that is suspected to host Majorana fermions[4]. In that regime, a single, spin-polarized, edge channel runs along the junction perimeter. At first sight, the spin-polarization of this edge state should prevent Andreev reflections to occur, the latter requiring for spin reversal between the incident electron and the Andreev-reflected hole. A way to circumvent this constraint invokes the spin-orbit coupling so that spin is no longer a valid quantum number. Such a strategy has already produced interesting results, including the observation of crossed Andreev conversion signatures in the $\nu = 1$ quantum Hall state using NbN-based contacts, the Niobium being known to have strong spin-orbit interaction (see Chapter 2 Section 2.5). Interestingly, for the specific case of a superconducting finger in contact with a 2DEG in the $\nu = 1$ spin-polarized quantum Hall state, a spin-orbit free mechanism allowing for crossed Andreev conversion was put forward by T.H. Galambos *et al.* [105]. Here the idea would consist in forming a superconducting electrode with tilted NS interfaces. Due to the Meissner effect, the latter would result in an in-plane magnetic

[3] The interested reader can find a dedicated review in [154].

[4] See the talk *The search for chiral Andreev edge states* given by C. Beenakker at the Virtual Science Forum during the ARQH workshop (https://virtualscienceforum.org/arqh/).

field component on either side of the finger. Importantly, this magnetic field component having opposite direction on either side of the superconducting finger, the spin symmetry of the $\nu = 1$ QH edge state is locally broken, hence allowing for crossed Andreev conversion. In the case of a Josephson junction, where the edge channel runs along only one side of each superconducting electrode, this approach could not work as such (although tilted by the Meissner effect, the spin polarization remains constant along the NS interface). However, we can imagine that a superconducting electrode with a tilted NS interface profile whose tilt varies discretely along the interface could break the spin symmetry via a similar mechanism.
Despite these encouraging results, it should be noted that J.A.M. van Ostaay *et al.* theory of spin-triplet supercurrent in quantum Hall Josephson junctions predicts that its amplitude is inversely proportional to $W/\mathcal{L}^3$, with W the NS interfaces length and $\mathcal{L}$ the junction's perimeter[5] [29]. As small junctions are already required for the observation of the chiral supercurrent in the $\nu = 2$ QH state (spin singlet), this last prediction is not very promising regarding the possibility of obtaining a $\nu = 1$ quantum Hall edge channel-mediated supercurrent.

- **Josephson effect in the fractional quantum Hall effect (FQHE) regime:** Josephson effect in the above-mentioned quantum Hall state is expected to yield Majorana fermions, quasiparticles which, despite their non-abelian nature, do not allow to encode the whole set of logical gates required to perform universal topological quantum computation [155]. In contrast, theories dealing with proximity-induced superconductivity in the fractional quantum Hall regime anticipate the emergence of the so-called parafermions, the latter allowing to encode the whole set of logical gates for topological quantum computation [154].
Yet, so far, only one result with transport signatures involving Andreev reflections in the fractional quantum Hall effect has been reported [43]. Importantly, these measurements were based on crossed Andreev conversion processes and not on the Josephson effect, the co-existence of the latter with the FQHE remaining a fascinating challenge to this day. On the theoretical side, the presence of parafermions in a Josephson junction in the $\nu = 2/3$ fractional quantum Hall state is predicted to result into a 6π-periodic current-phase relation [154][6], a striking feature that could be probe via Shapiro steps measurements. On the experimental side, we can mention the following lines of thought:

  1. A chiral supercurrent in the fractional quantum Hall regime necessarily requires consideration of a fractional state in the N = 0 Landau level, either 1/3 or 2/3, to ensure that the supercurrent is not mediated by the edge channels of the integer quantum Hall effect that run in parallel, for instance at $\nu = 7/3$ or $5/3$. This would involve inducing a Josephson effect in a junction whose normal state resistance would be about ~ 77 kΩ and ~ 39 kΩ respectively, which clearly stands out when compared to typical normal state resistance values in the literature.
  2. Having in mind the obtention of parafermions, the ideal would be to induce a chiral supercurrent within the $\nu = 1/3$ QH state, the latter having the largest gap among fractional QH states (about 20 K at $B = 14$ T[7] [158]), the characteristic energy scale translating the protection of the non-abelian excitations from decoherence effects[8].

[5] In the low temperature limit, i.e. when the Thouless energy is much larger than $k_B T$.

[6] Note that parafermions could also emerge from electron-electron interactions within a Josephson junction made out of a quantum spin Hall insulator [156]. In that configuration, the current-phase relation is expected to be 8π-periodic.

[7] According the review found in [157], the $\nu = 1/3$ gap scales in magnetic field B as 0.01 $e^2/\epsilon l_B$ with ϵ the 2DEG dielectric constant and $l_B = \sqrt{\hbar/eB}$ the magnetic length.

[8] In details, the error rate attached to non-abelian anyons-based qubits relates to the number of thermally excited quasiparticles hosted by the system. In particular, their density follows an Arrhenius law whose characteristic energy scale is the gap attached to the non-abelian state under consideration [159].

3. Fractional quantum Hall states are obtained using high mobility samples, which typically implies dual-gated architecture for encapsulated graphene [43; 160]. Interestingly, it has also been observed that fractional QH states are more easily resolved by bulk sensitive measurements (such as transport measurements in Corbino geometry devices [161] and magneto-capacitance measurements [162]) than by conventional Hall bar transport measurements[9]. This difference suggests that resolving FQHE signatures using transport measurements would be rather limited by details affecting the QH edge channels, to which are sensitive Hall bar measurements, rather than bulk disorder. This could include work-function mismatch issues between the contacts and the 2DEG (the latter resulting into regions surrounding the contacts having an electron density that differs from the bulk, which can deflect the QH edge channels) [4; 43]) and/or graphene boundary specificities such as edge disorder [163] to name but the most obvious.

   In the Harvard group's crossed Andreev conversion experiment [43] (see Chapter 2 Section 2.5), which was making use of dual-gated devices, a region of about $\sim$ 100 nm around the superconducting finger was not covered by the graphite topgate, a structural peculiarity used by the authors to control the distance between the QH edge states and the contact-induced local doping region using the backgate. In fact, ideally, a local gate should be implemented to compensate this contact-induced doping region, an idea that seems rather unrealistic in practice. Moreover, to return to QHJJs, such a "local gate strategy" would be difficult to apply to this type of device due to the small size required for the appearance of a chiral supercurrent.

   Regarding sensitivity to edge details, the gate-defined dual-gated Hall bar devices developed by R. Ribeiro-Palau *et al.* [160] are particularly appealing as such a strategy could be used for QHJJs. The idea here consists in placing the graphene in the $\nu = 0$ state, which is insulating in magnetic field, with a backgate while using a Hall bar-shaped topgate to locally define the region in which studying the quantum Hall effect, an approach that has proven to improve resolution of FQHE signatures in Hall bar transport measurements [160]. Similarly, for QHJJs, one could imagine to use a graphite back gate to set a graphene sheet in the $\nu = 0$ regime, and a nanoribbon-shaped top gate to define the normal part of the Josephson junction. Note aside, this approach would also eliminate the need to find graphene nanoribbons to fabricate the samples.

[9] The interested reader can find a particularly revealing comparison between Hall bar, Corbino geometry and magneto-capacitance measurements in [157] page 340.

Part III

Appendix

Appendix A

Fabrication details, catalog of the devices and additional data

We begin with a brief description of sample fabrication. Next, we provide a catalog of the devices used for this thesis work, in which all the important parameters related to each device are specified.
In a third part, additional data regarding devices characterization are provided. This includes field effect measurements, supercurrent dependence on the back-gate voltage at zero magnetic field, supercurrent interference patterns at low magnetic field and measurements of both the critical temperature T_c and the upper critical magnetic field $H_{c,2}$ of the MoGe superconducting electrodes.

A.1 Details on the samples fabrication

Prior to heterostructures assembling, we first exfoliate and select both hexagonal boron nitride (h-BN) and graphite flakes using optical microscope.
To further characterize the promising flakes, we systematically performed atomic force microscopy (AFM) imaging. This enables to visualize structural defects and glue tape residues that would be otherwise to small to be distinguished with optical microscope.

Note that for graphene flakes, the use of AFM also allows to locate and identify graphene nanoribbons. Importantly, we have tried to give preference to triangular graphene flakes, the one used for the sample HV088 being a perfect example (see Figure B.1.b in Appendix B). First, triangular-shaped flake are easier to find than constant-width nanoribbons with an optical microscope. Second, it turns out that triangular-shaped flakes are less prone to distortion and folding during the encapsulation process, hence translating into a higher success rate in sample fabrication.

Once the flakes were selected, our stacks were assembled using the standard van der Walls pick-up technique using a polycarbonate polymer as sticking layer. The latter allows for a good control over the polymer-to-hBN interface position which, ultimately, enables to push bubbles that may form during the encapsulation, thus improving the devices quality[1].
Ultimately, the top h-BN - graphene - bottom h-BN stack was deposited atop a graphite flake serving as a back-gate electrode.
Following the ultimate deposition step, the stack was then immersed in a chloroform bath to remove PC film

[1] In details, the PC front was moved by smoothly increasing the temperature up to about 110 °C.

residues (during $\sim$ 15 min), then followed by an IPA rinse bath.

In order to both locate the encapsulated ribbon as well as to check the final device quality, we then perform a new AFM image. Provided the device under study does not show anomalies such as bubbles or signs of dislocation, we then process it to implement the contacts.

In a first e-beam lithography step, we implement pads as well as the Ti/Au lines (5 nm/35 nm). Then, in a second lithography step, we define the superconducting electrodes. Importantly, the lines defining the latter do not extend more than $\sim$2 μm apart from the stack, in order to avoid resonance effects which, for long superconducting lines, were observed to yield self-induced Shapiro steps in the I/V curves without applying any external RF illumination.
Following the resist development, and prior to MoGe deposition, the exposed parts of the stack are etched using reactive ion etching (RIE). In details, we first apply an O_2 plasma for 10 seconds to remove the last resist residues. Then, a CHF_3/O_2 plasma mixture[2] is used to etch the top h-BN, the graphene as well as the bottom h-BN over 5 nm typically in order to compensate the uncertainty on the etching rate.

Once the etching process is over, the sample is transfered as fast as possible within the chamber of the sputtering machine we use to deposit the MoGe. Once the vacuum level reaches 10^{-6} mBar, an Argon plasma (45 sccm, $P_{RF} = 10$ W (DC)) is applied for 10 sec in order to clean the exposed graphene edges. Then, the MoGe crucible is cleaned for 30 minutes with an Argon plasma (45 sccm, $P_{RF} = 40$ W (DC)). Finally, the MoGe is sputtered on the sample with a deposition rate of 1.44 Å/s (the Argon plasma used to sputter the MoGe is done with 20 sccm and $P_{RF} = 60$ W (DC)).

Once the deposition is over, the sample is immersed in acetone or NMP for one night with a magnetic stirrer to keep the fluid moving. The lift-off is done using a small pipette and, if necessary, a smooth ultrasound bath.

[2] The etching rate of this plasma is estimated to be about 16 nm/min.

A.2 Device parameters

Device	L [nm]	W [nm]	V_D [V]	$V_{g,1}$ [V]	ρ_c [$\Omega.\mu$m]	$V_{g,2}$ [V]	Δ [μeV]	I_{excess} [nA]	R_N [kΩ]	T_{OBTK}	$eR_N I_s$ [μeV]	C_g [mF/m^2]	$V_{D,fit}$ [V]
HV088-B	140	177.5	-0.18	1	418.1	1	980.5	-	-	-	-	1.27	-0.16
HV088-C	170	210	-0.13	1	400.5	1	852	49	4.5	0.49	150	1.39	-0.14
HV088-D	200	247	-0.19	1	387.9	1	865	46	3.8	0.47	91	1.43	-0.15
HV088-E	240	288	-0.14	1	349.4	1	876	86	3.0	0.5	96	1.14	-0.25
HV088-F	270	334	-0.04	1	451.5	1	897	59	3.2	0.47	87	1.55	-0.08
HV088-G	107	2332	-0.52	1	444.2	2	762	552	0.34	0.48	146	2.12	-0.24
HV088-H	202	2434	-0.34	1	508.5	2	773	434	0.34	0.47	137	1.93	-0.23
HV088-I	307	2569	-0.26	1	106.1	2	808	456	0.24	0.45	143	-	-
DP024-C	170	125	-0.41	1	105.3	1	754	83	4.2	0.57	243	1.12	-0.12
DP024-D	200	125	-0.22	1	392.8	1	-	-	-	-	-	1.89	-0.18

Table A.1: **Devices parameters.** L is the lead-to-lead distance, W the width of the device, V_D the Dirac point voltage position measured at $B = 0$ T, $V_{g,1}$ denotes the gate voltage at which the contact resistivity ρ_c was estimated, $V_{g,2}$ denotes the voltage at which the superconducting electrode's gap Δ, the excess current I_{excess}, the normal state resistance R_N, the tranparency T_{OBTK} and the $eR_N I_s$-product were estimated, C_g and $V_{D,fit}$ the capacitance and the Dirac point voltage position deduced from a fit of the $\nu = 2$ QH plateau center at $I_{bias} = 160$ nA.

A.3 Additional data for device characterization

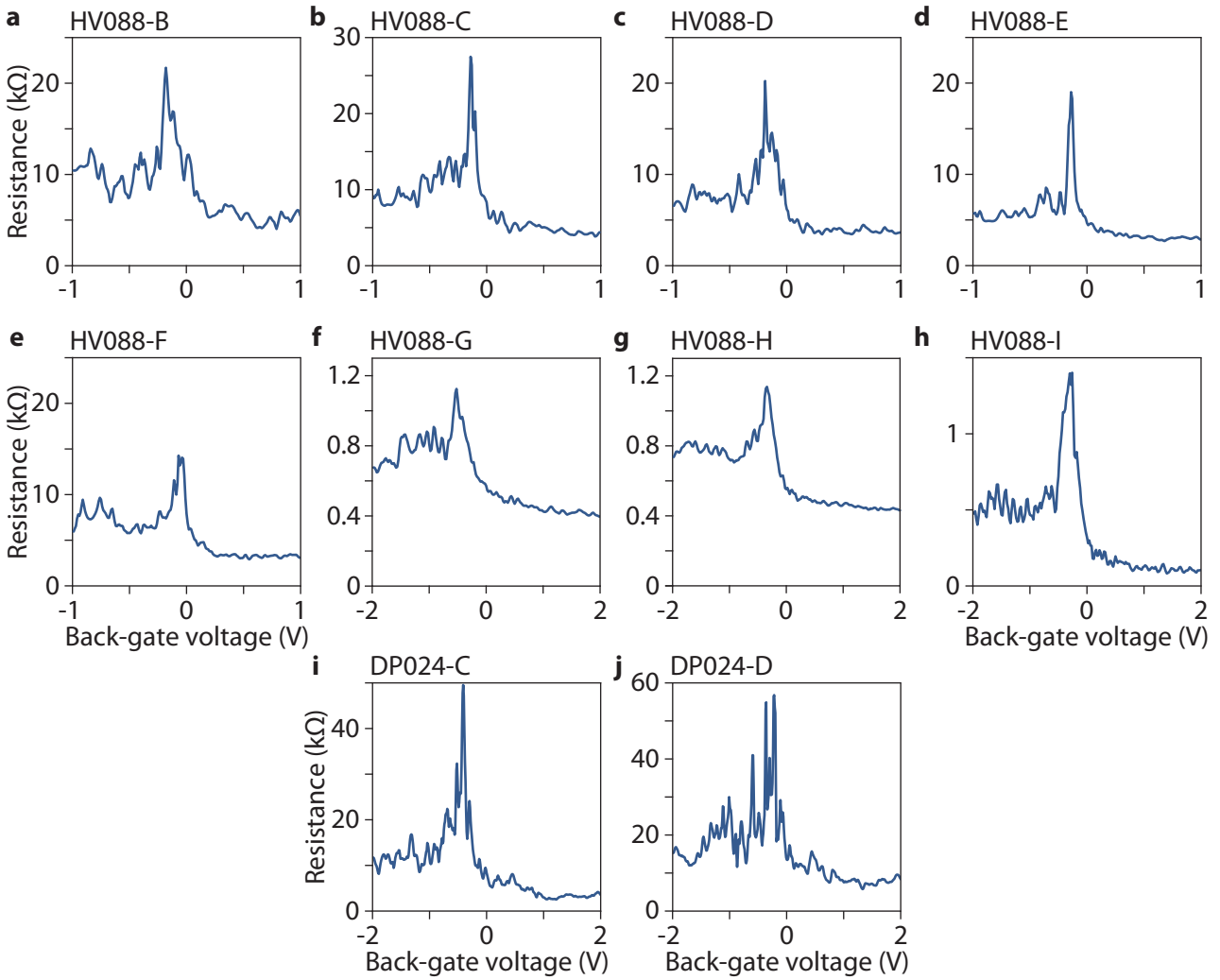

Figure A.1: **Graphene field effect. a)** Resistance versus back-gate voltage measured on Device B (L x W = 140 x 177.5 nm^2) in sample HV088 at T = 5.7 K, with I_{bias} = 10 nA using a pseudo-four probe terminal configuration. **b)** Similar measurement on Device C (L x W = 170 x 210 nm^2) in sample HV088. **c)** Similar measurement on Device D (L x W = 200 x 247 nm^2) in sample HV088. **d)** Similar measurement on Device E (L x W = 240 x 288 nm^2) in sample HV088. **e)** Similar measurement on Device F (L x W = 270 x 334 nm^2) in sample HV088. **f)** Resistance versus back-gate voltage measured on Device G (L x W = 107 x 2332 nm^2) in sample HV088 at T = 11 mK, with I_{bias} = 1 μA using a pseudo-four probe terminal configuration. **g)** Similar measurement on Device H (L x W = 202 x 2434 nm^2) in sample HV088. **h)** Resistance versus back-gate voltage measured on Device I (L x W = 307 x 2569 nm^2) in sample HV088 at T = 1.5 K, with I_{bias} = 10 nA using a pseudo-four probe terminal configuration. **i)** Resistance versus back-gate voltage measured on Device C (L x W = 170 x 125 nm^2) in sample DP024 at T = 4.7 K, with I_{bias} = 10 nA using a pseudo-four probe terminal configuration. **j)** Similar measurement on Device D (L x W = 200 x 125 nm^2) in sample DP024 at T = 4.8 K.

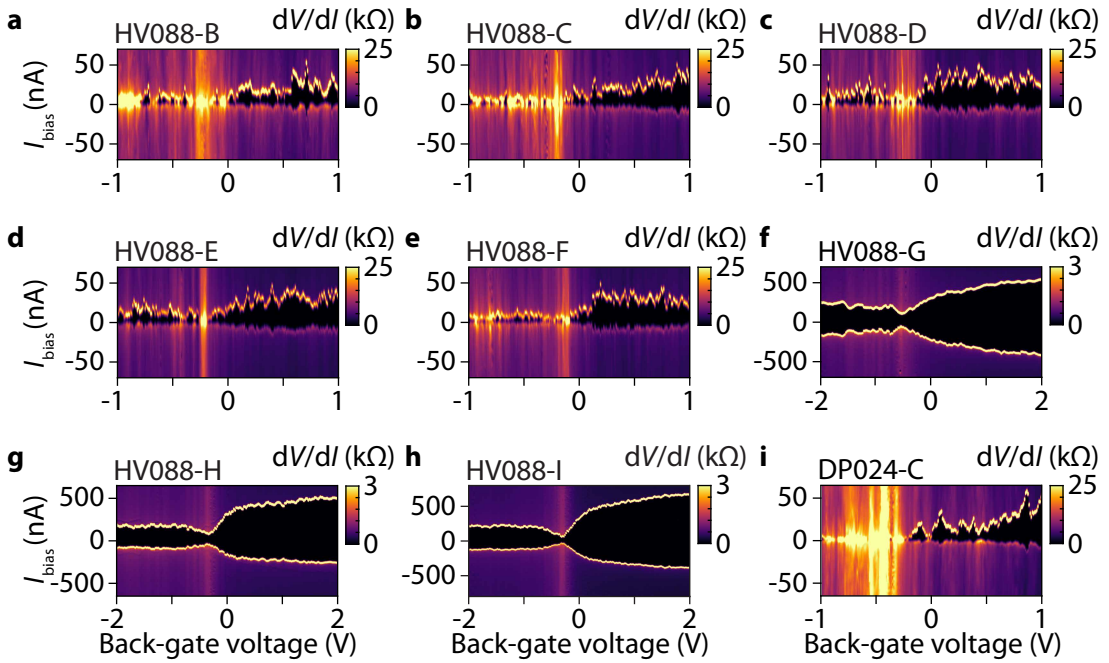

Figure A.2: **Bipolar supercurrent. a)** Differential resistance dV/dI versus both the back-gate voltage and the current bias I_{bias} for Device B (L x W = 140 x 177.5 nm^2) in sample HV088 at T = 10 mK using a pseudo-four probe terminal configuration. **b)** Similar measurement on Device C (L x W = 170 x 210 nm^2) in sample HV088. **c)** Similar measurement on Device D (L x W = 200 x 247 nm^2) in sample HV088. **d)** Similar measurement on Device E (L x W = 240 x 288 nm^2) in sample HV088. **e)** Similar measurement on Device F (L x W = 270 x 334 nm^2) in sample HV088. **f)** Differential resistance dV/dI versus both the back-gate voltage and the current bias I_{bias} for Device G (L x W = 107 x 2332 nm^2) in sample HV088 at T = 11 mK using a pseudo-four probe terminal configuration. **g)** Similar measurement on Device H (L x W = 202 x 2434 nm^2) in sample HV088. **h)** Similar measurement on Device I (L x W = 307 x 2569 nm^2) in sample HV088. **i)** Differential resistance dV/dI versus both the back-gate voltage and the current bias I_{bias} for Device C (L x W = 170 x 125 nm^2) in sample DP024 at T = 14 mK using a pseudo-four probe terminal configuration.

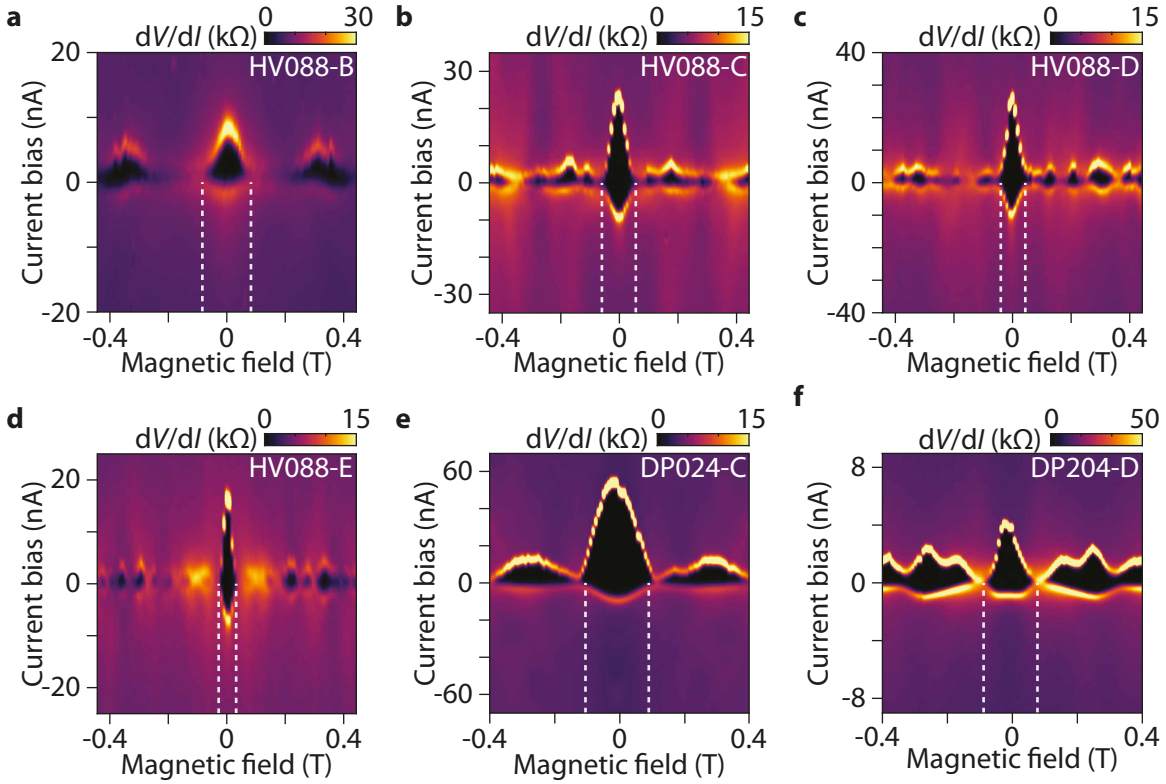

Figure A.3: **Supercurrent interference patterns under low magnetic field. a)** Differential resistance $\mathrm{d}V/\mathrm{d}I$ versus both the magnetic field and the current bias I_{bias} obtained for Device B (L x W = 140 x 177.5 nm^2) in sample HV088 at $V_{\mathrm{g}} = 1$ V and $T \approx 10$ mK. **b)** Similar measurement on Device C (L x W = 170 x 210 nm^2) in sample HV088. **c)** Similar measurement on Device D (L x W = 200 x 247 nm^2) in sample HV088. **d)** Similar measurement on Device E (L x W = 240 x 288 nm^2) in sample HV088. **e)** Differential resistance $\mathrm{d}V/\mathrm{d}I$ versus both the magnetic field and the current bias I_{bias} obtained for Device C (L x W = 170 x 125 nm^2) in sample DP024 at $V_{\mathrm{g}} = 1$ V and $T \approx 16$ mK. **f)** Similar measurement on Device D (L x W = 200 x 125 nm^2) at $T \approx$ 15 mK in sample DP024. The white dashed lines indicate the expected periodicity for a superconducting flux quantum $\Phi_0 = h/2e$ through the graphene area.

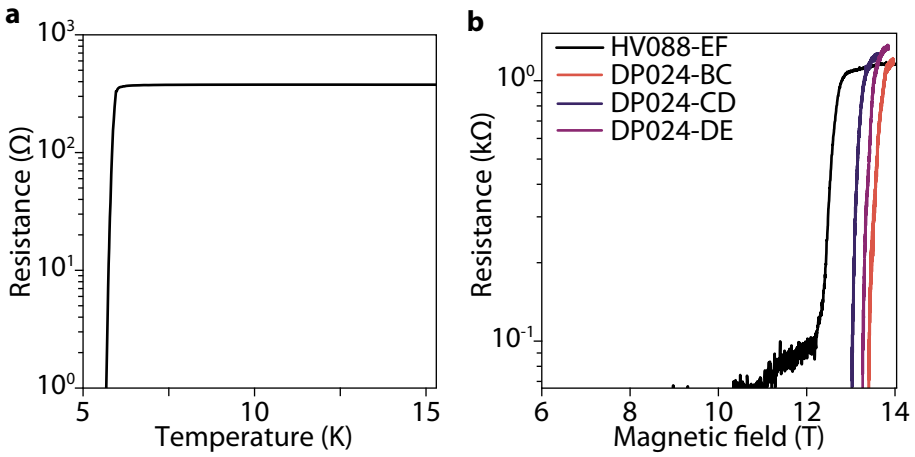

Figure A.4: **MoGe superconducting transition. a)** Four-terminal measurement of the resistance of a MoGe thin film as a function of temperature. The critical temperature T_c is 5.9 K. **b)** Two-terminal measurement of the resistance attached to the superconducting electrodes on sample HV088 and DP024 versus the magnetic field at $T = 50$ mK. A constant resistance of 1.06 kΩ was substracted to account for the wiring resistance in series with the electrodes. The legend indicates the MoGe electrode under consideration (e.g. HV088-EF corresponds to the electrode shared by the junctions HV088-E and HV088-F).

Appendix B

Evaluation of the uncertainty on the junctions area estimation

Each junction area A is estimated from the superposition of the lithographic design with the AFM image of the heterostructure as illustrated in Figures B.1. The precision on the flake width from the AFM image δW_{AFM} is estimated to be about $\pm$30 nm. The uncertainty on the junction width δW is dominated by δW_{AFM} with negligible contribution from lithographic alignment uncertainty δW_{al}. Indeed, a lithographic misalignment δy along the junction width direction, estimated to be smaller than 100 nm, has no effect on the junction width since the electrodes are parallel over more than 300 nanometers.
The alignment precision of the superconducting electrodes with respect to the flake in the x direction is estimated to be about $\delta x = \pm$ 130 nm. The resulting width uncertainty is given by $\delta W_{\text{al}} = \delta x \cdot \sin(\theta)$ with θ the nanoribbon opening angle as defined in Figure B.1.a. With $\theta_{\text{HV088}} = 7.5°$ and $\theta_{\text{DP024}} = 0.6°$, the alignment-related uncertainty on the width δW_{al} is about $\pm$ 17 nm for HV088 and $\pm$ 1.4 nm for DP024. The total uncertainty on the estimation of the junction width δW is thus given by $\delta W = \sqrt{\delta W_{\text{AFM}}^2 + \delta W_{\text{al}}^2}$, hence $\pm$ 35 nm for HV088 and $\pm$ 30 nm for DP024. The uncertainty on the junction length δL, that originates from lithographic development and etching, is estimated from dose test measurements to be about $\pm$ 20 nm. The resulting uncertainty in the estimation of the junctions area $\delta A = L\Delta W + W\delta L$ is reported in Table B.1.

Device	L [nm]	W [nm]	$[A \pm \delta A] \times 10^3$ µm^2
HV088-B	140	177.5	25 ± 8
HV088-C	170	210	36 ± 9
HV088-D	200	247	49 ± 11
HV088-E	240	288	69 ± 13
HV088-F	270	334	90 ± 14
HV088-G	107	2332	250 ± 50
HV088-H	202	2434	492 ± 56
DP024-C	170	125	21 ± 8
DP024-D	200	125	25 ± 8

Table B.1: **Devices areas** A is the geometric area of the graphene, δA is the associated uncertainty. The latter was evaluated using the procedure described in the main text.

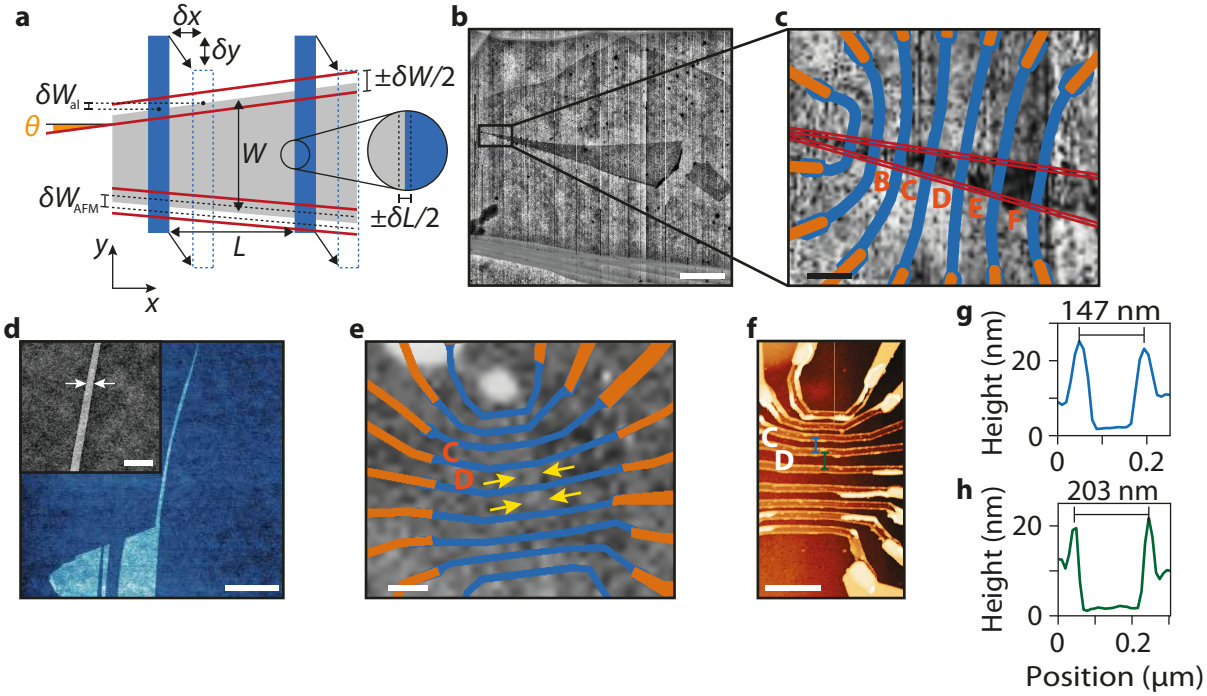

Figure B.1: **h-BN-encapsulated graphene nanoribbon samples. a)** Schematic describing the uncertainty in the junction width δW (red lines) and length δL (vertical black dashed lines in the zoom). Tilted black dashed lines indicate the uncertainty in the graphene width δW_{AFM} from AFM imaging. Blue rectangles represent MoGe electrodes correctly aligned, dashed blue lines indicate the MoGe electrode position with a misalignment $(\delta x, \delta y)$, which results in an uncertainty δW_{al} on the graphene edges position. **b)** AFM picture for sample HV088, the encapsulated graphene is readily visible with contrast enhancement. **c)** Zoom on the graphene narrow part in **(b)**, with the lithography pattern overlayed (Ti/Au lines in orange and MoGe electrodes in blue). Red lines indicate the total width uncertainty $\pm\delta W/2$ around the graphene edges. **d)** AFM picture of the graphene nanoribbon of sample DP024 before h-BN encapsulation. Inset: higher resolution AFM picture. The arrows indicate the nanoribbon width of 125 nm. **e)** AFM picture of sample DP024 after h-BN encapsulation. The yellow arrows indicate the nanoribbon position. The lithography pattern is overlayed on the picture. The scale bars are 5 μm **(b)**, 400 nm **(c)**, 2 μm **(d)**, 500 nm **(d)** inset, 500 nm **(e)**. **f)** AFM picture of sample DP024 after implementation of the MoGe contacts. The scale bar is 1 μm. **g)**, **h)** Height profiles along the blue and green lines in the AFM image shown in **(f)**. The excess thickness on the contact edge results from the lift-off process of the MoGe.

Appendix C

From gate voltage-to-filling factor: capacitor estimation

Here we describe our gate voltage-to-filling factor conversion procedure, the latter being delicate due to the pseudo-four probe terminal configuration employed for our measurements as we shall see below.
From the very definition of the filling factor, namely the ratio between the electron and flux quanta densities, respectively denoted n_e and n_B, we have:

$$\nu = \frac{n_e}{n_B} = \frac{\phi_0}{B}\frac{C(V_g - V_D)}{e} \tag{C.1}$$

where $\phi_0 = h/e$ is the flux quantum, C the capacitor value (per unit area) and V_D the Dirac point gate-voltage value. Key to our conversion procedure is the capacitor per unit area C estimation[1]. The latter will rely on assuming that filling factor integer value lies at the $\nu = 2$ quantum Hall plateau's center in the $V_g - B$ plan[2].

We extracted the capacitor value from the resistance plateau obtained with $I_{bias} = 160$ nA. Although arbitrary, this choice offers a good compromise between, on one hand the low bias resistance oscillations that strongly deviates from $h/2e^2 \approx 12.9$ kΩ (see Chapter 4 Section 4.3) and, on the other hand, the quantum Hall breakdown occuring at higher bias. The latter being not systematically symmetric between left and right plateau's edges, this might result into a schift of the estimated plateau's center with the applied bias.

In order to estimate the plateau's central position accross the $V_g - B$ plan, we first have to identify the plateau's edges. An arbitrary way to define these edges would consist in looking at the intersections between the experimental curve and crossing lines lying at $\pm$ 2 $\%$ of $R_{h/2e^2} \approx 12.9$ kΩ. Yet, $\nu = 2$ quantum Hall plateau resistance at $I_{bias} = 160$ nA was sometimes prone to slight deviations from the ideal quantized value, a fact we ascribe to the way the resistance was obtained, i.e. from I/V characteristics performed with a DC current acquisition

[1] Note that a parallel plate model also allows for estimating the capacitor per unit area (here estimated to be about $C = 1.26$ mF/m^2 using $\epsilon_{h\text{-}BN} = 3.3$ [109] and sample HV088 bottom h-BN thickness $d_{h\text{-}BN} = 23.2$ nm). Yet, graphene nanoribbons ($L = 2.5$ µm and $W = 2$ µm in reference [164]) were shown to display a position-dependent capacitance per unit area owing to the local focusing of the gate-induced electric field lines at graphene's edges. In particular, such a mechanism was invoked in reference [165] (using nanoribbons with 500 nm $< L <$ 1 µm and 100 nm $< W <$ 200 nm) whose capacitor par unit area value, estimated from the $\nu =$ -2 plateau's center, was higher than expected from the parallel plate model. We thus favoured a capacitor value estimation based on $\nu = 2$ plateau's center for each device in order to avoid any capacitor value underestimation with a simple parallel plate model.

[2] In all rigor, this assumption remains questionable. Using a combination of transport and scanning microwave impedance microscopy measurements, it was shown that for encapsulated graphene resting atop a Silicon chip caped by a 300 nm-thick insulating SiO_2 layer, gate-voltage value attached to the $\nu = 2$ quantum Hall plateau's center was corresponding to $\nu \approx 0.9$ x ($\nu = 2$) [166].

card in a pseudo-four probe terminal configuration. Note that having $R_{h/2e^2} I_{\text{bias}} > 2\Delta_{\text{a-MoGe}}(B = 0\text{T})$, these variations are unlikely to originate from Andreev reflections-related processes.

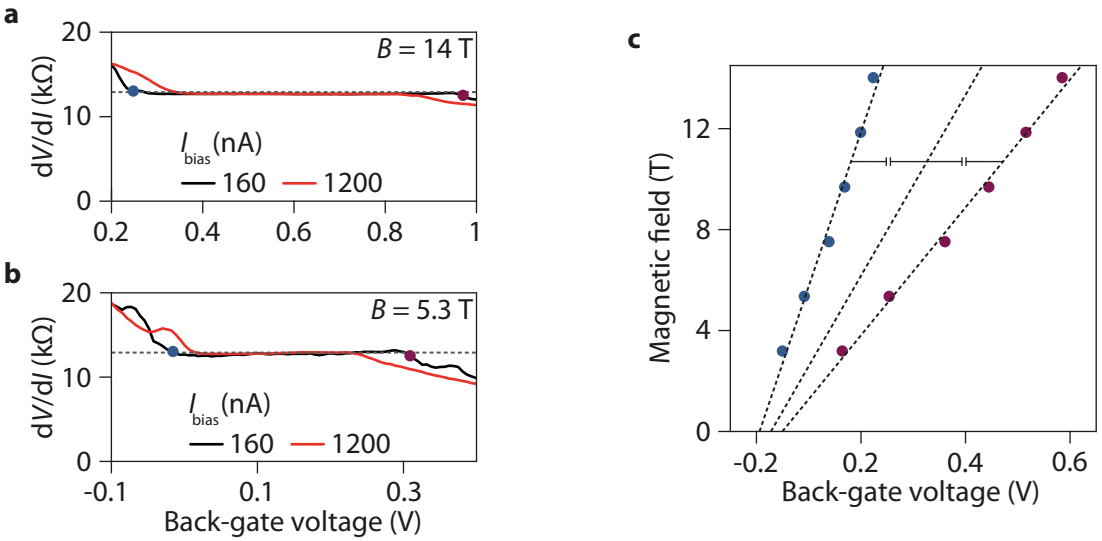

Figure C.1: **$\nu = 2$ quantum Hall plateau center estimation. a)** $\mathrm{d}V/\mathrm{d}I$ at $I_{\text{bias}} = 160$ nA versus gate voltage obtained at $B = 14$ T for narrow junction C (L x W = 170 x 210 nm^2) in sample HV088. The resistance was numerically derived from I/V-characteristics obtained using the acquisition card NI-6348. Gray dashed line indicates the plateau's resistance value deduced from the maxima of the resistance values histogram. Blue (resp. purple) corresponds to the intersect between the data and 1.02 (resp. 0.98) of the resistance value attached to the gray dashed horizontal line. **b)** Similar measurement on the same device at $B = 5.3$ T. **c)** $\nu = 2$ quantum Hall plateau's edges at $I_{\text{bias}} = 160$ nA we deduced applying the protocol described in the main text. The central diagonal line shows the plateau's center estimated from the fits to both of the plateau's edges.

Consequently, $\nu = 2$ plateau's edges were defined as the intersection between the experimental curve and crossing lines lying at $\pm 2\%$ of the resistance value to which the plateau is centered[3]. Applying this protocol to sample HV088 narrow junction C (L x W = 170 x 210 nm^2) data yields the plot shown in Figure C.1.c, the blue (resp. purple) denoting the left (resp. right) points delineating the $\nu = 2$ quantum Hall plateau. We can then estimate the plateau's center taking the middle position in-between the left and right edges at each magnetic field values.

Assuming the corresponding plateau's central position defines a line at constant filling factor $\nu = 2$, equation (C.1) implies a line's slope equating $\phi_0 C/\nu e$. A linear fit to this central line enables us to estimate both the capacitor per unit area C and the charge neutrality point position $V_{\text{D,fit}}$, the corresponding values being summarized in Table C.1 for sample HV088 junctions. A similar approach was conducted for sample DP024 junctions yielding values provided in Table C.2.
Leaving aside the junction E in sample HV088, the capacitor per unit area value appears smaller as the junctions size decreases, a feature suggesting electrodes-induced screening within the graphene.

[3]Note that taking the plateau's resistance averaged value would require to select a gate voltage range on which averaging the resistance, hence introducing some arbitrariness in the capacitor value estimation. Therefore, to overcome such a bias, we simply make a histogram of the resistance values, the peak of which being then taken as the plateau's effective resistance value.

Device	Capacitor per unit area [mF/m^2]	$V_{\text{D,fit}}$ [V]
B	1.2683	-0.1632
C	1.3890	-0.1443
D	1.4323	-0.1516
E	1.1370	-0.2473
F	1.5454	-0.0804

Table C.1: **Capacitor per unit area** and charge neutrality point position values obtained from fits to the center of the $\nu = 2$ QH plateaus in sample HV088 narrow junctions.

Device	Capacitor per unit area [mF/m^2]	$V_{\text{D,fit}}$ [V]
C	1.1151	-0.1162
D	0.8907	-0.1768

Table C.2: **Capacitor per unit area** and charge neutrality point position values obtained from fits to the center of the $\nu = 2$ QH plateaus in sample DP024 narrow junctions.

Bibliography

[1] Blonder, G. E., Tinkham, M. & Klapwijk, T. M. Transition from metallic to tunneling regimes in superconducting microconstrictions: Excess current, charge imbalance, and supercurrent conversion. Phys. Rev. B **25**, 4515--4532 (1982). URL https://link.aps.org/doi/10.1103/PhysRevB.25.4515.

[2] A., C. The many-body ground states of the graphene quantum hall effect and their edge channels. PhD thesis .

[3] von Klitzing, K., Dorda, G. & Pepper, M. New method for high-accuracy determination of the fine-structure constant based on quantized hall resistance. Phys. Rev. Lett. **45**, 494--497 (1980). URL https://link.aps.org/doi/10.1103/PhysRevLett.45.494.

[4] J., W. & von Klitzing, K. Metrology and microscopic picture of the integer quantum hall effect. Phil. Trans. R. Soc. A. **369**, 3954--3974 (2011). URL https://royalsocietypublishing.org/doi/10.1098/rsta.2011.0198.

[5] Novoselov, G. A. M. S. J. D. K. M. G. I. D. S. F. A., K. Two-dimensional gas of massless dirac fermions in graphene. Nature 197--200 (2005). URL https://www.nature.com/articles/nature04233#citeas.

[6] Coissard, A. The many-body ground states of the graphene quantum hall effect and their edge channels (2021).

[7] Tong, D. Lectures on the quantum hall effect (2016). 1606.06687.

[8] Goerbig, M. O. Quantum hall effects (2009). 0909.1998.

[9] Halperin, B. I. Quantized hall conductance, current-carrying edge states, and the existence of extended states in a two-dimensional disordered potential. Phys. Rev. B **25**, 2185--2190 (1982). URL https://link.aps.org/doi/10.1103/PhysRevB.25.2185.

[10] Abanin, D. A., Lee, P. A. & Levitov, L. S. Spin-filtered edge states and quantum hall effect in graphene. Phys. Rev. Lett. **96**, 176803 (2006). URL https://link.aps.org/doi/10.1103/PhysRevLett.96.176803.

[11] Büttiker, M. Absence of backscattering in the quantum hall effect in multiprobe conductors. Phys. Rev. B **38**, 9375--9389 (1988). URL https://link.aps.org/doi/10.1103/PhysRevB.38.9375.

[12] Brey, L. & Fertig, H. A. Edge states and the quantized hall effect in graphene. Phys. Rev. B **73**, 195408 (2006). URL https://link.aps.org/doi/10.1103/PhysRevB.73.195408.

[13] Cao, Y. et al. Unconventional superconductivity in magic-angle graphene superlattices. Nature **556**, 43--50 (2018).

[14] Garisto, D. Five years of superconductivity in magic-angle graphene. Physics Today (2023).

[15] Saint-James, D. Excitations élémentaires au voisinage de la surface de séparation d'un métal normal et d'un métal supraconducteur. J. Phys. France **25**, 899--905 (1964). URL https://doi.org/10.1051/jphys:019640025010089900.

[16] Andreev, A. F. Thermal conductivity of the intermediate state superconductors. Zh. Eksperim. i Teor. Fiz. **46** (1964).

[17] Giaever, I. Energy gap in superconductors measured by electron tunneling. Phys. Rev. Lett. **5**, 147--148 (1960). URL https://link.aps.org/doi/10.1103/PhysRevLett.5.147.

[18] Mendelssohn, K. & Olsen, J. L. Anomalous heat flow in superconductors. Phys. Rev. **80**, 859--862 (1950). URL https://link.aps.org/doi/10.1103/PhysRev.80.859.

[19] Andreev, A. F. Thermal conductivity of the intermediate state superconductors. ii. Zh. Eksperim. i Teor. Fiz. **47** (1964).

[20] Andreev, A. F. Electron spectrum of the intermediate state of superconductors. Zh. Eksperim. i Teor. Fiz. **49** (1965).

[21] Hoppe, H., Zülicke, U. & Schön, G. Andreev reflection in strong magnetic fields. Phys. Rev. Lett. **84**, 1804--1807 (2000). URL https://link.aps.org/doi/10.1103/PhysRevLett.84.1804.

[22] Zülicke, U., Hoppe, H. & Schön, G. Andreev reflection at superconductor–semiconductor interfaces in high magnetic fields. Physica B: Condensed Matter **298**, 453--456 (2001). URL https://www.sciencedirect.com/science/article/pii/S0921452601003611. International Conference on High Magnetic Fields in Semiconductors.

[23] Giazotto, F., Governale, M., Zülicke, U. & Beltram, F. Andreev reflection and cyclotron motion at superconductor---normal-metal interfaces. Phys. Rev. B **72**, 054518 (2005). URL https://link.aps.org/doi/10.1103/PhysRevB.72.054518.

[24] Takagaki, Y. Transport properties of semiconductor-superconductor junctions in quantizing magnetic fields. Phys. Rev. B **57**, 4009--4016 (1998). URL https://link.aps.org/doi/10.1103/PhysRevB.57.4009.

[25] Asano, Y. Magnetoconductance oscillations in ballistic semiconductor-superconductor junctions. Phys. Rev. B **61**, 1732--1735 (2000). URL https://link.aps.org/doi/10.1103/PhysRevB.61.1732.

[26] Abramowitz, M. & Stegun, I. A. Handbook of Mathematical Functions (Dover Publications, New York, 1972).

[27] Heida, J. P., van Wees, B. J., Klapwijk, T. M. & Borghs, G. Nonlocal supercurrent in mesoscopic josephson junctions. Phys. Rev. B **57**, R5618--R5621 (1998). URL https://link.aps.org/doi/10.1103/PhysRevB.57.R5618.

[28] Ma, M. & Zyuzin, A. Y. Josephson effect in the quantum hall regime. Europhysics Letters **21**, 941 (1993). URL https://dx.doi.org/10.1209/0295-5075/21/9/011.

[29] van Ostaay, J. A. M., Akhmerov, A. R. & Beenakker, C. W. J. Spin-triplet supercurrent carried by quantum hall edge states through a josephson junction. Phys. Rev. B **83**, 195441 (2011). URL https://link.aps.org/doi/10.1103/PhysRevB.83.195441.

[30] Alavirad, Y., Lee, J., Lin, Z.-X. & Sau, J. D. Chiral supercurrent through a quantum hall weak link. Phys. Rev. B **98**, 214504 (2018). URL https://link.aps.org/doi/10.1103/PhysRevB.98.214504.

[31] Stone, M. & Lin, Y. Josephson currents in quantum hall devices. Phys. Rev. B **83**, 224501 (2011). URL https://link.aps.org/doi/10.1103/PhysRevB.83.224501.

[32] Déprez, C. et al. A tunable fabry--pérot quantum hall interferometer in graphene. Nature Nanotechnology **16**, 555--562 (2021). URL https://doi.org/10.1038/s41565-021-00847-x.

[33] Mazin, I. I., Golubov, A. A. & Zaikin, A. D. "chain scenario" for josephson tunneling with π shift in $\mathrm{yba_2cu_3o_7}$. Phys. Rev. Lett. **75**, 2574--2577 (1995). URL https://link.aps.org/doi/10.1103/PhysRevLett.75.2574.

[34] Kataoka, M. et al. Time-of-flight measurements of single-electron wave packets in quantum hall edge states. Phys. Rev. Lett. **116**, 126803 (2016). URL https://link.aps.org/doi/10.1103/PhysRevLett.116.126803.

[35] McClure, D. T. et al. Edge-state velocity and coherence in a quantum hall fabry-pérot interferometer. Phys. Rev. Lett. **103**, 206806 (2009). URL https://link.aps.org/doi/10.1103/PhysRevLett.103.206806.

[36] Tinkham, M. Introduction to superconductivity, second edition. Dover publications .

[37] Manesco, A. L. R., Flór, I. M., Liu, C.-X. & Akhmerov, A. R. Mechanisms of andreev reflection in quantum hall graphene (2021). URL https://arxiv.org/abs/2103.06722.

[38] Akhmerov, A. R. & Beenakker, C. W. J. Boundary conditions for dirac fermions on a terminated honeycomb lattice. Phys. Rev. B **77**, 085423 (2008). URL https://link.aps.org/doi/10.1103/PhysRevB.77.085423.

[39] Amet, C. T. B. I. V. W. J. W. K. T. T. D. R. S. Y. M. B. Y. T. S. F. G., F.; Ke. Supercurrent in the quantum hall regime. Science **352**, 966--969 (2016). URL https://www.science.org/doi/10.1126/science.aad6203.

[40] Seredinski, A. et al. Quantum hall-based superconducting interference device. Science Advances **5**, eaaw8693 (2019). URL https://www.science.org/doi/abs/10.1126/sciadv.aaw8693.

[41] Zhao, L. et al. Interference of chiral andreev edge states. Nature Physics **16**, 862--867 (2020). URL https://doi.org/10.1038/s41567-020-0898-5.

[42] Lee, G.-H. et al. Inducing superconducting correlation in quantum hall edge states. Nature Physics **13**, 693--698 (2017). URL https://doi.org/10.1038/nphys4084.

[43] Gül, O. et al. Andreev reflection in the fractional quantum hall state. Phys. Rev. X **12**, 021057 (2022). URL https://link.aps.org/doi/10.1103/PhysRevX.12.021057.

[44] Clarke, D. J., Alicea, J. & Shtengel, K. Exotic non-abelian anyons from conventional fractional quantum hall states. Nature Communications **4**, 1348 (2013). URL https://doi.org/10.1038/ncomms2340.

[45] Rowell, J. M. Magnetic field dependence of the josephson tunnel current. Phys. Rev. Lett. **11**, 200--202 (1963). URL https://link.aps.org/doi/10.1103/PhysRevLett.11.200.

[46] Benistant, P. A. M., van Kempen, H. & Wyder, P. Direct observation of andreev reflection. Phys. Rev. Lett. **51**, 817--820 (1983). URL https://link.aps.org/doi/10.1103/PhysRevLett.51.817.

[47] Pfeiffer, L. & West, K. The role of mbe in recent quantum hall effect physics discoveries. Physica E: Low-dimensional Systems and Nanostructures **20**, 57--64 (2003). URL https://www.sciencedirect.com/science/article/pii/S1386947703005174. Proceedings of the International Symposium "Quantum Hall Effect: Past, Present and Future.

[48] Gao, J. R. et al. Low temperature current transport of sn-gaas contacts. Applied Physics Letters **63**, 334--336 (1993). URL https://doi.org/10.1063/1.110034.

[49] Marsh, A. M. & Williams, D. A. Granular superconductor contacts to two-dimensional electron gases. Journal of Vacuum Science & Technology A **14**, 2577--2581 (1996). URL https://doi.org/10.1116/1.579984.

[50] Kastalsky, A. et al. Observation of pair currents in superconductor-semiconductor contacts. Phys. Rev. Lett. **67**, 3026--3029 (1991). URL https://link.aps.org/doi/10.1103/PhysRevLett.67.3026.

[51] Taboryski, R. et al. Andreev reflections at interfaces between δ-doped gaas and superconducting al films. Applied Physics Letters **69**, 656--658 (1996). URL https://doi.org/10.1063/1.117796.

[52] De Franceschi, S. et al. Truly ohmic contacts in engineered al/si/ingaas(001) diodes. Applied Physics Letters **72**, 1996--1998 (1998). URL https://doi.org/10.1063/1.121244.

[53] De Franceschi, S. et al. Andreev reflection in si-engineered al/ingaas hybrid junctions. Applied Physics Letters **73**, 3890--3892 (1998). URL https://doi.org/10.1063/1.122926.

[54] Franceschi, S. D. et al. Andreev reflection in engineered al/si/inxga1−xas(001) junctions. Philosophical Magazine B **80**, 817--823 (2000). URL https://doi.org/10.1080/13642810008209788. https://doi.org/10.1080/13642810008209788.

[55] Moore, T. D. & Williams, D. A. Andreev reflection at high magnetic fields. Phys. Rev. B **59**, 7308--7311 (1999). URL https://link.aps.org/doi/10.1103/PhysRevB.59.7308.

[56] Takayanagi, H., Akazaki, T., Kawamura, M., Harada, Y. & Nitta, J. Superconducting junctions using algaas/gaas heterostructures with high hc2 nbn electrodes. Physica E: Low-dimensional Systems and Nanostructures **12**, 922--926 (2002). URL https://www.sciencedirect.com/science/article/pii/S1386947701004106. Proceedings of the Fourteenth International Conference on the Ele ctronic Properties of Two-Dimensional Systems.

[57] Wan, Z. et al. Induced superconductivity in high-mobility two-dimensional electron gas in gallium arsenide heterostructures. Nature Communications **6**, 7426 (2015). URL https://doi.org/10.1038/ncomms8426.

[58] Lenssen, K. ?. M. H. et al. Andreev reflection at superconducting contacts to gaas/algaas heterostructures. Applied Physics Letters **63**, 2079--2081 (1993). URL https://doi.org/10.1063/1.110598.

[59] Takayanagi, H. & Akazaki, T. Semiconductor-coupled superconducting junctions using nbn electrodes with high hc2 and tc. Physica B: Condensed Matter **249-251**, 462--466 (1998). URL https://www.sciencedirect.com/science/article/pii/S0921452698001641.

[60] Verevkin, A. A. et al. Multiple andreev reflection in hybrid algaas/gaas structures with superconducting nbn contacts. Semiconductors **33**, 551--554 (1999). URL https://doi.org/10.1134/1.1187726.

[61] Eroms, J., Weiss, D., Boeck, J. D., Borghs, G. & Zülicke, U. Andreev reflection at high magnetic fields: Evidence for electron and hole transport in edge states. Phys. Rev. Lett. **95**, 107001 (2005). URL https://link.aps.org/doi/10.1103/PhysRevLett.95.107001.

[62] Komatsu, K., Li, C., Autier-Laurent, S., Bouchiat, H. & Guéron, S. Superconducting proximity effect in long superconductor/graphene/superconductor junctions: From specular andreev reflection at zero field to the quantum hall regime. Phys. Rev. B **86**, 115412 (2012). URL https://link.aps.org/doi/10.1103/PhysRevB.86.115412.

[63] Rickhaus, P., Weiss, M., Marot, L. & Schönenberger, C. Quantum hall effect in graphene with superconducting electrodes. Nano Letters **12**, 1942--1945 (2012). URL https://doi.org/10.1021/nl204415s. PMID: 22417183, https://doi.org/10.1021/nl204415s.

[64] V.E. Calado, G. N. M. D. A. A. K. W. T. T. T. K. L. V., S. Goswami. Ballistic josephson junctions in edge-contacted graphene. Nature Nanotechnology **10**, 761--764 (2015).

[65] Allen, M. et al. Spatially resolved edge currents and guided-wave electronic states in graphene. Nature Physics (2016). URL http://www.nature.com/nphys/journal/v12/n2/full/nphys3534.html.

[66] M. Ben Shalom, V. F. A. M. A. K. K. N. C. W. K. W. T. T. A. G. J. P., M.J. Zhu. Quantum oscillations of the critical current and high-field superconducting proximity in ballistic graphene. Nature Physics **12**, 318--322 (2016).

[67] Zhi, J. et al. Coexistence of induced superconductivity and quantum hall states in insb nanosheets. Phys. Rev. B **99**, 245302 (2019). URL https://link.aps.org/doi/10.1103/PhysRevB.99.245302.

[68] Vignaud, H. et al. Evidence for chiral supercurrent in quantum hall josephson junctions (2023). 2305.01766.

[69] de C. Chamon, C., Freed, D. E., Kivelson, S. A., Sondhi, S. L. & Wen, X. G. Two point-contact interferometer for quantum hall systems. Phys. Rev. B **55**, 2331--2343 (1997). URL https://link.aps.org/doi/10.1103/PhysRevB.55.2331.

[70] Novoselov, K. S. et al. Electric field effect in atomically thin carbon films. Science **306**, 666--669 (2004). URL https://www.science.org/doi/abs/10.1126/science.1102896. https://www.science.org/doi/pdf/10.1126/science.1102896.

[71] Zhang, T. Y. S. H. K. P., Y. Experimental observation of the quantum hall effect and berry's phase in graphene. Nature 201--204 (2005). URL https://www.nature.com/articles/nature04235#citeas.

[72] Heersche, J.-H. P. O. J. V. L. M. A. F., H. Bipolar supercurrent in graphene. Nature 56--59 (2007). URL https://www.nature.com/articles/nature05555#citeas.

[73] Akhmerov, A. R. & Beenakker, C. W. J. Detection of valley polarization in graphene by a superconducting contact. Phys. Rev. Lett. **98**, 157003 (2007). URL https://link.aps.org/doi/10.1103/PhysRevLett.98.157003.

[74] Wang, L. et al. One-dimensional electrical contact to a two-dimensional material. Science **342**, 614--617 (2013). URL https://www.science.org/doi/abs/10.1126/science.1244358. https://www.science.org/doi/pdf/10.1126/science.1244358.

[75] Schneider, B. H., Etaki, S., van der Zant, H. S. J. & Steele, G. A. Coupling carbon nanotube mechanics to a superconducting circuit. Scientific Reports **2**, 599 (2012). URL https://doi.org/10.1038/srep00599.

[76] Park, J. et al. Short ballistic josephson coupling in planar graphene junctions with inhomogeneous carrier doping. Phys. Rev. Lett. **120**, 077701 (2018). URL https://link.aps.org/doi/10.1103/PhysRevLett.120.077701.

[77] Sze, S. Physics of Semiconductor Devices (John Wiley and Sons (WIE), 1981), 2nd edn.

[78] Giovannetti, G. et al. Doping graphene with metal contacts. Phys. Rev. Lett. **101**, 026803 (2008). URL https://link.aps.org/doi/10.1103/PhysRevLett.101.026803.

[79] Robinson, J. A. et al. Contacting graphene. Applied Physics Letters **98**, 053103 (2011). URL https://doi.org/10.1063/1.3549183.

[80] Octavio, M., Tinkham, M., Blonder, G. E. & Klapwijk, T. M. Subharmonic energy-gap structure in superconducting constrictions. Phys. Rev. B **27**, 6739--6746 (1983). URL https://link.aps.org/doi/10.1103/PhysRevB.27.6739.

[81] Flensberg, K., Hansen, J. B. & Octavio, M. Subharmonic energy-gap structure in superconducting weak links. Phys. Rev. B **38**, 8707--8711 (1988). URL https://link.aps.org/doi/10.1103/PhysRevB.38.8707.

[82] Niebler, G., Cuniberti, G. & Novotný, T. Analytical calculation of the excess current in the octavio–tinkham–blonder–klapwijk theory. Superconductor Science and Technology **22**, 085016 (2009). URL https://dx.doi.org/10.1088/0953-2048/22/8/085016.

[83] Ke, C. T. et al. Anomalous periodicity of magnetic interference patterns in encapsulated graphene josephson junctions. Phys. Rev. Res. **1**, 033084 (2019). URL https://link.aps.org/doi/10.1103/PhysRevResearch.1.033084.

[84] Ojeda-Aristizabal, C., Ferrier, M., Guéron, S. & Bouchiat, H. Tuning the proximity effect in a superconductor-graphene-superconductor junction. Phys. Rev. B **79**, 165436 (2009). URL https://link.aps.org/doi/10.1103/PhysRevB.79.165436.

[85] Rosenthal, P. A., Beasley, M. R., Char, K., Colclough, M. S. & Zaharchuk, G. Flux focusing effects in planar thin-film grain-boundary josephson junctions. Applied Physics Letters **59**, 3482--3484 (1991). URL https://doi.org/10.1063/1.105660.

[86] Borzenets, I. V., Coskun, U. C., Jones, S. J. & Finkelstein, G. Phase diffusion in graphene-based josephson junctions. Phys. Rev. Lett. **107**, 137005 (2011). URL https://link.aps.org/doi/10.1103/PhysRevLett.107.137005.

[87] Jo, M. et al. Quantum hall valley splitters and a tunable mach-zehnder interferometer in graphene. Phys. Rev. Lett. **126**, 146803 (2021). URL https://link.aps.org/doi/10.1103/PhysRevLett.126.146803.

[88] Chen, M. et al. Fluorination of edges and central areas of monolayer graphene by sf_6 and chf_3 plasma treatments. Journal of Nanoscience and Nanotechnology **13**, 1331--1334 (2013).

[89] Childres, I., Jauregui, L. A., Tian, J. & Chen, Y. P. Effect of oxygen plasma etching on graphene studied using raman spectroscopy and electronic transport measurements. New Journal of Physics **13**, 025008 (2011). URL https://dx.doi.org/10.1088/1367-2630/13/2/025008.

[90] Roulleau, P. et al. Direct measurement of the coherence length of edge states in the integer quantum hall regime. Phys. Rev. Lett. **100**, 126802 (2008). URL https://link.aps.org/doi/10.1103/PhysRevLett.100.126802.

[91] Hatefipour, M. et al. Induced superconducting pairing in integer quantum hall edge states. Nano Letters **22**, 6173--6178 (2022). URL https://doi.org/10.1021/acs.nanolett.2c01413. PMID: 35867620, https://doi.org/10.1021/acs.nanolett.2c01413.

[92] Zhao, L. et al. Loss and decoherence at the quantum hall - superconductor interface (2022). 2210.04842.

[93] Clarke, D. J., Alicea, J. & Shtengel, K. Exotic circuit elements from zero-modes in hybrid superconductor--quantum-hall systems. Nature Physics **10**, 877--882 (2014). URL https://doi.org/10.1038/nphys3114.

[94] Hou, Z., Xing, Y., Guo, A.-M. & Sun, Q.-F. Crossed andreev effects in two-dimensional quantum hall systems. Phys. Rev. B **94**, 064516 (2016). URL https://link.aps.org/doi/10.1103/PhysRevB.94.064516.

[95] Uday, A. et al. Induced superconducting correlations in the quantum anomalous hall insulator (2023). 2307.08578.

[96] Li, J. I. A. et al. Even-denominator fractional quantum hall states in bilayer graphene. Science **358**, 648--652 (2017). URL https://doi.org/10.1126/science.aao2521.

[97] Zibrov, A. A. et al. Tunable interacting composite fermion phases in a half-filled bilayer-graphene landau level. Nature **549**, 360--364 (2017). URL https://doi.org/10.1038/nature23893.

[98] Wakamura, T., Hasegawa, N., Ohnishi, K., Niimi, Y. & Otani, Y. Spin injection into a superconductor with strong spin-orbit coupling. Phys. Rev. Lett. **112**, 036602 (2014). URL https://link.aps.org/doi/10.1103/PhysRevLett.112.036602.

[99] Schiller, N. et al. Superconductivity and fermionic dissipation in quantum hall edges. Phys. Rev. B **107**, L161105 (2023). URL https://link.aps.org/doi/10.1103/PhysRevB.107.L161105.

[100] Barkeshli, M. & Qi, X.-L. Synthetic topological qubits in conventional bilayer quantum hall systems. Phys. Rev. X **4**, 041035 (2014). URL https://link.aps.org/doi/10.1103/PhysRevX.4.041035.

[101] Barkeshli, M., Oreg, Y. & Qi, X.-L. Experimental proposal to detect topological ground state degeneracy (2014). 1401.3750.

[102] Schiller, N., Cornfeld, E., Berg, E. & Oreg, Y. Predicted signatures of topological superconductivity and parafermion zero modes in fractional quantum hall edges. Phys. Rev. Res. **2**, 023296 (2020). URL https://link.aps.org/doi/10.1103/PhysRevResearch.2.023296.

[103] Michelsen, A. B., Schmidt, T. L. & Idrisov, E. G. Current correlations of cooper-pair tunneling into a quantum hall system. Phys. Rev. B **102**, 125402 (2020). URL https://link.aps.org/doi/10.1103/PhysRevB.102.125402.

[104] Svetogorov, A. E., Loss, D. & Klinovaja, J. Insulating regime of an underdamped current-biased josephson junction supporting z_3 and z_4 parafermions. Phys. Rev. B **103**, L180505 (2021). URL https://link.aps.org/doi/10.1103/PhysRevB.103.L180505.

[105] Galambos, T. H., Ronetti, F., Hetényi, B., Loss, D. & Klinovaja, J. Crossed andreev reflection in spin-polarized chiral edge states due to the meissner effect. Phys. Rev. B **106**, 075410 (2022). URL https://link.aps.org/doi/10.1103/PhysRevB.106.075410.

[106] Moehle, C. M. et al. Insbas two-dimensional electron gases as a platform for topological superconductivity. Nano Letters **21**, 9990--9996 (2021). URL https://doi.org/10.1021/acs.nanolett.1c03520. PMID: 34793173, https://doi.org/10.1021/acs.nanolett.1c03520.

[107] P.Blake, S. M. F. S. L. P. A. Z. R. N. I. G. K. N. A. G., R. Yang. Influence of metal contacts and charge inhomogeneity on transport properties of graphene near the neutrality point. Solid State Communications **149**, 1068--1071 (2009).

[108] E.J.H. Lee, R. W. M. B. K. K., K. Balasubramanian. Contact and edge effects in graphene devices. Nature Nanotechnology **3**, 486--490 (2008).

[109] Hong, S. et al. Ultralow-dielectric-constant amorphous boron nitride. Nature **582**, 511--514 (2020). URL https://doi.org/10.1038/s41586-020-2375-9.

[110] Courtois, H., Meschke, M., Peltonen, J. T. & Pekola, J. P. Origin of hysteresis in a proximity josephson junction. Phys. Rev. Lett. **101**, 067002 (2008). URL https://link.aps.org/doi/10.1103/PhysRevLett.101.067002.

[111] Titov, M. & Beenakker, C. W. J. Josephson effect in ballistic graphene. Phys. Rev. B **74**, 041401 (2006). URL https://link.aps.org/doi/10.1103/PhysRevB.74.041401.

[112] Likharev, K. K. Superconducting weak links. Rev. Mod. Phys. **51**, 101--159 (1979). URL https://link.aps.org/doi/10.1103/RevModPhys.51.101.

[113] Li, C., Guéron, S., Chepelianskii, A. & Bouchiat, H. Full range of proximity effect probed with superconductor/graphene/superconductor junctions. Phys. Rev. B **94**, 115405 (2016). URL https://link.aps.org/doi/10.1103/PhysRevB.94.115405.

[114] Du, X., Skachko, I. & Andrei, E. Y. Josephson current and multiple andreev reflections in graphene sns junctions. Phys. Rev. B **77**, 184507 (2008). URL https://link.aps.org/doi/10.1103/PhysRevB.77.184507.

[115] Clarke, J. & Braginski, A. I. The squid handbook, volume i: Fundamentals and technology of squids and squid systems (2004).

[116] Barone, A. & Paternò, G. Physics and applications of the josephson effect (1982).

[117] Miller, S. L., Biagi, K. R., Clem, J. R. & Finnemore, D. K. Critical currents of cross-type superconducting-normal-superconducting junctions in perpendicular magnetic fields. Phys. Rev. B **31**, 2684--2693 (1985). URL https://link.aps.org/doi/10.1103/PhysRevB.31.2684.

[118] Gubankov, V. N., Lisitskii, M. P., Serpuchenko, I. L., Sklokin, F. N. & Fistul', M. V. Influence of trapped abrikosov vortices on the critical current of the josephson tunnel junction. Sov. Phys. JETP **73**, 734 (1991). URL https://dx.doi.org/10.1088/0953-2048/5/3/011.

[119] van Baarle, G. J. C., Troianovski, A. M., Nishizaki, T., Kes, P. H. & Aarts, J. Imaging of vortex configurations in thin films by scanning-tunneling microscopy. Applied Physics Letters **82**, 1081--1083 (2003). URL https://doi.org/10.1063/1.1554481.

[120] Williams, J. R., Abanin, D. A., DiCarlo, L., Levitov, L. S. & Marcus, C. M. Quantum hall conductance of two-terminal graphene devices. Phys. Rev. B **80**, 045408 (2009). URL https://link.aps.org/doi/10.1103/PhysRevB.80.045408.

[121] Abanin, D. A. & Levitov, L. S. Conformal invariance and shape-dependent conductance of graphene samples. Phys. Rev. B **78**, 035416 (2008). URL https://link.aps.org/doi/10.1103/PhysRevB.78.035416.

[122] Rendell, R. W. & Girvin, S. M. Hall voltage dependence on inversion-layer geometry in the quantum hall-effect regime. Phys. Rev. B **23**, 6610--6614 (1981). URL https://link.aps.org/doi/10.1103/PhysRevB.23.6610.

[123] Dykhne, A. M. & Ruzin, I. M. Theory of the fractional quantum hall effect: The two-phase model. Phys. Rev. B **50**, 2369--2379 (1994). URL https://link.aps.org/doi/10.1103/PhysRevB.50.2369.

[124] Duerr, F., Oostinga, J. B., Gould, C. & Molenkamp, L. W. Edge state transport through disordered graphene nanoribbons in the quantum hall regime. Phys. Rev. B **86**, 081410 (2012). URL https://link.aps.org/doi/10.1103/PhysRevB.86.081410.

[125] Orlita, M. et al. Carrier scattering from dynamical magnetoconductivity in quasineutral epitaxial graphene. Phys. Rev. Lett. **107**, 216603 (2011). URL https://link.aps.org/doi/10.1103/PhysRevLett.107.216603.

[126] Alphenaar, B. W., McEuen, P. L., Wheeler, R. G. & Sacks, R. N. Selective equilibration among the current-carrying states in the quantum hall regime. Phys. Rev. Lett. **64**, 677--680 (1990). URL https://link.aps.org/doi/10.1103/PhysRevLett.64.677.

[127] Dubos, P. et al. Josephson critical current in a long mesoscopic s-n-s junction. Phys. Rev. B **63**, 064502 (2001). URL https://link.aps.org/doi/10.1103/PhysRevB.63.064502.

[128] Jarillo-Herrero, P., van Dam, J. A. & Kouwenhoven, L. P. Quantum supercurrent transistors in carbon nanotubes. Nature **439**, 953--956 (2006). URL https://doi.org/10.1038/nature04550.

[129] Josephson, B. Possible new effects in superconductive tunnelling. Physics Letters **1**, 251--253 (1962). URL https://www.sciencedirect.com/science/article/pii/0031916362913690.

[130] Shapiro, S. Josephson currents in superconducting tunneling: The effect of microwaves and other observations. Phys. Rev. Lett. **11**, 80--82 (1963). URL https://link.aps.org/doi/10.1103/PhysRevLett.11.80.

[131] Larson, T. F. Q. et al. Zero crossing steps and anomalous shapiro maps in graphene josephson junctions. Nano Letters **20**, 6998--7003 (2020). URL https://doi.org/10.1021/acs.nanolett.0c01598. PMID: 32902995, https://doi.org/10.1021/acs.nanolett.0c01598.

[132] Batov, I. E., Schäpers, T., Chtchelkatchev, N. M., Hardtdegen, H. & Ustinov, A. V. Andreev reflection and strongly enhanced magnetoresistance oscillations in $\mathrm{ga}_x\mathrm{in}_{1-x}\mathrm{AsInP}$ heterostructures with superconducting contacts. Phys. Rev. B **76**, 115313 (2007). URL https://link.aps.org/doi/10.1103/PhysRevB.76.115313.

[133] Chtchelkatchev, N. M. Conductance of a semiconductor(2deg)-superconductor junction in high magnetic field. Journal of Experimental and Theoretical Physics Letters **73**, 94--97 (2001). URL https://doi.org/10.1134/1.1358428.

[134] Chtchelkatchev, N. M. & Burmistrov, I. S. Conductance oscillations with magnetic field of a two-dimensional electron gas--superconductor junction. Phys. Rev. B **75**, 214510 (2007). URL https://link.aps.org/doi/10.1103/PhysRevB.75.214510.

[135] Eaves, L. & Sheard, F. W. Size-dependent quantised breakdown of the dissipationless quantum hall effect in narrow channels. Semiconductor Science and Technology **1**, 346 (1986). URL https://dx.doi.org/10.1088/0268-1242/1/6/002.

[136] Komiyama, S. & Kawaguchi, Y. Heat instability of quantum hall conductors. Phys. Rev. B **61**, 2014--2027 (2000). URL https://link.aps.org/doi/10.1103/PhysRevB.61.2014.

[137] Graef, H. Dirac fermion optics and plasmonics in graphene microwave devices (2019).

[138] Carrega, M., Chirolli, L., Heun, S. & Sorba, L. Anyons in quantum hall interferometry. Nature Reviews Physics **3**, 698--711 (2021). URL https://doi.org/10.1038/s42254-021-00351-0.

[139] Ronen, Y. et al. Aharonov--bohm effect in graphene-based fabry--pérot quantum hall interferometers. Nature Nanotechnology **16**, 563--569 (2021). URL https://doi.org/10.1038/s41565-021-00861-z.

[140] Halperin, B. I., Stern, A., Neder, I. & Rosenow, B. Theory of the fabry-pérot quantum hall interferometer. Phys. Rev. B **83**, 155440 (2011). URL https://link.aps.org/doi/10.1103/PhysRevB.83.155440.

[141] Roulleau, P. et al. Noise dephasing in edge states of the integer quantum hall regime. Phys. Rev. Lett. **101**, 186803 (2008). URL https://link.aps.org/doi/10.1103/PhysRevLett.101.186803.

[142] Zhang, Y. et al. Distinct signatures for coulomb blockade and aharonov-bohm interference in electronic fabry-perot interferometers. Phys. Rev. B **79**, 241304 (2009). URL https://link.aps.org/doi/10.1103/PhysRevB.79.241304.

[143] Tóvári, E., Makk, P., Rickhaus, P., Schönenberger, C. & Csonka, S. Signatures of single quantum dots in graphene nanoribbons within the quantum hall regime. Nanoscale **8**, 11480--11486 (2016). URL http://dx.doi.org/10.1039/C6NR00187D.

[144] Sahasrabudhe, H. et al. Optimization of edge state velocity in the integer quantum hall regime. Phys. Rev. B **97**, 085302 (2018). URL https://link.aps.org/doi/10.1103/PhysRevB.97.085302.

[145] Wang, Y. et al. Quantum hall phase in graphene engineered by interfacial charge coupling. Nature Nanotechnology **17**, 1272--1279 (2022). URL https://doi.org/10.1038/s41565-022-01248-4.

[146] Cai, J. et al. Signatures of fractional quantum anomalous hall states in twisted mote2. Nature **622**, 63--68 (2023). URL https://doi.org/10.1038/s41586-023-06289-w.

[147] Park, H. et al. Observation of fractionally quantized anomalous hall effect. Nature **622**, 74--79 (2023). URL https://doi.org/10.1038/s41586-023-06536-0.

[148] Xu, F. et al. Observation of integer and fractional quantum anomalous hall effects in twisted bilayer mote_2. Phys. Rev. X **13**, 031037 (2023). URL https://link.aps.org/doi/10.1103/PhysRevX.13.031037.

[149] Lu, Z. et al. Fractional quantum anomalous hall effect in a graphene moire superlattice (2023). 2309.17436.

[150] Nachtwei, G. Breakdown of the quantum hall effect. Physica E: Low-dimensional Systems and Nanostructures **4**, 79--101 (1999). URL https://www.sciencedirect.com/science/article/pii/S1386947798002513.

[151] Tian, S. et al. Nonlinear transport of graphene in the quantum hall regime. 2D Materials **4**, 015003 (2016). URL https://dx.doi.org/10.1088/2053-1583/4/1/015003.

[152] Bezryadin, A. Superconductivity in nanowires Fabrication and quantum transport (Wiley-VCH, Germany, 2013). URL http://inis.iaea.org/search/search.aspx?orig_q=RN:44016863. CONDENSED MATTER PHYSICS, SUPERCONDUCTIVITY AND SUPERFLUIDITY.

[153] Kim, H., Gay, F., Del Maestro, A., Sacépé, B. & Rogachev, A. Pair-breaking quantum phase transition in superconducting nanowires. Nature Physics **14**, 912--917 (2018). URL https://doi.org/10.1038/s41567-018-0179-8.

[154] Alicea, J. & Fendley, P. Topological phases with parafermions: Theory and blueprints. Annual Review of Condensed Matter Physics **7**, 119--139 (2016). URL https://doi.org/10.1146/annurev-conmatphys-031115-011336. https://doi.org/10.1146/annurev-conmatphys-031115-011336.

[155] Nayak, C., Simon, S. H., Stern, A., Freedman, M. & Das Sarma, S. Non-abelian anyons and topological quantum computation. Rev. Mod. Phys. **80**, 1083--1159 (2008). URL https://link.aps.org/doi/10.1103/RevModPhys.80.1083.

[156] Zhang, F. & Kane, C. L. Time-reversal-invariant Z_4 fractional josephson effect. Phys. Rev. Lett. **113**, 036401 (2014). URL https://link.aps.org/doi/10.1103/PhysRevLett.113.036401.

[157] Halperin, B. & Jain, J. Fractional Quantum Hall Effects: New Developments (2020).

[158] Ghahari, F., Zhao, Y., Cadden-Zimansky, P., Bolotin, K. & Kim, P. Measurement of the $\nu = 1/3$ fractional quantum hall energy gap in suspended graphene. Phys. Rev. Lett. **106**, 046801 (2011). URL https://link.aps.org/doi/10.1103/PhysRevLett.106.046801.

[159] Assouline, A. et al. Energy gap of the even-denominator fractional quantum hall state in bilayer graphene (2023). 2308.05729.

[160] Ribeiro-Palau, R. et al. High-quality electrostatically defined hall bars in monolayer graphene. Nano Letters **19**, 2583--2587 (2019). URL https://doi.org/10.1021/acs.nanolett.9b00351. PMID: 30839210, https://doi.org/10.1021/acs.nanolett.9b00351.

[161] Zeng, Y. et al. High-quality magnetotransport in graphene using the edge-free corbino geometry. Phys. Rev. Lett. **122**, 137701 (2019). URL https://link.aps.org/doi/10.1103/PhysRevLett.122.137701.

[162] Zibrov, A. A. et al. Even-denominator fractional quantum hall states at an isospin transition in monolayer graphene. Nature Physics **14**, 930--935 (2018). URL https://doi.org/10.1038/s41567-018-0190-0.

[163] Halbertal, D. et al. Imaging resonant dissipation from individual atomic defects in graphene. Science **358**, 1303--1306 (2017). URL https://www.science.org/doi/abs/10.1126/science.aan0877. https://www.science.org/doi/pdf/10.1126/science.aan0877.

[164] Vera-Marun, I. J. et al. Quantum hall transport as a probe of capacitance profile at graphene edges. Applied Physics Letters **102**, 013106 (2013). URL https://doi.org/10.1063/1.4773589. https://doi.org/10.1063/1.4773589.

[165] Ki, D.-K. & Morpurgo, A. F. Crossover from coulomb blockade to quantum hall effect in suspended graphene nanoribbons. Phys. Rev. Lett. **108**, 266601 (2012). URL https://link.aps.org/doi/10.1103/PhysRevLett.108.266601.

[166] Cui, Y.-T. et al. Unconventional correlation between quantum hall transport quantization and bulk state filling in gated graphene devices. Phys. Rev. Lett. **117**, 186601 (2016). URL https://link.aps.org/doi/10.1103/PhysRevLett.117.186601.